

AD-A089 143

CAI BARRINGTON ILL  
ADVANCED ELECTRO-OPTICAL TRACKER/RANGER. (U)  
JUN 80 R A BENNETT, D N DEFOE  
CAI-7323-0180-5

F/6 17/8

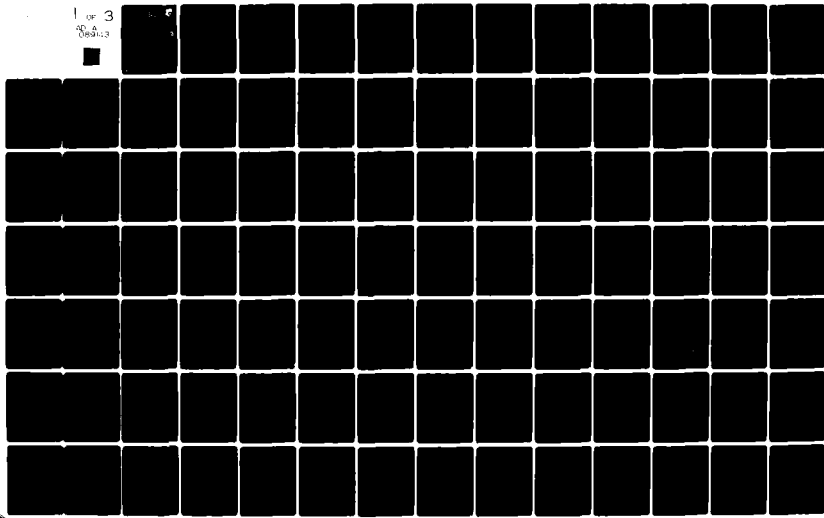
F33615-78-C-1562

AFWAL-TR-80-1034

NL

UNCLASSIFIED

1 OF 3  
0609142



AFWAL-TR-80-1034

LEVEL  
2



AD A 089143

## ADVANCED ELECTRO-OPTICAL TRACKER/RANGER

CAI, a Division of Recon/Optical, Inc.  
Barrington, Illinois 60010



May 1980

Final Report for Period October 1978 - February 1980

Approved for public release, distribution unlimited

ONE COPY

AIR FORCE AVIONICS LABORATORY  
Air Force Wright Aeronautical Laboratories  
Air Force Systems Command  
Wright Patterson Air Force Base, Ohio 45433

80 9 12 051

NOTICE

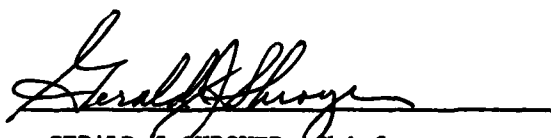
When Government drawings, specifications, or other data are used for any purpose other than in connection with a definitely related Government procurement operation, the United States Government thereby incurs no responsibility nor any obligation whatsoever; and the fact that the government may have formulated, furnished, or in any way supplied the said drawings, specifications, or other data, is not to be regarded by implication or otherwise as in any manner licensing the holder or any other person or corporation, or conveying any rights or permission to manufacture use, or sell any patented invention that may in any way be related thereto.

This report has been reviewed by the Office of Public Affairs (ASD/PA) and is releasable to the National Technical Information Service (NTIS). At NTIS, it will be available to the general public, including foreign nations.

This technical report has been reviewed and is approved for publication.



RAYMOND C RANG, Project Engineer  
Reconnaissance Systems Group



GERALD J SHROYER, Chief  
Reconnaissance Systems Group

FOR THE COMMANDER



GALE D URBAN, Chief  
Electro-Optics and Reconnaissance Branch  
Recon & Weapon Delivery Division  
Avionics Laboratory

"If your address has changed, if you wish to be removed from our mailing list, or if the addressee is no longer employed by your organization please notify AFWAL/AARI, W-PAFB, OH 45433 to help us maintain a current mailing list".

Copies of this report should not be returned unless return is required by security considerations, contractual obligations, or notice on a specific document.

SECURITY CLASSIFICATION OF THIS PAGE (When Data Entered)

<b>(19) REPORT DOCUMENTATION PAGE</b>		READ INSTRUCTIONS BEFORE COMPLETING FORM											
1. REPORT NUMBER <i>AFWAL-TR-80-1034</i>	2. GOVT ACCESSION NO. <i>AD-A089 143</i>	3. RECIPIENT'S CATALOG NUMBER											
4. TITLE (and Subtitle) <i>Advanced Electro-Optical Tracker/Ranger</i>	5. TYPE OF REPORT & PERIOD COVERED <i>Final Report October 1978 - February 1980</i>												
6. AUTHOR(s) <i>R.A. Bennett and D.N. DeFoe</i>	7. PERFORMING ORGANIZATION NAME AND ADDRESS <i>CAI, a Division of Recon/Optical, Inc. Barrington, Illinois 60010</i>												
8. CONTROLLING OFFICE NAME AND ADDRESS <i>AFWAL/AARI Wright-Patterson Air Force Base, Ohio</i>	9. PROGRAM ELEMENT, PROJECT, TASK AREA & WORK UNIT NUMBERS <i>Project 7629 Task 03 Work Unit 55</i>												
10. MONITORING AGENCY NAME & ADDRESS (if different from Controlling Office)	11. REPORT DATE <i>Jun 1980</i>												
12. NUMBER OF PAGES <i>218</i>	13. SECURITY CLASS. (of this report) <i>Unclassified</i>												
14. DISTRIBUTION STATEMENT (of this Report)  <i>Approved for public release; distribution unlimited</i>	15a. DECLASSIFICATION/DOWNGRADING SCHEDULE												
16. DISTRIBUTION STATEMENT (of the abstract entered in Block 20, if different from Report)													
17. SUPPLEMENTARY NOTES													
18. KEY WORDS (Continue on reverse side if necessary and identify by block number)  <table> <tr><td>Electro-optical tracker/ranger</td><td>Charge coupled device (CCD)</td></tr> <tr><td>Passive ranging</td><td>Correlation processing</td></tr> <tr><td>Target tracking</td><td>Stereometric ranging</td></tr> <tr><td>Air-to-air fire control</td><td>Automatic target detection</td></tr> <tr><td>Gun fire control</td><td>Target identification</td></tr> </table>				Electro-optical tracker/ranger	Charge coupled device (CCD)	Passive ranging	Correlation processing	Target tracking	Stereometric ranging	Air-to-air fire control	Automatic target detection	Gun fire control	Target identification
Electro-optical tracker/ranger	Charge coupled device (CCD)												
Passive ranging	Correlation processing												
Target tracking	Stereometric ranging												
Air-to-air fire control	Automatic target detection												
Gun fire control	Target identification												
19. ABSTRACT (Continue on reverse side if necessary and identify by block number)  <p>The preliminary engineering design study of an Advanced Electro-Optical Tracker/Ranger (AEOTR) to provide passive target tracking and rangefinding for air-to-air gun fire control is described. Area correlation processing is used in the comparison of stereo image pairs for stereometric ranging and in the comparison of successive images for tracking. The application of these techniques to the AEOTR, the limitations imposed by packaging, environmental and state-of-the-art sensor and processing hardware constraints, and the projected per-</p>													

DD FORM 1 JAN 73 1473 EDITION OF 1 NOV 65 IS OBSOLETE

SECURITY CLASSIFICATION OF THIS PAGE (When Data Entered)

405 421 set

(20)

formance are evaluated. Principal emphasis is given to the use of AEOTR in the gun director engagement mode in which target track and range data is provided to a gun fire control computer. The feasibility of use of the AEOTR to provide target video as an aid to visual target identification, and to provide automatic airborne target detection, is also evaluated. The necessary functions and subsystems are defined and integrated into a preliminary design, whose performance is estimated and compared with the program goals. In addition, a preliminary mounting location study for the F-15, F-16 and F-18 advanced fighters is included. CAI-built hardware was used to successfully demonstrate the feasibility of the ranging and tracking concepts employed in the AEOTR.

## FOREWORD

This report was prepared by CAI, a Division of Recon/Optical, Inc., Barrington, Illinois 60010, under U.S. Air Force Contract F33615-78-C-1562. The program was administered by the Air Force Avionics Laboratory, Wright-Patterson Air Force Base, Ohio. Technical aspects of the study were directed by Air Force project engineers Dr. Harold W. Rose and Mr. Raymond C. Rang. The work was performed during the period October 1978 - February 1980. The draft of this report was submitted during February 1980.

The authors of the report were R. A. Bennett, who served as project engineer, and D. N. DeFoe. Significant contributions to the study made by A. Weigandt, S. Beran, R. Buck, J. Lecuyer and E. Waller are gratefully acknowledged.

Accession For	
NTIS GRA&I	
DDC TAB	
Unannounced	
Justification _____	
By _____	
Distribution _____	
Availability Codes _____	
Distr	Availablity or special
A	

## TABLE OF CONTENTS

<b>SECTION 1.0 INTRODUCTION AND SUMMARY</b>	<b>1</b>
1.1 Fundamental Concept	1
1.2 Report Overview	3
1.3 Summary	3
1.3.1 Gun Director Engagement Mode	4
1.3.2 Target Identification Mode	7
1.3.3 Target Detection Mode	7
1.3.4 Concept Analysis Summary	8
1.3.5 Mounting Location Study	9
1.3.6 Hardware Configuration	9
1.3.7 Laboratory Demonstration Unit	11
1.3.8 Performance of the AEOTR	12
1.3.8.1 Reduction of Range Error	13
1.4 Conclusion	13
1.5 Recommendation	15
<b>SECTION 2.0 THEORETICAL BASIS</b>	<b>16</b>
<b>SECTION 3.0 TECHNICAL ANALYSIS</b>	<b>21</b>
3.1 Gun Director Engagement Mode	21
3.1.1 Introduction	21
3.1.2 Accuracy Requirements	23
3.1.2.1 LOS Angle and Angle Rate	24
3.1.2.2 Range	24
3.1.2.3 Range Rate	25
3.1.3 Optical Stability Requirements for the Rangefinder	26
3.1.4 GDEM Window Considerations	27
3.1.4.1 Window Bowing	29
3.1.4.2 Air Wedge	31
3.1.4.3 Window Wedge	31
3.1.5 Ranging Optics Configuration	34
3.1.6 Rangefinder Calibration	36
3.1.6.1 Autocalibration Subsystem	40
3.1.6.2 Residual Error	43
3.1.6.3 Rangefinding Calibration	46
3.1.6.4 Summary	46

## TABLE OF CONTENTS (Cont'd)

3.1.7	Closed-Loop Ranging	47
3.1.8	Target Aspect	49
3.1.9	Sensor Selection	50
3.1.9.1	Sensor Options	51
3.1.9.2	Field of View	52
3.1.9.3	Video Readout	52
3.1.9.4	Readout Mode	55
3.1.9.5	Hardware Complexity	58
3.1.9.6	Sensor Selection	59
3.1.10	Tracker Gimballing	60
3.1.11	System Cooling Requirements	63
3.1.11.1	Internal Heat Load	63
3.1.11.2	External Temperatures	64
3.1.11.3	Cooling Options	67
3.1.11.4	Conclusion	69
3.2	Target Identification Mode	71
3.2.1	Introduction	71
3.2.2	Packaging Constraints	71
3.2.3	Sensor Options	72
3.2.4	Resolution Requirements	77
3.2.5	Conclusion	81
3.2.6	Scene Lighting and Sensor Exposure	82
3.2.7	Display of Target Video	83
3.2.8	Summary	83
3.3	Mounting Location Study	84
3.3.1	General	84
3.3.2	Specific Aircraft	86
3.3.2.1	F-15	86
3.3.2.2	F-16	88
3.3.2.3	F-18	88

## TABLE OF CONTENTS (Cont'd)

3.4 Target Detection	92
3.4.1 Introduction	92
3.4.2 Description of Method	92
3.4.2.1 Concept	92
3.4.2.2 Processing Implementation	94
3.4.2.2.1 Raw Maps	94
3.4.2.2.2 Composite Map	94
3.4.2.2.3 Weighting and Thresholding for the Composite Map	97
3.4.3 Performance	98
3.4.3.1 False Alarm Probability	98
3.4.3.2 Detection Probabilities	100
3.4.4 Summary	103
3.5 Search Pattern	109
3.5.1 Target Discrimination During Search	111
SECTION 4.0 AEOTR DESIGN	115
4.1 Introduction	115
4.2 Mechanical Layout	115
4.3 Optical Layout	118
4.4 Electronic Layout	121
4.4.1 Introduction	121
4.4.2 CCD Readout	121
4.4.3 Tracking Correlation Description	121
4.4.4 Ranging	125
4.4.5 AEOTR System Control	126
4.4.6 Target Detection	127
4.4.7 Areas of Development Effort	128
4.4.7.1 Technology Impact	129
4.4.8 Weight and Volume Estimates	129

## TABLE OF CONTENTS (Cont'd)

<b>SECTION 5.0 CAI DEMONSTRATION HARDWARE</b>	<b>130</b>
<b>5.1 Description</b>	<b>130</b>
<b>5.2 Performance</b>	<b>132</b>
<b>5.2.1 Static Correlation Accuracy</b>	<b>137</b>
<b>5.2.2 Closed-Loop Ranging</b>	<b>139</b>
<b>5.2.3 Ranging and Tracking Performance</b>	<b>139</b>
<b>5.3 Summary</b>	<b>140</b>
<b>SECTION 6.0 SUMMARY ERROR ANALYSIS</b>	<b>141</b>
<b>6.1 Introduction</b>	<b>141</b>
<b>6.2 Tracker Errors</b>	<b>141</b>
<b>6.2.1 LOS Angle</b>	<b>141</b>
<b>6.2.2 LOS Angle Rate</b>	<b>142</b>
<b>6.3 Range Errors</b>	<b>143</b>
<b>6.3.1 Range</b>	<b>143</b>
<b>6.3.2 Reduction of Range Error</b>	<b>144</b>
<b>6.3.3 Range Rate</b>	<b>145</b>
<b>Appendix A Thermal Environment of the AEOTR</b>	<b>146</b>
<b>Appendix B AEOTR Window Considerations</b>	<b>153</b>
<b>Appendix C Design of a Thermally Compensating Window</b>	<b>165</b>
<b>Appendix D Optical Configurations</b>	<b>169</b>
<b>Appendix E Detector Radiometric Considerations</b>	<b>178</b>
<b>Appendix F Display of Target Video</b>	<b>183</b>
<b>Appendix G Correlation Modeling Program Computer Results</b>	<b>189</b>
<b>Appendix H Composite Mapping for Target Discrimination</b>	<b>211</b>

## LIST OF ILLUSTRATIONS

Figure 1 Stereometric Rangefinder Geometry	2
Figure 2 Advanced E-O Tracker/Ranger	10
Figure 3 Ranging Accuracy	20
Figure 4 Rangefinder Thermal Errors	28
Figure 5 Optical Configuration Alternatives (page 1 of 2)	37
Figure 5 Optical Configuration Alternatives (page 2 of 2)	38
Figure 6 Ranging Optics Schematic	41
Figure 7 Calibration Mirror Mounting	45
Figure 8 Circuit Block Diagram	54
Figure 9 Scanning Fields	56
Figure 10 Interlaced Readout Mode	56
Figure 11 Noninterlaced Readout Mode	56
Figure 12 Pod Temperature vs Altitude and Airspeed	66
Figure 13 Tracker Thermal Environment	70
Figure 14 Modulation Transfer Function for the CCD 211	75
Figure 15 Modulation Transfer Function for the CCD 221	76
Figure 16 Resolution as a Function of Range and Target Test	78
Figure 17 Range vs Angular Resolution	80
Figure 18 F-15 for Obscuration, Wing Root Mounting	87
Figure 19 F-16 for Obscuration	89
Figure 20 F-18 for Obscuration, Under Nose Mounting	90
Figure 21 F-18 for Obscuration, Engine Intake Mounting	91
Figure 22 Subfield Processing	95
Figure 23 Probability Per Frame of a Single Noise Spike Above Threshold - Offset = 1.83	101
Figure 24 Probability Per Frame of a Single Noise Spike Above Threshold - Offset = 3.6	102
Figure 25 Probability of Detection - Range and Brightness Information Only	104
Figure 26 Probability of Detection - Range and Brightness Information Only	105

## LIST OF ILLUSTRATIONS (Cont'd)

Figure 27 Probability of Detection	106
Figure 28 Probability of Detection	107
Figure 29 Probability of Detection - Motion Information Only	108
Figure 30 Tracker Head	116
Figure 31 AEOTR Optical Schematic	119
Figure 32 AEOTR Electronic Block Diagram	122
Figure 33 Demonstration E-O Tracker/Ranger	131
Figure 34 LDU Response to Real World Film Target	134
Figure 35 LDU Response to Sine Wave Targets	136
Figure 36 CAI Demonstrator Image Displacement vs Apparent Range	138

## LIST OF TABLES

Table 1 AEOTR Performance Summary	14
Table 2 AEOTR Performance Goals	22
Table 3 $\Delta T$ for $1.3\text{-}\mu\text{rad}$ Error	30
Table 4 Window Bending	30
Table 5 Air Wedge - Temperature and Pressure Limits	32
Table 6 AEOTR Optical Configurations	39
Table 7 Sensor Field of View	53
Table 8 Major Internal Heat Sources	65
Table 9 SSID Technology Comparison	73
Table 10 Target Hierarchy	113
Table 11 Laboratory Demonstration Unit	133

## SECTION 1.0

### INTRODUCTION AND SUMMARY

This report covers the preliminary engineering design study for an Advanced Electro-Optical Target Tracking and Rangefinding System. The objective of this system is the accurate, passive measurement of range and line-of-sight angle parameters of airborne fighter targets while at gunfire ranges. These parameters are delivered to an onboard fire control computer which calculates optimal gun pointing vectors and attack fighter flight paths. The purpose of the study is the determination and demonstration of feasibility of the development of an Advanced E-O Tracker/Ranger (A EOTR) for current and forthcoming generations of tactical fighters as an alternative to radar for air-to-air missions.

#### 1.1 FUNDAMENTAL CONCEPT

The approach to passive rangefinding upon which this study is based is the stereometric measurement of target image parallax using area correlation processing techniques. This is demonstrated in Figure 1. Two identical, parallel optical systems with focal length  $f$  are spaced by a distance  $B$ . A target at very long range is imaged in the respective focal planes with images spaced a distance  $B$ . At a smaller range,  $R$ , the target images are spaced by a greater amount,  $B + P$ . The determination of the image offset,  $P$ , allows the computation of the range according to the formula:

$$R = BF/P$$

Computational techniques developed by CAI since 1975 using area correlation processing and charge coupled device (CCD) image detectors allow the determination of the image offset,  $P$ , with sufficient precision to allow the fabrication of stereometric rangefinders with practically small baseline-focal length (BF) products.

The similar measurement of the displacement of images at different times allows the detection of image motion and, through the use of appropriate servo techniques, the potential for image stabilization or image

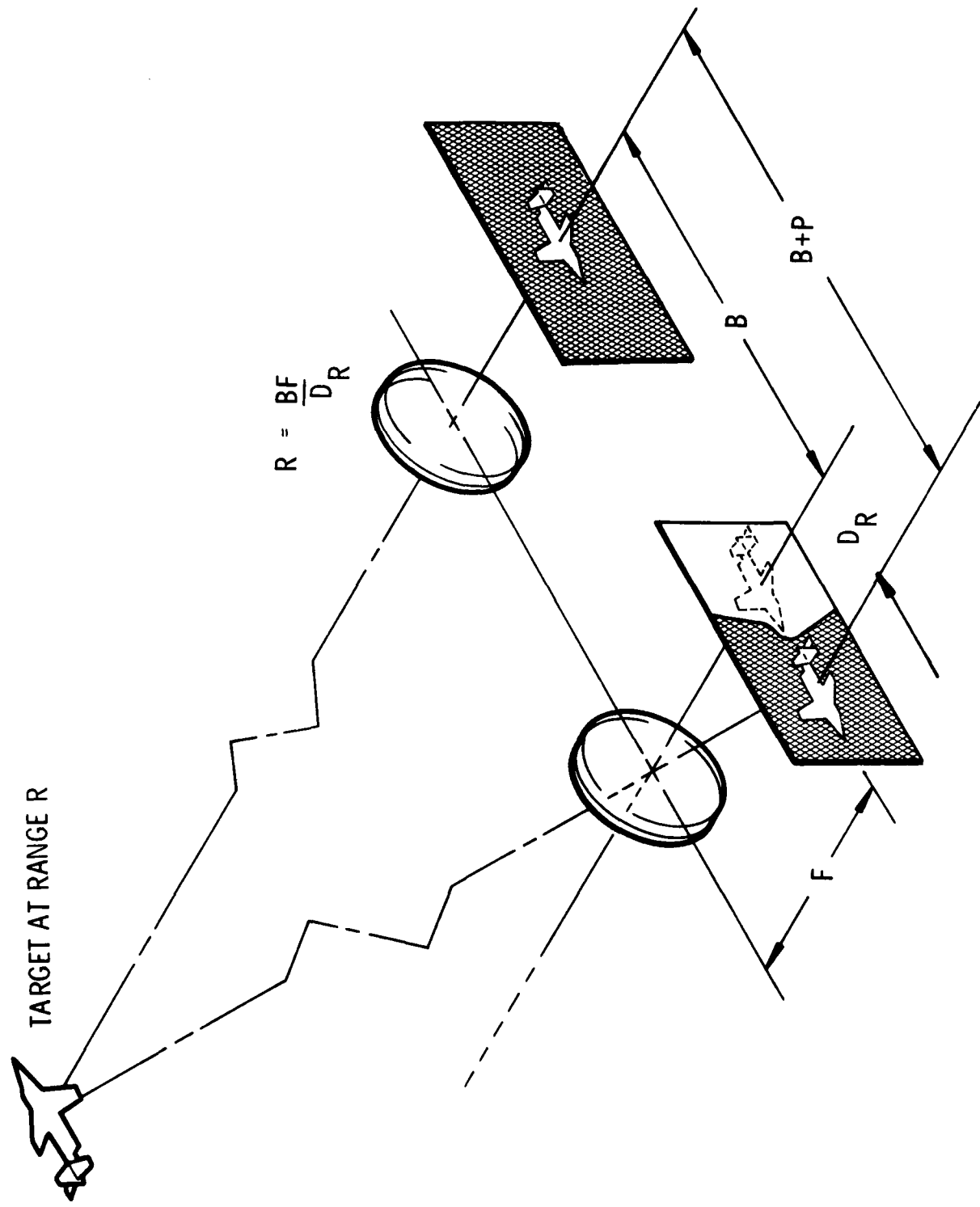


Figure 1 Stereometric Rangefinder Geometry

tracking. Further, the ability to use only a portion of the image rather than the entire image for analysis allows the detection of the relative motion of parts of the image. One application of this is moving target detection. A portion of the AEOTR study is devoted to the use of moving target detection as one function employed in support of an automatic target detection mode (TDM).

### 1.2 REPORT OVERVIEW

Two techniques relying on correlation processing, namely ranging and tracking, are thus the basis for the AEOTR. The application of these techniques to the AEOTR, the practical limitations imposed upon it by the environment and by the present and anticipated state of the art in processing capability, and the expected performance of an AEOTR are the subject of this study. Primary emphasis is given to the use of the AEOTR in the gun director engagement mode in which target track and range data is provided to a gun fire control computer. Two auxiliary functions of providing video of the target as an aid to visual target identification and of automatic target detection were also evaluated. All necessary functions and subsystems of the AEOTR were defined and integrated into a preliminary tracker design whose performance was estimated. A preliminary mounting location study for three advanced fighter aircraft, namely the F-15, F-16 and F-18, was also conducted. Finally, the feasibility of the ranging and tracking concepts proposed for the AEOTR was successfully demonstrated using CAI-built demonstration hardware.

### 1.3 SUMMARY

The technical approach to the AEOTR was analyzed in considerable detail with the intent of identifying the true limits of performance of the technique when implemented in realizable hardware. This concept analysis was divided unequally among four areas: the application of the AEOTR in three operational modes or functions and the mounting location study.

### 1.3.1 Gun Director Engagement Mode

In the gun director engagement mode (GDEM), the basic design options for the AEOTR were evaluated. The degree of susceptibility of the AEOTR to a multitude of optical and mechanical perturbations was determined, and methods to prevent the translation of these effects into performance limitations were devised.

An error budget imposed by the ranging and tracking performance requirements was established. Each of a large number of effects in the AEOTR head can use the entire ranger optical error budget of  $1.3 \mu\text{rad}$  many times over given the excursions in speed, altitude and temperature expected for the normal operational flight envelope. The effects were divided into three general classes: those occurring forward of the AEOTR; those occurring at the window; and those occurring behind the window.

While little can be done to control or measure the effects in the first class, their effect can be somewhat reduced or avoided by proper choice of mounting location and technique and by proper AEOTR design to minimize the effects near the system.

At the window, the optical effects cannot be directly measured since the window is forward of any potentially suitable instrumentation (the E-O hardware), although some of the effects could possibly be inferred from, for example, temperature and pressure measurements. The adopted approach, however, is to design the window so that all of the predictable effects are below the threshold of significance. This means that the window must first be at normal incidence for each ranging channel to avoid the introduction of wedge, and that it must be self-compensating for the expected thermal environment. Such a window has been designed and is considered feasible. Also, the air immediately aft of the window must be circulated to prevent the formation of thermal gradients across the ranger optical apertures.

The third class of effects, those in the ranging system itself, can be addressed by proper design techniques to minimize their magnitude and by calibration methods to sense and eliminate the residuals. A wide selection of optical configurations was evaluated to find one which would eliminate, or reduce to manageable proportions, the sources of ranging error associated with maintaining the alignment and the essentially identical characteristics of the two channels. The configurations suffered from such problems as high light loss, signal crosstalk, sensitivity to mechanical or thermal stress, bulkiness, image asymmetry and focal length equality (in two lens configurations). The configuration which was selected for the AEOTR was the two independent channel configuration using two lenses and two CCD's because it avoided the intolerable errors of the other schemes and had as residual problems alignment and focal length equality which can be satisfactorily addressed in the AEOTR.

An internal calibration system for the rangefinder was devised which would impose a minimum additional load on the AEOTR in terms of hardware complexity and functional workload. The system uses the rangefinder itself to monitor its own alignment by detecting the image of a reference reticle target located at the edge of the format of one CCD and optically coupled to the other ranger channel. The precision with which the ranger alignment can then be determined is very high, being determined by the correlation accuracy for images with known spatial structure and high contrast and signal levels with minimal noise. It is believed that the autocalibration system can be built with sufficient insensitivity to mechanical and thermal stress to permit the detection and compensation of the referenced residual error sources in the AEOTR.

A computer modeling study of correlation processing was conducted to determine the limits and characteristics of the techniques when applied to tracking and ranging. The results were generally very favorable for correlation-based tracking and ranging. One feature which was revealed by the program and which was corroborated by measurements made on the laboratory demonstration unit is a sensitivity of correlation processing accuracy to image spatial frequency. For low frequency (relative to the sensor Nyquist frequency) images, the accuracy is high and ranger

performance is well defined, but for Nyquist and higher frequencies, the error is significant and frequency and offset dependent. At integer pixel shifts, accuracy is very high and frequency independent, but at noninteger shifts, the accuracy is image dependent. For fixed controlled patterns such as the autocalibration pattern, for example, the detected offset follows an accurately repeatable although nonlinear curve. The developing sensor technology discussed below is significant here since the threshold frequency for these effects increases with Nyquist frequency, and the magnitude of the errors is reduced because of the reduced pixel pitch.

These response characteristics lead to the use of closed-loop ranging in the AEOTR. In closing the ranging loop, the target image in one ranger channel is displaced until it is detected with high accuracy to be at an integer pixel shift with respect to the image in the other channel. The measurement of the amount of image shift required to meet this condition is done with high accuracy using the autocalibration pattern. Ranging errors which could arise from targets with arbitrary spatial distributions can therefore be avoided by performing the critical image offset measurement with the autocalibration pattern. It is believed that the inclusion of the closed-loop ranging function in the AEOTR is feasible and is required to provide the necessary accuracy.

The modeling study also showed that vibration-induced image blur is not a significant error source since it reduces the high frequency content of the image. For high amplitude transients such as in-flight buffet, however, the track lock will be broken when the amplitude reaches one FOV in one sampling period necessitating a reversion to an acquisition mode.

An analysis of the gimbaling requirements showed that a three-axis system is required if continuous target tracking is to be provided. The use of roll as the outer gimbal is desirable since it permits roll stabilization, and the use of pitch as the second tracking axis is desirable since it, in general, allows a symmetrical airflow across the AEOTR window to minimize external errors. A small amount of yaw motion is then required if track lock is to be maintained when the target is near the roll axis. These features have been integrated into the AEOTR design.

The thermal environment of the AEOTR and the resultant cooling requirements were estimated. The AEOTR is in a "cooling required" condition over nearly all of its operational flight envelope, and at some corners of the envelope, the skin temperatures are very high. If insulation is provided to minimize the inward heat transfer for these conditions, the outward transfer is also inhibited and the system always requires cooling. The cooling requirements were estimated to lie between 500 and 1000 W depending on flight conditions, true electrical load and thermal transfer characteristics. A first look suggests that a 1000-W capacity system can be fitted within the AEOTR pod.

#### 1.3.2 Target Identification Mode

In the target identification mode (TIM), an auxiliary AEOTR function of providing target video to the pilot as an aid to visual target identification was evaluated. The size limitation of the AEOTR is dominant in limiting the target video potential. Solid-state imagers are the only available imagers which are compatible with the restrictions of space in the GDEM. A survey of solid-state sensor technology established the near and medium term limits of resolution. The two limits of sensor technology and focal lengths of under 9 inches for the AEOTR determine the maximum resolution capability. Several effects are expected which would limit resolution to less than this maximum, the most significant being the scan conversion required to provide image derotation and sensor/display compatibility. Several methods of implementing the scan conversion were assessed and involved temporal and spatial resampling and image truncation, all of which are image degrading operations.

The conclusion was that visual identification/enhancing resolution could not be provided with available and medium term technology in a system with the space and functional constraints of the AEOTR.

#### 1.3.3 Target Detection Mode

The use of the AEOTR in an automatic TDM to allow covert detection and enhanced long range tracking capability in tactical environments was found to hold very high potential. Significantly high probabilities of

detection and very low false alarm rates are found to occur when the triad of target information types (contrast, motion and range) available in the AEOTR is properly used. A method to use this information was devised and involves the generation of a map of the FOV composed of an overlay of separate FOV maps containing properly normalized and discriminated contrast, motion and range data. The composite map can be generated at the image sensor frame rate since the correlation processor is a pipeline implementation of the algorithm, and this allows the automatic search of the entire field of regard (or portion thereof) in a realistically small time interval. It is believed that this function can be implemented with present technology and that a significant increase in target detection capability would be provided.

#### 1.3.4 Concept Analysis Summary

An advanced E-O tracking and ranging capability based on area correlation processing can in principle meet the performance requirements. Proper design techniques can adequately limit or avoid the performance degrading error sources in the AEOTR. The AEOTR can be designed to perform quite adequately in the gun director engagement mode and in the target detection mode, but insufficient resolution is available to permit the generation of target video as a useful aid to visual target identification.

The functions required in the GDEM mode are:

- Tracking
- Ranging (closed loop)
- Autocalibration
- Cooling

In the TDM, the required functions are:

- Ranging (with pipeline processing)
- Pointing/searching
- Autocalibration
- Cooling
- Moving target detection

### 1.3.5 Mounting Location Study

The preliminary mounting location study covered three aircraft: the F-15, F-16 and F-18. In addition, a number of relevant factors involving aircraft integration including operational angles of attack, upstream and downstream airflow, masking of the field of regard, mounting techniques, structural support, packaging configurations and precedent installation were evaluated. The airframe manufacturers were visited. The only location seriously considered for the F-15 is the port wing root where much of the starboard hemisphere is vignetted. Good locations appear to be available on the F-16 and the F-18. On the F-16, the AEOTR would have to fit in the Pave Penny location, and this provided an impetus to configure the AEOTR in a pod of 54 inches maximum length.

### 1.3.6 Hardware Configuration

A preliminary system design effort was carried to a level sufficient to establish that all components needed to perform the required functions could be fitted within a reasonable package envelope and to permit the estimation of the performance characteristics of the resultant system.

The AEOTR is configured in two parts: a tracker head subassembly and a remote electronics processing subassembly. The tracker head subassembly is contained within an 8-inch diameter by 54-inch long pod and is shown in Figure 2. The optical systems and image sensors are contained in the gimballed sphere at the forward end, and mechanical, electrical and thermal support systems require the remainder of the pod. Approximately one-half ( $0.5 \text{ ft}^3$ ) of the electronics fit within the pod and one-half must be located elsewhere. The TDM hardware requires an additional  $0.5 \text{ ft}^3$  of electronics.

The gimballed sphere is suspended at the center to maximize the baseline available to the ranger. A  $90^\circ$  full angle cone field of regard is reached through motions of  $+20^\circ$ ,  $-45^\circ$  in pitch and continuous roll. The  $\pm 30^\circ$  yaw travel permits continuous tracking near the roll axis. Acceleration and slew rates are adequate to meet the tracking requirements.

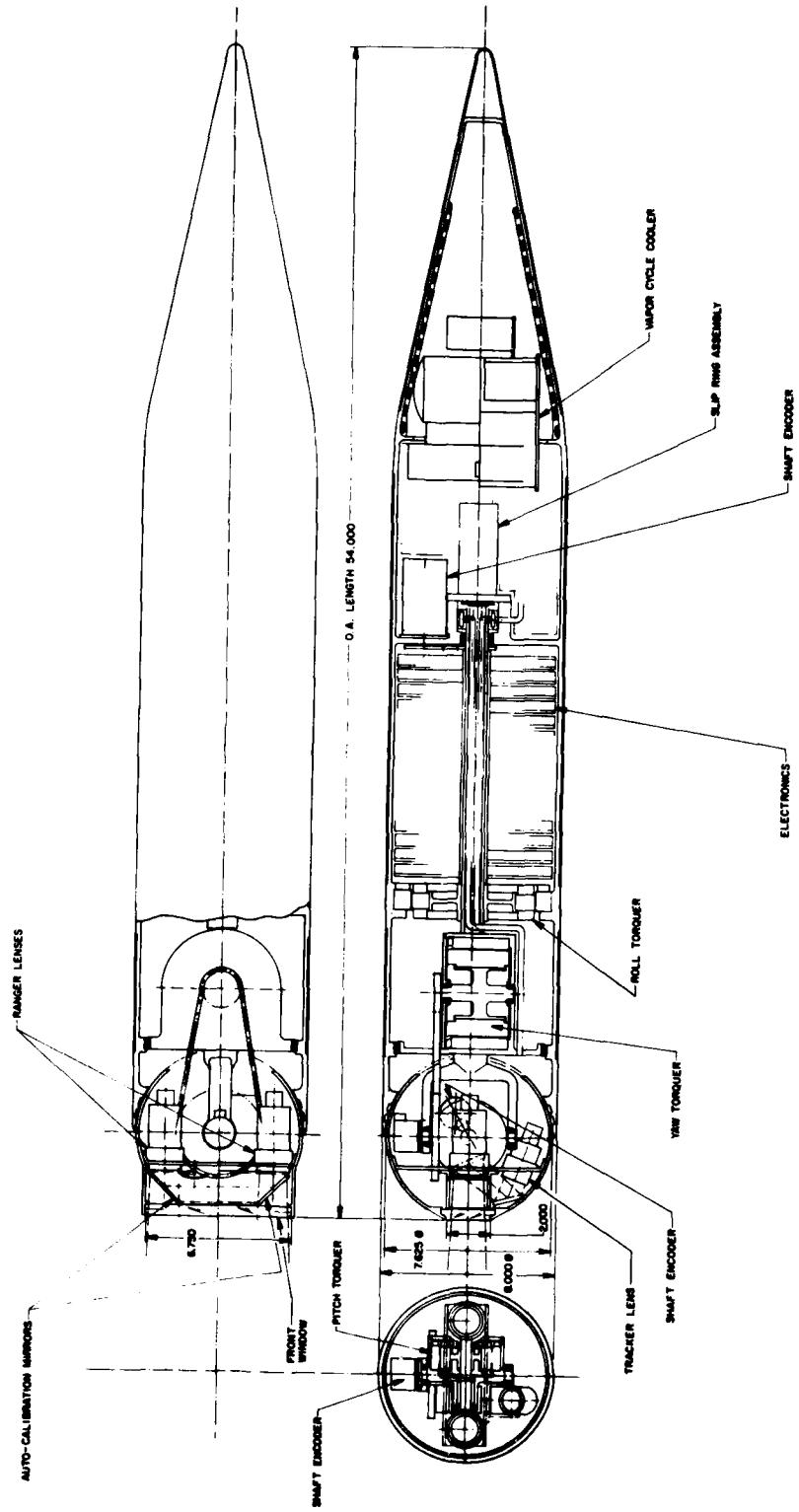


**Figure 2 Advanced E-O Tracker/Ranger**

The ranging and tracking channels are served by a thermally compensating normal incidence window spanning the width of the sphere. The tracking channel is folded to lie below the plane of the rangefinder which views the world through the window and the cross-coupling mirrors of the autocalibration system. The 5-inch focal lengths and 5-inch separation of the ranger lenses determine the ranger scale of  $Bf = 25 \text{ in}^2$ . The other significant dimension is the  $30\text{-}\mu\text{m}$  pixel pitch of current CCD's.

This basic layout illustrates the integration of all functions required by the AEOTR into a single, relatively compact subsystem. It is believed that the 8-inch diameter represents a reasonable compromise between rangefinder baseline and the minimum size considerations relevant to integration potential.

#### 1.3.7 Laboratory Demonstration Unit

In support of an internally funded R & D program, CAI built the laboratory demonstration unit (LDU) to verify the applicability of correlation processing techniques to passive stereometric ranging and to identify problem areas, sensitivities and limits of the methods. The LDU was built primarily to demonstrate ranging with a simplified correlation-based tracking capability provided only to establish a target for the rangefinder.

The LDU consists of a pair of parallel, nearly identical video channels mounted on a servo-controlled two-axis gimballed platform. Video from CCD image detection is processed according to the correlation algorithm to determine image misregistration and consequently range. The video from one channel is also used to determine image displacement between successive frames in providing a correlation-derived tracking error signal to the servo drive amplifier chain. The scale of the LDU is smaller than that of the AEOTR with 100-mm focal length lenses, a  $Bf$  product of  $11.81 \text{ in}^2$ , and an effective pixel dimension of  $80 \mu\text{m}$ .

The LDU demonstrated the practical feasibility of the approach taken for the AEOTR. Correlation-based tracking was shown to be highly target adaptive and tenacious against background clutter and against all

except high contrast foreground clutter which does not occur in the air-to-air scenario. Ranging was demonstrated with about 10 percent accuracy on a vehicle at ranges between 500 and 1300 ft. Testing of the LDU under controlled conditions in the laboratory established a sensitivity of correlation processing to spatial frequency which was also verified in the computer modeling study. This effect can be greatly reduced by using higher resolution sensors (technology growth area), and it can be practically eliminated in the AEOTR through the use of closed-loop ranging which is proposed. Finally, correlation accuracy measurements made on the LDU permitted the prediction of the accuracy performance of the AEOTR.

#### 1.3.8 Performance of the AEOTR

The performance which the AEOTR can provide was estimated in order to compare with system goals and to identify key areas of technology which can impact on ultimate performance potential.

The tracking capability of the AEOTR is adequate to meet the goals in angle and angle rate. The total error (rms) in LOS angle is 0.33 mrad. At a 10-Hz output rate, the rms error in LOS angle rate error is 3.8 mrad/s.

With present technology, the projected range error at 4000-ft range is 121 ft. The increase of this number above the design goal of 50 ft is attributed to the sensitivity of correlation processing to high frequency scene information and to the need to operate present image detectors in a noninterlaced mode for present correlation hardware which results in a 30- $\mu$ m, rather than an 18- $\mu$ m, pixel. Several factors are expected to permit reduction of the range error to the goal of 50 ft, and these are discussed below.

The range rate error is estimated to be 170 ft/s at a 1-Hz data rate. This error is proportional to the range error, and an improvement in range accuracy will be reflected proportionally in range rate performance.

#### 1.3.8.1 Reduction of Range Error

The reduction of the AEOTR range error to 50 ft is considered realistic for several reasons involving existing or nearly existing technology.

Improved sensor resolution is now available which impacts range performance at a greater than linear rate. Area array CCD's with 25- $\mu\text{m}$  pixels and fully active formats are now available. Projections of 15 to 17- $\mu\text{m}$  pixels in area arrays for the midterm ( $\leq 2$  years, conditional upon funding) are being made. This technology will improve range performance by (a) the reduction of the basic correlation error (all of the image is detected), (b) improved responsivity, and (c) reduced pixel size which increases the ranger scale factor (Bf/pitch) and increases the sensor Nyquist frequency, further reducing image frequency-related error.

Spatial scene filtering and/or temporal data filtering may reduce scene-dependent error. Also, an alternate version of the processing algorithm may exhibit reduced error.

Finally, careful matching of the ranger lenses in the AEOTR should reduce the scale-related errors which contributed to the overall error estimate derived from the LDU.

CAI is confident that by using one or more of these methods, the goal of a 50-ft error at a 4000-ft range can be reached or exceeded.

The projected performance of the AEOTR is summarized in Table 1 along with the performance goals and the steps necessary to reach those goals.

### **1.4 CONCLUSION**

The practical feasibility of an AEOTR using correlation processing for tracking and stereometric ranging has been evaluated and demonstrated. The components required to effect accurate, passive tracking and ranging with automatic target detection can be fitted into an 8-inch diameter pod

TABLE 1  
AEOTR PERFORMANCE SUMMARY

Parameter	Performance	Goal	Future Performance
<b>Tracking</b>			
LOS angle	0.33 mrad	1.0 mrad	
LOS angle rate	3.8 mrad/s	4.0 mrad/s	
Angle rate limit	>60°/s	60°/s	
<b>Ranging</b>			
Range	121 ft @4000 ft	50 ft	50 ft with 1982 sensor technology
Range rate	170 ft/s @ 1 Hz	50 ft/s	71 ft/s @ 1 Hz
<b>Acquisition</b>			
Cued	0.34 s	0.3 s	
Automatic	10 s for 90° cone search		Less with higher speed memories and multi- pliers/dividers
<b>Size</b>			
Head subassembly	8-inch diameter 54-inch length		
Electronics sub- assembly	0.5 ft <sup>3</sup> GDEM 0.5 ft <sup>3</sup> TDM		Smaller with higher integration

plus an electronics processing subassembly. The tracking performance goals can be met or exceeded, and the ranging performance goal can be achieved using existing or midterm technology.

#### 1.5 RECOMMENDATION

The recommendation of this study is the continued development of the AEOTR. The risk relative to the state of the art is judged to be low since existing technology now permits most of the performance goals to be met, and the foreseen improvements in sensor technology, digital memory size and speed, and in digital multiplier/divider technologies required to reach and exceed the goals are developing rapidly.

## SECTION 2.0 THEORETICAL BASIS

As previously stated, CAI's passive ranging technique is based upon the precept that the image of an object shifts in the focal plane as a function of its angular position relative to the optical axis. Given two optical imaging systems displaced in space and imaging the same object, the relative angular position of that object in each of the systems varies with range and, hence, the relative position of the images in each focal plane varies with range.

Figure 1 shows the simplified geometry of the situation. By similar triangles,  $R/B = F/P$  or  $R = BF/P$ . Passive ranging rests on the ability to determine the relative image shift,  $P$ . Succinctly, it is required to measure how far one image must be displaced to match the second image. The first task is then to define "match" in mathematical terms.

Since brightness is the only information with which to work, "match" must be defined as occurring when each sample in one image plane has the same amplitude as its corresponding sample in the second image plane. Thus,  $P_1(i, j) = P_2(i + \Delta i, j + \Delta j)$  for all  $i$  and  $j$  where  $\Delta i$  and  $\Delta j$  define the shift required to make the match using some coordinate system. In reality, noise, lens mismatch, specular reflections and the like prevent the difference from ever being precisely zero over all  $i$  and  $j$ ; hence, the need to find the best match or fit. One common measure of fit, given numerous samples, is to take the least squares approach in which parameters are varied until the sum of the squares of the differences shows a minimum. In this case, the parameters to be varied are  $\Delta i$  and  $\Delta j$ . There are, of course, other measures of fit such as minimizing the sum of the absolute values of the differences. In this vein, it can be generalized to minimize  $\left\{ [P_1(i, j) - P_2(i + \Delta i, j + \Delta j)]^2 \right\}^Q$  where, for example,  $Q = 1$  and  $1/2$ , respectively for the two cases mentioned. It can be shown that the least squares approach is mathematically equivalent to the statement that the mean of a statistical sample is the best estimator of that sample, while the least absolute value is equivalent to the statement that the median is

the best estimator. Much early work in correlation matching was devoted to determining which statement is the more valid for imagery, with the conclusion that the least squares approach yields a less noisy correlation curve.

Deciding a priori that average brightness and gain differences between the two images are to be ignored in determining match, the sample sets are normalized by subtracting the mean and dividing by the standard deviation. For the least squares approach, a match is defined by locating the minimum of:

$$\sum \left[ \frac{P_1(i, j) - \bar{P}_1}{\sigma_{P_1}} \right]^2 + \left[ \frac{P_2(i + \Delta i, j + \Delta j) - \bar{P}_2}{\sigma_{P_2}} \right]^2.$$

Expanding:

$$\begin{aligned} \text{Min } (\Delta i, \Delta j): & \sum \left[ \frac{P_2(i, j) - \bar{P}_1}{\sigma_{P_1}} \right]^2 + \sum \left[ \frac{P_2(i + \Delta i, j + \Delta j) - \bar{P}_2}{\sigma_{P_2}} \right]^2 \\ & - 2 \sum \left[ \frac{P_1(i, j) - \bar{P}_1}{\sigma_{P_1}} \right] \left[ \frac{P_2(i + \Delta i, j + \Delta j) - \bar{P}_2}{\sigma_{P_2}} \right]. \end{aligned}$$

Simplifying:

$$\text{Min } (\Delta i, \Delta j): \quad \sum P'_1^2 + \sum P'_2^2 - 2 \sum P'_1 P'_2.$$

The first two summations both equal 1 by definition of mean and standard deviation which leaves finding the minimum of  $2 \left[ 1 - \sum P'_1 P'_2 \right]$ . This is equivalent to finding the maximum of  $\sum P'_1 P'_2$ , which is recognized as the peak correlation coefficient. Thus, correlation is nothing more than a statement that match is defined by minimizing the least squares difference between two signals as a function of relative shift, with the implication that the mean of the sample-by-sample differences is the best estimator of the degree of match.

By plotting the correlation product as a function of image shift, a correlation curve is generated. Because the images are, in this case, focused on CCD sensors, the images are sampled in a discrete regular pattern. With the images sampled discretely, the correlation curve is only defined at discrete intervals. Nevertheless, these correlation samples do in fact represent a continuous curve. Furthermore, this curve shifts precisely with the relative shift of the two images.

Clearly, the image shift can be determined in a gross sense merely by locating the peak correlation sample. However, in order to measure shift smaller than the sample spacing (i.e., pixel spacing), the curve must be interpolated. In essence, this means assuming a mathematical shape for the curve and calculating the necessary constants based upon the samples obtained by autocorrelation (the correlation of one image with itself) which is known to be centered at the origin. Once the constants are evaluated, then the fractional pixel shift can be determined by applying these values to the samples of the correlation curve obtained by cross correlation of the two different images. This procedure assumes that the curve maintains its shape as it shifts with the relative image shift. In practice, the mathematics can be arranged so that the constants never need to be evaluated explicitly, but the cross correlation sample values and autocorrelation sample values are combined in one equation to directly yield the fractional pixel displacement.

The actual shape assumed for the curve can be gaussian, exponential, polynominal, spline, trigonometric or any one of a wide variety with various levels of generalization. The performance of any algorithm making an assumption of curve shape must be assessed both in terms of how well the assumed shape fits actual shapes generated with real imagery, ease of implementation and processing speed. A mismatch between the assumed shape and actual shapes of correlation curves obviously produces errors in the calculated interpolation. Furthermore, care must be taken in deciding which samples of the curve to use since the curve is quickly dominated by noise effects immediately around the peak, yet the peak itself on the autocorrelation curve has correlated noise included which will not be found in cross correlation. Finally, filtering of the scene can help or hurt the correlation accuracy by shaping the correlation curve to some extent.

Even if real correlation curves could be well described in practice by some mathematical shape, two error sources remain. The first is naturally noise, which is always present to degrade results. The second is fine scene structure. Spatial frequencies about and greater than Nyquist frequency are strongly phase dependent in their effects on sample amplitudes. This phase dependence can produce fluctuations in the correlation curve which are not detectable solely by autocorrelation samples. Filtering can be a solution to this problem only so long as the filter does not greatly reduce the slightly lower spatial frequencies which help to sharpen the correlation curve and allow the accurate measurement of small displacements.

Passive ranging based on correlation processing is simply the measurement of how far one image has to be displaced to match a second image. This displacement is a reciprocal measure of object range. Assumptions about the best estimator and curve shape are made and the accuracy is then limited by noise and the effects of high spatial frequency scene information. Neglecting baseline (B) and focal length (F) variations, the equivalent range error ( $\Delta R$ ) is found by differentiating  $P = BF/R$  to obtain  $\Delta R = -\frac{R^2}{BF} \Delta P$  where  $\Delta P$  is the displacement measurement error. Note that the range error is proportional to the square of the range. This error can only be reduced by increasing the BF product, decreasing the pixel size or reducing the correlation error. CAI has expended considerable effort in determining the best assumed shape consistent with ease of implementation and speed of operation. The findings have shown that without filtering, RMS correlation error of 1/50th of a pixel can be achieved. Further improvement may be obtained with noise and/or scene filtering.

Given this 1/50th of a pixel error, range error can be plotted versus range and BF product assuming a pixel size. This done for a 30- $\mu$ m pixel in Figure 3. Techniques discussed in subsequent portions of this report permit the reduction of range error to meet the design goals without the inordinate increases in system scale indicated by the figure.

PERFORMANCE

— — — OPEN LOOP

— — — CLOSED LOOP

CURRENT TECHNOLOGY

— — — CLOSED LOOP

1982 SENSOR TECHNOLOGY

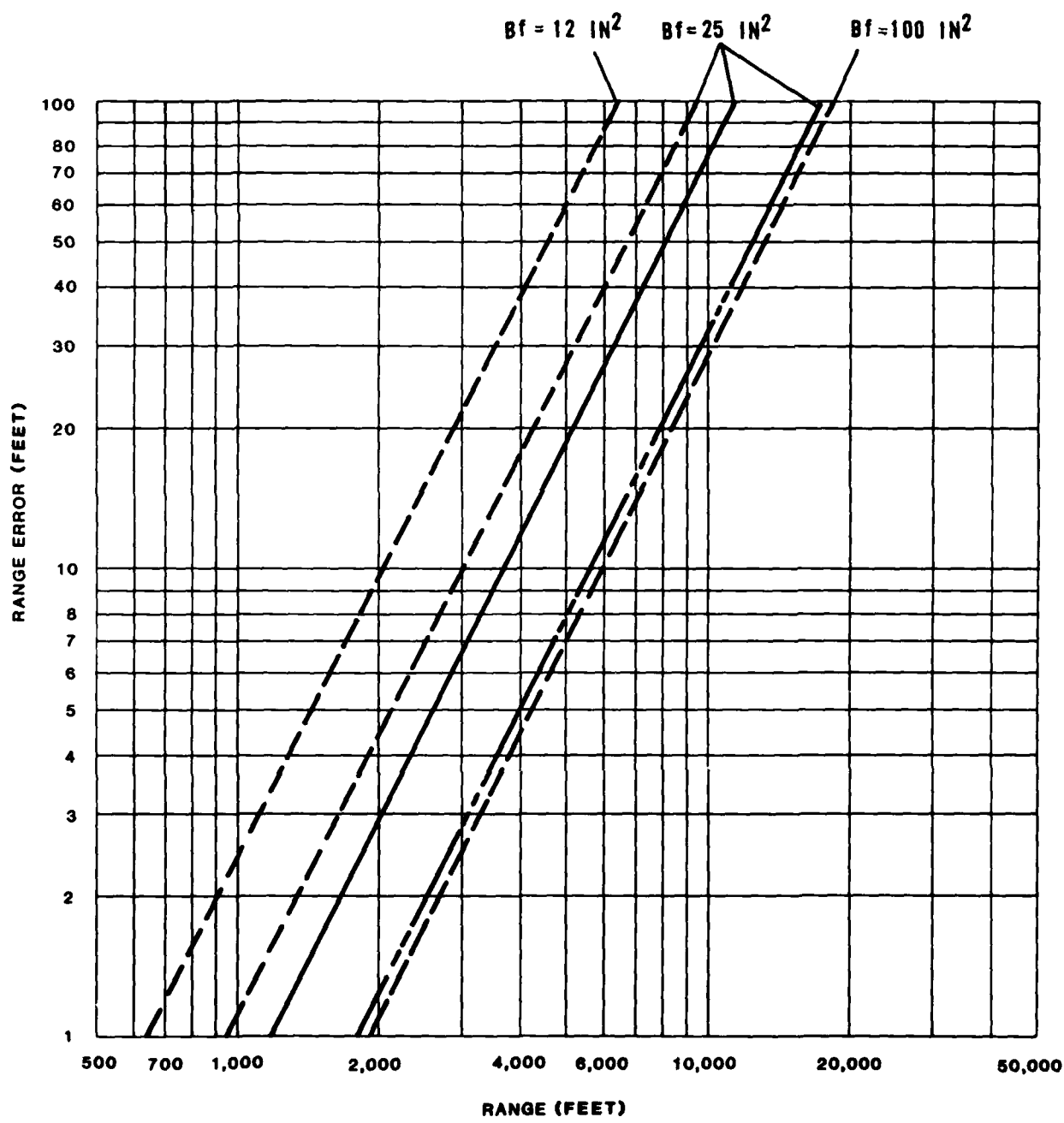


Figure 3 Ranging Accuracy

## SECTION 3.0

### TECHNICAL ANALYSIS

#### 3.1 GUN DIRECTOR ENGAGEMENT MODE

##### 3.1.1 Introduction

Early analysis established the feasibility of building an AEOTR which would satisfy all of the functional requirements of an advanced fire control system sensor. The proposed AEOTR is believed to be capable of providing the required timely target track and range information to a fire control computer with sufficient accuracy to warrant its integration into advanced fighter aircraft. Earlier efforts also detailed many of the physical parameters of such an AEOTR being driven by stated performance requirements. As a review, these are summarized in Table 2 along with attacker and target characteristics.

Preliminary design efforts readily established such parameters as a gimballed rather than staring configuration, the stereometric ranging concept, approximate focal lengths and approximate system size, but could not address specific design considerations or make highly accurate performance projections. The concept analysis portion of the study was effective in permitting a detailed consideration of the implications of the performance requirements and operational environment on the AEOTR design and on the applicability of the technologies being brought to bear on the general problem.

In the concept analysis, the accuracy requirements were translated into optical stability requirements, and permissible thermal and mechanical excursions were estimated. The conclusion, given the thermal and mechanical stresses of the operational environment, is that the best approach is to design the system to minimize the known error sources and to calibrate out the residual errors with an appropriate calibration system. A wide range of rangefinder optical systems was evaluated to determine an optimal configuration which would minimize both residual error and the workload of the calibration system and which would permit the maximum transfer of the correlation processing accuracy to the ranging problem.

TABLE 2  
AEOTR PERFORMANCE GOALS

Passive tracking and ranging of airborne targets	
Acquisition upon cue through the director computer to a $5^\circ \times 5^\circ$ angular direction of the target	
Acquisition at 18,000 ft (required) to 24,000 ft (desired)	
Accurate ranging between 500 and 8000 ft	
Angular coverage: $120^\circ$ full angle cone	
Accuracy	
LOS angle	1 mrad at 0 to $60^\circ/\text{s}$
LOS angle rate	4 mrad/s at 0 to $60^\circ/\text{s}$
Range	$\pm 50$ -ft error at 4000-ft range
Range rate	$\pm 50$ ft/s for ranges $\leq 4000$ ft
Aspect angle	$\pm 5^\circ$ each in yaw, pitch and roll
Acquisition time	0.3 s
Attacker flight regime	
Altitude	Sea level to 50,000 ft
Speed	600 to 1500 ft/s
Yaw rate	0 to $\pm 10^\circ/\text{s}$
Pitch rate	0 to $\pm 25^\circ/\text{s}$
Roll rate	0 to $\pm 300^\circ/\text{s}$
Target characteristics	
Speed	600 to 1500 ft/s
Wing span	24 to 72 ft
Fuselage length	40 to 120 ft
Fuselage diameter	5 to 10 ft
Reflectance	10%
Attacker/target velocity ratio	0.8 to 1.2

The correlation modeling study and the testing of the laboratory demonstration unit revealed a sensitivity of ranging accuracy to target image spatial frequency. A method was devised to avoid an accuracy limitation resulting from this sensitivity and involves operation of the ranger in a closed-loop mode.

An analysis of target aspect determination identified key considerations related to providing this function in the AEOTR.

An evaluation of sensors which are or may become available for the AEOTR identified which sensor parameters are particularly important for the application and impose constraints on the design of the electronic processing circuitry.

Tracker gimbaling options were evaluated and tradeoffs in complexity and performance were identified. Recommendations were made to make pitch and roll the primary tracking axes, with a limited freedom yaw axis permitting continuous tracking near the roll axis.

Finally, cooling requirements for the AEOTR were estimated and a system was suggested which could provide adequate cooling for the head and electronic hardware of the AEOTR.

### 3.1.2 Accuracy Requirements

In the statement of work, several accuracies are given which the AEOTR is to be designed to meet:

LOS angle:	1 mrad at 0 to 60°/s
Angle rate:	±1 mrad/s at 0 to 60°/s
Range:	±50 ft at 4000 ft
Range rate:	±50 ft/s at 4000 ft
Aspect angles	±5° in each axis

The first four are discussed here, and the last item is considered in the TIM analysis, Section 3.2.

### 3.1.2.1 LOS Angle and Angle Rate

Of the possible error sources for measuring LOS angle, all are readily evaluated except for the determination of the target image position on the sensor. A target body is expected to cover considerably more than 1 mrad for all cases within the initial performance envelope, and only reach as small a coverage as 1 mrad in the worst case of head-on approach at the outer limit of an 8000-ft range. The implication in the LOS angle tolerance is that the target center is to be calculated to that tolerance. For such a calculation, some form of detection logic is required to define the boundary of the target image. The necessary logic is discussed in Section 3.4, Target Detection Mode. At these ranges, the boundary is easily defined, and the error estimates use a value of  $\pm 1/2$  pixel error in determining the target center. Without such logic, however, the target center is relatively indeterminable, and only the correlation window center can be used with no guarantee that the window is centered on the target.

The angle rate is more directly determined because the need to assess the position in the image plane is replaced by the correlation calculation which indicates image shift between integrations.

### 3.1.2.2 Range

The range accuracy needs to be interpreted in several ways to relate to system design parameter tolerances. The equation for range calculation has been given as:

$$R = BF/P$$

Differentiating for all the variables:

$$dR = \frac{R}{B} dB + \frac{R}{F} dF - \frac{R^2}{BF} dP$$

Given the values of  $dR = 50$  ft for  $R = 4000$  ft with the design values of  $B = 5$  inches and a pixel size of  $30 \mu\text{m}$ , the equivalent allowable errors

taken alone are  $dB = .0625$  inches,  $dF = .0625$  inches and  $dP = 6.5 \times 10^{-6}$  inches or  $1/181$  pixel. The latter figure can be given as an angular tolerance by  $d\theta = \sin^{-1} \frac{dP}{F} = 1.3 \mu\text{rad}$ . Each of these numbers is equivalent to the entire error budget. The first two error variables, baseline change ( $dB$ ) and focal length change ( $dF$ ), are systematic in nature, while the last, pixel shift error ( $dP$ ), is a composite of both calculation or statistical error and systematic error derived from imperfect physical integrity. The calculation error has been discussed in Section 2 and is evaluated in Section 5. A number of design and processing techniques have been evaluated with the goal of limiting or avoiding the calculational, statistical and systematic errors, and these are discussed in subsequent subsections. The most promising method to limit the pixel shift error is closed-loop ranging augmented by an internal calibration system. The goal of  $\pm 50$ -ft error at a 4000-ft range appears approachable, but even with closed-loop ranging and autocalibration implemented in the system, it would still be necessary to include some scene filter and/or increase the (BF/pixel size) scale factor in order to achieve such accuracy.

### 3.1.2.3 Range Rate

Range rate is calculated from range change divided by the time interval over which the change was measured. This leads to extending the range change measurement over as long a period as possible, but by so doing, the uncertainty in the validity of the results increases because of possible accelerations during that period. Because of the difficulty in achieving the range rate accuracy, the rate of information output is optimized at just greater than 1 Hz.

The results of the work presented in Section 6 are summarized below:

LOS angle	0.34 mrad at 1 kHz
Angle rate	3.84 mrad/s for 10 Hz
Range	121 ft at 4000 ft at 100 Hz
Range rate	71 ft/s at 4000 ft a 1 Hz

The LOS angle and angle rate accuracies are easily achieved at reasonable information rates and, although no requirement for angle acceleration was made, this can be provided with significant accuracy. The range accuracy appears possible, but remains somewhat elusive. Assuming the range accuracy is achieved, range rate information can be provided but not with the specified accuracy and only at low rates.

The next paragraphs describe the effect which the range accuracy requirement has on the system design. The reason that this requirement has become a driving force for the design effort is clear from the very small  $1.3\text{-}\mu\text{rad}$  error tolerance.

### 3.1.3 Optical Stability Requirements for the Rangefinder

In order to define the problem of accounting for the required range error tolerance, the potential sources of error are listed here.

1. Air mass between the target and the system - optical path deviation
2. Boundary layer - optical path deviation
3. Air wedge at the window boundary - temperature and pressure gradients
4. Window/optical path deviation (bowing, index gradients, wedging)
5. Air wedge between window and lens - temperature gradient
6. Baseline separation - thermal and mechanical stability
7. Lens focal length - thermal and mechanical stability
8. Lens alignment - thermal and mechanical stability
9. Optical aberrations - design and thermally induced
10. Optical folding reflective surfaces - thermal and mechanical stability
11. CCD - mechanical stability
12. Correlation - processing accuracy

Of these, the first two cannot be reasonably assessed by existing theoretical methods and the tolerances on both the baseline separation and focal length are not sufficiently severe to be of concern. The remainder involve severe constraints on temperature, pressure and mechanical stability. These constraints are discussed in more detail in Section 5. However, a

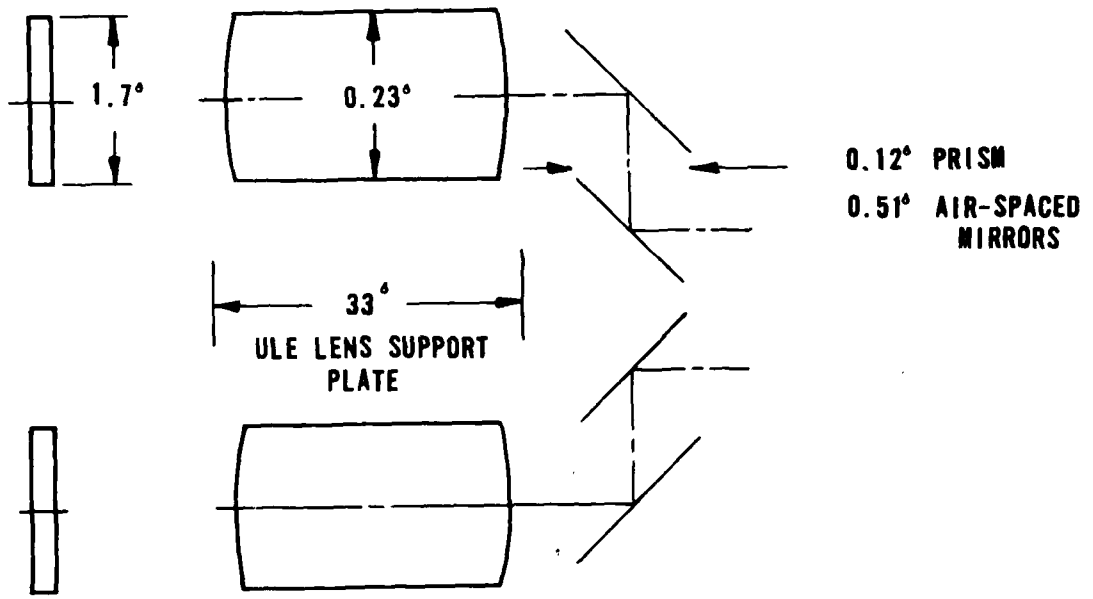
quick preview of the results is in order here. Windows normal to the optical path are required to tolerate the temperature and pressure gradients expected in an operational system. Further, specially designed athermal windows are needed to alleviate bowing problems due to the temperature gradient through the window. With these potential sources eliminated, Figure 4 shows some of the temperature gradients which would, by themselves, use the entire tolerance.

It is clear that there is little hope of controlling internal temperatures with such constancy given the severe environment in which the system will be used. Some method of compensating for the alignment errors which are produced by the gradients, and other problems not yet considered, is required. Such a method is described under the heading "Rangefinder Calibration". The method described accounts for all the alignment errors from the image planes to, but not including, the windows. Allowing that the air near the windows is circulated to eliminate temperature gradients, only one new error source is introduced. This error is also assessed in Section 6 and the results show that there should be little problem in maintaining the necessary optical path alignment.

Thus, the problem of optical stability is largely circumvented and there should be little systematic error affecting the rangefinding accuracy, aside from any errors produced from outside the system.

### 3.1.4 GDEM Window Considerations

As an airborne instrument mounted externally to a high performance fighter aircraft, the AEOTR must not only survive, but function acceptably under extremes of temperature, pressure, turbulence and vibration. The tracker must look at the world through a boundary layer whose effects are not well defined and depend upon aerodynamic design, flight parameters and meteorological conditions. While no one of these areas can be completely described and the effects precisely determined, it is desired to take the approach of minimizing sensitivity to each effect without adversely degrading system performance or integration potential. Because errors introduced by effects at the window and forward of the window cannot be eliminated by downstream sensing and calibration methods, it is mandatory that they be kept to a minimum.



TEMPERATURE DIFFERENTIALS IN  $^\circ\text{C}$   
 COMPONENT SUPPORT MATERIAL = ULTRALOW EXPANSION (ULE) CERAMIC

Figure 4 Rangefinder Thermal Errors

With temperature excursions on the order of 250°F. airspeeds of Mach 0.5 to 1.5, and flight altitudes of sea level to 50,000 ft. the thermal and pressure environments of the tracker are severed. An estimate of the thermal environment is made in Appendix A. Assurance of acceptable performance under these conditions requires careful attention to the design of the tracker windows as the first element in the optical train. For each of the following considerations, the derivations of the necessary equations are given in Appendix B. Only the numerical results are given in this section.

#### 3.1.4.1 Window Bowing

Each of the rangefinder windows is asymmetrical since it separates two different environments. Errors will be contributed at the windows due to temperature effects in the window and due to temperature and pressure differences between the environments.

A temperature gradient through the window from face-to-face will bend the window into a watchglass. Using the equation for the deflection of a ray through such a window as a function of temperature, the temperature difference,  $\Delta T$ , which will use an error budget of  $d\theta = 1.3 \mu\text{rad}$  can be calculated. This is done in Table 3 for three glasses and for several window tilt angles. A slant angle of 60° corresponds approximately to windows which are tangent to an 8-inch diameter hemispherical head with a 5-inch rangefinder baseline.

The thermal environment of the AEOTR is such that temperature excursions on the order of 150 C° can be expected. The implication of the results in Table 3 is that the entire error budget is used 650 times if the window is tangent to the sphere. A normal incidence window is therefore required if the rangefinder is to tolerate any temperature excursion.

The pressure differential through the window has the same effect as temperature in bowing the window. The magnitude of this effect is tabulated in Table 4 for FK51 glass in terms of  $\Delta P$ , the pressure differential required

TABLE 3  
 $\Delta T$  FOR 1.3- $\mu$ RAD ERROR

Window Tilt Angle	Window Material		
	FK51	FK5	LGSK2
60°	.190 C°	0.23	0.21
33°	0.31	0.39	0.35
10°	1.01	1.31	1.13
1.0°	10.1	13.1	11.3
0.1°	10.1	13.1	11.3

TABLE 4  
WINDOW BENDING

Window Tilt Angle	$\Delta P$ Allowed by 1.3- $\mu$ rad Error Budget (lb/in <sup>2</sup> )	Deflection Error with $\Delta P = 1$ Atmosphere (rad)
60°	2.0	$9.5 \times 10^{-6}$
33°	3.7	$5.2 \times 10^{-6}$
10°	12.3	$1.6 \times 10^{-6}$
1.0°	123	$1.6 \times 10^{-7}$
0.1°	1230	$1.6 \times 10^{-8}$

to use the entire error budget and in terms of  $\delta$  for  $\Delta P = 1$  atmosphere. For FK51 glass, Young's modulus ( $E$ ) is  $11.4 \times 10^6$  lb/in<sup>2</sup>. A nominal diameter and thickness for the window of 1.25 inch and 0.25 inch, respectively, is assumed.

#### 3.1.4.2 Air Wedge

The window slant creates an air wedge if there is a difference in pressure or temperature from one side to the other. The allowances for a  $1.3 \mu\text{rad}$  error are tabulated in Table 5. Nominal values of room temperature and one-half an atmosphere are used.

Each of the three effects considered above strongly indicates the need to avoid slanted windows in the rangefinder channels. The errors computed above are compounding rather than cancelling. An angular error of  $\delta$  relative to the system symmetry axis for one channel is matched by an error of  $-\delta$  in the other channel. The differential error for the system is then  $2\delta$ . This increased sensitivity is further motivation to use normal incidence windows for the rangefinder.

The error budget for the tracking channel is 1.0 mrad. Since the effect computed above are linear in  $\delta$ , the allowable temperature and pressure excursions for the tracking channel are 770 times larger. From the above results, there is therefore no reason that the tracker window cannot be slanted to improve aerodynamic performance of the tracker head. The combined effects of the temperature and pressure excursions will use only a small part of the error budget, leaving the major portion for electronic sampling and processing error.

#### 3.1.4.3 Window Wedge

Given a flat window normal to the optical axis, there remains the effect of wedge caused by a transverse temperature gradient (across the window as opposed to through the window). Such a gradient produces both relative thermal expansion of the glass from one side of the aperture to the other, a physical wedge, as well as a refractive index gradient across

TABLE 5  
AIR WEDGE - TEMPERATURE AND PRESSURE LIMITS

Window Tilt Angle $\beta$	Tolerable $\Delta P$ with Constant Temperature (lb/in <sup>2</sup> )	Tolerable $\Delta T$ with Constant Pressure (C°)
60°	- .04	1.6
33°	- .10	4.2
10°	- .39	15.7
1.0°	- 3.9	157
0.1°	- 39	1570

the aperture, an optical wedge. No glasses exist for which these effects cancel each other. However, there is one glass which has a net negative effect, while others have net positive effects. Thus, for a laminated window composed of contacted glasses, the deflections add to produce zero net deflection. The thicknesses of the two glasses need to be in inverse ratio of their composite thermal coefficients. To minimize reflection losses at the boundary, the refractive indexes need to be as closely matched as possible. Filling the space between the elements with a liquid having a similar index will reduce reflection losses at the boundary.

Two examples of window designs using the above criterion are given below using FK51 as the negative beta glass.

Material Properties

Material	$\nu \times 10^6$	$\alpha \times 10^6$	$n - 1$	$\beta \times 10^6$
FK51	- 7.9	13.6	.487	- 1.28
FK5	- 2.3	9.2	.487	2.18
LGSK2	- 4.5	12.1	.586	2.59

For a window composed of FK51 and FK5, typical thicknesses would be

$$b (\text{FK51}) = .170 \text{ inch}$$

$$\text{and } b (\text{FK5}) = .100 \text{ inch}$$

There is no index step at the interface, although the thermal expansion coefficients are mismatched by a factor of 1.5.

For a window of FK51 and LGSK2, the thicknesses are

$$b (\text{FK51}) = .202 \text{ inch}$$

$$b (\text{LGSK2}) = .100 \text{ inch}$$

Here, the thermal expansion coefficients differ by only 12 percent, while the refractive index step is 0.099 or 6 percent.

Thus, it is possible to design a window for the tracker to negate any optical deflection at this boundary of the system.

### 3.1.5 Ranging Optics Configuration

Earlier analysis has shown that limiting ranging error is inversely proportional to the product of lens focal length times the stereo baseline separation between lenses. For a maximum range measurement of 4000 ft, with an accuracy of  $\pm 50$  ft, this product must be at least 20 in<sup>2</sup>. The further constraint of fitting within the small spherical volume available for tracker packaging led to the selection of a 5-inch focal length and a baseline separation of 5 inches.

Establishment of the focal length and the baseline separation is the starting point for a detailed optical configuration layout. Additional considerations influencing and controlling a detailed layout are:

- Light collection efficiency
- Size and spatial relationships
- Performance equality between the two "eyes" of the ranger
- Most importantly, the optical/mechanical stability of the configuration

As discussed elsewhere (3.1.2), the optical/mechanical tolerance requirements are extremely stringent being on the order of 1.3  $\mu$ rad or less. Further, any configuration is subject to thermal effects which in the present case are potentially catastrophic because of the severe environment in which the ranger must operate.

An optimum configuration would eliminate, or reduce to manageable proportions, sources of ranging error associated with maintaining alignment between the two channels and essentially identical characteristics in each channel. Any configuration will, in each channel, have the following components:

- Entrance window
- Objective lens
- Fold optics (prisms, mirrors) at lens input and/or lens output, as dictated by packaging considerations
- CCD image focal plane
- Suitable support and alignment structures

Detailed consideration of entrance window requirements and problem is presented in Appendix B where account is taken of pressure and temperature effects along with ranging performance requirements.

Five basic techniques, separately or in combination, are available in evolving a suitable design:

- Use of materials, where possible, having the highest mechanical and thermal stabilities, both for components and support structures.
- Use of materials having complementary properties, in particular, thermal characteristics, so that self-compensating characteristics are achieved.
- Tightest practical tolerances on component parameters such as lens focal length and optical aberrations to provide best channel matching.
- Use of a built-in self-calibrating (autocollimating) subsystem to correct for alignment and parameter changes.
- Sharing of components between channels to eliminate or cancel error, e.g., use of a common lens with split or shared pupil.

The first three techniques represent normally good design practice when applied in a degree consistent with cost effectiveness and reasonable component yield. In the present case, it is not clear that tolerance and material choices alone, regardless of cost expended, achieve the required performance.

The fourth technique of adding a self-calibration function adds complexity and cost, but can very well result in an improved performance level beyond that achievable with the first three techniques. i.e., in the present instance, the required performance level.

The last technique, commonality of components between channels, offers the possibility of circumventing many error sources due to differences between channels. For example, use of a common lens with a split or shared pupil avoids the need to match focal lengths, as well as alignment

between individual lenses. Implementation of such commonality requires that channel discrimination be maintained by techniques such as spatial or spectral filtering, polarization selectivity or time multiplexing.

A number of optical configurations using the above techniques were examined for expected performance, particularly the degree to which they could provide self-alignment or error cancelling properties. That is, considerable emphasis was placed on configurations employing component commonality because of the potential for performance improvement and packaging advantages. The configurations studied are shown schematically in Figure 5. Table 6 summarizes the advantages and disadvantages of each configuration.

As Table 6 shows, each of the configurations suffers from one or more of the following problem areas:

- High illumination loss (50 percent)
- Signal crosstalk between channels
- Sensitivity to mechanical or thermal stresses
- Physical space requirements
- Asymmetric image problems
- Lens focal length equality in two lens configurations

In effect, those configurations which attempt to circumvent the problems of alignment, stability and focal length equality by sharing of components introduce problems as great or greater than the configuration using two independent channels. Appendix D provides additional detail on the comparison of the various configurations.

The approach which remains is the two independent channel configuration augmented by an autocollimation self-calibration subsystem.

### 3.1.6 Rangefinder Calibration

The problems in designing the AEOTR in terms of temperature and pressure environments have been discussed in detail. Aberrations in the optical path which cause an error in the misregistration calculation for

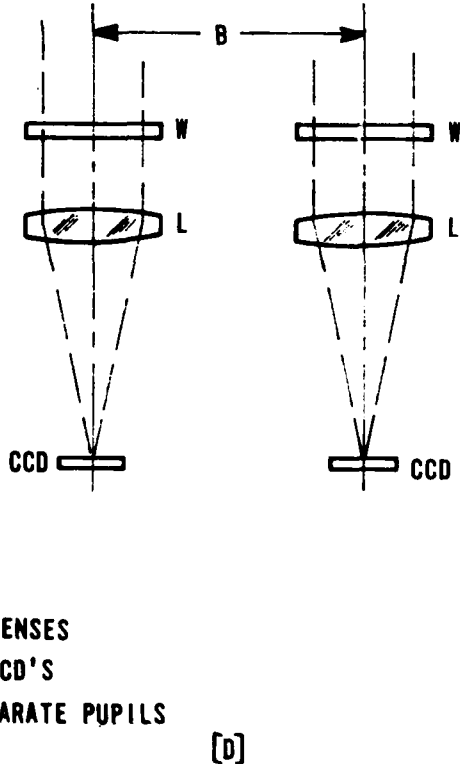
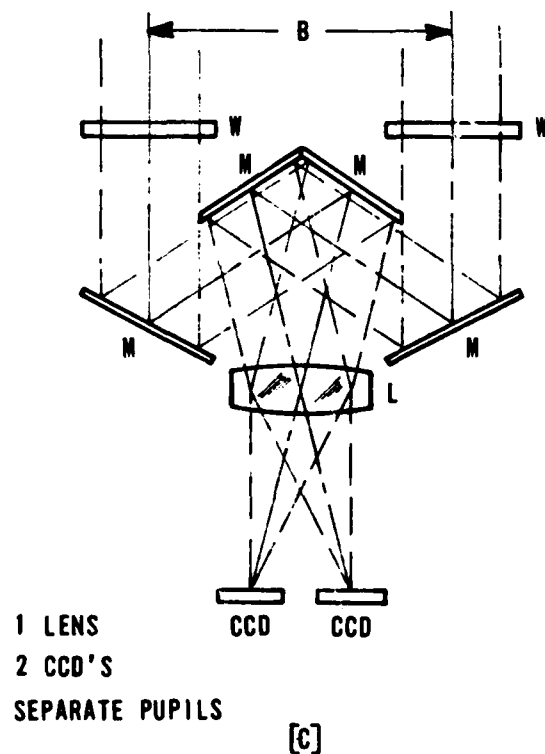
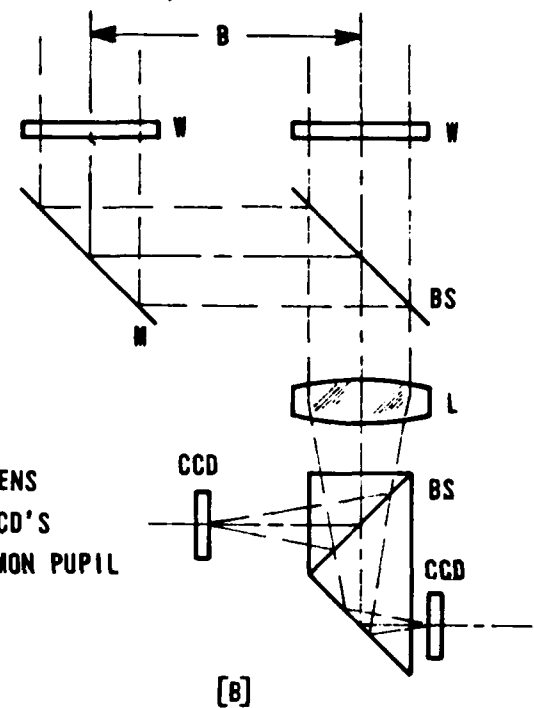
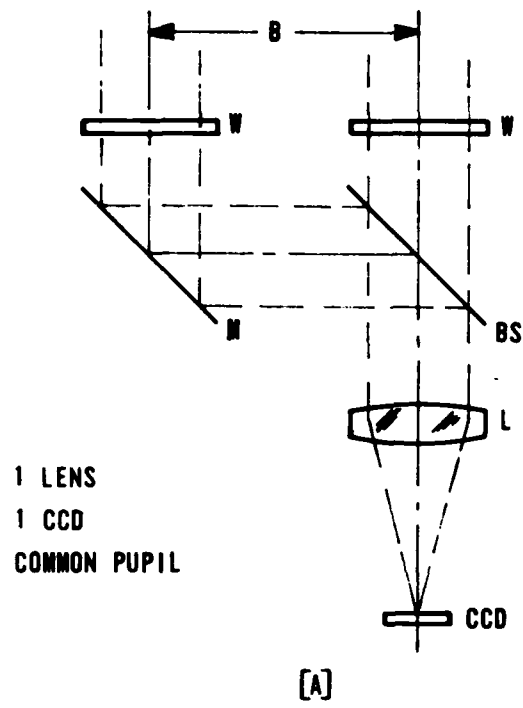


**Figure 5 Optical Configuration Alternatives**  
*(Page 1 of 2)*

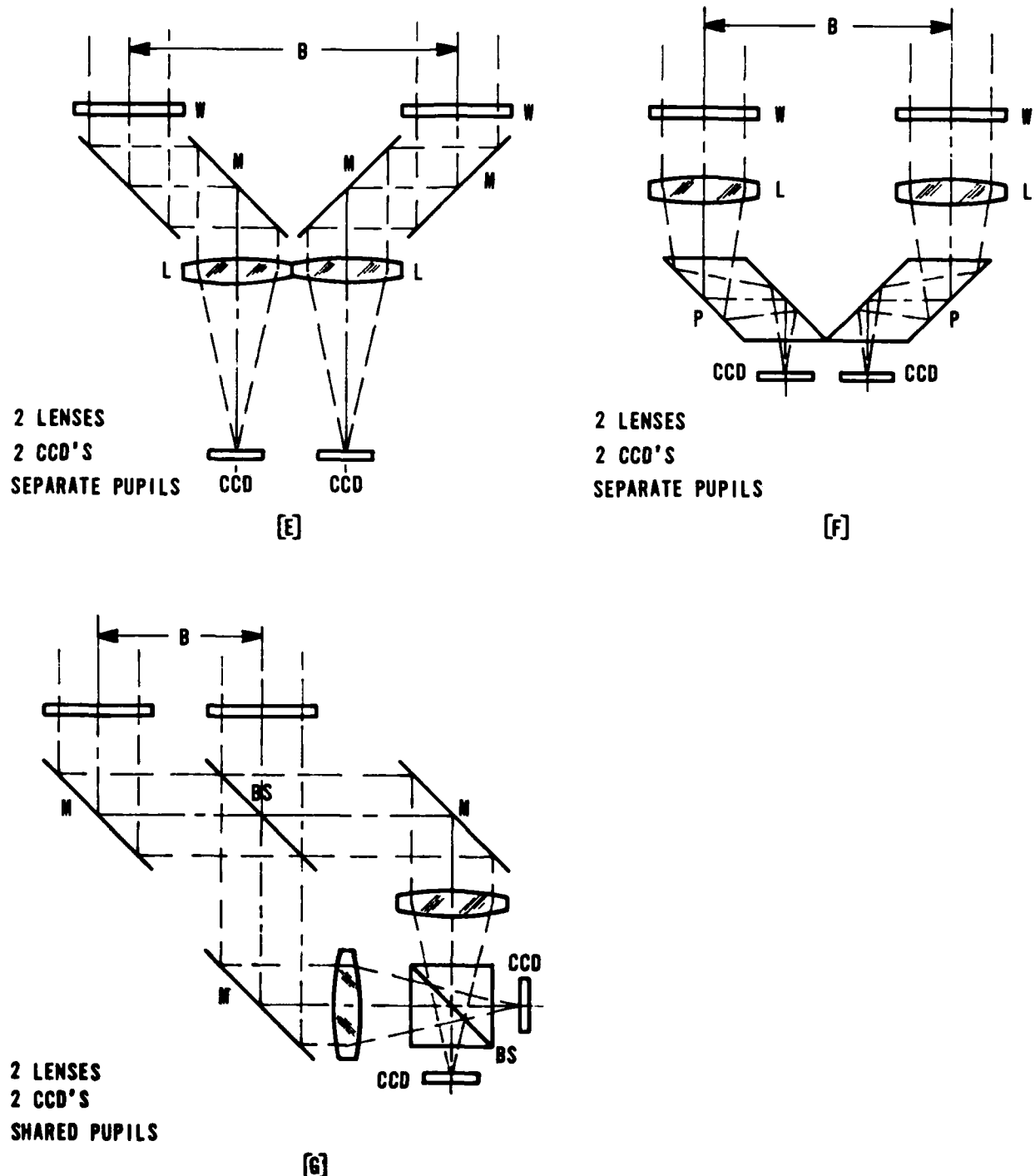


TABLE 6  
AEOTR OPTICAL CONFIGURATIONS

Description	Functional Operation	Advantages	Disadvantages
I. Two lenses Two CCD's Separate Pupils	Two completely independent channels	No crosstalk	Requires matched components and most stringent alignment tolerances and mechanical/thermal stability
II. One lens One CCD Common Pupil	Combining optics send each image through common channel	1. Greatest commonality of components - smallest number of components required 2. No focal length matching 3. Residual aberrations cancelled 4. Minimum alignment requirements 5. Best cancellation of mechanical/thermal instabilities	1. Requires time multiplexing to effectively implement 2. Presently available CCD cannot function at multiplex rates necessary to maintain range accuracy 3. 50 percent light loss
III. One lens Two CCD's Common Pupil	Combining optics send each image through shared pupil of lens with dichroic or polarization beam separation to each CCD	Same as configuration II, though not quite as insensitive to mechanical/thermal instabilities and does require a beamsplitter	1. Crosstalk - estimated signal to crosstalk ratio is 4:1 to 6:1 2. 50 percent light loss
IV. One lens Two CCD's Separate off-axis pupils	The two detectors are symmetrically positioned on opposite sides of the lens axis	1. Complete channel separation, i.e., no cross-talk 2. No light loss due to beamsplitting 3. Relative insensitivity to mechanical/thermal instabilities	1. Asymmetrical lens aberrations in each channel 2. "Handedness" of pupils
V. Two lenses Two CCD's Shared Pupils	Each lens contributes to each channel by shared pupil operation	1. Averages the difference in lens characteristics between the two channels 2. No inherent 50 percent light loss	1. Requires dichroic or polarization beamsplitters to separate channels 2. Crosstalk - at best, signal to crosstalk ratios of 4:1 to 6:1 available 3. More components - greater susceptibility to mechanical/thermal instabilities and requires most packaging volume

ranging can have many sources, and can occur all along the optical path. There are several possible methods of attacking the problem:

- Design to eliminate the sources of aberrations
- Design counteractive effects for each of the causes
- Detect the sources and calculate their effects
- Detect the effects of the causes
- A combination of the above

From the foregoing discussion, it is clear that the very small scale of some of the sources which will cause intolerable effects leaves little hope of eliminating all of these sources for reasonable expenses of money, volume and complexity. Designing counteractive effects will also prove costly and difficult if the attempt is made for each cause. Detecting the sources is indirect, expensive in volume and processing, and uncertain due to the undefinability of some causes and possible omissions. Detecting the effects is direct, and thus attractive, but requires a reference point. The reference point can be an object known to be at infinity, an object at a known distance, or an artificial object projected into the system by a second optical system. Each of these is unattractive for in-flight operation considering the need for constant calibration, let alone the uncertainty of truly knowing any of these reference points. A fourth possibility is to make the reference point one of the image planes. That is, if one image plane "sees" the other through the same optical path as each "sees" the outside world, then correlating the imaged plane with what that image plane is known to be produces a misregistration which is due solely to the aberrations of the optical path. By subtraction, the misregistration between the two images of the outside world which is due to range alone can then be determined.

#### 3.1.6.1 Autocalibration Subsystem

Figure 6 shows a schematic of the ranging optics. The sum of aberrations giving rise to false misregistration is shown in Figure 6A as resulting from a single optical wedge in one channel. The autocalibration function is implemented as shown in Figure 6B by causing a pattern at one CCD sensor to serve as a target for the other CCD. With the ranging optics

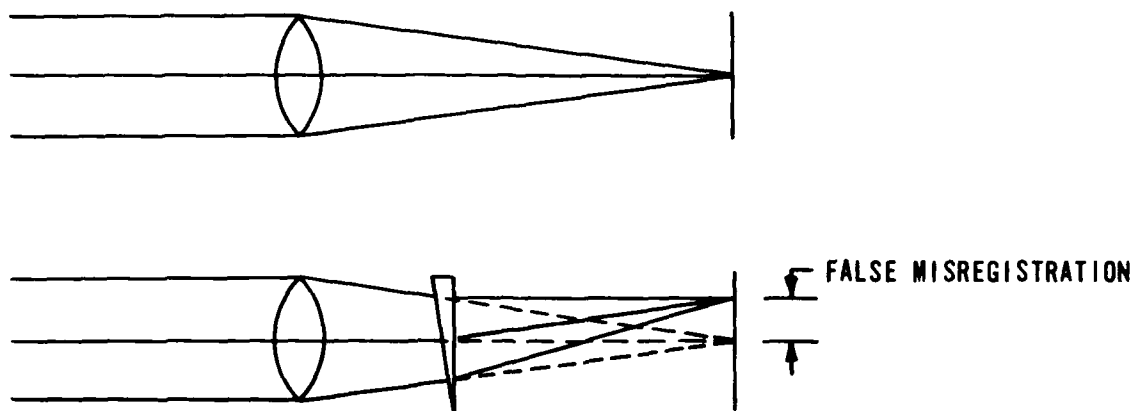


Figure A) False Misregistration Resulting From an Optical Wedge

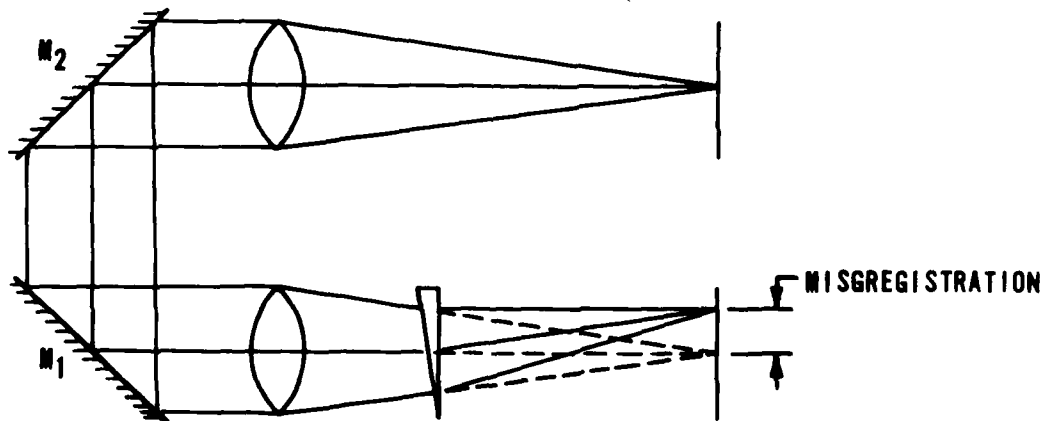


Figure B) Autocalibration System

Figure 6 Ranging Optics Schematic

in ideal alignment, the calibration target CCD pixel(s) will be in perfect registration with the calibration sensor pixel(s). Misregistration can be sensed and a correction applied to the range computation routine. This correction can be carried out at a very high rate, i.e., the viewing frame rate of the rangefinder. It is necessary that an even number of reflections be introduced so that aberrations on each side add in the same way as they do without the mirrors.

The beam splitting mirrors,  $M_1$  and  $M_2$ , which fold the self-calibrating CCD target signal(s) over to the CCD sensing pixels are transmissive to outside world images, but reflective for the wavelength of the calibration light. The region of the CCD array used for self-calibration targetting and sensing is assigned to be outside the rangefinding FOV. It should be noted that only misalignment in the plane of the rangefinding channels affects ranging accuracy, at least in a first order sense.

A target source pattern which would permit a measurement of the horizontal misregistration of the CCD's as a whole could consist of several vertical CCD lines (the order of five to ten pixels in length to insure against loss of calibration signal due to vertical perturbations), with either a square wave or sine wave reflective pattern deposited in the horizontal direction. A sine wave pattern is probably preferred because it has no high frequency harmonic content which can disturb correlation processing. Similarly, the pattern spatial frequency must be appropriately chosen to obtain the best balance between sensitivity and CCD aliasing effects, i.e., an appropriate fraction of the sampling frequency. It is possible to use only a few rows of pixels on the top and/or bottom of the image planes for calibration purposes, leaving the rest of the plane for imaging the world.

Two possible methods for producing the self-calibration pattern are immediately evident. The pattern could be projected onto one CCD to be imaged directly, allowing some of the projected light to be reflected into the optical path to be imaged on the second CCD. Because CCD's tend to be highly reflective, this method requires only suitable projection optics within the head of the tracker. The second possible method is to deposit a reflective material directly on a portion of the CCD or its cover glass in a pattern. Then, simple illumination of the pattern allows the image

of the pattern to be focused on the second CCD, while the illuminated CCD receives the complementary pattern of light directly. A simple mathematical inversion of one of the signals prior to correlation allows the proper processing for false misregistration calculation. This latter method is more economical in volume and more simply implemented.

If possible, it is desirable that the calibration function and the ranging function be performed simultaneously as opposed to dividing time between the two functions. To permit simultaneous operation, it is necessary that the two mirrors be only partially reflective in some manner to allow transmission of light from the outside into the system. The most efficient technique is to use light of a special wavelength for calibration with filters which reflect only that wavelength, and not the rest of the band to which the image planes are sensitive. The wavelength chosen can be near either end of the spectral sensitivity curve with the appropriate high pass or low pass dichroic filter, or in an atmospheric absorption band with an appropriate band reflecting filter if possible. By this means, little or none of the important information from the outside world is lost. Furthermore, to avoid adverse interaction between the calibration image and the image of the world, the areas should be separate.

### 3.1.6.2 Residual Error

The autocalibration method accounts for all false misregistration to the rear of the mirrors. Aberrations in the optical paths not common to the "world view" and "self view" are not accounted for. The unaccounted aberrations can be in the two mirrors, the air path between the two mirrors and the paths forward of the mirrors. Clearly, the mirrors should be located as near to the front of the system as possible in order to account for as many of the components as possible. However, since the front surfaces need to be of normal incidence, the optimum location for the mirrors is immediately behind the front windows.

The accuracy of this calibration is the accuracy inherent in the registration detection process, in this case correlation. However, the conditions can be made to be as nearly ideal as possible. The price of

calibrating out all the aberrations to the rear of the mirrors is the introduction of three new potential causes - the two mirrors and the air between them.

The remaining unaccounted aberrations are those of the two mirrors and the air between them (the air outside the system and the windows are discussed elsewhere), the latter can be circulated to avoid any problems of air wedge. The mirrors, being in collimated space, need to be maintained at right angles to assure absence of unaccountable aberrations to the calibration optical path. However, to avoid aberrations to the ranging optical paths, wedging and lensing effects must be avoided or detected. The constraints for the mirrors are no less severe than for tilted windows as discussed elsewhere, but being located inside the system allows better control over the sources of aberrations. Pressure differentials across the mirrors and through them can be discounted, as can temperature differentials through them due to circulation of the air. Temperature differentials across the mirrors cannot be discounted. Hence, the mirrors should be as thin as possible and athermally designed similar to the outside windows, but allowing for increased optical path due to nonnormal incidence. To maintain the two mirrors perpendicular to one another, they should be mounted between two plates of a rigid athermal material. Because the only concern is to maintain the angle, only the temperature gradients from front to rear of the plates and between the two plates need be considered. These are shown in Figure 7.

For the front to rear gradient ( $\Delta T_H$ ):

$$\Delta\Theta = 2 \operatorname{Tan}^{-1} \left\{ \frac{(b + a) [1 + \alpha(T' - T_o + \Delta T_H)] - (b - a) [1 + \alpha(T' - T_o)]}{2a} \right\} - \pi/2$$

where:

b = baseline separation (5 inches)

a = aperture diameter (1.25 inches)

T' = absolute temperature at front of plates

$T_o$  = absolute temperature at time of test calibration

$\alpha$  = coefficient of expansion ( $0.00 \pm 0.03 \times 10^{-6}/C^\circ$  for ULE)

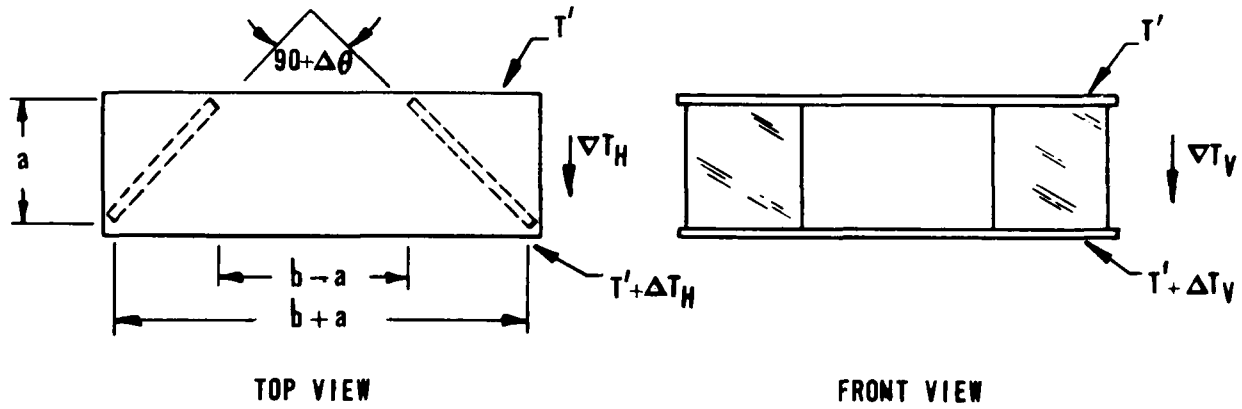


*Figure 7 Calibration Mirror Mounting*

### 3.1.6.3 Rangefinding Calibration

Since the tolerance is one-half of the usual angular tolerance because of doubling, the error in reflection:

$$\Delta\Theta = \left| 2 \tan^{-1} \left\{ 1 + \alpha \left[ T' - T_o + \frac{b+a}{2a} \Delta T_H \right] \right\} \right| - \pi/2 < .5 \times 10^{-6} \text{ rad}$$

$$\text{for the values given: } (T' - T_o) + \frac{6.25}{2.5} \Delta T_H < 16-2/3^\circ\text{C}$$

This is not an unreasonable tolerance to be controlled; furthermore, the effect is well defined and predictable from either a few temperature sensors or strain gauges if necessary.

Somewhat less well defined is the effect of a temperature differential between the two plates. Such a gradient would cause strain in the mirrors, possibly deforming them from planes and causing them to become dependent on the bonding strength and elasticity of the adhesive used to bond the mirrors to the plates. Assuming a perfectly rigid bond as a first approximation, the effect can be considered to be the average of the two excursions of the individual plates and thus one-half of the effect of absolute temperature change with no front-to-rear differential. Thus, the tolerance for the top to-bottom differential ( $\Delta T_v$ ) is:

$$\Delta T_v < 33-1/2^\circ\text{C}$$

### 3.1.6.4 Summary

The autocalibration technique allows the effects of all the causes of false misregistration behind the two mirrors to be measured to the accuracy of the correlation processing under virtually ideal conditions, specifically, high contrast, relatively large area, nearly motionless, sharply imaged, well defined optimum patterns with no background content. The remaining and newly introduced potential causes of false misregistration within the boundary of the system can be controlled, designed against, and if necessary, sensed to sufficiently obviate any effects without undue penalties in expense, volume and complexity.

### 3.1.7 Closed-Loop Ranging

Both computer and experimental test of the correlation process indicates a nonlinear behavior of the fractional pixel shift calculation relative to the actual shift. This problem did not appear in earlier results because the previous computer program considered only integral pixel shifts. At integer shifts, the stated accuracy is correct, or more likely conservative.

One of the results of the correlation modeling efforts summarized in Appendix G was the identification of the source of this nonlinear characteristic. The nonlinearity at fractional shifts is due to the fact that image information of frequency greater than 1/2 Nyquist correlates over finite windows with power distributed towards integer shifts. Nyquist frequency information, for example, can exhibit correlation power only in integer shifts. On the other hand, attempting to prefilter the information content of the image reduces the signal-to-noise ratio and spreads the correlation function in the spatial domain with attendant loss of accuracy. Given an ideal rectangular frequency filter, the optimum cutoff frequency appears to be .75 Nyquist. Using real (RC) filters with characteristically slow rolloff, results did not demonstrate an appreciable enhancement of the correlation accuracy.

Hence, in order to meet the required accuracy for post-acquisition ranging calculations, a closed-loop system is indicated. An element is required which displaces one target image until integer shift is calculated, with the actual displacement measured by means of autocalibration. (For some situations, the appropriate image shift is actually one-half integer rather than whole integer.) The autocalibration works on a well defined image with well behaved, if nonlinear, correlation response. By this means, the task of measuring an arbitrary shift of an unspecified image is translated into the measurement of an arbitrary shift of a specific controlled image by a system whose response to shifts of that image is well known. The problem then reduces to moving the target image in a controlled fashion until the specified fractional pixel shift is reached.

Image displacement can be accomplished by reflection, refraction or mechanical means. Because the autocalibration mirrors are immediately adjacent and forward of the ranger lenses, the most convenient place for the displacement to be done is in the back focal length. The use of a refractive method of displacement is preferred over reflective methods because of the small displacements and the high stabilities required, the refractive methods being less sensitive. The refractive methods involve the introduction of either a wedge (counter rotating wedges) or a parallel plate in the back focal region. The parallel plate method, being mechanically simpler and not introducing significant distortion for the small tilt angles involved, is probably the preferred method.

The image displacement,  $\Delta$ , produced by a parallel plate glass is given by the formula:

$$\Delta = t \sin \Theta \left[ 1 - \frac{1}{\sqrt{\frac{n^2 - 1}{\cos^2 \Theta} + 1}} \right] \div \text{pixel size}$$

where:

$t$  = plate thickness

$n$  = refractive index

$\Theta$  = angle between the optical axis and the normal to the plate

For small angles:

$$\Delta \approx 0.0417 \Theta$$

Numerically, with  $t = 1/8$  inch,  $n = 1.5$ , and a pixel of  $30 \mu\text{m}$

$$\Delta \approx 35.3 \Theta \text{ or } \Delta \approx 0.62 \text{ pixel/degree}$$

Several mechanical means are available to drive a plate by this order of angle, including very small dc motors with gear drives, wound armature galvanometers and piezoelectric devices. Adequate space is available in the AEOTR head to include either a motor drive or a galvo drive, as well as the flat plate with support structure. Position sensing is provided by the correlation processing itself.

The rates associated with loop closure are quite manageable. At a maximum closure rate of 3000 ft/s, the pixel shift per integration at a 24,000-ft range is only 0.000020 pixel and at a 4000-ft range is 0.00073 pixel. Clearly, the loop can be closed and locked within a few integrations.

Closed-loop ranging then is a feasible technique which will permit the application of the high accuracy potential of correlation processing to ranging on targets of arbitrary shape and contrast structure.

### 3.1.8 Target Aspect

As an auxiliary function of an airborne E-O imaging system, pattern recognition could potentially be of use in predicting target intentions and thus permit greater anticipation of future target path. This information, if reliable, could lead to quicker or more accurate solutions to the gun aiming problem and an increase of firing opportunities. It is assumed that there exists a connective relationship between aspect and intention, and that the attacker would have knowledge of the relationship.

Determination of aspect requires either the ability to interpret a two-dimensional image, or to acquire a three-dimensional image, or a combination of both. The former will require either extensive computational analysis or a potential delay until one of several specific aspects can be recognized and thereafter tracked. A three-dimensional image, on the other hand, requires a highly resolved image and highly accurate ranging on points of the target. A preferred approach might be to provide fairly gross relative ranging on the target as a starting point for a pattern recognition program.

In general, the determination of aspect requires a pattern recognition capability to tell which target body axis is closest to the LOS axis. Relative ranging can then provide the orientation of the other two axes. The LOS angle rate and range rate are, of course, strong clues as to whether the target aircraft centerline is parallel, antiparallel or orthogonal to the LOS since ownship motion is well known and target performance characteristics

are generally known. Given an initial determination that relative motion is primarily along the LOS, a simple pattern matching technique could determine target image roll angle and possibly roll rate. A moderately high video resolution would be required for even this elementary level of aspect determination.

Aspect rates are again suited to determination either by sequential aspect measurements or correlation methods. Roll rate is particularly suited to correlation which, conceptually, rotates two images with respect to one another and cross multiplies the corresponding image points. The correlation peak is a direct measure of the angle of rotation. Note that this is specifically a measure of image roll about an axis, which does not necessarily correspond to the roll of the target about its line-of-flight axis. Image pitch and yaw rates are conceptually possible by correlations which scale either the vertical direction or the horizontal direction, respectively, of one of the images. Now the position of the correlation peak is a measure of the change in the cosine of the rotation. This method requires initial knowledge of pitch or yaw, and may be difficult to distinguish from range changes by which both axes scale. Furthermore, the origin of the scale should be at the axis of rotation. For these reasons, measurement of yaw and pitch rates seems more likely to be accomplished by sequential aspect determination.

### 3.1.9 Sensor Selection

The basic operation of the AEOTR begins with the generation of target image video. The two ranging sensors are operated under identical electrical conditions to permit the measurement of the stereometric displacement of simultaneous images. The tracking sensor may be operated under different electrical conditions to optimize the determination of image displacement between successive video frames. A careful consideration of candidate sensors is appropriate since they represent a fundamental constraint upon system design and resultant performance.

### 3.1.9.1 Sensor Options

The sensors in the AEOTR must be solid state since their small size and low operating voltages are required by the tight system packaging, and their freedom from scan geometry distortion is indicated by the precision of the correlation processing hardware. The two classes of solid-state image detectors under consideration for the AEOTR are the CCD typified by the Fairchild CCD 211 and the charge injection device (CID) typified by the General Electric TN2500.

With the Fairchild CCD 211, the video produced takes the form of a raster containing 244 horizontal lines with 190 picture elements each. The total active area is 5.7 mm horizontal by 4.4 mm vertical. Individual pixels measure  $14\text{ }\mu\text{m}$  by  $18\text{ }\mu\text{m}$  and lie on 30 by  $18\text{ }\mu\text{m}$  centers. The  $16\text{-}\mu\text{m}$  wide inactive region in the horizontal direction is required between the vertical columns for vertical charge transfer registers. No inactive area exists between horizontal rows of picture elements. Photogenerated charge is integrated in the active pixel photosite areas of the CCD until it is transferred out of the photosites and into the vertical transfer register, the entire field being transferred at one time. Since there are two interlaced fields in the video frame, each transfer represents interlaced halves of the entire image. The charge representing the image is transferred vertically, a line at a time, into the horizontal transport register. In the horizontal transport register, charge is serially transferred to a charge detector.

The GE TN2500, like the CCD, uses a raster image readout with a self-scanning internal structure. The basic difference lies in the fact that the charge accumulated at the photosite is interrogated by an x-y addressing scheme which injects it into an electronic backplane for conversion to an output voltage. The format of pixel readout from this device can be either interlaced or noninterlaced raster readout. Since the charge is transferred as the photosite is addressed, the exact time of image readout varies depending on position in the array in contrast to the CCD where the entire image charge pattern is transferred into the internal shift registers in one single operation, permitting all pixels to integrate over the same time period.

Because the CID requires no charge transport registers, the entire image format is photosensitive with no dead space. This may reduce the effects on correlation processing of high image spatial frequency aliasing discussed elsewhere. The array consists of 248 horizontal by 244 vertical pixels. Each pixel has a dimension of 45.7  $\mu\text{m}$  horizontal by 35.6  $\mu\text{m}$  vertical, with the center-to-center spacing being the same. The active area dimensions are 11.3 mm by 8.7 mm. Both the CID and the CCD have an image aspect ratio of approximately 4 to 3.

#### 3.1.9.2 Field of View

The fields-of-view (FOV) of these sensors in the AEOTR are given by  $2 \tan^{-1} (1/2f)$ , where  $f$  is the focal length and  $l$  is the characteristic dimension (horizontal, vertical or diagonal). For the CCD and the CID, the FOV is given in Table 7.

#### 3.1.9.3 Video Readout

Several problems arise with the use of either of these sensor types, and are associated with the manner in which the video is presented to the correlation electronics (interlaced or noninterlaced). The fundamental design of the video generation electronics, however, is the same for either sensor, and a circuit block diagram is illustrated in Figure 8. Following preamplification, the analog video signal is immediately digitized into 8-bit words. All processing beyond this point is digital to preserve signal quality and to capitalize on available digital hardware.

Also illustrated in Figure 8 are the necessary sensor timing logic and sensor clock drivers. The CID and CCD both require several sets of variable amplitude timing pulses with typical clock voltages ranging between 0 and + 15 V to produce the video output. In addition to generating clock waveforms and start conversion commands to the A/D converters, the sensor timing logic also controls the basic operation of all the correlation electronics since it must be synchronized with the video pulse train.

TABLE 7  
SENSOR FIELD OF VIEW

Sensor	Format H x V x diagonal (mm)	Pixel H x V ( $\mu$ m)	Sensor FOV Tracker $f = 2$ inches $f = 5$ inches	Pixel FOV Ranger
CCD 211	5.7 x 4.4 x 7.2	30 x 36	6.4 x 5.0 x 8.1°	2.6 x 2.0 x 3.2°
CID	11.3 x 8.7 x 14.3	45.7 x 35.6	112 x 87 x 141 mrad	45 x 35 x 56 mrad

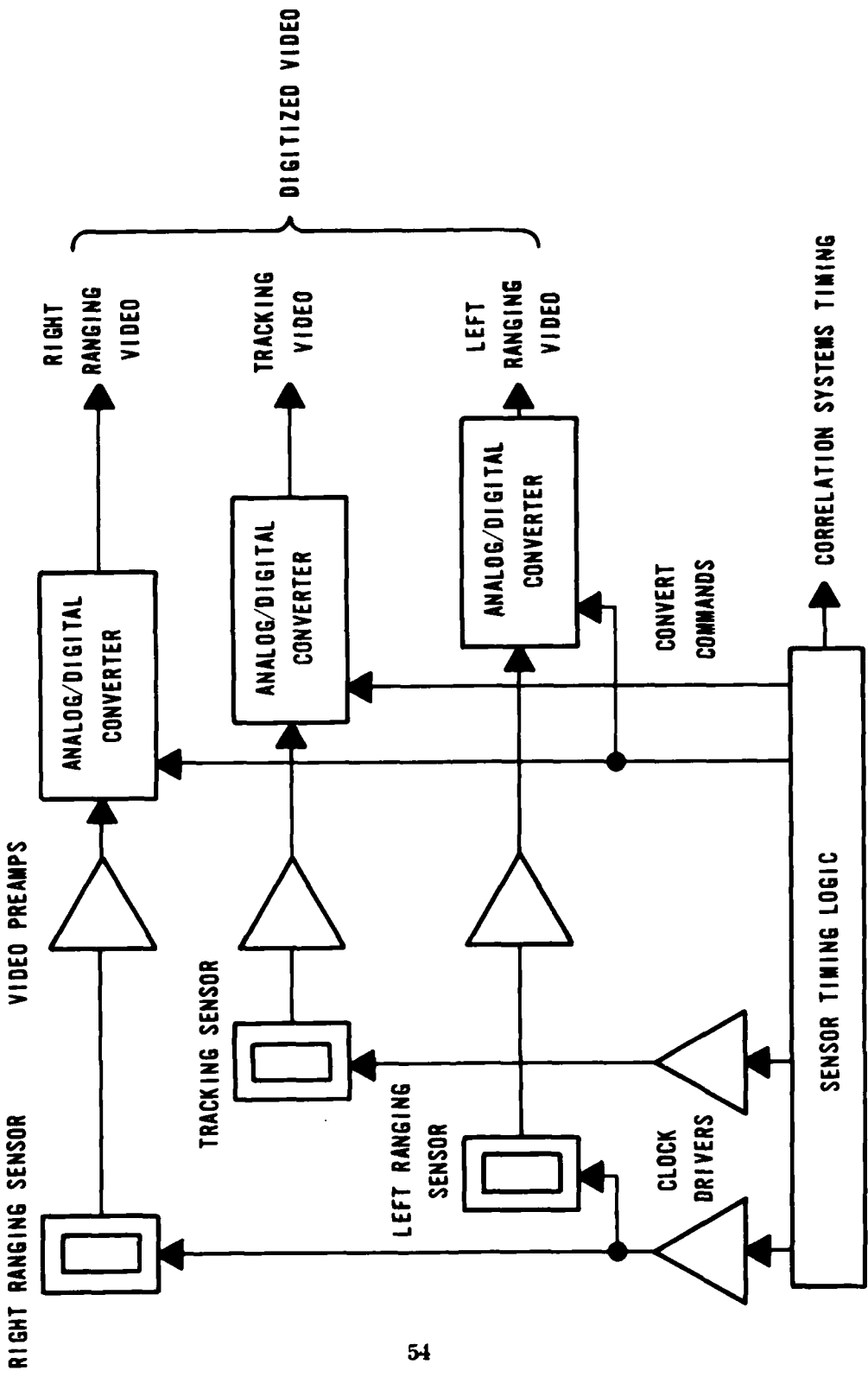


Figure 8 Circuit Block Diagram

It will be observed in Figure 8 that the two ranging sensors are driven synchronously by the same clock waveforms. Matching of the left and right range sensors is used throughout, including the mechanical, optical and electrical alignment of both sides. This is to ensure that the only differences between the video images will be due to image displacement rather than intrachannel electrical differences. The tracking sensor, on the other hand, performs a different function and need not be matched to the other two sensors. In fact, the tracking sensor may even be operated at a different frame rate and could conceivably be of the other type of sensor.

The basis of the correlation technique described for this program lies in correlation matching algorithms to determine relative image translation between successive video frames in the tracking case and identical but misregistered simultaneous video images for target ranging. These video images are processed through a standard correlation equation to determine the magnitude of image translation. Algorithms developed by CAI allow determination of the misregistration to accuracies many times that of the sensor video resolution, and displacements equivalent to extremely small fractions of a picture element can be measured.

#### 3.1.9.4 Readout Mode

One difficulty in using the solid-state sensors for image correlation relates to the mode of sensor readout. If the sensor selected uses two-field interlaced readout, a problem is created for the tracking correlation electronics. As shown in Figure 9, a target is scanned in the two separate fields. If the correlation processing is on a field-by-field basis, then even under the best conditions, there will be a 1-pixel jitter with every frame. This occurs because the two fields contain similar, but nonoverlapping, video images of the target, the  $\pm 1$ -pixel displacement being detectable by correlation processing. This simple picture assumes that the video produced in one field is quite similar to that produced in the other. This is not necessarily the case since an image containing high spatial frequencies in the vertical direction in one field may have quite dissimilar characteristics in the other field. This will result in a poor correlation match and significantly higher processing noise.

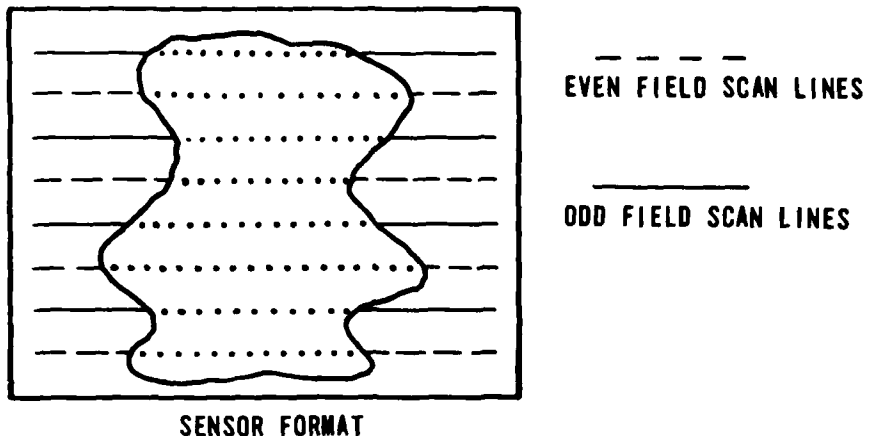


Figure 9 Scanning Fields

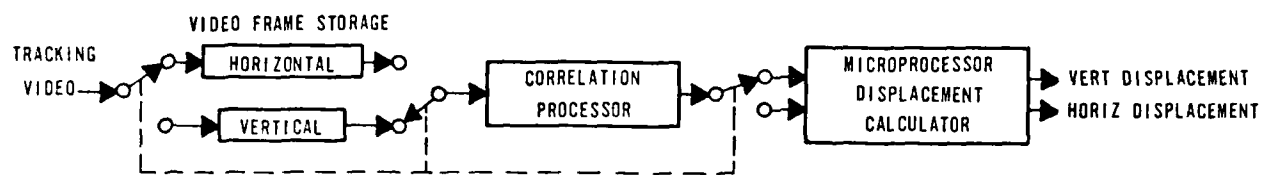


Figure 10 Interlaced Readout Mode

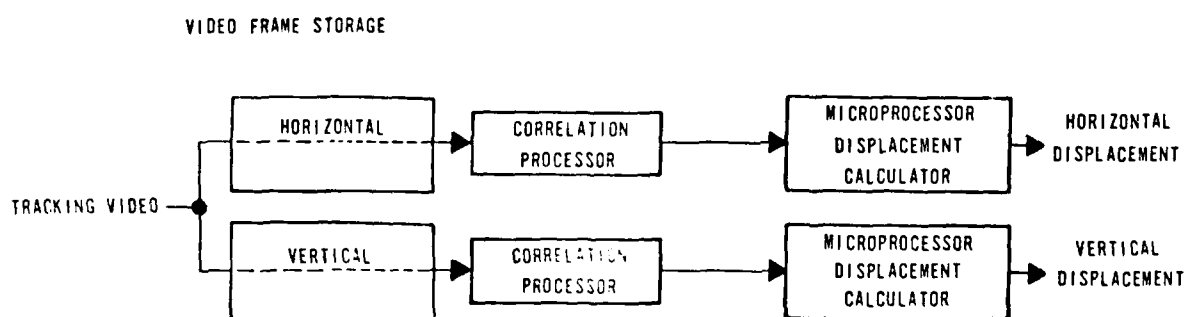


Figure 11 Noninterlaced Readout Mode

The simplest solution to the interlace problem is to perform the correlation computation on every other field. This approach has one distinct advantage in implementing the tracking function, namely that since each axis of the tracking function needs to be processed only on alternate video fields, the two axes can be staggered in time permitting the correlation hardware to be shared by both. This configuration is shown in Figure 10. Through the use of time sharing, hardware for the tracking function is nearly halved since only one correlation processor is required for tracking, and the computer required to determine the target displacement can be time multiplexed between axes. This approach, however, has several limitations. First, since the processing is between single fields, the distance between processing pixels in the vertical direction is two sensor pixels. The vertical resolution is then cut in half, and the accuracy of the vertical axis tracking function is also reduced by a factor of two. The second problem encountered with the approach given in Figure 10 also arises from the use of alternate fields. Because there is an intermediate field between any two fields which are used, the period of time between the two useful fields is twice that which would occur if successive fields were used. Thus, the amount of displacement measured due to target motion is also doubled since the measurement period is extended. The correlation electronics limits the maximum displacement permitted during each field and, because of this measurement doubling, the actual target angular rate limitations are reduced by one-half.

These two problems are, of course, related to the use of a sensor with interlaced readout. It is possible, however, to eliminate one of the two problems associated with the CCD's by operating the CCD in a noninterlaced mode through the addition of the two fields internally before video readout. The penalty is the reduction of the vertical resolution by one-half. In the former case, effective pixels measured 18- $\mu$ m vertically on 36- $\mu$ m centers. In the present case, effective pixels measure 36  $\mu$ m vertically with the same 36- $\mu$ m pitch. deleterious effects of high spacial frequencies in the vertical direction may be significantly reduced in the vertical direction by combining pixels of each field.

The elimination of vertical interlace removes the problem of doubled integration time and, thus, measurement doubling as stated for the first case. However, the vertical resolution is halved and several other parameters of system operation are also affected. In noninterlaced operation, the two sensor fields are combined and read out in one interlaced field integration time. While the integration time is one-half of that used during interlaced operation, the photosensitive area is doubled resulting in the same average sensor photocurrent. The dynamic range burden of the photosite area is reduced by virtue of the doubled storage area. This is beneficial since excess charge in a photosite tends to spill into the bulk substrate causing total image loss, whereas the greater dynamics of the charge transfer register affords a greater tolerance of overload which, at worst, causes an image blooming in the vertical direction, but only for those columns that are severely overloaded. Image integrity is thus maintained for much higher levels of optical overload.

### 3.1.9.5 Hardware Complexity

One major disadvantage encountered with the elimination of interlace is the increased system hardware complexity to permit both axes of the tracking function to be computed simultaneously using successive frames. The implication is a duplication of correlation processing hardware to allow simultaneous operation for each axis. Further, any memory for each axis must be approximately doubled in size to allow correlation processing of stored video at the same time as new information is being stored in another section of the same memory. The block diagram for this approach is shown in figure 11.

The CID is capable of operating in either a field or frame mode. There are a total of 60,512 pixels (244 x 248) in each frame. This presents a serious limitation in the use of the CID. Upper limits readout rates are around 15 Mpixels/s for the CCD and 8 Mpixels/s for the CID. Minimum integration times are then:

$$\text{CCD} \quad \frac{1}{15 \times 10^6 \text{ pixel/s}} \cdot (122 \times 190) \text{ pixels} = 1.5 \text{ ms}$$

$$\text{CID} \quad \frac{1}{8 \times 10^6 \text{ pixel/s}} \cdot (244 \times 248) \text{ pixels} = 7.6 \text{ ms}$$

The integration time for the CID is excessively long as far as the tracking system is concerned. Five times more target motion may occur during one CID frame integration than in one CCD frame integration period. This is similar to the problem discussed in the first CCD example where the intervening field caused a doubling of the effective integration period. In the CID case, image blur will degrade the computed correlation function implying a less accurate displacement determination.

A further complication is the fact that pixel integration begins at the time it was last read out. Different pixels integrate the light over noncoincident periods of time which depend on position in the array. Even if the target has uniform motion, different pixels will see different effects caused by this motion. This too will lower the correlation between the two successive frames and will introduce more noise in the displacement calculations.

With a CID operating in a frame mode, the electronics required for the tracking function are the same as for the CCD used in a frame mode as shown in Figure 11. The video storage memory required here does not contain the entire asor frame, but only the subframe, that is the tracking window into which the target must fall. This window is approximately the same with either a CCD or CID. Thus, the total memory requirements are not influenced by the much greater number of pixels from the CID as opposed to the CCD.

#### 3.1.9.6 Sensor Selection

In summary, then, the CID has a competitive pixel size and a non-interlaced readout format, but suffers from lag and an unsuitably slow readout rate. The CCD has competitive pixel size even in noninterlaced readout format, no lag, and a high readout rate, but it is limited by format

size, and less than 50 percent of the format is photosensitive. Experience with the CCD has shown that these two limitations can be tolerated. For these reasons the CCD is preferred over the CID for image detection on the AEOTR. If, in the future, device technology relieves some of the listed disadvantages of the CID, a reevaluation of the choice would be in order.

### 3.1.10 Tracker Gimballing

A fundamental problem in the design of a tracking system with a small field-of-view is the choice of axes of rotation which will enable the tracker to follow the target. The desire is to provide sufficient flexibility to encompass all tracking situations without redundancy. The use of three axes is redundant since pointing in a general direction requires only any two of roll, pitch and yaw. Without a compelling reason based on mechanical design or performance considerations, no more than a pair of these should be used. The pitch/yaw pair is essentially the basis of a rectangular coordinate system, and the roll/pitch or roll/yaw pairs are essentially the bases of a spherical coordinate system.

While the pitch/yaw pair is conceptually easy to deal with and relatively simple to implement, a definite problem in using such a system aboard a high performance aircraft is that the very high roll rates of such an aircraft mean very high sinusoidal velocities and accelerations in rectangular coordinates. In order to accommodate these high accelerations for tracking, the system design arrives at a tradeoff between short integration and long integration feedback. Short integration allows the high accelerations required, but tends to break lock during momentary signal loss and is highly susceptible to noise, while long integration feedback is less likely to break lock and is less susceptible to noise, but does not allow high accelerations. Further, early design efforts established the difficulty of maintaining a small envelope for the AEOTR without severely compromising the field of regard in one axis.

The choice of the roll/cone (either roll/pitch or roll/yaw) pair would seem to alleviate these tracking problems immensely for two reasons. First, roll is one of the natural rotational axes of the aircraft and high accelerations are not needed to accommodate the roll velocity. Second, the system's own inertia means that low torque is required to handle aircraft roll acceleration. The problem, however, is translated to high tracker roll rate and acceleration required for linear tangential target motion near, but not through, the pole. Motion through and within the field-of-view of the pole is tracked with the cone axis, that is, with radial motion since negative cone angles are allowed. Motion far from the pole does not require excessive acceleration. Thus, just as the pitch/yaw pair may require a minor roll axis to accommodate aircraft roll, the roll/cone pair may require a minor third axis to accommodate linear motion near the pole. The advantage of the latter choice lies in the fact that the minor third axis may be needed only in limited area of coordinate space, and thus the angular freedom required is limited. For the former choice, the minor third axis may be needed anywhere in coordinate space and is not inherently limited in angular coverage required since the aircraft may roll any number of times.

For these reasons, the preferred axes for the AEOTR would appear to be either roll/pitch or roll/yaw, provided that target motion near the roll axis can be dealt with. One option is to permit short periods of loss of target lock when the target is near the system roll axis. This is particularly undesirable since the axis position is expected to be a frequently desired target position. Small errors in pointing angle would automatically mean loss of lock and necessitate reversion to an acquisition mode at a time when the most precise tracking and ranging operation is required. Such inefficiencies cannot be tolerated by an AEOTR.

Two general mechanical options exist for tracking near the roll axis. One is to point the optical axis of the tracking system at the target using a third gimbal axis. The other is to operate the tracking system in an off-axis configuration by displacement of the image sensor in the focal plane or by tilting the sensor field of view with a reflective element. Off-

axis operation for tracking implies that both the dedicated tracking channel and the ranging channels be operated off-axis since track information is derived from range channel video part of the time. While the pointing direction of the tracker could be varied by several degrees while maintaining an overall accuracy of  $\pm 1$  mrad, it is considered counter-productive to attempt to change the ranger pointing by several degrees while attempting to maintain the relative parallelism of the rangefinder channels of better than  $1 \mu\text{rad}$ . If off-axis pointing is achieved by sensor displacement, the scale difference between tracker and ranger channels requires unequal sensor movement. The vignetting of autocalibration light resulting from the displacement of range sensors by more than one format height (field of view) will degrade the ability to perform autocalibration. Additionally, a question of increased autocalibration and ranging error is associated with off-axis lens aberrations as compared to axial operation. For these reasons, off-axis operation is particularly unattractive.

While the first pointing option of providing a third axis gimbal represents redundant hardware, it is required if track lock is to be maintained when the target is near the roll axis. The use of this third gimbal represents a functionally modular approach to the system design in that the functions of tracking and ranging are isolated. This avoids the coupling of errors between the two system functions and permits a significantly more straightforward and feasible mechanical design. With a three-axis tracking system, angle measurement errors are accumulated from an additional axis over a two-axis system, but the additional tracking angle error can be small. More significant is the ability to continuously and simultaneously track and range accurately, which the third axis permits. On the basis of these considerations, it is believed that three-axis gimbaling is the best choice for the AEOTR, and this is the approach taken for the preliminary design (see Section 4).

A choice between roll/pitch and roll/yaw as the primary pointing angles is driven by a requirement to minimize optical errors forward of the system, rather than solely by mechanical design considerations. With

the pitch axis defined as lying in the rangefinder plane and connecting the rangefinder lenses, the yaw axis is then orthogonal to the pitch axis. In the absence of airflow disturbances produced by the host platform, the tracking of targets using the pitch axis permits airflow across the window to be symmetrical from side to side. The use of yaw for tracking imposes an asymmetry on the system by making one side of the window a leading edge and the other a trailing edge. While no suitable models exist to predict the magnitude of effects associated with this unsymmetrical airflow, analysis summarized in Subsection 3.1.3 reveals a high sensitivity of ranging error to slanted window effects. By using pitch as a primary tracking axis, a possibly significant error source can be at least minimized, if not avoided. Unsymmetrical conditions may arise with nonzero yaw for tracking near the roll axis, but the fraction of time spent with nonzero yaw is expected to be small compared to time with nonzero pitch angles.

Initial attempts to incorporate pitch/yaw gimbaling with the search field angles on each axis were unsuccessful without prohibitive compromises in envelope size or rangefinder scale. Subsequent design efforts using roll/pitch for primary axes with suspension at the center of the tracker head permits the increase of rangefinder scale and the incorporation of  $\pm 20^\circ$  of yaw travel without a serious envelope penalty.

### 3.1.11 System Cooling Requirements

The AEOTR cooling requirements are herein estimated. The head is modeled as a cylindrical pod with an 8-inch outside diameter and a 54-inch length. Heat sources are the power dissipated by the internal electronic and mechanical systems, and the ram air heating of the pod surface.

#### 3.1.11.1 Internal Heat Load

The major contributors to the internal heat load are the gimbal drive motors and the drive electronics. The motor stall loads and an estimate of the average power required in normal operation are listed in

Table 8. This electronics power estimate includes all control and data processing functions, as well as such incidental loads as CCD coolers and internal calibration sources. In the absence of any cooling provisions, the transfer of this heat load to the walls of the pod by convection will be effected when there is a temperature differential,  $\Delta T$ , between the ambient fluid and the walls of magnitude:

$$\Delta T = \frac{q}{h_c A},$$

where:

$q$  = heat flow

$h_c$  = surface coefficient of heat transfer

$A$  = area

The most uncertain factor in this equation is  $h_c$  which depends upon several factors including the temperature and density of the ambient fluid and the thermal properties of the pod walls. For a heat load of 465 W = 1590 BTU/hour, a surface area of  $7.7 \text{ ft}^2$ , and a best estimate for  $h_c$  of  $1.2 \text{ BTU}/\text{hour-ft}^2 - \text{F}^\circ$ , the temperature rise is  $172 \text{ F}^\circ$ .

It will be shown that for most cases, this represents a net cooling requirement for the systems if a stable operating temperature is to be maintained.

### 3.1.11.2 External Temperatures

For the present program, estimates of system external temperatures have been based upon stagnation temperatures at the pod leading surface and recovery temperatures near stagnation at the sides. Figure 12, taken from Appendix A, displays pod side temperature as a function of altitude for two extremes of airspeed, 600 ft/s and 1500 ft/s, for three standard temperature/altitude profiles. The temperature excursion is large for flight between sea level and 50,000 ft, and indicates the need for system temperature control. Even for low speed flight at high altitude, the system internal temperature can be expected to reach  $130^\circ\text{F}$  in the absence of thermal control, and for higher speed flight at medium altitude, temperatures will

TABLE 8  
MAJOR INTERNAL HEAT SOURCES

Source	Stall Load (W)	Average Load (W)
Roll motor	260	130
Pitch motor	290	145
Yaw motor	180	90
Electronics	100	100
Peak power	830	
Average power		465

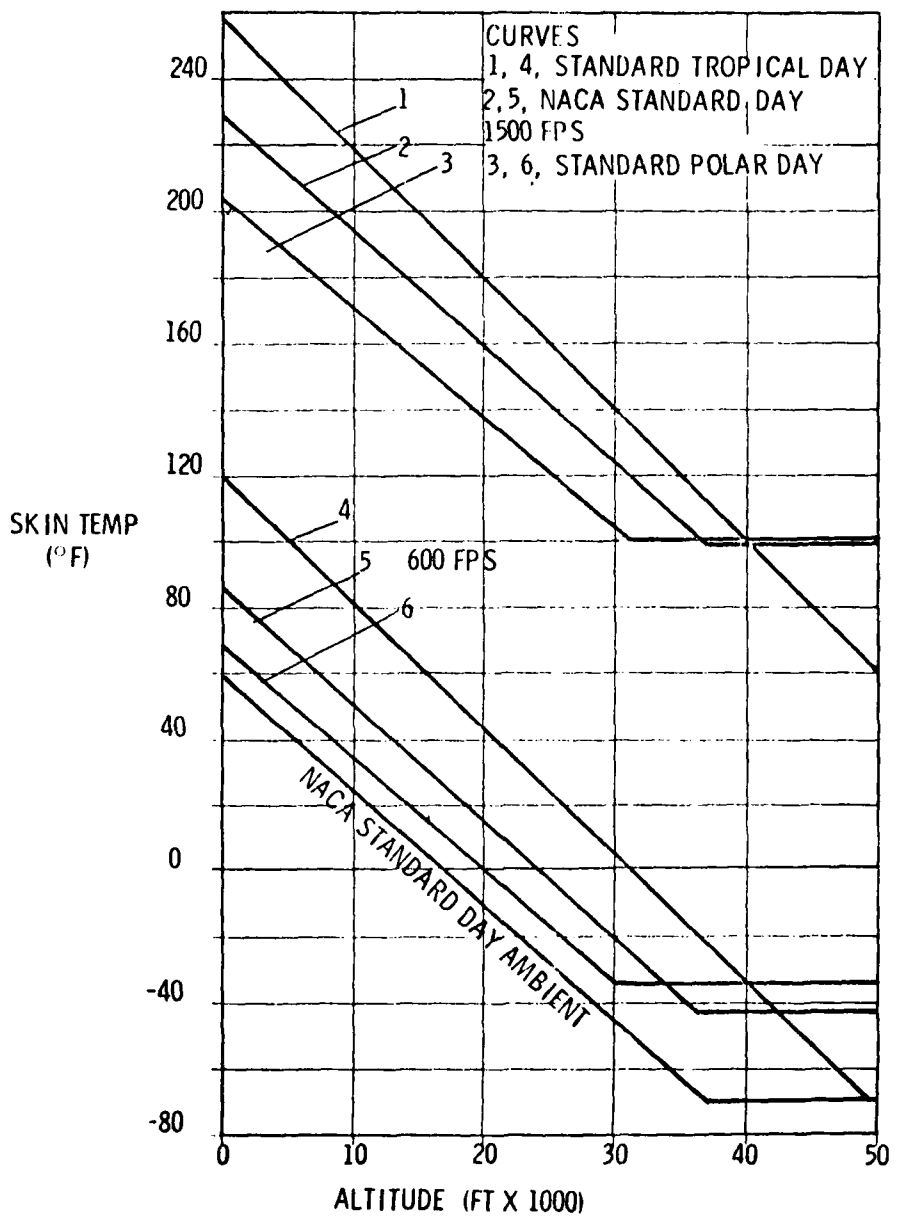


Figure 12 Pod Temperature Vs Altitude & Airspeed

exceed 300°F. Since the electronic hardware and some of the mechanical and optical components cannot perform at these temperatures, and because of the high mechanical stabilities required by the rangefinder, cooling is required to limit temperature excursions to an acceptable range.

Rather than attempting to control the entire system temperature, the most efficient approach is to isolate the system components from the pod skin temperatures and to deal directly with the internal heat generation plus leakage from the outside. Insulation can be placed over much of the internal cylindrical surface of the pod and over some of the forward surfaces of the gimballed head, and, although complete isolation from the outside is impossible, the transfer of heat into the system can be significantly reduced.

### 3.1.11.3 Cooling Options

The transfer of the internally-generated heat to an appropriate heat sink may be accomplished in one of several ways, the applicability of which may depend upon the particular aircraft installation and mounting location. An analysis of all the acceptable possibilities and the suitability of each is beyond the scope of this study, but the approach here will be to identify at least one suitable option using available data. One source of relevant data is a study of thermal control systems for pod-mounted electronic systems<sup>(1)</sup> which covers the performance boundaries of 18 separate cooling subsystems. Reliance is made upon that study as well as the recommendations of manufacturers experienced in the cooling of airborne equipment.

The simplest approach to system cooling is to use cool forced air supplied by the host aircraft. Sufficient air is available at some fuselage locations on the F-15, for example, to restrict system internal temperatures to 130°F (34°C). This is not available in each possible mounting location on

(1) Thermal Control of Pod-Mounted Electronic Systems, Volume 1, Book 1. AFFDL-TR-XX-XXXX. Garrett Airesearch Report 69-5574-1.1.

the F-15, and is unavailable on the F-16. The availability of cooling air at the potential mounting locations on the F-18 is in doubt. A general solution, then, cannot rely upon aircraft-supplied cool air.

For all applications where the AEOTR is configured in a pod, or where the system is mounted at least partially outside the aircraft boundary layer, a self-contained cooling system is recommended to minimize mounting complexity and possible aircraft modifications, and to contain the system within one package to the greatest extent. One potentially-suitable approach is to use a closed-loop vapor cycle cooling unit. This generic class is appropriate for flight envelopes typical of air-to-air gun engagements, namely, from low altitudes to 50,000 ft and speeds below Mach 1.6. The cited pod cooling study identifies the freon vapor cycle system as the most suitable for service in all corners of this envelope. Further, a substantial base of manufacturer experience in the design and fabrication of freon vapor cycle cooling systems for service on airborne pod systems exists and is available for application to the present problem.

A preliminary look at cooling system sizing shows that a cooler with a 100-W cooling capacity can be fitted within the aft portion and conical end of the 8-inch diameter pod proposed here. Some excess of cooling capacity beyond the average 465 W listed above is desirable to more safely accommodate peak electrical loads, leakage through and around insulation, and reductions in cooling efficiency resulting from high recovery temperatures following low altitude "dash" operation, but whether a safety factor of two is necessary is not clear. A more complete design will be required before the cooling system can be sized more precisely.

One very significant corner of the flight envelope which impacts upon system capacity is the high speed, low altitude case. The upper family of curves in Figure 12 reveals the high recovery temperatures to be expected with high speed flight at low altitude. Extended high speed flight at low altitude is not expected for fighter aircraft for several reasons, not the least of which is the high rate of fuel consumption. For short duration, such flight can be expected to occur and the choice of a ranger performance

goal will have to be made. Satisfactory performance for flight anywhere within the given flight envelope will require greater cooling capacity than if a short period of recovery following a "dash" condition is allowed. The weight of a cooling subsystem with a 1000-W capacity is estimated to be 31 lb. Any additional cooling capacity required for operation in the "hot corner" of the flight envelope will add further to the projected system size and weight and will influence ultimate integration potential for the AEOTR.

As an example of the benefits gained by the restriction of the required operating envelope, Figure 13 is a plot of the temperature increase over ambient as a function of airspeed. This  $\Delta T$  curve reflects a recovery temperature which is 90 percent of stagnation. It is primarily a function of airspeed and a much weaker function of ambient temperature. The curve is based upon a NACA standard day ambient temperature reference, and for polar or tropical references, must be decreased or increased respectively by about 5 percent. These three standard temperature/altitude distributions are plotted, as well as an extremely hot standard. The recovery (skin) temperature is the sum of ambient and the instantaneous velocity dependent  $\Delta T$ . To limit recovery temperatures to a reasonable maximum of perhaps 170°F (design point for the above 1-kW cooler), the low altitude speed must not exceed 960 ft/s (Mach 0.83 or 570 kn) on a hot day or 1300 ft/s (Mach 1.2 or 780 kn) on a cold day. At sea level, this limit increases at an average rate of approximately 25 ft/s per 1000 ft of altitude. Such a flight envelope restriction would be for rangefinder performance reasons and not for considerations of flight safety.

#### 3.1.11.4 Conclusion

The best estimate of the thermal situation is that the AEOTR presents a continuous requirement for cooling with the possible exception of low speed, high altitude flight. The exterior temperatures of the pod are high and so widely varying with flight conditions that the interior must be thermally isolated as much as possible if the temperature is to be stabilized. With isolation, any possible cooling benefit resulting from low speed, high altitude flight will be minimized and the system will always be in a cooling-

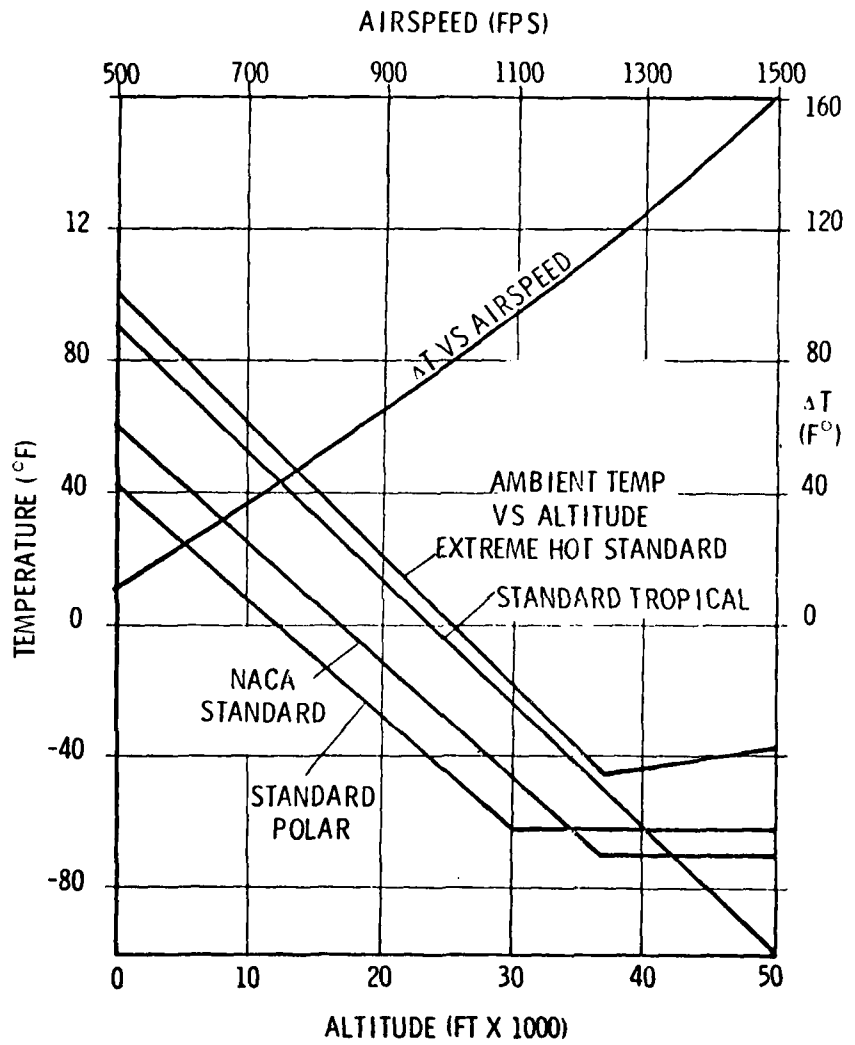


Figure 13 Tracker Thermal Environment

required condition. To minimize the capacity of the cooling unit and yet limit the magnitude of temperature excursions about an acceptable operating temperature, it is desirable to select an operating temperature which is somewhat elevated from normal surface ambient, but which is low enough to permit reliable operation of the electronics and the CCD thermoelectric coolers.

### 3.2 TARGET IDENTIFICATION MODE

#### 3.2.1 Introduction

In addition to the performance of the required functions for the GDEM, it is desirable to provide a visual TIM to permit target identification beyond the limits of unaided vision. The inclusion of this mission-enhancing function is suggested by the fact that the addition of a second E-O sensor to a fighter aircraft is contra-indicated by several considerations, including, among other, cost and aerodynamic load.

The factors which have been included in the TIM study are the following:

- Packaging constraints
- Sensor options
- Resolution requirements
- Field-of-view requirements
- Display scale
- Radiometric considerations
- Compatibility with other tracker functions
- Scan conversion and display options

#### 3.2.2 Packaging Constraints

The goal of the subject preliminary engineering design study is the development of a device to perform the required functions while retaining maximum integration potential. One of the critical factors in assessing integration potential is package size. A goal for the present development has been a package size with a 6.0-inch diameter. Preliminary layouts indicate that this is the minimum required for the basic functions of tracking

and rangefinding. Adequate support structures for these basic components increase the size to 7.0 to 7.5 inches. Because the system will be a gimballed rather than strapdown system, all of the optics and detectors must fit within a sphere of this diameter. The implications of this are that even with folding the optical paths, very little sensor space is available. For the 5-inch focal length of the rangefinding system, less than 2 linear inches are available for image sensing.

An increase in system diameter beyond 8.0 inches is considered so detrimental to integration potential that this option has not been considered.

### 3.2.3 Sensor Options

Sensor options for the TIM fall into two categories: conventional TV vidicons and solid-state detectors. The smallest vidicon is greater than 6 inches in length and requires high voltage for operation. While the resolution of a vidicon is superior to that of available solid-state sensors, the size and voltage requirements are greater than the present system can tolerate. Therefore, vidicons are excluded from serious consideration as candidate image sensors in the TIM.

Solid-state image detectors (SSID) exhibit many characteristics that qualify them for use as image sensors in the TIM including small size and power requirements. A thorough discussion of the characteristics of available and anticipated SSID's is contained in Table 9 which is updated from reference 2. The primary criteria for device selection here are device size, pixel count, pixel size and pitch, photoresponsivity, noise characteristics, dynamic range, readout rates and availability. On the basis of those parameters, the devices tentatively selected for the TIM are the Fairchild CCD211 or CCD221.

(2) "Solid State Array Tracker Applications", AFAL-TR-77-182, Volume 1  
(A FAL/RWT, WPAFB, OH 45433) 1977

TABLE 9\*  
SSID TECHNOLOGY COMPARISON

	Number of Elements Horizontal x Vertical	Type (see note)	Commercially Available
Fairchild	100 x 100	IT, BCCD	Yes
	190 x 244		Yes
	380 x 488		Yes
RCA	320 x 512	FT, SCCD	Yes
TI	800 x 800	?	No
	400 x 400	FT (Back illuminated)	No
	327 x 490	FT (Back illuminated)	No
Bell Labs	475 x 496	FT	No
GE	100 x 100	CID	Yes
	188 x 244		(As cameras only)
	248 x 244		(As cameras only)
Reticon	32 x 32	SPA	Yes
	50 x 50		Yes
	100 x 100		Yes
Hughes	100 x 100	IRFT	Intended

SPA      Silicon Photodiode Array  
 BCCD     Buried Channel CCD  
 SCCD     Surface Charge Transfer CCD  
 IRFT     Illuminated Register Frame Transfer CCD

\* Primary source: Reference 2

The Fairchild devices use interline transfer with buried charge transfer channels. The CCD 211 has a format of 190 columns of 244 pixels each. Picture element dimensions are  $18 \mu\text{m}$  vertically by  $14 \mu\text{m}$  horizontally. Center spacings are  $18 \mu\text{m}$  vertically and  $30 \mu\text{m}$  horizontally. The CCD 221 has four times as many pixels as the CCD 211, namely 380 columns of 488 pixels each. The CCD 221 pixel dimensions are  $18 \mu\text{m}$  vertically by  $12 \mu\text{m}$  horizontally. The center spacings are the same as on the CCD 211.

Some of the consequences of the use of SSID's are shown in the modulation transfer function (MTF) plots of Figures 14 and 15 for the cases of the CCD 211 and CCD 221, respectively. The MTF is taken as a pure sinc function with the first zero crossing determined by the reciprocal picture element dimension. For vertical resolution, this is the vertical sampling frequency. For horizontal resolution, this cutoff occurs at more than twice the horizontal sampling frequency. Useful resolution is still limited by the horizontal sampling frequency,  $f_{SH} = (30 \mu\text{m})^{-1}$  and the horizontal Nyquist frequency  $f_{NH} = 1/2 f_{SH}$ . For the CCD 211,  $f_{NH} = 71.3 \text{ TVL/PH}$ , and for the CCD 221,  $f_{NH} = 142.5 \text{ TVL/PH}$ . The vertical Nyquist frequencies,  $f_{NV}$ , are 122 TVL/PH for the CCD 211, and 244 TVL/PH for the CCD 221. Aliasing effects become significant at frequencies above  $f_{NH}$  and  $f_{NV}$ , the degree of significance depending upon the scene and the ultimate use of the video data. Only under limited conditions, however, will useful resolution approach the sampling frequency.

The implications of Figures 14 and 15 are that useful resolutions for available SSID's are no better than approximately 200 TVL/PH horizontally and 300 TVL/PH vertically, and the more readily available devices allow only one-half of this resolution. For standard 525-line displays, limiting resolutions of 350 TVL/PH represent the practical and theoretical limits<sup>(3)</sup> so that the performance of the AEOTR in the TIM will clearly be sensor limited. The greater resolution capability of present cockpit display systems emphasizes these sensor limitations. The availability of higher resolution sensors in the near term is unlikely to improve, but substantially higher resolution arrays could appear in the 5 to 10 year time frame<sup>(2)</sup>.

(3) Fink, D. G., *Television Engineering*, McGraw-Hill, New York, 1952, Chapter 2

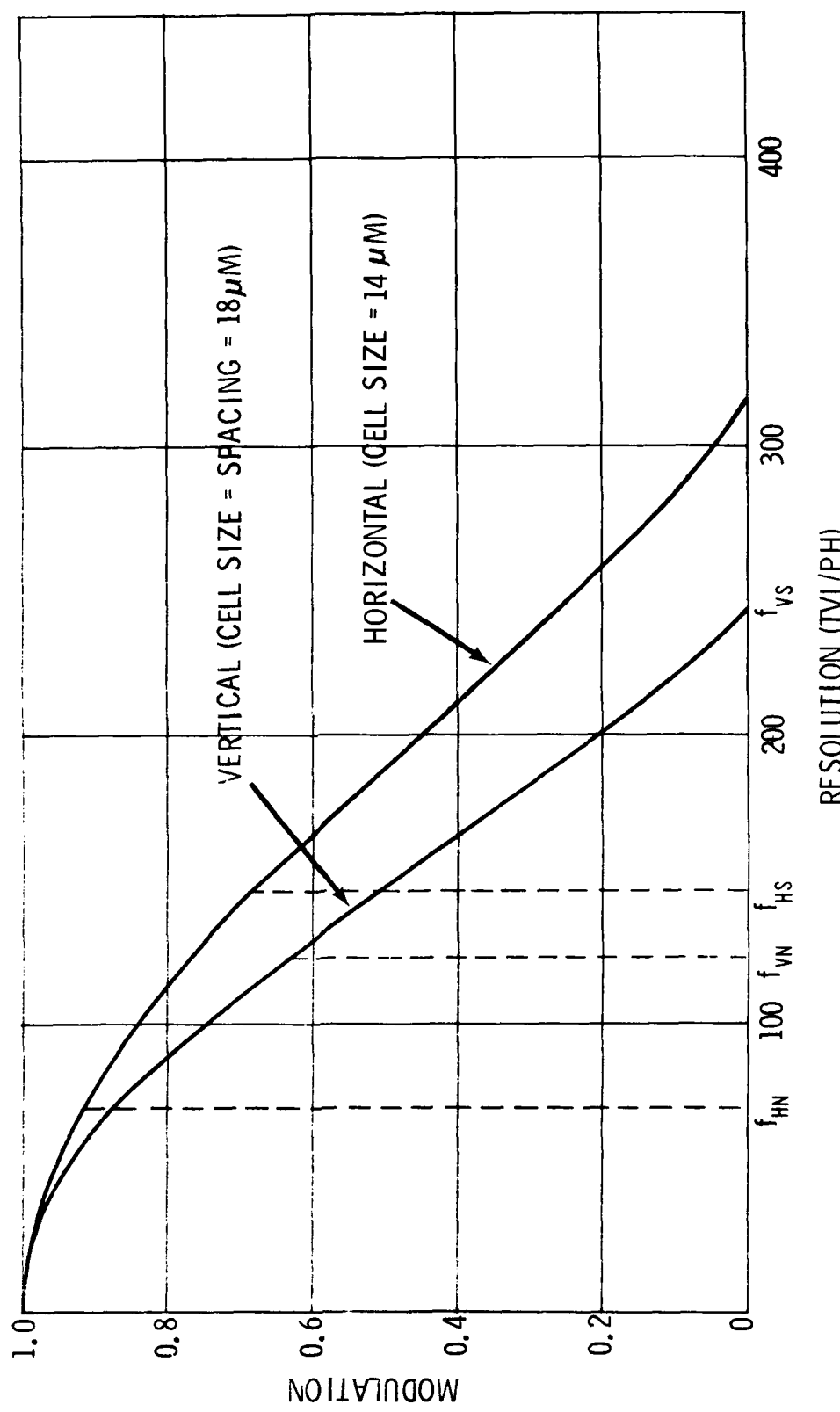


Figure 14 Modulation Transfer Function For The CCD 211

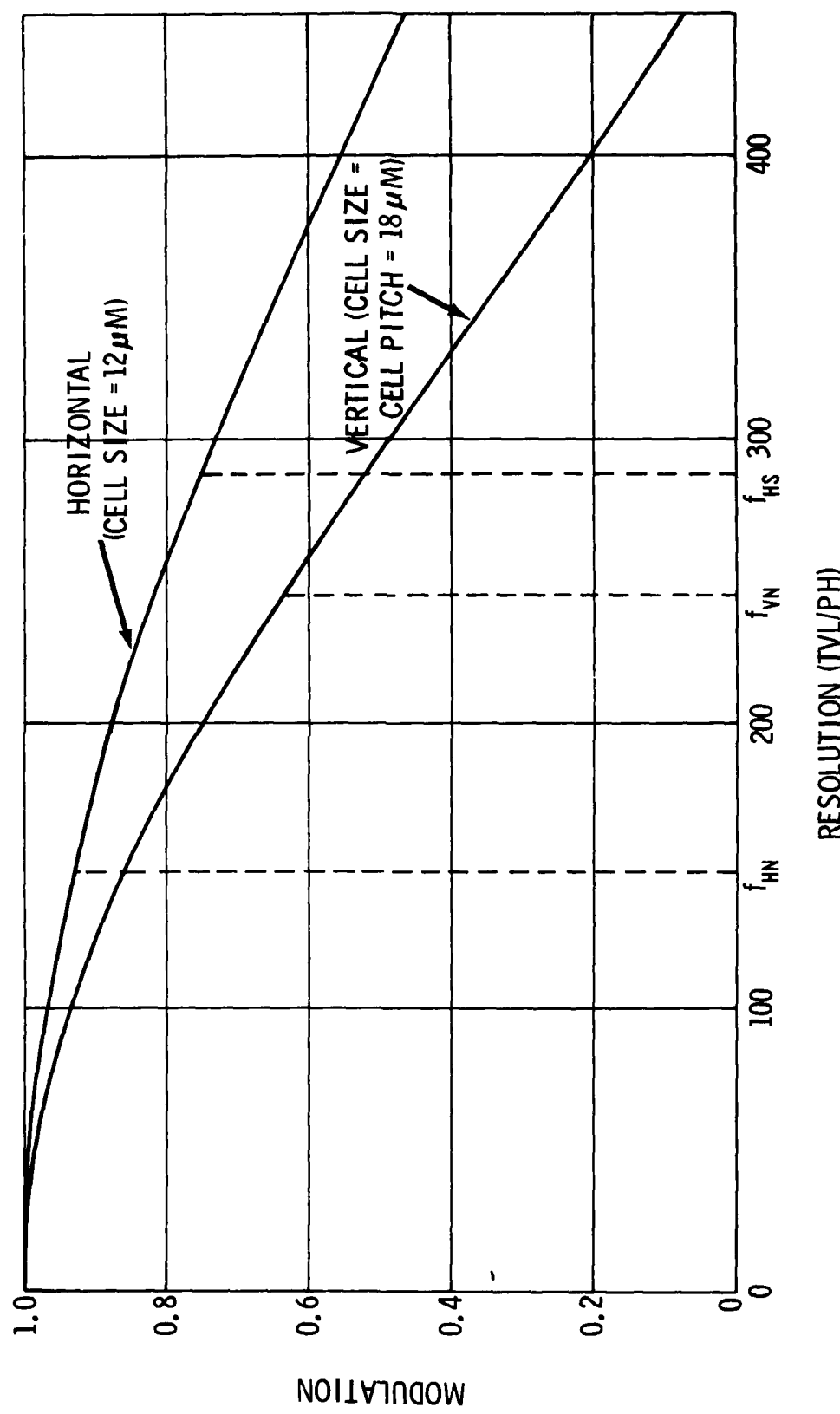


Figure 15 Modulation Transfer Function For The ODD 221

### 3.2.4 Resolution Requirements

Given an image sensor, the only other major component to be selected for the TIM is the lens. If field of view is the primary determining factor, the focal length is determined by the sensor active area. A factor of two difference in focal length then results when a final choice between the CCD 211 and the CCD 221 is made. On the other hand, if resolution is of primary importance, the identical sampling format (pixel spacings) of the two devices imply the same (maximum) focal length for either device. Since the objective of the TIM is to augment identification beyond normal visual ranges, the latter is the case here.

No unambiguous answer is available to the question of the minimum resolution required for target identification. Simple detection with unaided vision requires a target subtense of about one arc minute ( $290 \mu\text{rad}$ )<sup>(4)</sup>, while detection through a video system requires that the target cover a few sensor pixels as well as be presented with sufficient scale for identification which typically requires a subtense of 12 to 20 arc minutes at the observer. While there are many factors affecting identification threshold, including target contrast, brightness, background clutter, target orientation and angular size, visual detection is capable of using such subjective information as position and motion to aid in identification. One common standard of threshold resolution for identification is the Johnson criterion, 10 TVL or 5 line pairs across the target to allow identification, but this resolution is frequently associated with target recognition, not identification<sup>(4)</sup>. An even higher resolution may be required to distinguish between similar aircraft. Except for extraordinary circumstances, it is unlikely that reliable identification can be made with fewer than 10 TVL/target.

An estimate of the resolution available at the tracking and ranging sensors of the AEOTR is shown in Figure 16 as a function of target size and target range, assuming a CCD 211 or CCD 221 image sensor. Of particular interest is the number of pixels (TVL) covered by a target at ranges of 18,000

(4) Human Engineering Guide to Equipment Design, H.D. vanCott and R.G. Kinkade, Ed. USGPO, 1972, Chapter 3

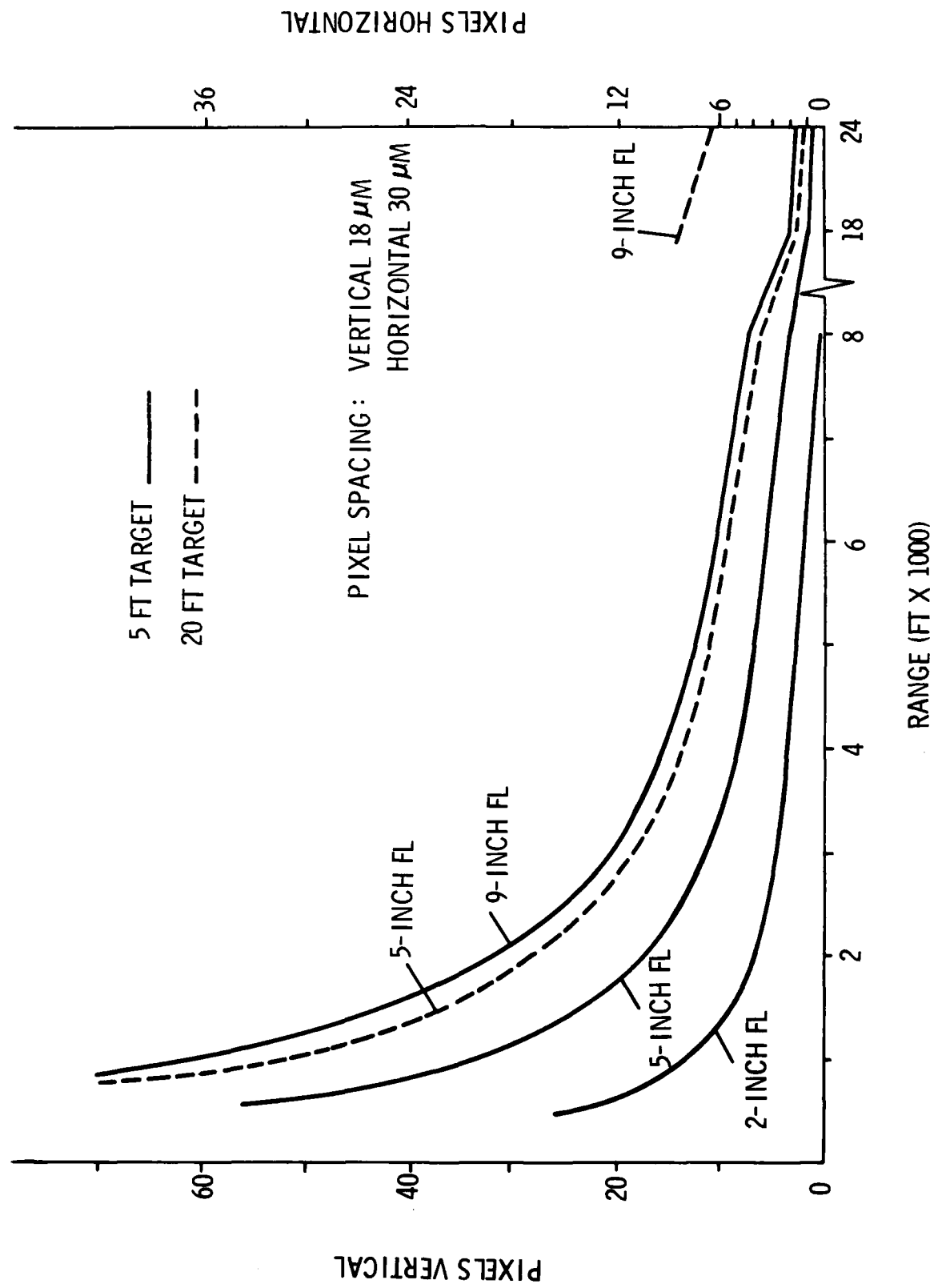


Figure 16 Resolution As A Function Of Range And Target Test

and 24,000 ft. In addition to the 2-inch and 5-inch focal length systems for tracking and ranging, the image size for a 9-inch focal length dedicated video channel is also plotted. Of particular significance are image sizes at a 24,000-ft range. Even for a 20-ft target and the 9-inch system, the image size is only 10 pixels vertically or 6 pixels horizontally. This resolution estimate takes into account only lens and sensor, but allows for no degradation by signal processing or display. Since most airborne targets are smaller than this 20 ft, the range for 10 TVL coverage is under 4 nmi, which is very small for identification in air-to-air combat situations, particularly for the high closure rates associated with head-on approaches.

The resolution requirement may be reexpressed in terms of field at range. Typical dimensions for airborne targets in a head-on approach are 5 to 10 ft for fuselage diameter, and 24 to 74 ft for wingspan. A 10-TVL (5 line pairs) coverage of such a target corresponds to a resolution of 2 to 3 ft/lp. Figure 17 is a plot of range versus angular resolution required for these target resolutions. The resolution capability of several lens/sensor combinations is indicated along the abscissa. A high resolution vidicon (80 lp/mm) is assumed for system 1. The CCD in systems 2 through 4 may be either the CCD 211 or the CCD 221. The implication of Figure 17 is that the 10-lp/target identification criterion requires long focal length (> 9 inches) for targets beyond a 3-nmi range. Referring to packaging constraints once again, a 9-inch focal length refractive system is about all that can be accommodated by a 6-inch diameter sphere, and that involves two folds of the back focal length. The 600-mm lens cited in system 2 is a commercial, catadioptric, f/8 system with length and diameter of 3.3 inches and 4.2 inches, respectively. Use of this minimal aperture system increases the tracker head size to about 9 inches when the rangefinding function is included in a manner that will preserve the performance level.

One method, dynamic sampling<sup>(5)</sup>, exists whereby the system resolution could be increased beyond the static limits just described. The technique involves movement of the sensor relative to the scene by a fraction of a

(5) A. Nordbryhn, The dynamic sampling effect with charge-coupled device (CCD) imagers, *Appl. of El. Imag. Syst.*, SPIE Vol. 143, 42 (1978)

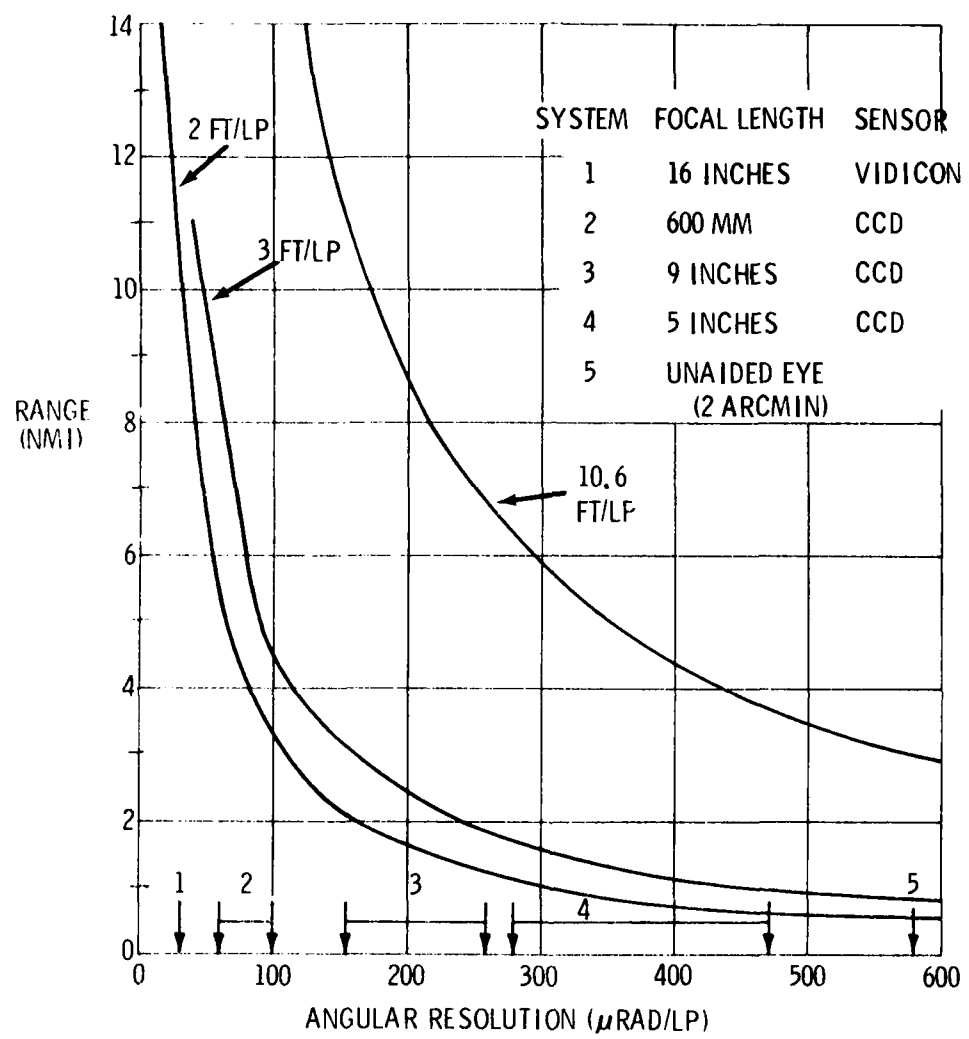


*Figure 17 Range Vs Angular Resolution*

and 24,000 ft. In addition to the 2-inch and 5-inch focal length systems for tracking and ranging, the image size for a 9-inch focal length dedicated video channel is also plotted. Of particular significance are image sizes at a 24,000-ft range. Even for a 20-ft target and the 9-inch system, the image size is only 10 pixels vertically or 6 pixels horizontally. This resolution estimate takes into account only lens and sensor, but allows for no degradation by signal processing or display. Since most airborne targets are smaller than this 20 ft, the range for 10 TVL coverage is under 4 nmi, which is very small for identification in air-to-air combat situations, particularly for the high closure rates associated with head-on approaches.

The resolution requirement may be reexpressed in terms of field at range. Typical dimensions for airborne targets in a head-on approach are 5 to 10 ft for fuselage diameter, and 24 to 74 ft for wingspan. A 10-TVL (5 line pairs) coverage of such a target corresponds to a resolution of 2 to 3 ft/lp. Figure 17 is a plot of range versus angular resolution required for these target resolutions. The resolution capability of several lens/sensor combinations is indicated along the abscissa. A high resolution vidicon (80 lp/mm) is assumed for system 1. The CCD in systems 2 through 4 may be either the CCD 211 or the CCD 221. The implication of Figure 17 is that the 10-lp/target identification criterion requires long focal length (> 9 inches) for targets beyond a 3-nmi range. Referring to packaging constraints once again, a 9-inch focal length refractive system is about all that can be accommodated by a 6-inch diameter sphere, and that involves two folds of the back focal length. The 600-mm lens cited in system 2 is a commercial, catadioptric, f/8 system with length and diameter of 3.3 inches and 4.2 inches, respectively. Use of this minimal aperture system increases the tracker head size to about 9 inches when the rangefinding function is included in a manner that will preserve the performance level.

One method, dynamic sampling<sup>(5)</sup>, exists whereby the system resolution could be increased beyond the static limits just described. The technique involves movement of the sensor relative to the scene by a fraction of a

(5) A. Nordbryhn, The dynamic sampling effect with charge-coupled device (CCD) imagers, *Appl. of El. Imag. Syst.*, SPIE Vol. 143, 42 (1978)

sampling element between successive frames. The scene is thus sampled more densely than the geometrical sampling density with a stationary sensor. To avoid the introduction of serious aliasing patterns in the displayed image, it is necessary to use an integrating medium for the display. Such media include the human retina, long persistence CRT phosphors and scan converter image storage tubes. The suitability of existing cockpit video display units (VDU's) for use with dynamic sampling has not yet been demonstrated. In a laboratory setup, however, dynamic sampling has increased system resolution up to 3.5 times the Nyquist limit.

The implementation of dynamic sampling to improve TIM performance would require additional hardware to perform image dither. A dedicated video channel would almost certainly be required for this since image motion in the rangefinding channels is not permissible, and resolution in the tracking channel is too low to be of use in target identification even with dynamic sampling. Because of packaging constraints, the addition of even more hardware to the tracker head, particularly that requiring moving components, is considered to be prohibitively detrimental to the tracker design, and the use of dynamic sampling is not considered a viable alternative.

### 3.2.5 Conclusion

The conclusion from the foregoing analysis is that target video cannot be provided in the AEOTR with sufficient resolution to be a useful identification aid beyond visual ranges, given the present and near term limits of sensor technology and the tracker size limitations. It is therefore recommended that the TIM not be provided as one of the operating modes of the AEOTR. Should significant advances be made in sensor technology in the future, this conclusion may justly be questioned, but it is not now possible to provide sufficient resolution to justify the costs of implementing the function. Inadequate scale also obviates the possibility of providing target aspect as a clue to target intentions.

The subsequent portions of this section represent analysis conducted simultaneously with the foregoing and establish that the primary limitations of the TIM are of scale and not other foreseen complexities.

### 3.2.6 Scene Lighting and Sensor Exposure

In addition to the evaluation of the minimum scale which is necessary for a video aid to visual target identification, it is also appropriate to consider the scene lighting conditions required for the generation of usable video. The operating limits of the video channel may be estimated by comparing the detector irradiance for a given scene irradiance, target contrast and optical transmission with the noise equivalent exposure of the sensor.

The performances of four imaging systems were considered, namely the tracker channel with f/2 optics, a ranger channel with f/4 optics and dedicated video channels with apertures of f/7.2 and f/8. For the tracker and ranger channels, conservative (high) frame rates of 2000/s and 500/s respectively were used. For the video channels, a standard 30 frames/s was assumed. The response characteristics of the Fairchild CCD 211 were assumed.

The details of the analysis are presented in Appendix E. The results show that the video signal-to-noise ratio (SNR) is good (10 percent or more) with rather modest lighting and target contrast conditions (overcast day, 5 percent target/background reflectance difference). The performance of the four systems is similar since compensation for the reduced apertures of the dedicated video channels is made by the longer integration times. The apertures selected are thus considered adequate for the different functions in the AEOTR. The tracker frame rate of 2000/s and the ranger frame rate of 500/s are considered upper practical limits for the available optical aperture and signal processing capability. A reduction of these rates by a factor of two or three should not cause sensor saturation except under conditions of target specular reflection.

### 3.2.7 Display of Target Video

The display of video detected by a sensor in the AEOTR presents several technical difficulties which can be surmounted by appropriate scan conversion techniques. It is desired to present to the user a faithful reproduction of the target image which will allow a maximum information extraction without overcomplicating the interface between sensor and display.

Several technical difficulties must be overcome to present useful video from the AEOTR. In general, if the sensor is not a dedicated sensor operating at a standard frame rate, some compensation for the sensor/display rate differences must be made. Video display units (VDU's) in current generation fighters operate at 525/60 and 875/60 video standards and with aspect ratios of 1:1. The video sensors considered for the AEOTR have aspect ratios of 3:4. The display of such video on a unity aspect VDU implies a scale reduction or a loss of one-fourth of the video information. The most significant difficulty relates to the primary axes of the AEOTR being the pitch/roll axes. In general, the AEOTR roll angle is nonzero, and the target image is rotated relative to the attacker platform.

These difficulties can be separately and collectively addressed by scan conversion techniques. Appropriate scan conversion methods are discussed in detail in Appendix F, and a general solution is therein derived. The necessity of resampling the stored image to effect image derotation and the subsequent degradation of resolution represents the primary performance disadvantage of scan conversion. If the image rotation resulting from the pitch/roll gimbaling can be tolerated, the frame rate disparity and the VDU unity aspect problems can be solved using straightforward scan conversion methods with no loss of resolution.

### 3.2.8 Summary

The size limitation of the AEOTR plays a dominant role in limiting the potential for providing target video as an aid to target identification. Solid-state imaging devices are the only imagers which are compatible with the restricted space available for image detection, while permitting the primary tracker

AD-A089 143

CAI BARRINGTON ILL  
ADVANCED ELECTRO-OPTICAL TRACKER/RANGER.(U)

JUN 80 R A BENNETT, D N DEFOE

F/G 17/8

F33615-78-C-1562

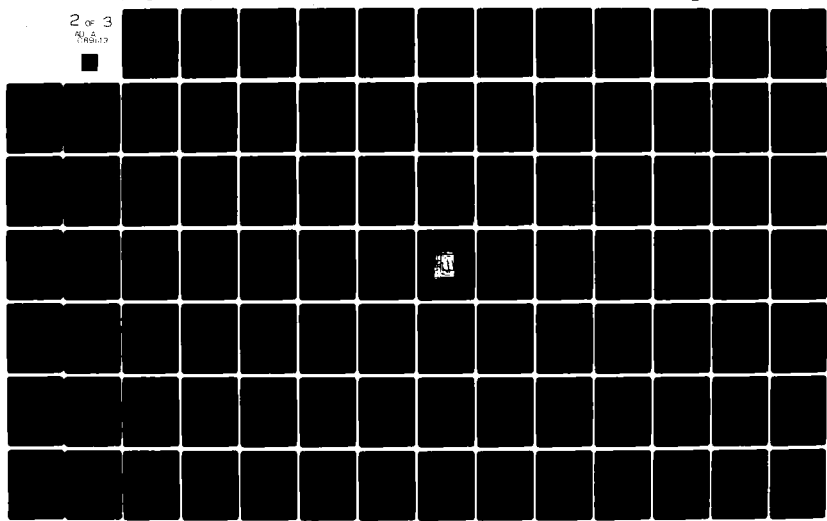
UNCLASSIFIED

CAI-7323-0180-5

AFWAL-TR-80-1034

NL

2 of 3  
RLS  
CWB/13



functions of ranging and tracking. Maximum focal plane resolution is then determined by the present limits of sensor technology. Also, imaging system focal lengths are limited to less than 9 inches. The two limits of sensor technology and focal length then determine system maximum resolution. Several effects are expected which will limit resolution to less than this maximum, the most significant of which is scan conversion to provide image derotation and sensor/display compatibility. Several methods of implementing the required scan conversion have been assessed and involve temporal and spatial resampling and image truncation, all of which are degrading operations. With a separate lens system, as indicated earlier, scan conversion is not required for rate compatibility of sensor and display. Derotation could be accomplished opto-mechanically at the sensor (but at a size penalty).

An analysis of the resolution required for target identification shows that the requirements cannot be met using video from the AEOTR. Hardware and appropriate design techniques exist to provide target video to the pilot, and scene lighting is sufficient under expected operational conditions to provide video of good quality. However, the scale of the entire system is insufficient to warrant providing target video as an identification aid. It is therefore the recommendation of this substudy that video not be provided with the intent that it be used to augment or enhance visual target identification.

### 3.3 MOUNTING LOCATION STUDY

#### 3.3.1 General

Finding a suitable location for an AEOTR on the aircraft involves balancing installation and performance requirements of a general nature against a multitude of constraints, some of which are general, but most of which are peculiar to each airframe. Many factors were considered in the mounting location study, including the angles of attack for operational conditions, masking of the field of regard (FOR), suitable mounting techniques and packaging configurations to optimize performance and minimize deleterious effects on downstream airflow, the availability of adequate structural support and any precedent for similar systems. The two principal requirements are, very obviously, an unobstructed FOR and total absence of motion relative to the

aircraft armament datum line (ADL). The mounting location study involved the attempt to meet these fundamental requirements, while also adequately addressing the above considerations for the F-15, the F-16 and the F-18.

The original FOR design goal was a 120° included angle cone. This was proven impossible to achieve for quite valid mechanical considerations. The current FOR is a cone with an included angle of approximately 90° (20° up, 45° down, ±30° azimuth and continuous roll). Even with this reduced requirements, there are few locations on contemporary aircraft which offer such an unobstructed FOR.

The most desirable location is obviously at the point of the nose. However, this has been preempted by the radar system which is incapable of tolerating the effects of any metallic presence in front of the antenna. There is the possibility that, at some future time, a phased array antenna might be designed which could cope with such a presence.

A second choice would be to mount the tracker on a short pylon immediately aft of the radome. Except in the case of a very short (blunt) radome, a form currently not much in vogue, there will be some obstruction of the field of view. Two advantages to this location which will tend to offset the obstruction are that close proximity to the structure carrying the radar dish will introduce minimal structural flexing between the two sensors, and that mounting the AEOTR on a short pylon will ensure that it will be outside of the boundary layer under most conditions. The decision as to where the sensor should be located around the radome tends to be academic: a top-center line location, or indeed any location where it can be seen from the cockpit, will quite properly be unacceptable because it will reduce the pilot's field of view. Locations on either side of the nose that are sufficiently low to satisfy the pilot's vision requirement would suffer from gross blockage of the FOR. Depending on which side the sensor is mounted, this would be in the 8 o'clock through 12 o'clock, or 12 o'clock through 4 o'clock zones. This leaves only an undernose location where the obstruction will be of the order of 10 o'clock through 2 o'clock.

There are, of course, other locations where the sensor might be mounted, but in each case the disadvantages far outweigh any gain. Mounting farther aft on the fuselage, especially about the center of gravity, would seem ideal. Unfortunately, the obstruction would probably approach 50 percent of the FOR. A midwing mounting would permit an unobstructed field of view, but aeroelastic deformation of the airframe, even in gentle maneuvering, not to mention the violent maneuverings of heat of combat, would render any pointing data that might be derived from the sensor virtually meaningless. This is similarly true for a tail location where the vignetting of the lower hemisphere is far more serious for air-to-air combat than the upper hemisphere vignetting associated with the belly mount just mentioned.

With these considerations, it can be generalized that a location under the nose, just aft of the radome, on a short pylon offers the best available choice. There are, however, specific constraints imposed by each proposed airframe which further limit mounting location choices.

### 3.3.2 Specific Aircraft

#### 3.3.2.1 F-15

The undernose location is totally unacceptable to the airframe manufacturer since nothing can be permitted to disturb airflow to the engine intakes, especially at high angle of attack. The situation is so serious that there is consideration of relocating the ILS blade antenna further aft. The only location offered in this case is in the port wing root fairing where there is adequate structural rigidity, ready access to cabling and copious cooling capacity. Unfortunately, this location so restricts the FOR of the sensor, as shown in Figure 18, as to make its addition to the aircraft a complication of dubious value. Approximately 43 percent of the total FOR is vignetted. Because much of this is in the lower hemisphere, the wing root position is not considered a desirable AEOTR mounting location.

A centerline underside location aft of the nose gear was not given serious consideration because of complete vignetting of the upper hemisphere and possible lateral vignetting by rocket stores located at the outside lower corners of the air intakes.

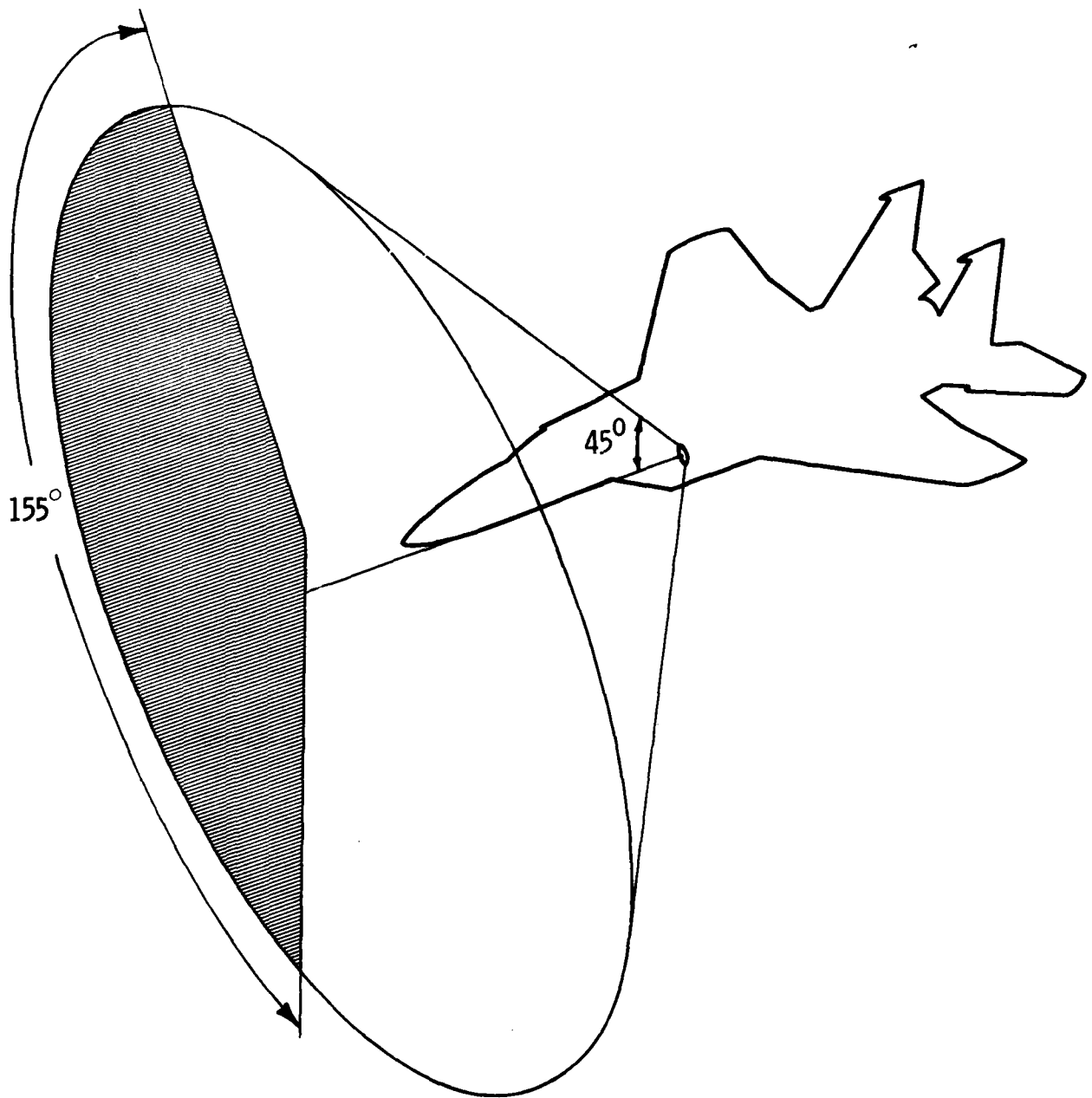


Figure 18 F-15 FOR Obscuration, Wing Root Mounting

### 3.3.2.2 F-16

The ideal location of undernose, aft of radome is unacceptable because of engine air intake requirements at all angles of attack.

The location suggested by the airframe manufacturer, on the lower starboard "corner" of the engine air intake, offers adequate structural rigidity since the frames in question also carry the "nose" gear anchor points. There is already provision for an external sensor pod (Pave Penny) at this location, including cabling, but there is no provision for cooling air. Most importantly, this location offers a good FOR which, although asymmetric, is less obstructed than that for a comparable undernose mounting. This results from the air intake serving as a very tall pylon, but without the weight and drag penalties of such a device. The FOR for the AEOTR at this location on the F-16 is shown in Figure 19.

Because of the very high density construction of the F-16, room for additional avionics within the cockpit is almost nonexistent, and any new system for the F-16 will need to be self-contained. For this reason, the AEOTR has been designed to fit the Pave Penny envelope (8 inches diameter, 54 inches long), including a self-contained cooling system. The requirements of trailing the leading edge of the air intake by three inches and access to a panel aft of the pod impose the 54-inch length limit.

### 3.3.2.3 F-18

Two possible locations were offered for the F-18: the centerline aft of the radome, which is the preferred mounting, and an engine intake trunk location. The FOR vignetting for those locations is shown in Figures 20 and 21. The FOR for the undernose mounting is quite good, and there is adequate structure to assure rigidity. Further, both cable ducting and cooling air trunking pass nearby. However, the availability of this undernose location is conditional upon being proven nondetrimental to downstream airflow.

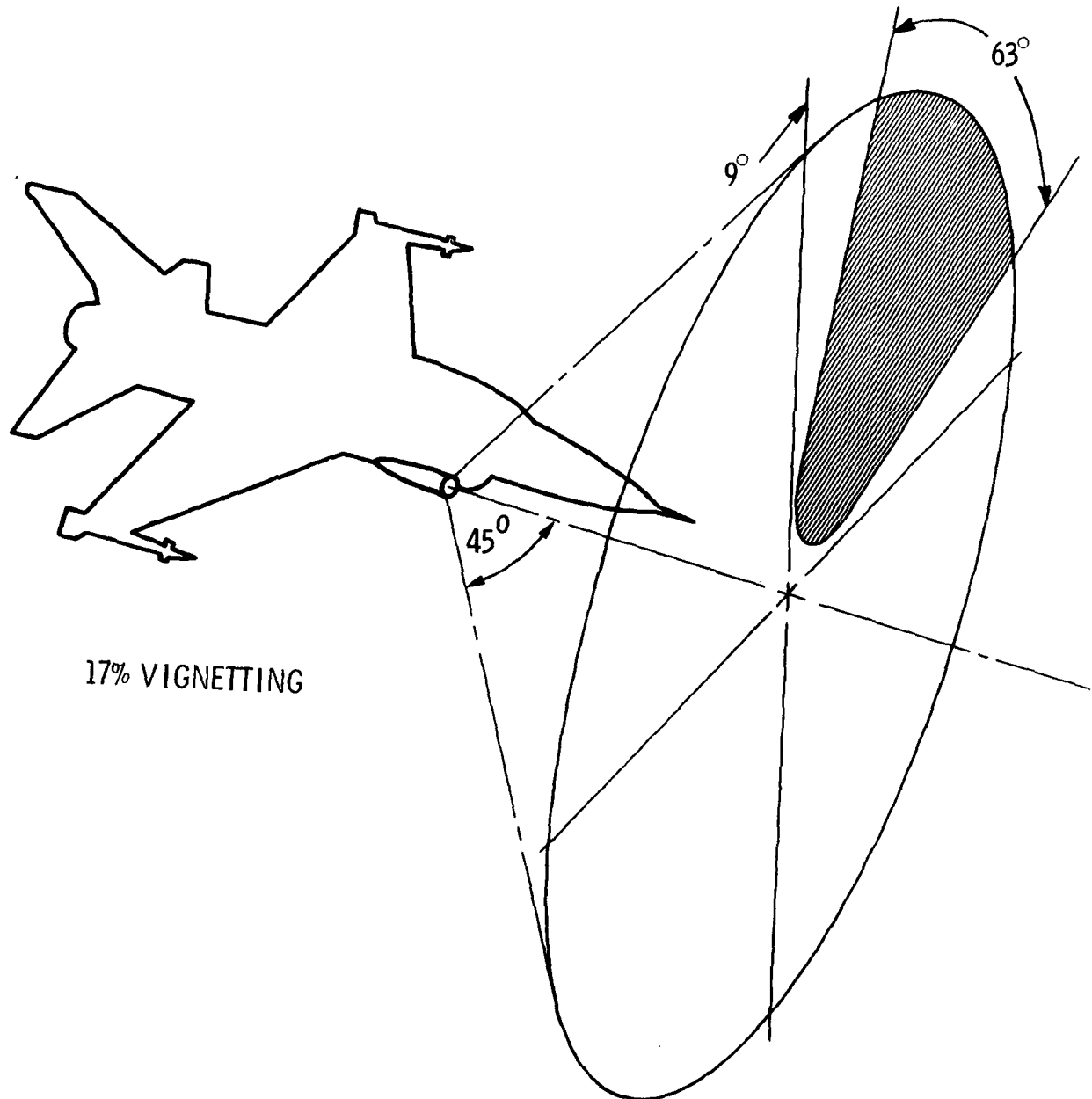


Figure 19 F-16 FOR Obscuration

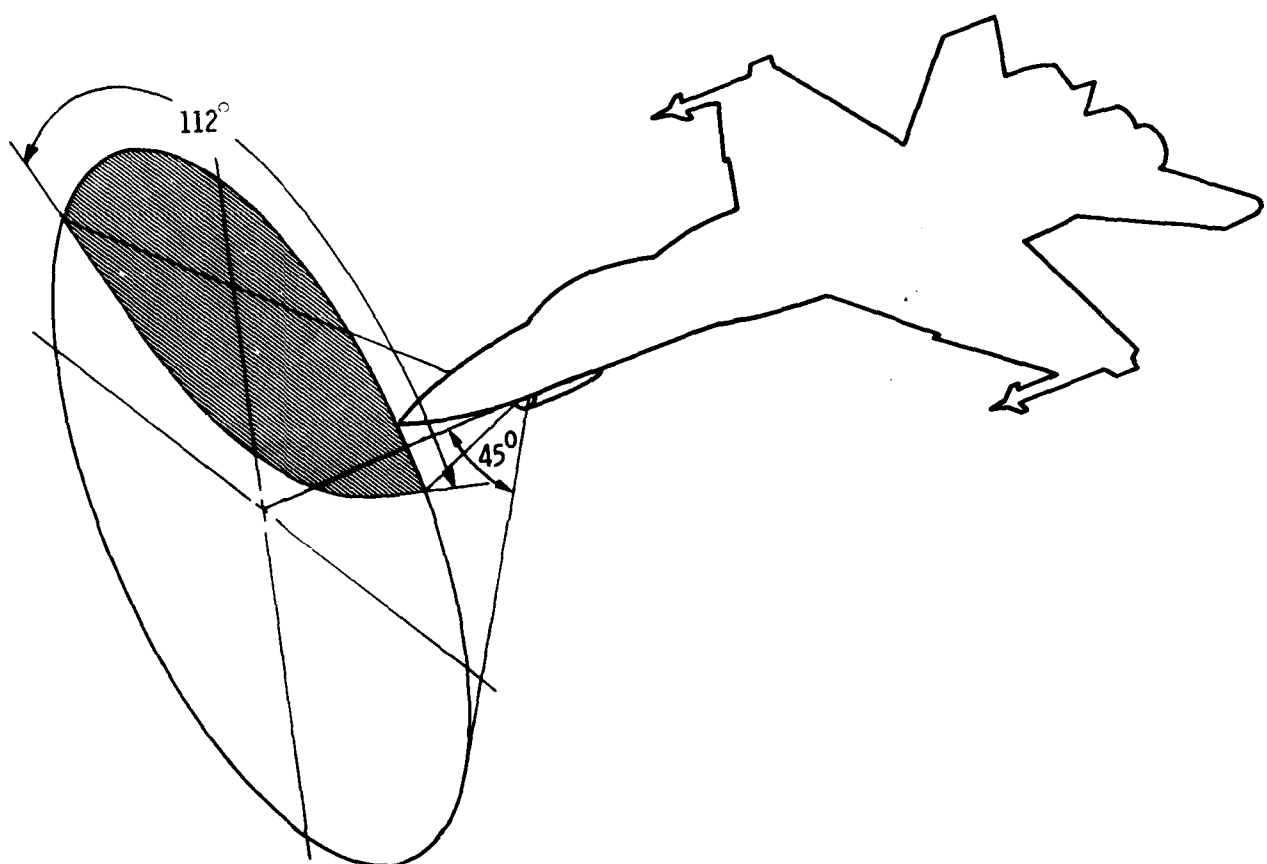


Figure 20 F-18 FOR Obscuration, Under Nose Mounting

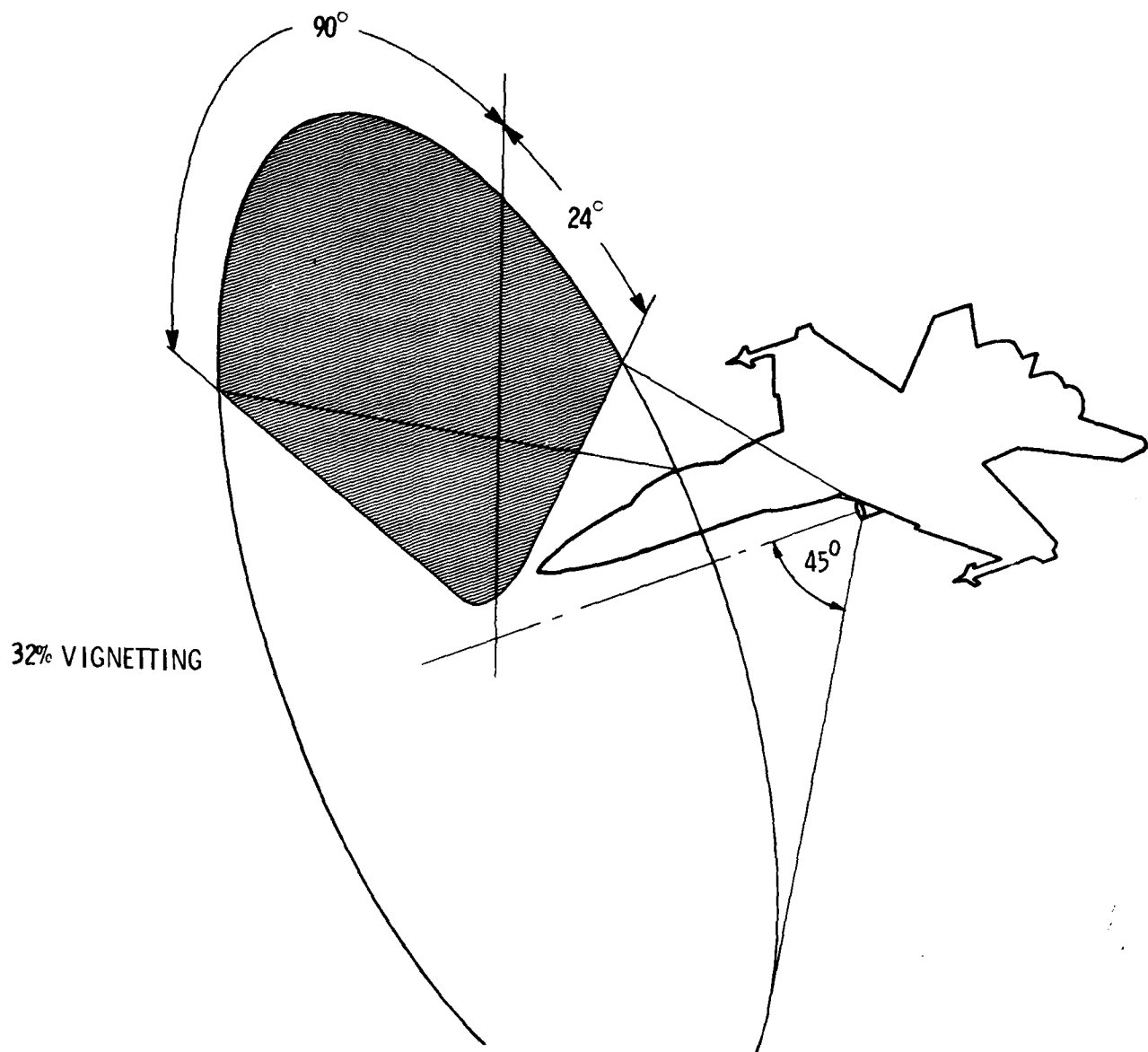


Figure 21 F-18 FOR Obscuration, Engine Intake Mounting

The alternative engine intake trunk location at the lower port side offers a quite good FOR, but the obstruction is asymmetric, as shown in Figure 21. This location is also used for the Pave Penny pod, and structural hardpoints and cabling ducts are present. This alternative mounting location would not require any additional wind tunnel testing to assess engine intake effects.

### 3.4 TARGET DETECTION

#### 3.4.1 Introduction

The AEOTR is unique in potential for target detection, acquisition and windowing because it produces three independent pieces of information about the world as viewed by it: motion, range and grey scale. This section describes a method to optimally employ this information so as to detect targets well beyond the critical tracking range of 8,000 ft with a high probability of detection and low false alarm rate. Included in the method are the logic functions to provide target acquisition and windowing after detection, as well as reacquisition if breaklock occurs after initial acquisition. The method to be described requires no adaptive logic to account for the structure of the background. Further, it can detect multiple targets within the field of view providing relevant information to a threat assessment program.

#### 3.4.2 Description of Method

##### 3.4.2.1 Concept

The method of target detection, using the independent gray scale, range and motion information contents of the scene, is structured as described below.

Subfields of the field of view are processed to determine measures of motion, range and gray scale content for each subfield. For each of these contents, a "map" is generated describing the scene in terms of motion, range and gray scale profiles. Targets in varying degrees will represent anomalies in all of these profile maps as compared to the background.

The size of the subfields (6 x 6 pixels out of a 190 x 122-pixel FUV) is chosen to provide a subfield small enough to exclude unnecessary background with respect to expected target sizes at detection ranges (8.000 ft to 24.000 ft) yet also provide sufficient pixel content for useful processing.

The array of subfields is organized both horizontally and vertically in increments of a 1-pixel shift from subfield to subfield in each direction.

The resulting maps of motion, range and gray scale anomalies are matched using appropriate weighting and threshold criteria to generate a target map of the field of view.

The processing operations to detect the motion, range and gray scale content of each subfield involve the correlation of corresponding subfields of time successive or baseline separated image frames. These, together with the weighting and threshold operations, are implemented on a pipeline processing basis. The speed of the CAI processor is such that complete processing operations can be carried out at 108 frame sets/s (one map per two image frames for motion).

Logical operations on the processed information to implement four required tracker functions are:

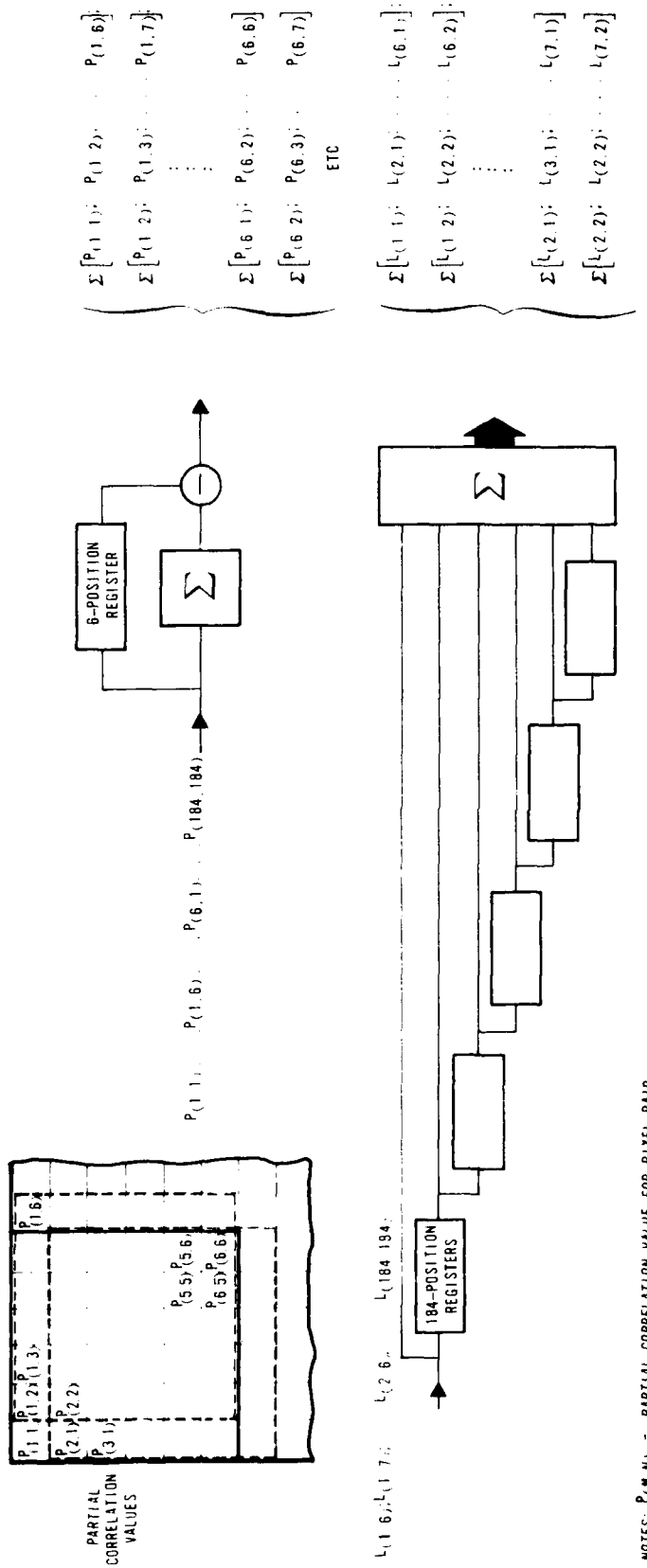
- Target detection, which consists of searching the processed scene image for sets of subfields which exhibit unusual characteristics, particularly such characteristics which a target is likely to possess and a nontarget is unlikely to possess.
- Acquisition, which consists of choosing one such subfield and fixing the attention of the system on that set.
- Windowing, which consists of defining the boundary of the subfield, or several adjacent subfields which encompass the target.
- Reacquisition, which, if breaklock occurs, consists of detection of the specific characteristics which the target was last known to exhibit. As the time since breaklock lengthens without reacquisition, the limits on those characteristics broaden. Note that in this case, the term characteristics can include the angular track of the target.

### 3.4.2.2 Processing Implementation

3.4.2.2.1 Raw Maps - It is clearly desirable that each of the raw maps has as high a resolution as possible. For the first two, high resolution maps are achieved by minimizing the size of the subfields and maximizing the degree of overlap. The former is limited by the minimum number of pixels necessary for meaningful correlation in the presence of noise, and the combination of both minimum size and maximum overlap is limited by the allotted processing time. From previous work in correlation, CAI has determined that the minimum feasible size for a subfield is approximately 30 pixels. Hence, a subfield should be no less than 4 by 8 or 6 by 6 pixels. For a 6 x 6 subfield size, a 190 x 122-pixel array can be subdivided into  $(122-6) \times (190-6) = 21,344$  subfields.

Subfield processing starts at the point in the correlation process where individual pixel pair multiplication values (between time successive frames for motion detection and between baseline separated frames for range detection) have been computed. The summing to obtain the correlation coefficients necessary to compute registration shift between corresponding subfields is done with shift register techniques, first to obtain a series of six pixel product value sums successively shifted in increments of 1 pixel, and then a series of six line sums successively shifted by one line. Figure 22 illustrates the technique.

3.4.2.2.2 Composite Map - Turning now to the problem of combining the maps in a useful manner, it is reasonable to begin by putting the maps on an equal basis to make them independent of the particular external parameters. This naturally leads to normalizing the maps by subtracting the mean and



NOTES:  $P_{(M,N)} =$  PARTIAL CORRELATION VALUE FOR PIXEL PAIR  
AT FIELD POSITION, ROW  $M$  COLUMN  $N$

$L_{(M,N)} =$  SUM OF PARTIAL CORRELATION VALUES IN ROW  $M$ ,  
COLUMN POSITIONS  $N$  TO  $(N+5)$ ; I.E.,  
 $L_{(M,N)} = \sum [P_{(M,N)}, \dots, P_{(M,N+5)}]$

$P_{(M,N)} =$  SUM OF PARTIAL CORRELATION VALUES FOR  
6x6-PIXEL SUBFIELD EXTENDING FROM ROW  $M$   
TO  $(M+5)$  AND COLUMNS  $N$  TO  $(N+5)$ ; I.E.,  
 $P_{(M,N)} = \sum [L_{(M,N)}, \dots, L_{(M+5,N)}]$

Figure 22 Subfield Processing

dividing by the standard deviation.\* For efficient hardware realization, it should suffice to rely on the means and standard deviations from previous raw maps generated, providing of course that maps containing targets large in the field of view are excluded. There is, however, a danger that if an extremely different background is suddenly imaged (for example, on crossing the horizon), the maps will not be well normalized. Additional considerations involved in defining a composite mapping equation are explained in the following paragraphs.

The motion map is initially in vector form. By subtracting the mean vector and taking the magnitude, this map is reduced to scalar form with strictly positive values. The vectors nearest the mean vector produce scalar values near zero and the vectors most different from the mean vector produce scalar values most positive. When this scalar map is normalized, it is only known that positive values came from unusual vectors and negative values from usual vectors. However, it is not known whether a target would give rise to unusual values (small in the field of view) or usual values (large in the field of view).\*\* The range information resolves this ambiguity.

The raw range map has intrinsically positive values, inversely proportional to range. Upon normalization, nearer ranges become positive and farther ranges negative. Excluding the possibility of picking out a target through a break in otherwise fairly complete cloud coverage, the rule that targets are nearer in range than background is appropriate. Thus, after normalization, positive range map values, especially relatively large values, probably correspond to targets, whereas negative range map values almost surely correspond to background. Hence, range should provide the sign to the normalized motion map components.

\* i.e., normalizing a random variable,  $X^* = \frac{X-\mu}{\sigma}$  where:

$X^*$  = normalized random variable

$X$  = random variable

$\mu$  = mean value of the set of random variables under consideration

$\sigma$  = standard deviation of the set

\*\* A target which is large in the field of view would contribute significantly to the mean and standard deviation values, and thus might not produce a significant positive value.

For fairly close backgrounds, i.e., less than a 25,000-ft range, either range or motion of a target will generally be distinguishable from the background. Against a near infinity distant background, there will exist a distinct difference in range for a target out to the desired detection range of 24,000 ft. Because of image size considerations, there is little likelihood of detecting targets farther in range. For the cases in which the mean range is greater than 25,000 ft, it is fair to weight the composite map in favor of detecting distinct range differences for target ranges of 24,000 ft or less, albeit at the expense of reducing the probability of detecting targets farther than 24,000 ft in range. Such a procedure enhances the detection performance for head-on views of targets with little or no detectable motion.

A difference in mean brightness or glint should not be considered significant in the absence of range or motion information indicating the probable presence of a target, but should be considered corroborating information when range or motion information does indicate the presence of a target.

3.4.2.2.3 Weighting and Thresholding for the Composite Map - The weighting in favor of range information when the mean range is large, as called for in the second consideration above, can be accomplished by imposing an offset on the normalized range map to reduce the mean below zero. The effect is to make it very difficult for background components to achieve positive values in the composite map with little effect on target components. The result is to greatly reduce the threshold level needed to maintain a low false alarm rate and thus significantly raise the probability of detection. As the mean range decreases, the certainty of distinct range difference disappears and this procedure is counter-productive. A useful, though not necessarily optimum, offset is one set as the midpoint between the displacements of the mean range ( $d$ ) and the maximum detection range. Thus, the offset is used for mean ranges from infinity to 24,000 ft, and is not used for shorter ranges. A composite map component ( $c_{ij}$ ) is then determined by the following relationship:

$$C_{ij} = \left[ |Dm_{ij}| \frac{DR'_{ij}}{|DR'_{ij}|} + DR'_{ij} \right] \times \left[ |B_{ij}| + 1 \right] \quad (1)$$

where:

$Dm_{ij}$  = component of the normalized scalar motion map

$DR'_{ij}$  = component of the normalized range map, but with the mean range ( $\bar{d}'$ ) redefined as:

$$\bar{d}' = \text{MAX} \left\{ \bar{d}, \frac{\bar{d} + .073}{2} \right\}^* \quad (2)$$

$B_{ij}$  = component of the gray level map

Before examining the two cases for background and target, a further constraint is imposed which discriminates very heavily against noise with minimal effect on the detection of targets. Specifically, the constraint is imposed that at least three adjacent subfields \*\* must be greater than the threshold level for the system to register a probable target in that area of the image. Because noise is expected to be randomly distributed and targets must be localized in the image plane, this is a powerful constraint.

### 3.4.3 Performance

#### 3.4.3.1 False Alarm Probability

To determine the probability of false alarm, a Poisson distribution is assumed for the number of occurrences per frame that a noise spike will be above the threshold, and a generalized binomial distribution is used for the probability of adjacency, so that:

\*  $d'$  and  $d$  are given here in fractional pixel shifts; the value 0.073 corresponds to a range of 24,000 ft. To evaluate the expression in normalized terms, it is noted that the normalized value of  $\bar{d}$  is always zero, and that the normalized value of  $\bar{d}' + 0.073$ , the offset, is determined by scaling against the standard deviation of the background (see Section 3.4.3.1).

\*\* Note that adjacent subfields have a separation of 1 pixel.

$$P_{FA} = \sum_{K=3}^n P_{3(K)} e^{-\lambda} \lambda^K / K! \quad (3)$$

where:

$P_{3(K)}$  = the probability that three noise spikes are adjacent, given  $K$  noise spikes in the frame

$\lambda$  =  $np$  which is the product of  $n$ , the number of subfields in the frame and  $p$  = probability per frame of a single noise spike greater than threshold. Neglecting edge and corner effects  $P_3$  for a 21,344-subfield array is given by:

$P_{3(3)} = 2.63 \times 10^{-7}$  for three noise spikes present

$(K>3) P_{3(K)} = \frac{K!}{3! (K-3)!} P_{3(3)}$  for three noise spikes present

From trial calculations, it has been determined that a false alarm rate in the range of 1/10 min to 1/hour is a reasonable requirement for this detection method. For a processing rate of 108 frame sets/s, the respective false alarm probabilities for rates of 1/10 min [ $P_{FA(10)}$ ] and 1/hr [ $P_{FA(60)}$ ] are,  $P_{FA(10)} = 1.54 \times 10^{-5}$  and  $P_{FA(60)} = 2.57 \times 10^{-6}$ . Solving equation 2 for  $\lambda$  yields values of  $\lambda_{(10)} = 7.06$  and  $\lambda_{(60)} = 3.88$ . The corresponding simple probabilities (from  $\lambda = np$ ) are  $P_{(10)(\lambda = 7.06)} = 3.31 \times 10^{-4}$  and  $P_{(60)(\lambda = 3.88)} = 1.82 \times 10^{-4}$ . At this point, a study of the statistics for mapping of the background is necessary to set a threshold level.

Assuming that target objects make no significant contributions to the raw data maps, all the normalized maps must by definition have variances equal to 1, and with the exception of the range map, have means equal to 0. Assuming a reasonably flat (physically) background, the major contribution to standard deviation of range is correlation noise, which for single samples is on the order of .02 pixels of displacement. Then the offset for the normalized range map is  $\frac{0 + 0.073/0.02}{2} = 1.83$  for approximately infinite background, and by definition, 0 for background equal to or less than 24,000 ft in range.

The statistical curves, relating required threshold to  $P_{FA}$ , for the composite map background values have been generated and are shown in Figures 23 and 24. They show that to achieve the previously stated false alarm probabilities, the threshold levels in the case of infinitely distant background should be  $T_{(10)} = 8.1$  and  $T_{(60)} = 9.0$  and for the case of background of 25,000 ft, should be  $T_{(10)} = 12.7$  and  $T_{(60)} = 13.6$ .

### 3.4.3.2 Detection Probabilities

Having determined threshold values, the probability of detection for various cases can now be examined. The detection probabilities so calculated from the distributions for noise and signal plus noise are those for a single target pixel \* appearing above threshold. Actual targets cover several pixels, e.g., a MIG 23 viewed head on at 24,000 ft covers at least 4 pixels. Computer results show no difficulty correlating on a target this small even against clutter.

The probability  $P_{3(D)}$  that at least three target components out of four are above threshold, given the probability  $P_{1(D)}$  of any one of them being so, is given by:

$$P_{3(D)} = \frac{4!}{3! 1!} P_{1(D)}^3 + \frac{4!}{4! 0!} P_{1(D)}^4 = 4P_{1(D)}^3 - 3P_{1(D)}^4 \quad (4)$$

Recalling that the three components must be adjacent to register as a target (or noise, i.e., false alarm), the condition is automatically met for a 4-pixel target size with 3 pixels detected. For larger targets, probability reasoning similar to that in section 3.4.3.1 is applied to obtain the target probability of detection. Taking this into account, results have been generated which show the probability of detection for a head-on target against an infinitely distant background at both 24,000 and 18,000-ft ranges.

\* Note that at this point in the processing, a target "pixel" is actually a processed 6 x 6 pixel array of original detected imagery.

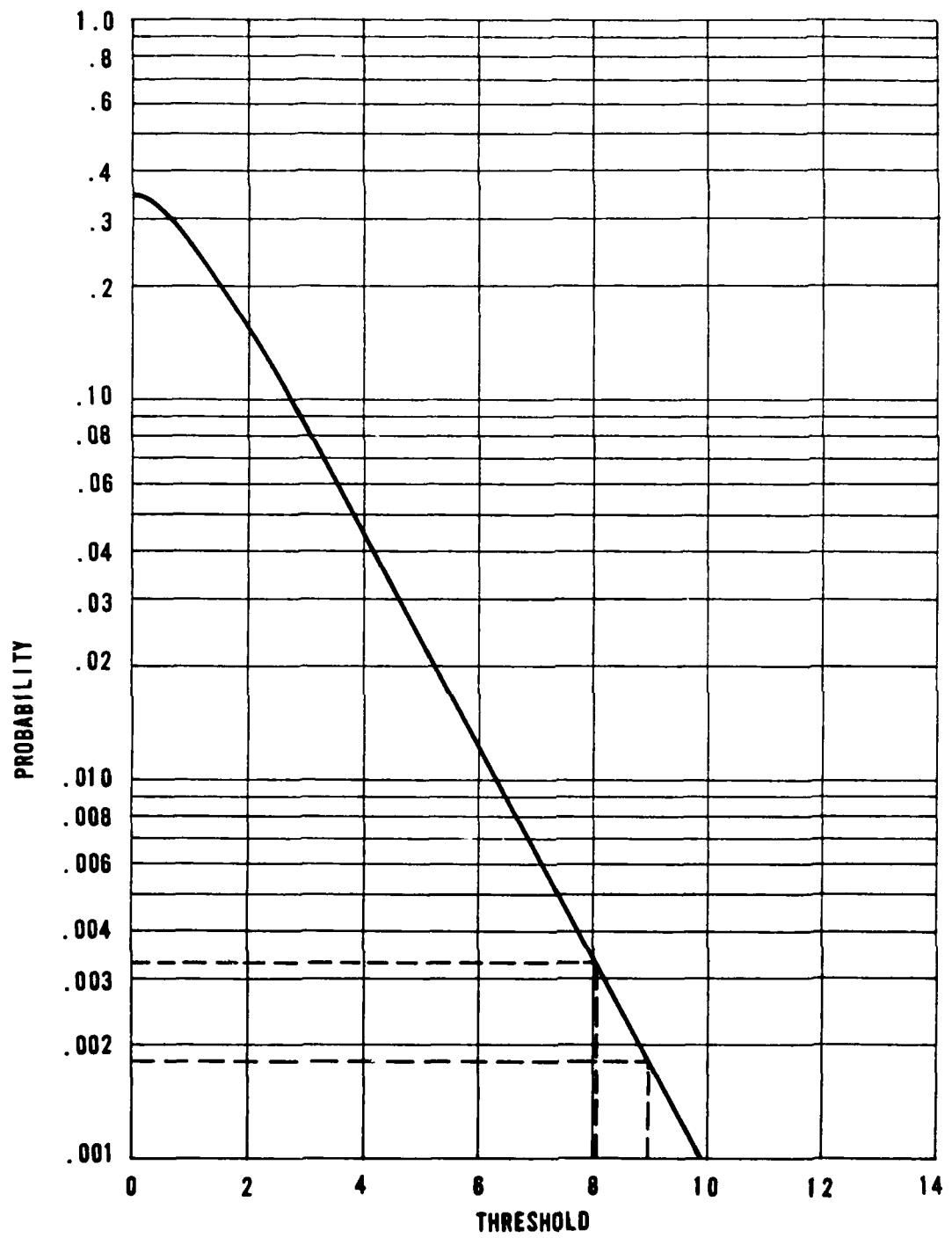


**Figure 23 Probability Per Frame of a Single Noise Spike Above Threshold - Offset = 1.83**

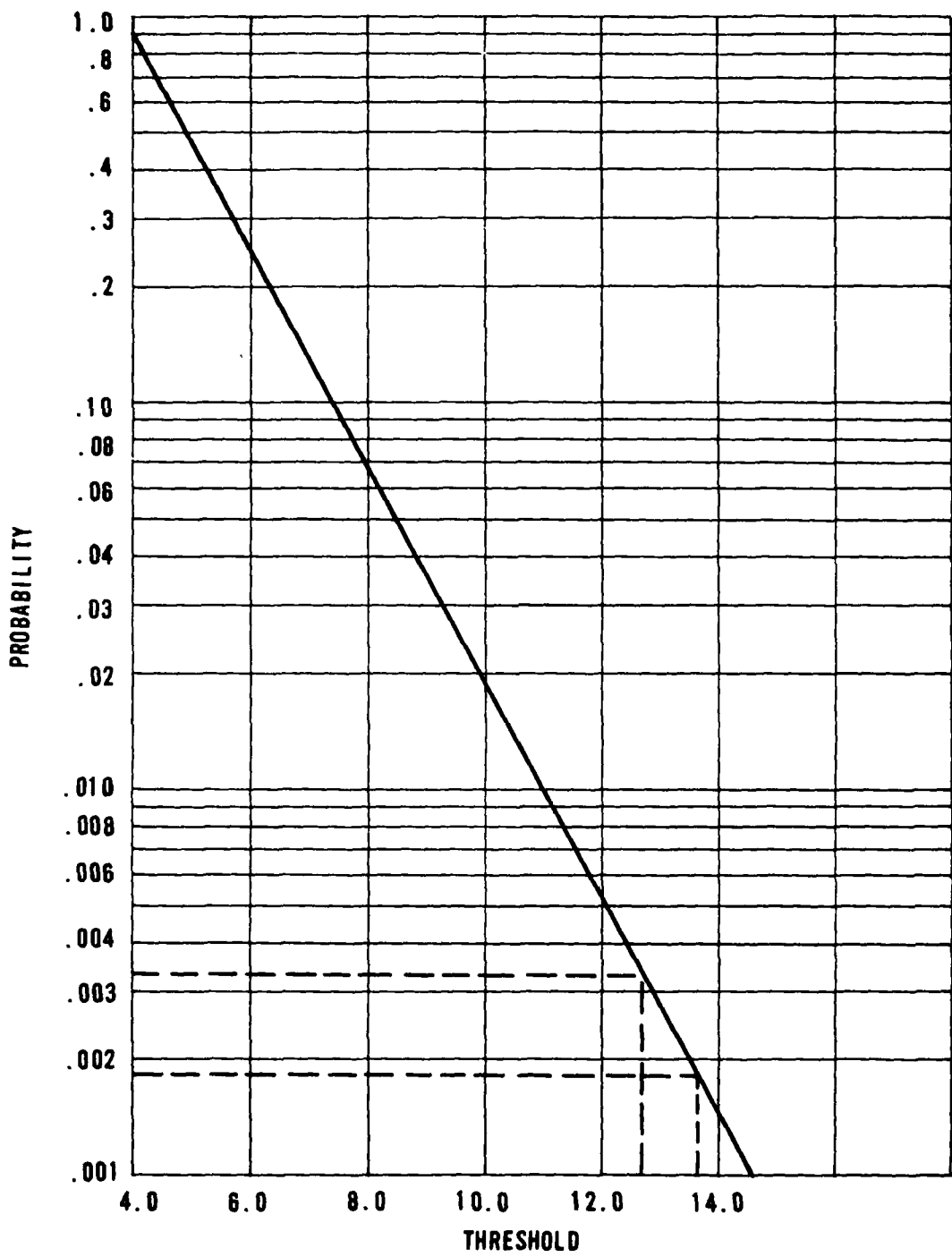


Figure 24 Probability Per Frame of a Single Noise Spike  
Above Threshold- Offset = 3.6

The first set of results, Figures 25 and 26, shows the effect of the magnitude of a normalized brightness difference, assuming no discernable motion. The second set of results, Figures 27 and 28, shows the effect of motion (perpendicular to the line of sight), assuming the brightness is statistically the same as the background. Note that this motion is motion relative to the background, and may arise from target motion and/or ownship motion. Clearly, only minimal contributions from either map is required to virtually assure detection for this worst case of head-on approach. When the view of the target shows greater cross-sectional coverage on the image plane, the probabilities of detection are greatly increased.

For the case in which there is essentially no distinction in range between target and background, the system relies primarily on motion detection. The target pixel coverage may vary substantially. As it is a driving factor in determining probability of detection, a number of cases must be examined to provide comprehensive results\*. To give a single, fairly easily calculated result, a target at 24,000 ft with a velocity of 400 kn, and covering an area  $2 \times 2$  pixels square in the image, has an average probability of detection of 0.34, while the same target covering a  $3 \times 3$  pixel square has a probability of 0.84, and covering a  $4 \times 4$  square, 0.98. As the velocity increases or the area coverage increases, the probability increases. This is shown in Figure 29.

#### 3.4.4 Summary

Operationally, the ranger channel is used exclusively for the target detection logic because of its greater resolution. The FOR is searched through successive fields of view with two frames at each position so that motion may be detected. Each pair of frames (range detection and motion detection pairs) is processed with pipeline correlation so that the set (21, 344) of overlapping subfields are correlated to yield high resolution maps of motion and range.

\* Where range and background are not substantially separated, target aspects encountered will include top and side profiles as well as front and rear profiles. Also, the spread of possible range, background values is substantial.

TARGET RANGE: 24,000 FT  
BACKGROUND:  $\infty$   
MOTION: 0

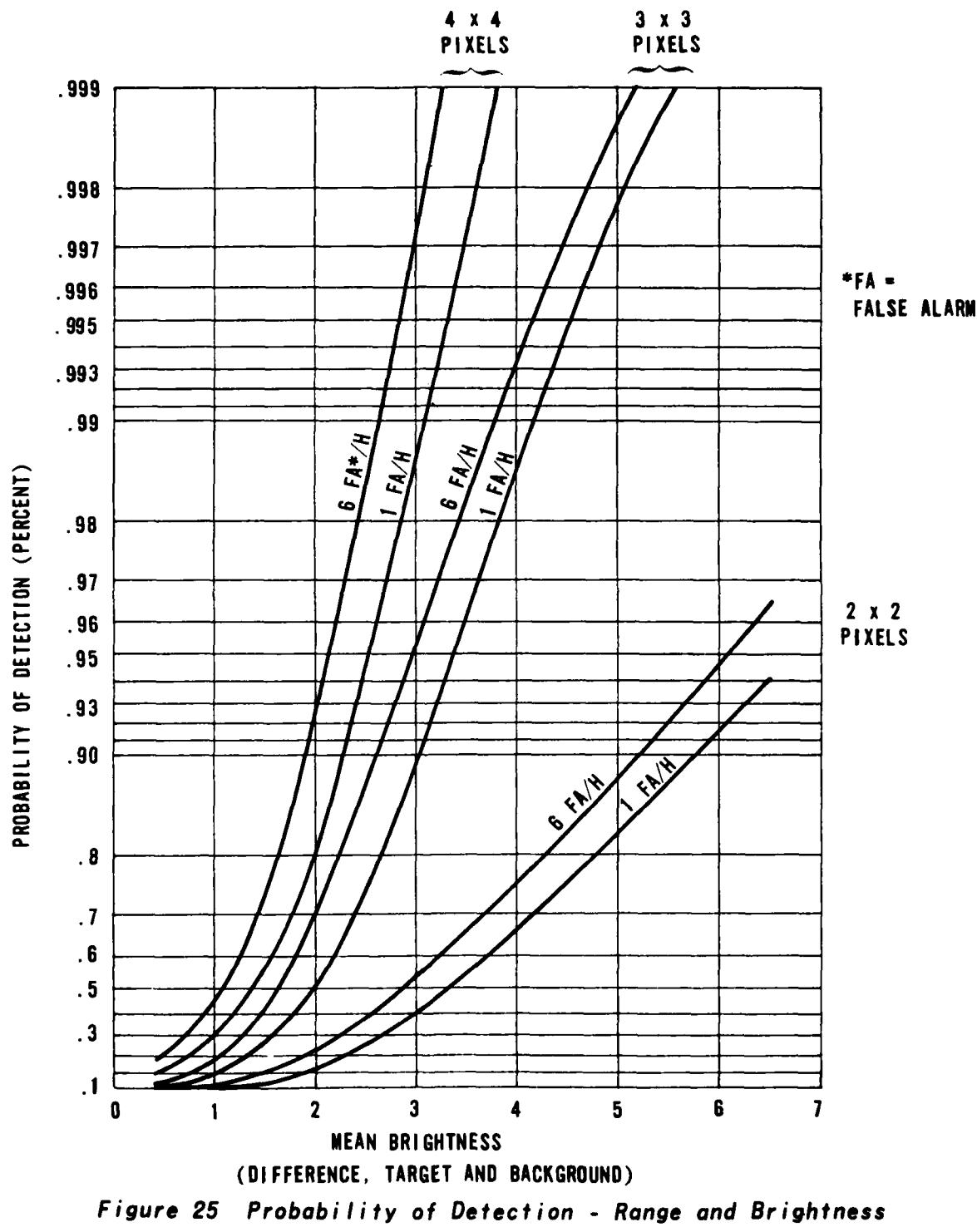


Figure 25 Probability of Detection - Range and Brightness Information Only

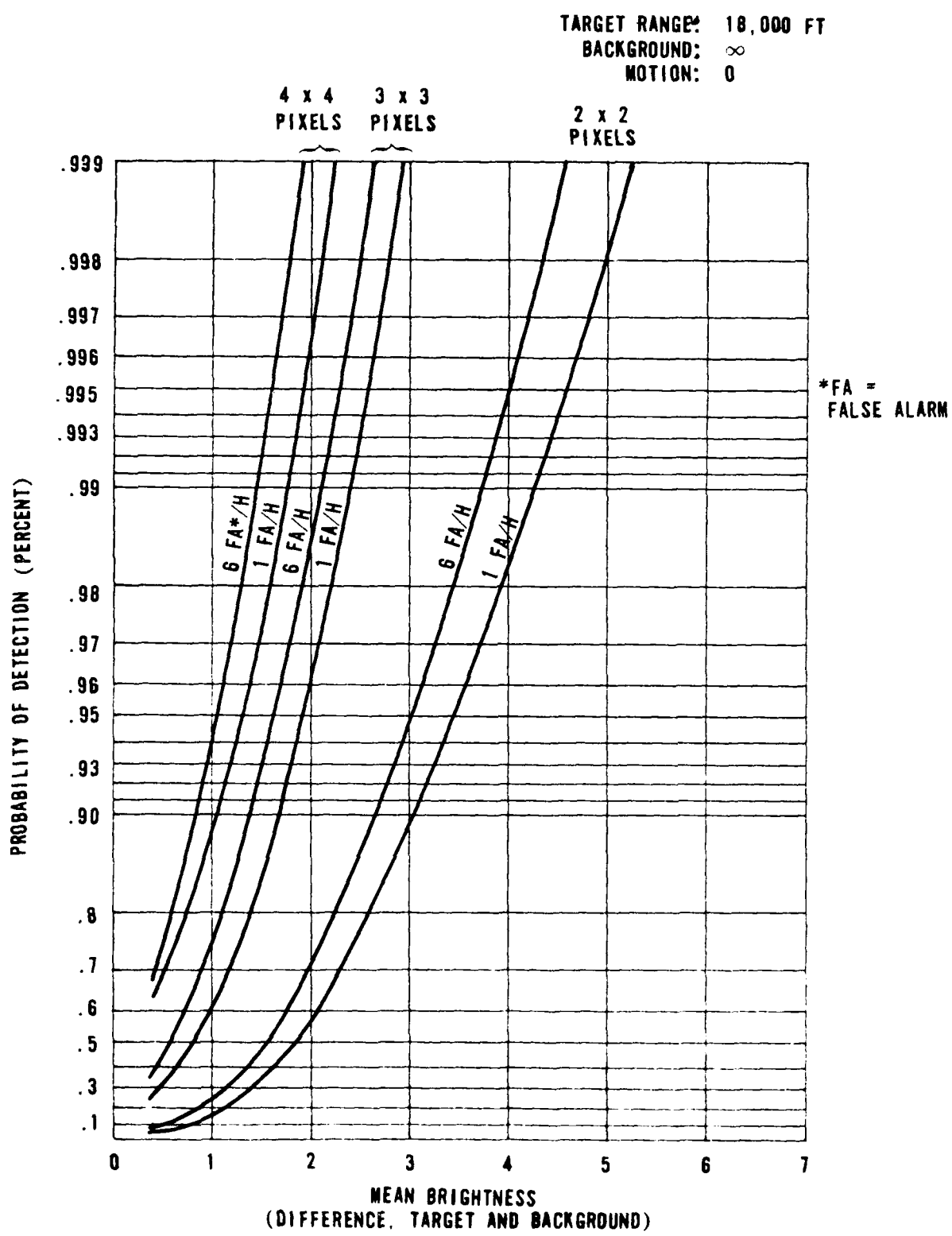


Figure 26 Probability of Detection - Range and Brightness Information Only

TARGET RANGE: 24,000 FT  
BACKGROUND:  $\infty$   
BRIGHTNESS: 0

4 x 4  
PIXELS      3 x 3  
PIXELS

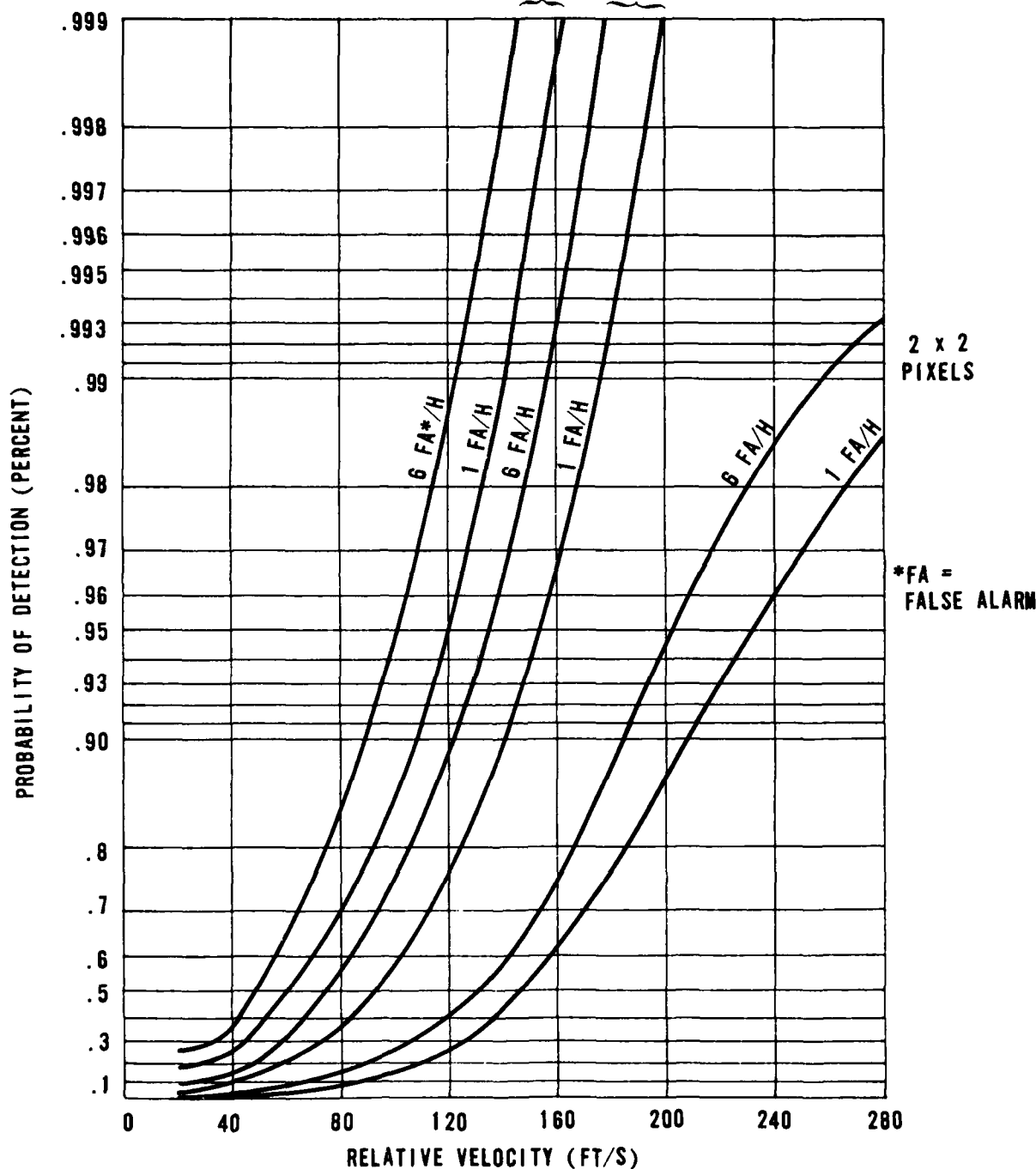


Figure 27 Probability of Detection

TARGET RANGE: 18,000 FT  
BACKGROUND:  $\infty$   
BRIGHTNESS: 0

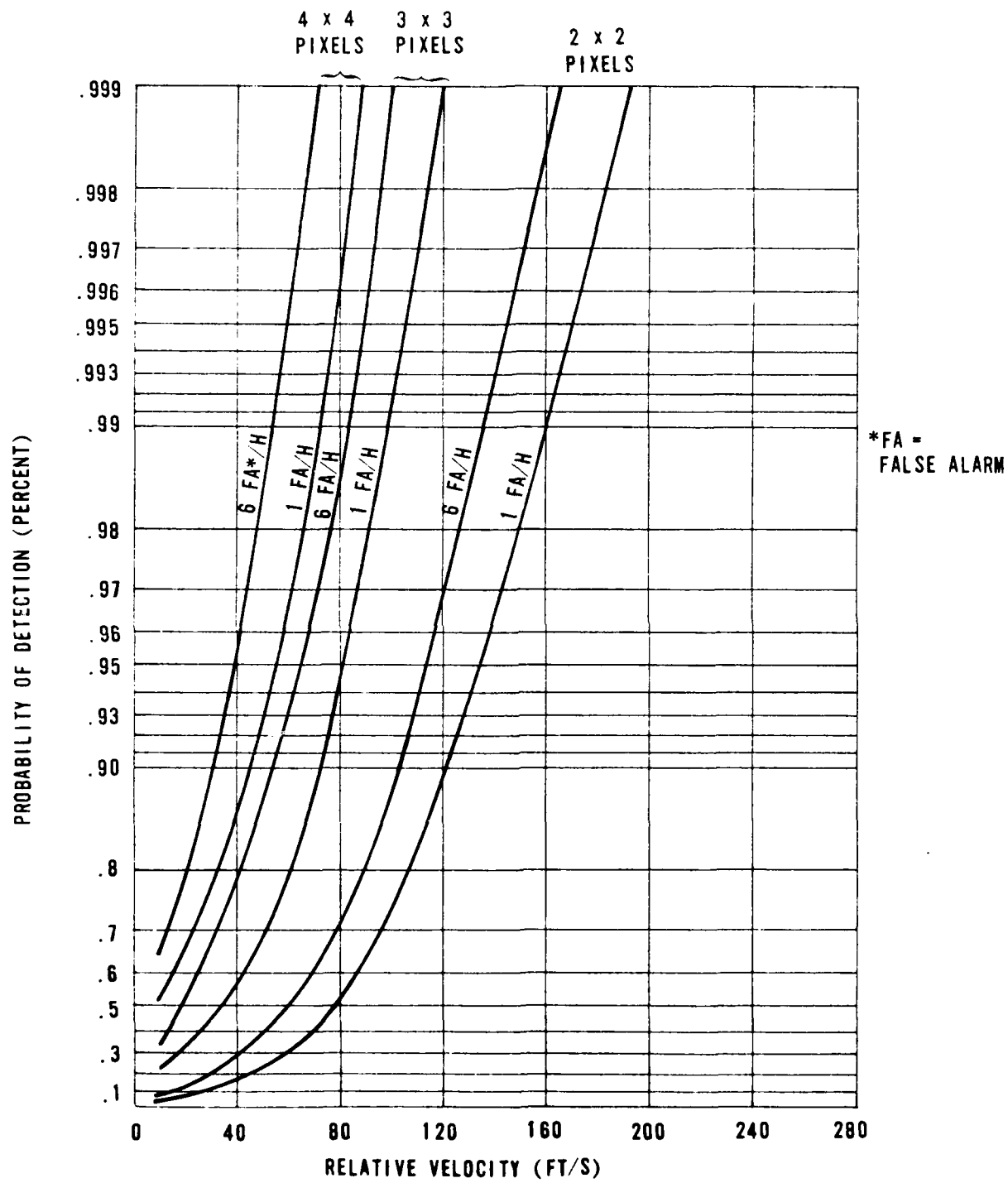


Figure 28 Probability of Detection

TARGET RANGE: 24,000 FT  
BACKGROUND: 25,000 FT  
BRIGHTNESS: 0

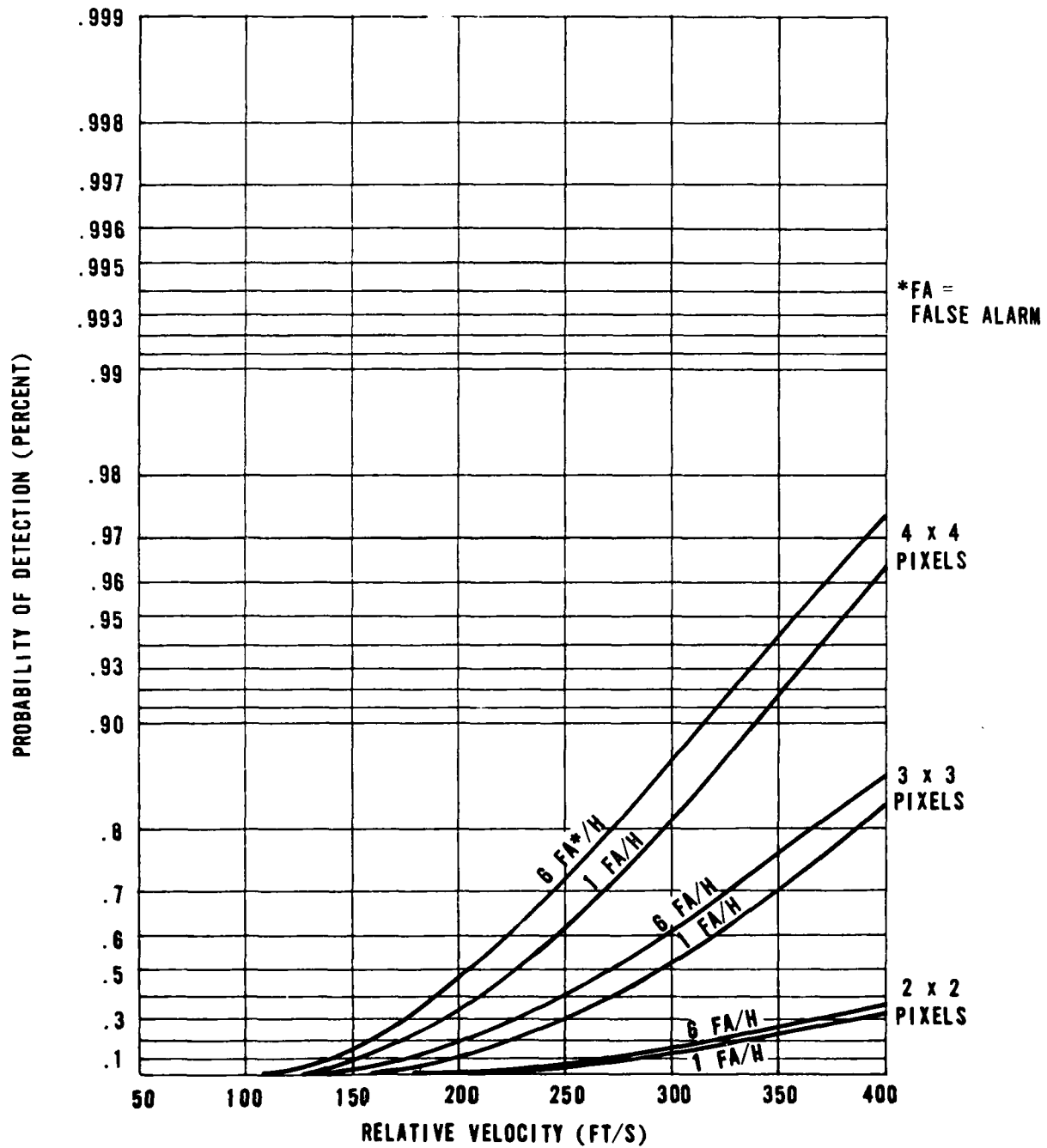


Figure 29 Probability of Detection - Motion Information Only

This processing is performed at the readout rate so that the search is governed by integration time and mechanical scanning considerations. The results presented above assume that the background is essentially flat in range and motion, so that the only contribution to the variances of these two maps arises from electronic correlation noise. This correlation noise is lumped into the .02 pixel rms error figure quoted elsewhere.

### 3.5 SEARCH PATTERN

In the absence of cue commands from the pilot or other on-board sensors, the AEOTR can autonomously search its FOR to increase the probability of detection of enemy aircraft. Without attempting to evaluate tradeoffs in time to cover the FOR versus the desirability of overscanning given sectors of the FOR due to potential threat considerations, since these are basically software functions, the approach taken here is to search the entire FOR in as short a time as possible. For a conical FOR, and neglecting ownship obscuration, this is accomplished by minimizing overscan with a spiral scanning geometry.

The major problem is to stabilize the image for the two integrations necessary to detect motion. This may be done by halting the roll at each LOS frame, using the third axis, yaw, to counter-rotate the head for that period, or incorporating an additional scanning mechanism, such as a galvanometer, to counter-rotate or stabilize only the image. While the gimbaling arrangement and torque motors are described more fully in Section 4.0, the necessary figures for discussion of search time are given here. Accounting for aerodynamic loads and inertia, the maximum roll rate is 27 rad/s and the maximum accelerations possible are:

Roll axis	$57.4 \text{ rad/s}^2$
Yaw axis	$278.8 \text{ rad/s}^2$

Clearly, if the choices for stabilizing the image were limited to the above, the yaw axis would be preferred. The time ( $t$ ) to move from one LOS frame to the next is limited by angular acceleration and given by:

$$t = 2 \frac{FOV/2}{\alpha}$$

where:

FOV = frame field-of-view

$\alpha$  = acceleration

Because the ranger channel is used by the detection logic, the field of view is .0449 by .0346 rad. The orientation of the array is such that the longer dimension is used in this formula to yield a time of 17.9 ms between LOS frames, added to which are 8 ms for the two integrations, for a total of 25.9 ms per frame pair. The search pattern requires approximately 1250 frame pairs to cover the FOR, resulting in a total of 32.4 s. Note that this scanning is never limited by the roll rate.

The alternative is to stabilize only the image maintaining a smooth continuous head motion. In this case, the time to move the LOS becomes negligible. The number of revolutions (N) to cover the 45° cone is given by:

$$N = \frac{\pi/4}{.0346} - 1/2 = 23$$

The time per revolution ( $t_{rev}$ ) is:

$$t_{rev} = \frac{2\pi n (.0449)(.008 s)}{(.0346)}$$

where n is the ring number counting from the center of the FOR and the rate for each revolution is  $2\pi/t_{rev}$ . However, since the roll torque motor can only achieve 27 rad/s the central 5 revolutions are limited to this figure. Hence, the time to cover the FOR is given by:

$$t = \frac{(5)(2\pi)}{27 \text{ rad/s}} + \frac{(2\pi)(.0449)(.008 s)}{(.0346)} \sum_{n=6}^{23} n = 11.3 \text{ s}$$

This is a 65 percent reduction in time at the expense of one more component. Offsetting this additional complexity is the reduced wear and mechanical stress otherwise produced by discontinuous head motion, and the fact that the same component could be used for image dither discussed in Section 6.0 under the summary error analysis for range.

### 3.5.1 Target Discrimination During Search

During a given search pattern, 0 to n targets may be detected. It becomes necessary, then, to implement some procedure to store and classify detected targets in terms of their threat potential and/or attack vulnerability. Specifics of such a storage/classification procedure are outside the present scope. However, some general requirements and characteristics can be delineated to outline the essential nature of a target discrimination procedure.

The principal elements of such a target discrimination procedure are:

1. Rapid classification of each detected target as to its threat/vulnerability potential.
2. Storage of each target threat/vulnerability value, together with pertinent target location and motion, range values.
3. A supervening criteria which recognizes a target having an immediate and large threat potential so that search is interrupted and tracking started immediately.
4. Provision for dropping from storage lowest classification targets as the storage capacity becomes filled and if additional targets of higher classification continue to be acquired during a search cycle.
5. In the absence of 3.. selection and reacquisition of the highest priority target at the end of the search cycle.
6. Suitable display to the pilot of the target situation during and upon completion of the search cycle.

Effective design of such a target discrimination procedure involves the specification of parameters such as:

1. The number of target storage locations to be provided. This has direct bearing on the amount and complexity of required electronics hardware. Tradeoff is necessary between hardware budgeting and expected operational requirements. It seems

probable that the number of storage locations provided would range between 4 and 12. A consideration entering into the tradeoff is element 4 above, i.e., the provision for deleting low priority targets to prevent storage overload.

2. Specification of a target hierarchy. The principal target characteristics available are:

- Range
- Heading
- Location in the field of view

A possible target hierarchy in terms of threat/vulnerability potential is given in Table 10.

Priority A, and possibly B would constitute immediate threats requiring intervening lock-on. Ranking G, and probably F are reasonable candidates for dropout with storage overload, if higher priority targets are acquired.

Pilot display involves the usual tradeoff between the amount of useful information available versus the essential information which the pilot can assimilate. The minimum information items for such a display include:

- Immediate threat (together with track lock-on) warning confirmation
- Significant threats (including number)
- Total targets in FOR (number)

A very important consideration in the effective implementation of a target discrimination procedure is that of providing assurances that a "cataloged" target can be returned to once the FOR search cycle is completed. The storage of target location and motion parameters were previously mentioned. If the first target detected turns out at the end of the search cycle to be the only one detected, or to have the highest priority, the intervening search time may obsolete the stored target parameters to such a degree that a new search cycle may have to be initiated to relocate the target. For distant targets, the problem may not be severe or highly important. For closer targets (in particular, for

TABLE 10  
TARGET HIERARCHY

Priority	Range	Heading	FOR Location	Likely Potential
A	Close	Closing	Anywhere	Threat
B	Intermediate	Closing	Anywhere	Threat
C	Close or intermediate	Beam	Central	Threat/vulnerability
D	Close or intermediate	Beam	Peripheral	Vulnerability/threat
E	Far	Closing	Central	Threat
F	Far	Closing	Peripheral	Threat
G	Far	Beam	Anywhere	Vulnerability

those with large motion rates), the problem could be crucial. Significant mitigation of the problem in those cases can be obtained by weighting the upper end of the hierarchy of priorities with target motion data. This would have the effect of "upping" the priority of more targets to the "immediate intervening target lock-on" category where delay time in target reacquisition is too risky.

Proper evaluation and quantitative consideration of all the factors and parameters involved in a target discrimination procedure will require a follow-on detailed design study.

## SECTION 4.0 A EOTR DESIGN

### 4.1 INTRODUCTION

In support of the program objective, namely the determination and demonstration of the feasibility of developing an advanced E-O tracker/ranger for air-to-air gun fire control, a preliminary system design effort was conducted. The design was carried to a sufficient level to establish that all the components needed to perform the required functions could be fitted within a reasonable package envelope and to permit the estimation of the performance characteristics of the resultant system. This was achieved within the limits imposed by the scope of the program and the degree of detailed design effort that could be applied to this portion of the study. The basic design philosophy uses the design principles discussed in Section 3.1.4. namely to minimize mechanical and optical errors and to calibrate out those errors which defy elimination.

### 4.2 MECHANICAL LAYOUT

The AEOTR is configured in two parts, a tracker head subassembly and a remoted electronics processing subassembly. The tracker head, shown in Figure 30, is contained within an 8-inch diameter by 54-inch long pod. The optical system and image sensors are contained in the gimballed sphere at the forward end of the pod. Mechanical, electronic and thermal support systems are contained in the aft portion of the pod. The electronic processing subassembly requires approximately  $1 \text{ ft}^3$  and one-half of this must be located elsewhere within the aircraft. Across the front of the sensor head is the  $2 \times 6.75$ -inch laminated normal incidence front window which serves both rangefinder channels and the tracking channel. The 5-inch f1 rangefinder lenses are separated by 5 inches, yielding the basic rangefinder scale factor  $B_f = 25 \text{ in}^2$ . Sufficient space is available aft of the lenses proper for the CCD and thermoelectric cooler in each channel. The field of the 2-inch f1 tracker lens is folded to permit placement below the rangefinder plane.

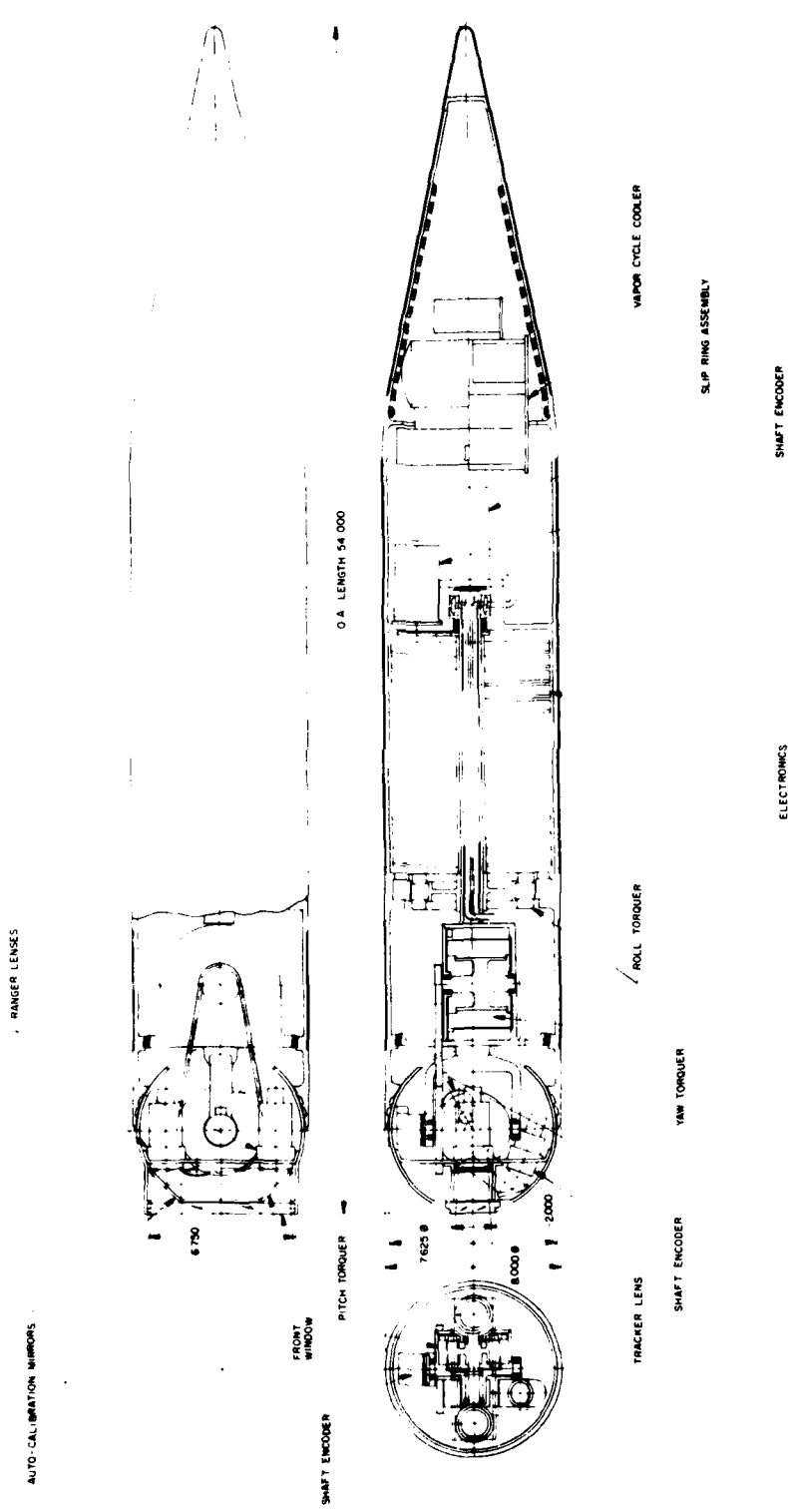


Figure 30 Tracker Head

The sensor head is gimballed in pitch, yaw and roll. The head suspension is at the center of the sphere, rather than at the sides, to permit maximum use of the full head diameter by the ranging optics. The pitch torquer and pitch angle shaft encoder are contained between the rangefinder lenses and are supported by a shaft and yoke assembly coupled to the forward roll axis bearing. The yaw torquer lies behind the sensor head to conserve head space and couples to the yaw axis via a steel belt and pulley. The yaw axis angle encoder is direct coupled and lies above the plane of the range lenses opposite the tracker lens. The roll torquer is positioned aft of the yaw torquer and rotates both the sensor head and its torquers, as well as the sensor head support electronics which are supported by the roll axis shaft. A slip ring assembly couples power, sensor control data and sensor video across the moving boundary at the rear roll axis bearing.

The FOR is  $+20^\circ$ ,  $-45^\circ$  in pitch,  $\pm 30^\circ$  in yaw and continuous roll, providing coverage of a full  $90^\circ$  included angle cone except for ownship masking. The choice of limited or continuous roll coverage was made on the basis that loss of target lock during an engagement is extremely undesirable, that multiple roll tracking situations are likely to occur when roll is a primary pointing axis, and that continuous roll is not significantly more difficult to provide than  $2\pi$  or  $4\pi$  rad of roll.

The stationary shell and aft portion of the pod may be supported on the host aircraft by a strongback extending over both roll bearings in the case of external pod installations, or by other appropriate means in internal installations where space may not accommodate a strongback.

A vapor cycle cooler in the rear of the pod is sized to have sufficient capacity for environmental control, particularly in the head. A final choice of cooling medium has not been made, although the existence of the primary heat load in the head region suggests that the air/coolant heat exchange be performed as near to the head as possible, such as near the yaw torquer. This in turn implies the use of a liquid coolant coupled to the head region through the pod strongback. Adequate space exists to permit this, although other possibilities have not been ruled out.

For internal installations with cooling air supplied, the optimum point for introducing it is clearly at the sphere where the heat load is greatest and air circulation and turbulence are required to minimize optical aberrations. After cooling the head, the air may be used to cool the electronics package whose thermal constraints are less severe.

#### 4.3 OPTICAL LAYOUT

A simplified layout of those components pertinent to the optical train is shown in Figure 31. The mechanical layout (Figure 30) is the more detailed drawing of the total design and shows the tracker lens with its relay mirrors.

The first optical element is a single window which spans the head to simplify the design. It is normal to the optical axis, and is a bonded two-material design as described in Section 3.1 and Appendix C.

The next elements are a pair of spectral beam splitters which filter by reflection the spectral wavelength used for autocalibration.

The rangefinder lenses are matched 5-inch f1, f/4 lenses with spectral correction covering the silicon CCD response correction. Based on design experience for a 5-inch f1, f/2.8 lens, and both design and fabrication experience of a 2-inch f1, f/1.0 lens with both wide spectral correction and nearly-diffraction-limited performance at CCD Nyquist frequencies, it is believed that an MTF of better than 0.95 at these frequencies can be achieved for the 5-inch f1, f/4 lenses required for the AEOTR.

Behind one lens is a plane parallel plate used for closed-loop ranging. Its purpose is to shift the one image minutely up to 1/2 pixel until the two target images in each channel are precisely registered on a whole pixel basis. To accomplish this, the plate is rotated a few degrees relative to the optical axis driven by the target image correlation until the calculation indicates zero fractional pixel misregistration. The ratio of image shift ( $\delta$ ) to plate thickness (t) is given by the formula:

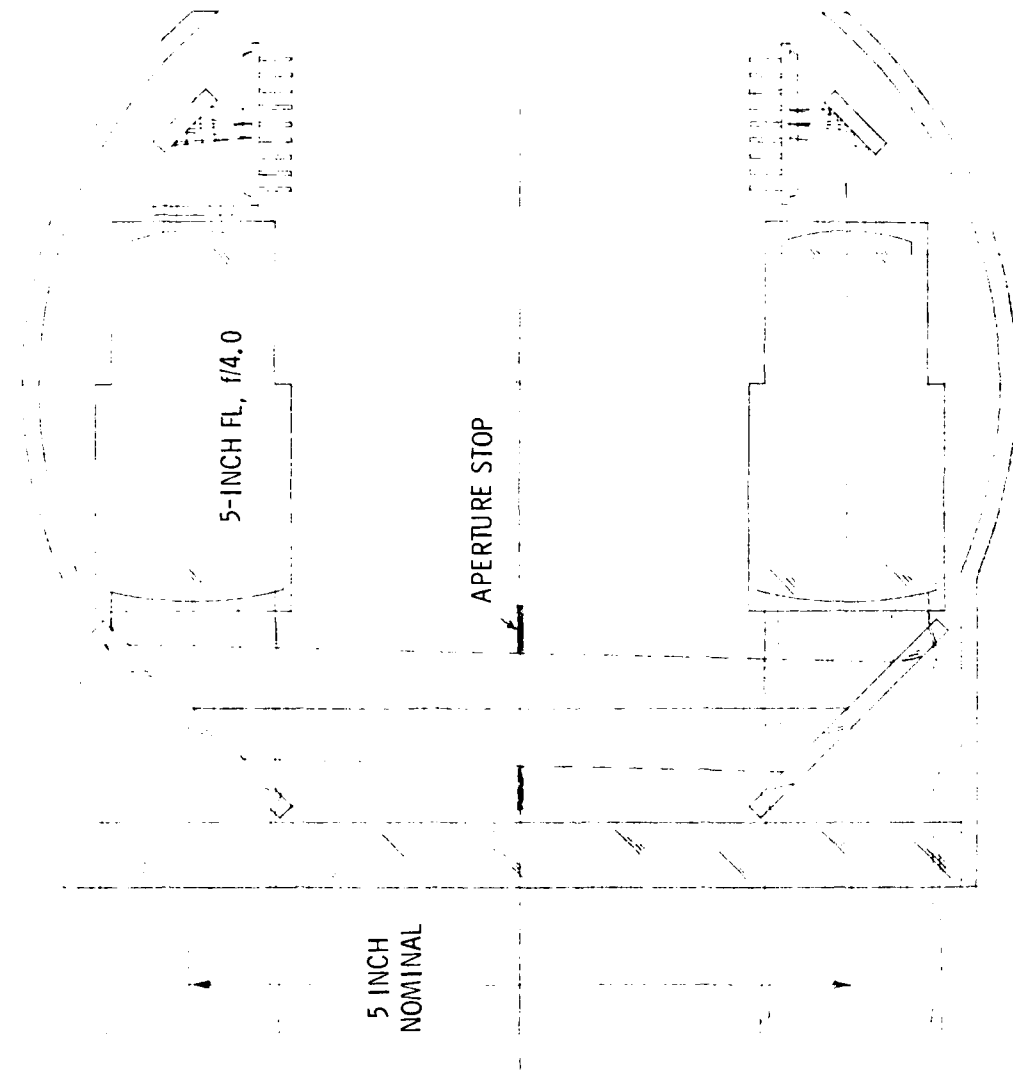


Figure 31 AEOTR Optical Schematic

$$\frac{\delta}{t} = \sin \phi \left[ 1 - \frac{\cos \phi}{\sqrt{n^2 - \sin^2 \phi}} \right]$$

where:

$\phi$  = angle between the optical axis and the plate normal

$n$  = index of refraction

Assuming a nominal index of 1.5 rad and for  $\phi$  less than 3°, the ratio  $\delta/t$  is approximately .00582  $\phi$ ; thus, the plate can be on the order of 1/10-inch thick for a one-half pixel shift per degree.

Except for the beamsplitters, the optical layout does not show the components necessary for autocalibration. These include a source, a diffusely reflective pattern on one cover glass, the beamsplitters and an aperture stop. The source is a commercially-available LED such as a GaAs edge emitter which has a 2.5-mW output at .94  $\mu$ m, with an 80° beam spread. With this type of source, CCD saturation occurs when the LED is closer than 1.87 inches to the sensor. This distance allows the LED to be located, for example, above the optics and reflected onto the chip by means of a 45° reflective face on the top edge of the appropriate folding mirror. The pattern deposited on the cover glass is a low frequency sinusoidal amplitude bar grating. Because the pattern is single frequency, both spatially and spectrally, both transmission and transfer function losses result only in decreased contrast which can largely be restored electronically. The bar pattern covers only a few rows of the sensor array, so the two areas used for scene imaging and autocalibration need to be optically divided by spectral filters. That portion of each cover glass over the scene imaging area should have the same short pass or notch filter as the front beamsplitters while the portion over the autocalibration area should not pass the scene light. The front beamsplitters are maintained at precise angular separation (as nearly right angles as possible) by thermally coupled ULE support plates above and below. There is a hole in the lower plate to transmit the tracker ray bundle, but this should not affect the angular stability. Finally, an aperture stop is located midway between the lenses to assure a zero coma condition and to eliminate lateral chromatic aberration.

## 4.4 ELECTRONIC LAYOUT

### 4.4.1 Introduction

To meet the requirements for a large FOR with high accuracy ranging and tracking, the AEOTR system has been configured in a gimballed head using CCD's as image sensors. Tracking information generated by assessing image motion is fed back to servos which control the system pointing. As the accuracy to which image motion can be detected increases, the target image is stabilized on the sensor array to greater degree.

A block diagram of the AEOTR is shown in Figure 32. The AEOTR uses digital techniques and CAI-developed correlation algorithms to measure image shift with accuracies well beyond the basic sensor resolution. Present hardware, both in the lab and in the field, show such measurement with errors less than .02 times the scene resolution. Digital techniques presently being tested indicate potential for significantly improved accuracies.

### 4.4.2 CCD Readout

Because the chosen area CCD's are structured for TV use to be read out in interlaced mode, and because this is undesirable for correlation processing, the clocking has been arranged to add on to the chip the pixels which would normally be interlaced. This is done by shifting the odd rows of scene information into the vertical readout registers, applying one shift pulse to align this information with the even numbered rows, shifting those rows into the readout registers effectively adding the two signals in the registers, and then reading out this information in the normal fashion.

### 4.4.3 Tracking Correlation Description

For tracking, target image shift as a function of time must be determined. To accomplish this, two sequential images are stored in two memories. Subsequent images are alternately stored in each memory so that one memory stores odd numbered images and the other stores even numbered

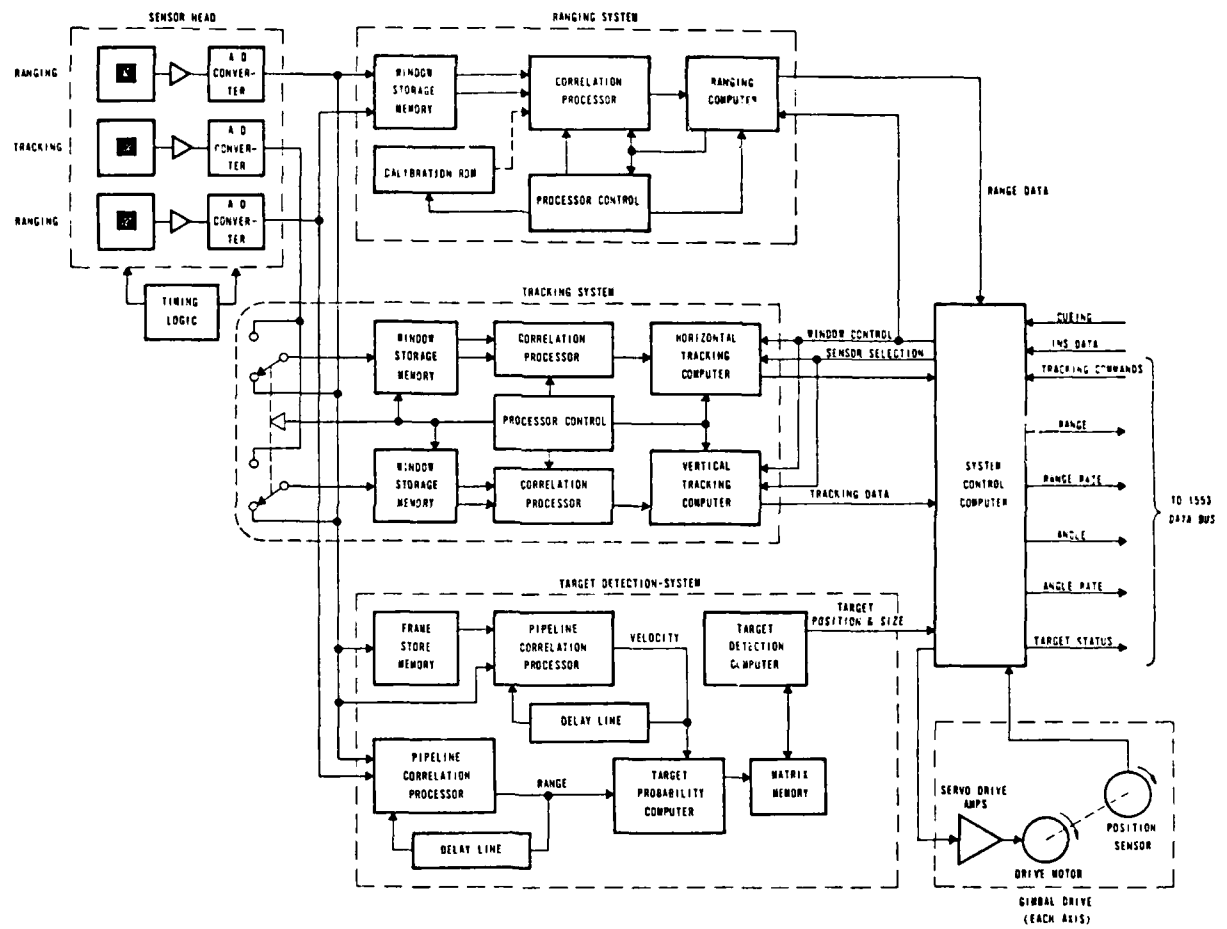


Figure 32 AEOTR Electronic Block Diagram

images. Because no more than a small area of the entire field of view is required for accurate correlation calculation, each memory need only be sufficiently large to store a window plus some boundary. The boundary allows calculating the correlation curve over several shifted positions. Note that the windows are not required to be in fixed positions within the array, but can be dynamically controlled to follow the target image over the format.

Having two sets of data, the hardware computes the correlation function  $[F(s)]$ :

$$F(s) = \int V_1(x) \cdot V_2(x-s) dx$$

where:

$V_1$  and  $V_2$  = two video waveforms

$s$  = relative shift between the two windows

Because the data consists of discrete image samples, the integral is in fact a summation of pixel products over the boundaries of the windows and the correlation function is defined only at integer shifts. Since each sample of the correlation curve at these integer values of  $s$  requires a sum of products, the process is repeated for each shift position. As discussed in Section 2.0, the location of the peak of the correlation curve corresponds to the relative displacement between the two imaged scenes to the nearest pixel.

The fractional part of the displacement is calculated by a formula involving slope measurements of the cross-correlation curve relative to the autocorrelation curve (the correlation of one waveform with a shifted version of itself). This part of the calculation is performed by a micro-processor which also checks the data for conditions which can result in unreliable data and outputs the appropriate error signals. The conditions checked for include insufficient image modulation, displacements exceeding the bounds of the stored image, excessive amplitude differences and abrupt changes in image.

Once the image displacement has been calculated, the result is added to an accumulator which, after a coordinate transformation, provides a drive signal to the gimbal servos in an attempt to reposition the image. If the repositioning is successful, the next correlation calculation, using the second image of the first set and a new image, will produce a result equal in magnitude but opposite in sign to the previous result. This is added to the accumulator which, if the sum is zero, signals that no further drive is required. In this way, even if the image is not immediately repositioned, the servos will be driven until it is accomplished. Alternatively, the window can be moved in the field of view between frames without informing the accumulator in order to bracket the target image within the field of view.

The number of pixels contained in the window is limited at the lower end by the number of samples required for statistically meaningful correlation plus additional width (border) which must be stored to allow enough shifts to account for expected image displacement and to define enough of the correlation curve to allow the fractional pixel displacement calculation. At the high end, both processing speed and the desirability of cropping background image limit both window size and border width. If N is the number of pixels in the window proper and S the number of shifted positions to be calculated, then  $N \times S$  multiplications are required to generate one correlation surface. The allotted time is one integration period. Since the video data must be processed and stored in several levels of hardware, the lower limit on integration period is set by the maximum rate at which pixels can be processed, or by the rate at which they can be read out of the sensor. CCD clock rates are typically 15 MHz maximum, which corresponds to 640 frames/s for CCD 211 in noninterlaced operation. In the GDEM, a  $32 \times 32 = 1024$  word memory is considered adequate, and these can be accessed at 15-MHz rates. The framing rate is then limited either by the sensor clock rate or by adequate focal plane irradiance to generate adequate signal.

In the TDM, several full frame video stores are required. The RAM's for this must have high bit densities in order to limit both power consumption and package size. At present, comfortable access times for

large RAM's are 200 ns to 150 ns (5 to 6.7-MHz word rates). Faster devices with sufficient storage capacities are available only as experimental devices. This limit is expected to be relieved in the near future by a rapidly advancing state of the art for memory devices.

A second limitation of hardware for the target detection function rises from the need to multiply and divide digitally at the pixel rate. Using TTL requires 1  $\mu$ s minimum, but ECL permits operations at 150 ns to 200 ns. A worst case estimate of maximum frame rate for the TDM is then 216 frames/s, corresponding to a 5-MHz pixel processing rate. This second limitation is also expected to be eased by improved device capability in the near future.

Finally, it is noted that window shapes are not limited to rectangles, but can in fact be any closed form. Completely adaptable window shapes would increase complexity by requiring storage and control of the pixel numbers to be used for correlation, but the advantage would be to allow optimum window shaping to crop virtually all background.

#### 4.4.4 Ranging

The ranging correlation is for the most part identical to the tracking function described. The correlation microprocessor has two additional functions to perform. The first is an error checking to ensure that the calculated image displacement is reasonable in terms of physical realities. Secondly, the microprocessor must convert displacement ( $p$ ) to range ( $R$ ) by the reciprocal relationship  $R = C/p$  where  $C$  is a constant (the baseline-focal length product divided by the pixel dimensions). Because accuracy increases with decreasing pixel dimension, the range sensors are oriented to align the minimum pixel dimension (30  $\mu$ m) parallel to the baseline.

A unique aspect of the ranging subsystem is the need to calculate displacement in absolute terms; hence a method of autocalibration is used to provide the base value of displacement corresponding to infinite range. The target range displacement is then the autocalibration displacement subtracted from the measured target image displacement. With the auto-

calibration pattern fixed on one sensor, and because it is inverted in amplitude, it is appropriate to store the pattern for that sensor in a ROM for correlation calculation. To avoid time sharing the autocalibration and target correlations or doubling the required hardware, it is possible to calculate the autocalibration correlation on the ranging hardware and the target ranging correlation on the detection hardware described below. In this case, the target range is tapped before going into the detection mapping hardware, and can be used to drive an image shifter for high accuracy, closed-loop operation.

#### 4.4.5 AEOTR System Control

Having generated the motion vector in the rectilinear coordinates of the sensor array, a separate microprocessor performs the necessary coordinate transformation to drive the cylindrical coordinate system of the gimbal arrangement. Each of the three axes of rotation (roll, pitch and yaw) requires a torque motor and drive amplifier with rate feedback to linearize the slew rate. An angle encoder on each axis is used for LOS angle determination. The encoders are used both in the GDE mode for current LOS angle and in the acquisition mode when external cues for target location are received. For the initial system design, it is assumed that rate information derived from the 13-bit angle encoders will be sufficient for the servo rate feedback. If a detailed design indicates a requirement for tachometers on each axis, the mechanical design will be altered to accommodate them.

The system is controlled by the system control computer which accepts commands from the aircraft interface such as autosearch initiation, cueing and tracking commands. Its outputs include whether or not a target is present in the FOV and if so, it determines range, range rate, LOS angle and angle rate. In addition, the computer interrogates the tracking and ranging microprocessors as to the validity of the data and outputs an assessment to the gun director computer. Finally, the computer applies the appropriate filtering to minimize noise and increase accuracy prior to transmission of the data.

#### 4.4.6 Target Detection

As described to this point, the system will track any scene within its field of view. To provide the system with some level of discriminatory ability, target detection logic should be included. This logic uses only the ranging sensors to produce motion vector and range data for each distinct window of given dimensions in the set of all such windows possible bounded by the array boundaries. Obviously, this is a large number of windows to be processed in the integration period, so a modified version of the correlation hardware is used for extremely high speed operations. In this version, no attempt to locate the peak is made and only the fractional pixel calculation is implemented, but in a pipeline algorithm. By this method, correlation results for each window are output at rates determined by the pixel clocking and thus limited by the single multiplication required for each pixel. The limitation of less than 1 pixel displacement accounts for ranges from infinity to 1763 ft and angular rates up to .059 rad/s.

The correlation data is combined with brightness, as described in Subsection 3.4, to produce a video-like signal, the amplitude of which is related to the uniqueness of range, motion and/or brightness in that portion of the field of view, and hence the likelihood that a target is imaged at that location. The signal is scanned by a microprocessor which determines the probable presence of a target. If a target is suspected, its size, shape and centroid are outputted and the system computer generates commands to initiate acquisition and tracking, and a window is defined. If the normal correlation tracking should fail for any reason, the computer issues commands to the detection logic to reacquire or track on its own.

Because of pipelining, the detection logic is relatively small at about  $0.5 \text{ ft}^3$  and weighs approximately 20 lb. On the other hand, the high speed operation requiring multiplications in 200 ns leads to relatively high power consumption on the order of 25 to 30 W. There is, however, no reason these electronics need to be incorporated inside the AEOTR pod.

#### 4.4.7 Areas of Development Effort

Most of the major functions in the AEOTR are well understood and represent the result of extensive laboratory and field testing. The video processing and correlation tracking functions are in this category. The ranging function has been tested extensively using the laboratory demonstration hardware which was constructed principally to demonstrate ranging, rather than tracking, the latter serving only to provide a ranging target. Field testing of this hardware has been more limited, but is very encouraging. The servo techniques which will be required for the AEOTR are well understood, and CAI has extensive background experience in servo system design. Here the pixel data must be added, subtracted, multiplied and divided at the pixel rate at the CCD clock rate. The division is the major problem, for even at a pixel period of 200 ns, the operation is difficult. Higher rates, while feasible, increase power consumption and package size considerably. As for the memories, the speed is not limited by unavailability of suitable hardware, but by its present configuration.

Because correlation is a statistical measure, accuracy increases with the number of points sampled. Experience has shown that at least 30, but more comfortably 100, pixels should be used for accurate results. Allowing for up to 3 pixels of image displacement, a border width of at least 4 pixels is required. The extra width permits checking that a peak has been located and permits calculating slope on the far side of the curve. Hence, storage for at least 324 pixels is needed for a square 10 x 10 window and more for rectangular windows of the same area. With a 4-pixel border, displacements up to 3-1/2 pixels can actually be calculated. Dividing by the focal length and integration time shows that angular rates of .446 rad/s relative to the LOS can be tracked, while the minimum rate is limited by the correlation accuracy to 2.55 mrad/s, the noise limit of the LOS angle rate.

The major uncertainty presented by the AEOTR is the application of microprocessor techniques for overall system control. Basically, a microprocessor controls the collection and disbursement of information. A principal effort will be involved in developing the software for this control

operation. A significant effort will be associated with the coordinate conversions. Finally, the implementation of the target detection function will require a substantial software effort.

From a hardware standpoint, the optional target detection subsystem will be the most complex. Although the algorithms for both the ranging and tracking have been previously tested, the high speed pipeline architecture will involve extra design effort. In all these circuits, the mathematical operations must be performed at the basic pixel clock rate. Of greatest concern will be the need to compute arithmetic divisions at this high speed, and divider circuits with speeds of around 200 ns will need to be designed. Considerable detailed effort will be required to implement this subsystem.

#### 4.4.7.1 Technology Impact

As previously discussed, growing memory and processing device technologies should permit the reduction of the ultimate volume and power requirements for the video memories and correlation processing operations, as well as increasing the operational rates. This would have direct impact on the AEOTR.

#### 4.4.8 Weight and Volume Estimates

The electronics hardware for the basic AEOTR (GDEM) is estimated to require about 1 ft<sup>3</sup>. The additional hardware for TDM requires 0.5 ft<sup>3</sup>. The hardware is distributed as follows:

<u>Hardware</u>	<u>Volume</u>	<u>Weight</u>	<u>Power</u>	<u>Location</u>
GDEM	0.5 ft <sup>3</sup>	16 lb	30 W	Pod
GDEM	0.5 ft <sup>3</sup>	28 lb	20 W	Remote
TDM	0.5 ft <sup>3</sup>	20 lb	30 W	Remote

## SECTION 5.0

### CAI DEMONSTRATION HARDWARE

The area correlation processing techniques upon which the AEOTR is based are the result of CAI internally-funded research and development efforts. Software and hardware implementations have been useful in demonstrating and testing various aspects of correlation processing. The Laboratory Demonstration Unit (LDU), shown in Figure 33, has been used on the AEOTR study to verify the applicability of these techniques to passive stereometric ranging and to identify problem areas, sensitivities and limits of the methods involved. The LDU was built primarily to demonstrate ranging, with the simplest tracking capability provided only to establish a target for the rangefinder.

#### 5.1 DESCRIPTION

The LDU consists of a pair of parallel, identical video channels mounted on a servo-controlled, two-axis gimballed platform. Video from CCD image detectors is processed according to the correlation algorithm to determine the image misregistration and consequently range. The video from one channel is also used to determine image displacement between successive frames in providing a tracking error signal to the servo drive amplifier chain.

Principal mechanical features of the LDU are summarized in Table 11. The lenses, 100-mm fl, f/2.8 telephoto lenses designed for 25-mm photography are spaced a distance of three inches, yielding a rangefinder  $B_f$  product of  $11.81 \text{ in}^2$ . The image detectors, Fairchild CCD 202's, and their proximate clocking and preamp circuitry are mounted to the same optical baseplate as the lenses. Micropositioning capability in three axes permits precise and stable CCD alignment flexibility. The optical baseplate is gimballed in two axes to permit x-y target tracking. A resolver and tachometer on each axis provide position and rate feedback information to



Figure 33 Demonstration E-O Tracker/Ranger

the servo drive amplifiers which are mounted on the frame of the LDU. The LDU is constructed of heavy aluminum fixture plate to provide the high stiffness and mass appropriate for the isolation of external disturbances from the genuinely inherent characteristics of area correlation processing.

The CCD 202 image detector is a 100 x 100 array of detector elements with 30- $\mu$ m vertical and 40- $\mu$ m horizontal center spacings. The device is operated in a noninterlaced mode with horizontal pixel doubling, resulting in effective pixel dimensions of 60  $\mu$ m vertically by 80  $\mu$ m horizontally, the 80- $\mu$ m dimension being parallel to the rangefinder baseline. After preamplification, the analog video is digitized (8 bits), and all subsequent processing is digital. The digital processing hardware is contained on eight externally-mounted, wire-wrapped circuit boards accompanied by power supplies. The system has been tested at rates of up to 666 frames/s and is capable of operation at 1000 frames/s.

An outboard control box permits the manual cuing of the field of view for target acquisition and the selection of mode (lock, slew or track). Sensor video is displayed on an oscilloscope.

Each axis of the tracking system is basically in a rate loop with position sensing (correlation). The responses of the rate loops are given in Table 11. The limiting frequency for the total loop is the correlation processing Nyquist frequency, where the loop phase shift is 180°.

## 5.2 PERFORMANCE

Early testing of the LDU with real-world targets revealed two principal problems relating to ranging performance. The image misregistration output was very noisy and appeared to depend on both the target and the range. The inverse dependence upon range could not be verified. Testing using a collimator (73.3-inch fl, 4.9-inch aperture) with targets of controlled size and content established that the computed image offset was nearly a double-valued function when the actual offset was near a half-integer (half-pixel) value as shown in Figure 34. There was also evidence of scene dependence on the response.

TABLE 11  
LABORATORY DEMONSTRATION UNIT

Lenses	100-mm nominal focal length f/2.8 aperture focal length difference 0.32%
Baseline	3 inches
Bf	11.811 in <sup>2</sup>
Sensor	Fairchild CCD 202
Sensor format	100 x 100
Pixel size	30 $\mu\text{m}$ vertically x 40 $\mu\text{m}$ horizontally
Pixel size as operated	60 $\mu\text{m}$ x 80 $\mu\text{m}$
Pixel size for ranging	80 $\mu\text{m}$
Limiting precision for ranging (real targets)	1/80 pixel = 1.0 $\mu\text{m}$
Tracking	
Horizontal response	3 dB down @ 30 Hz, phase shift 56° 10 dB down @ 100 Hz, phase shift 106° 10 dB resonance @ 63 Hz
Horizontal acceleration	16.3 rad/s <sup>2</sup> maximum
Vertical response	Flat to 100 Hz with no phase shift resonance at 170 Hz
Vertical acceleration	57.1 rad/s <sup>2</sup> maximum
Size	15 x 20 x 9 inches (H x W x D)
Weight	50 lb

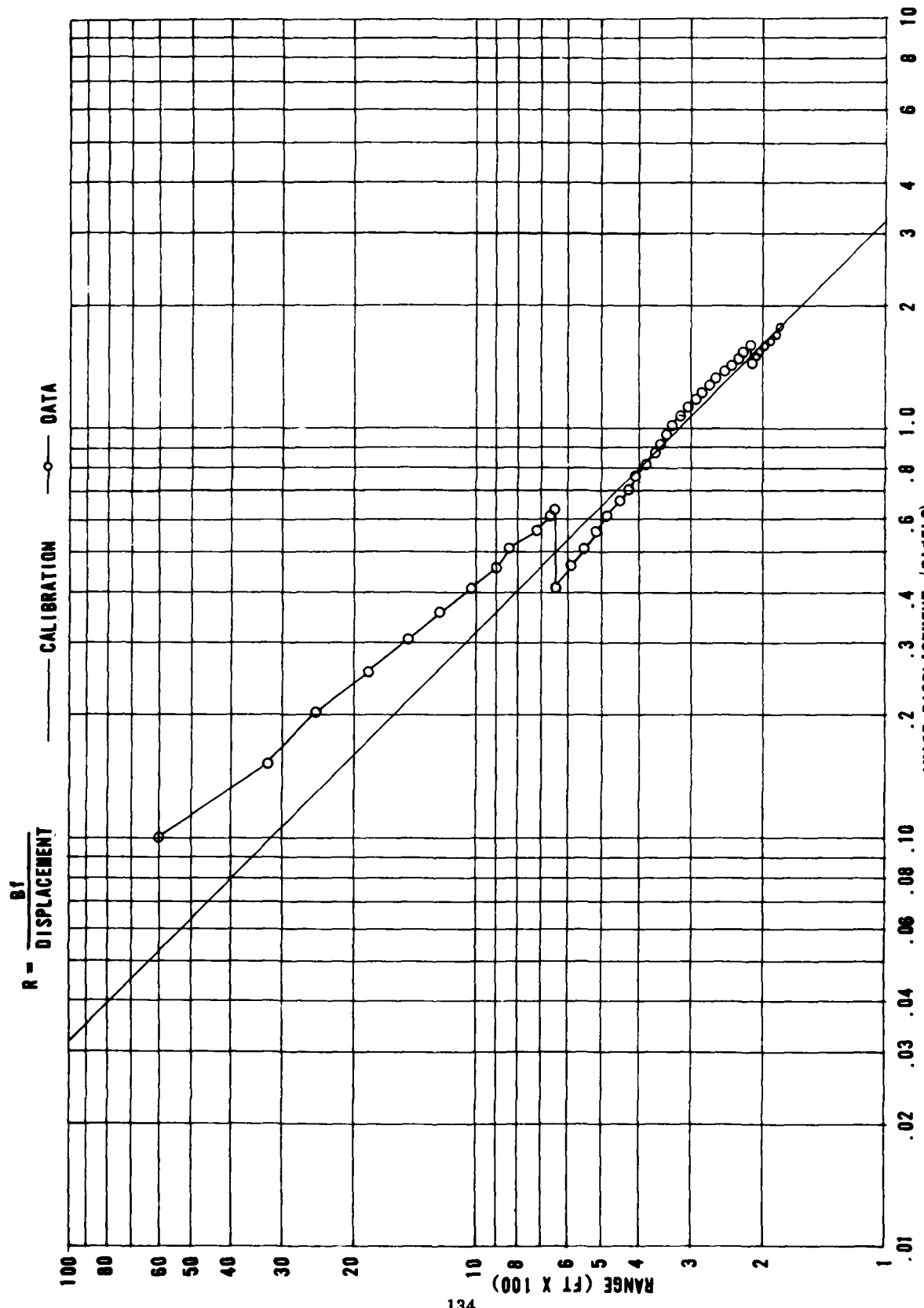


Figure 34 LDU Response to Real World Film Target

The jump in apparent offset at half-integers was found to be due to the use of points too widely separated on the correlation curve in the calculation of the misregistration. The hardware was modified to use adjacent points in computing image offset. The resultant elimination of the half-integer discontinuity is shown in Figure 35 where sine wave targets of increasing spatial frequency were used. While this computation of the misregistration eliminated the instability of half-pixel offsets, it was limited by the hardware to offsets of less than 1 pixel. The extension of the offset range to more than 1 pixel required little additional hardware for a peak search routine, but it was not implemented in the interest of investigating the more significant features revealed in Figure 35.

The spatial frequency dependence of the correlator response was verified at additional spatial frequencies. The effect was consistent with the observation that circular portions of film targets exhibited anomalous range versus displacement slopes when rotated in the target holder by small amounts, thus changing the horizontal spatial frequency, but not the basic scene content presented to the LDU. As discussed in Appendix F, modeling of correlation processing predicts such sensitivity to frequency as resulting from the correlation of high frequency components of the target image.

No appropriate spatial filters were available to optically filter real-world scenes, but an RC filter on the analog video produced no significant change in frequency dependence. This negligible effect with a filter with such slow rolloff supports the conclusion of the modeling study that a sharp cut-off filter is desirable.

The failure of the data to coincide with the calibration curve, even with very low frequency targets, was not fully explained. Several effects could be responsible for such a result, but the key effect was never isolated. One such cause would be a small dc offset in the value of the image displacement which would only be significant at small displacements. While the LDU lenses were purchased as matched, a careful measurement of the lens focal lengths late in the program established a difference in focal length of 0.32

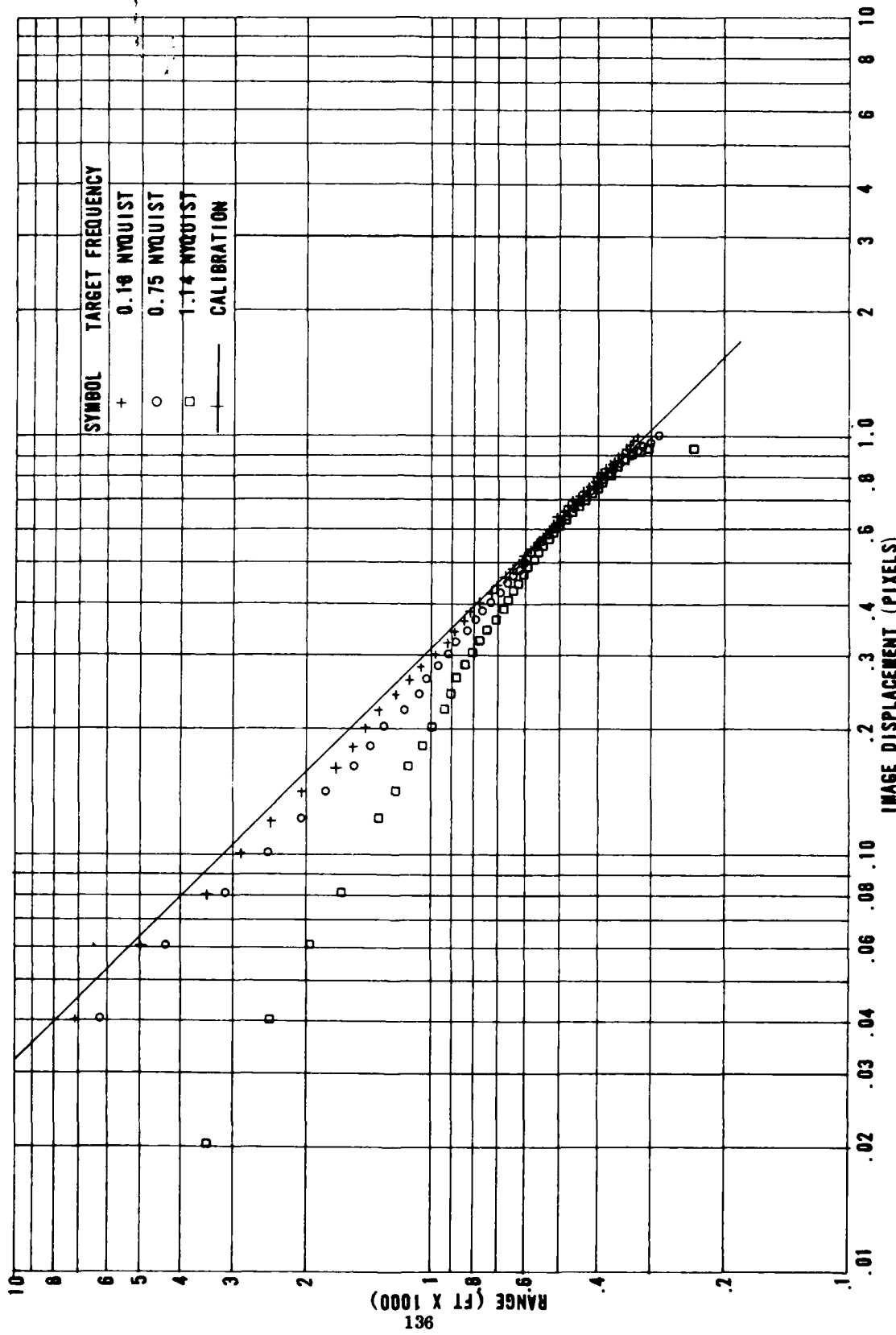


Figure 35 LDU Response to Sine Wave Targets

percent which may be significant, since focal length scale errors translate directly into range error. Also, a marked difference in lens quality, particularly astigmatism, made it difficult to match images feature for feature, and this may have contributed to the residual error.

For fixed real targets, it was possible to obtain very repeatable and linear range data of the quality shown in Figure 36. The key factor in this was the matching of the signal levels for the two video channels. The fact that such data can be repeatable is the basis for the autocalibration function proposed for the AEOTR. For the autocalibration function, the reference pattern can be memorized and recalled at an appropriate scale for the auto-correlation computation. Either the amplitude of the recalled reference image may be adjusted or the signal level of the projected image may be regulated to permit normalization. The method is expected to exhibit the same repeatability as seen here for both real and sinusoidal targets.

#### 5.2.1 Static Correlation Accuracy

Testing of the LDU performance using real-world film targets on the collimator also permitted the estimation of the limiting accuracy for correlation processing using the fully digital hardware. A large number of measurements were made of image offset using random target orientations and image offsets between 0.02 and 0.9 pixel. The standard deviation of the error in target position for 930 measurements was 0.0127 pixel or 1/79 pixel. This represents the limiting precision for determining the lower curve in Figure 36.

The corresponding precision for a low frequency target (0.18 Nyquist) is the precision with which the position of an autocalibration target image can be determined. For a set of 330 measurements, this was found to be 0.004 pixel.

The rms sum for these uncorrelated errors is 0.0133 pixel (1/75 pixel) which represents the limiting accuracy for the ranging system.

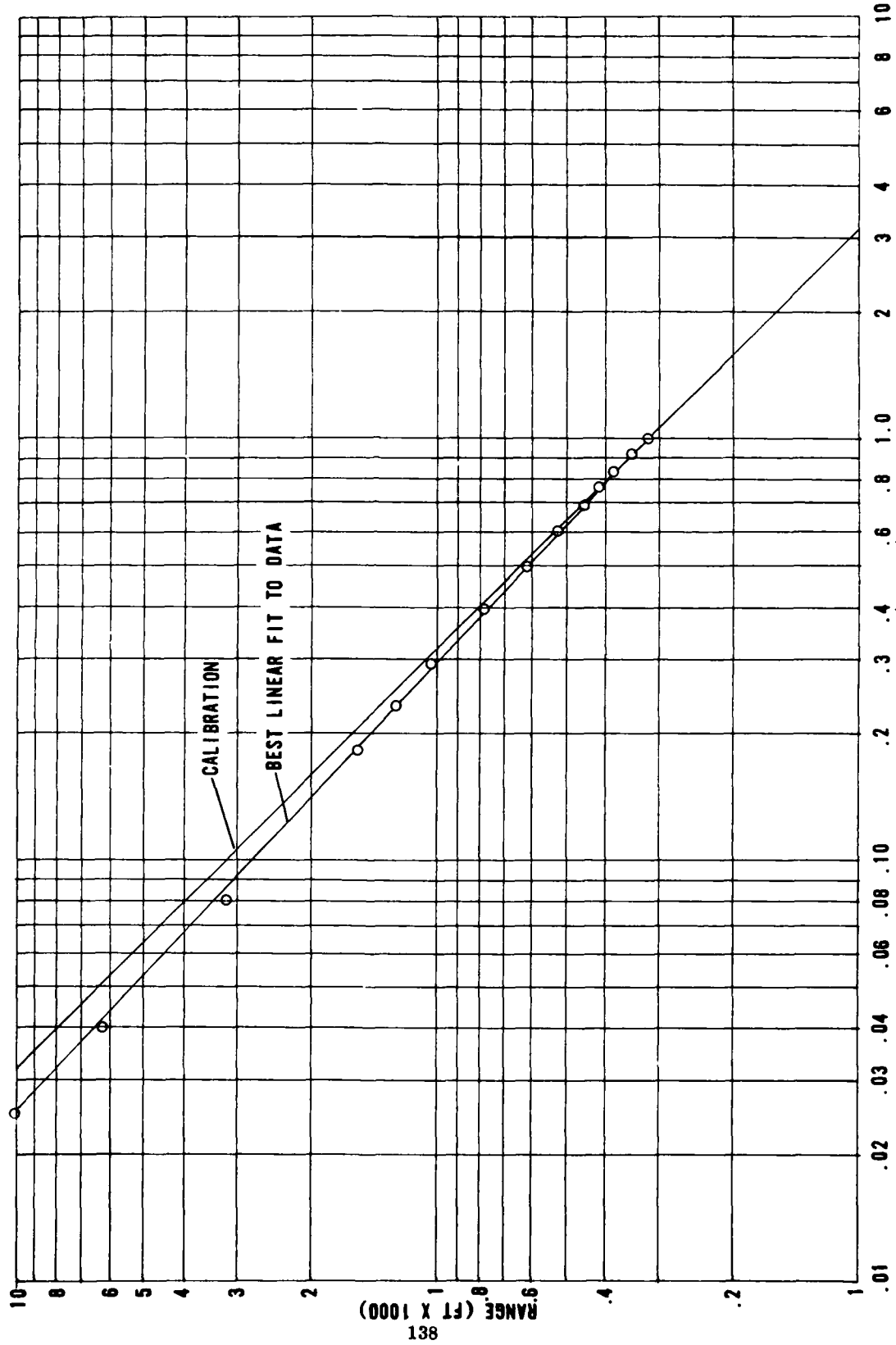


Figure 36 CAI Demonstrator Image Displacement vs Apparent Range

### 5.2.2 Closed-Loop Ranging

The basis for closed-loop ranging as discussed in Section 3.0 lies in the coincidence of the detected range curve with some part of the calibration curve for a variety of scenes, as shown in Figure 35 near  $P = 0.75$  pixel. This pattern holds true for real scenes, as well as the sinusoids used in the figure. In practice, a target image would be displaced until the offset reached a reference value, such as 0.75 pixel. The autocalibration reference image would then be used to measure how far the target pattern had been displaced to reach its nominal offset. Since the autocalibration pattern is unchanging and follows a known curve, the range can be computed with high precision.

### 5.2.3 Ranging and Tracking Performance

The completion of the LDU, and the isolation of the effects described above, required much of the duration of the study program. Late in the program, however, tracking and ranging on real targets were demonstrated.

The tracking capability designed into the LDU was kept at a minimum to permit the cost-effective implementation of the more sophisticated and technically significant ranging function. The tracker is based on error detection derived from the cross correlation of successive video subframes. As a result, the tracker is highly scene adaptive and accepts targets of low, high or changing contrast with similar facility.

The servo system contains no velocity memory or other intelligence and tends to breaklock with high contrast foreground clutter. Background clutter, however, whether of low or even high contrast, does not cause loss of lock unless the target contrast integrated over the tracking window is small compared to the integrated clutter contrast. The tracking function as proposed for the AEOTR includes an adaptive windowing feature to further reduce clutter-induced breaklock. For air-to-air tracking, foreground clutter is almost nonexistent and tracking against background is the essential consideration. The tracker was tested on vehicle targets with high and low background clutter and worked very successfully. Tracking of airborne

targets was not tested, although attempts to lock onto clouds of moderate contrast were unsuccessful. This would suggest that, as a minimum, tracking of targets against cloud backgrounds should not be a problem. Tracking against high contrast background clutter could be difficult only if no effort were made to improve tracking performance above the present level.

The ranging function of the LDU was demonstrated, although on a more restricted scale than the tracking function because of test range limitations. Because the hardware was configured for ranging with image shifts of less than 1 pixel, the minimum range for the LDU was about 300 ft (see Figure 34). The only immediately available test range was the CAI camera target range which has a camera station located on the second floor of the CAI manufacturing facility overlooking a 1300-ft test range. The usable portion of the range for continuous target tracking extends from 500 to 1300 ft. Tracking and ranging of a vehicle moving along this range was demonstrated with an accuracy of about 10 percent. While the  $R^2$  dependence of accuracy on range could not be verified because of insufficient filtering of the image shift output, the practical feasibility of stereometric ranging using area correlation processing was proven.

### 5.3 SUMMARY

The LDU has been used to demonstrate the practical feasibility of the approach taken for the AEOTR. The LDU has demonstrated the application of correlation processing to target tracking and passive ranging. In addition to being instrumental in identifying an incorrect image offset estimation method and an undesirable sensitivity of correlation processing to high spatial frequencies, the LDU permitted the discovery of means to circumvent the latter sensitivity through closed-loop ranging. Also, the measurement of correlation processing accuracy using the all-digital LDU hardware permits a projection of accuracy for the AEOTR. It is believed that the further development of the AEOTR is justified because of the positive results of the LDU.

## SECTION 3.0

### SUMMARY ERROR ANALYSIS

#### 6.1 INTRODUCTION

A system level error analysis for the AEOTR is presented, along with an identification of where improvements in state-of-the-art component performance can significantly impact the overall performance level of the AEOTR.

#### 6.2 TRACKER ERRORS

##### 6.2.1 LOS Angle

The possible major error sources for the determination of LOS angle are:

- Angle encoder
- Window
- Fold mirrors
- Lens/CCD alignment
- Target image position detection
- Tracker-to-aircraft boresight integrity

Because gimbal redundancy is required to assure smooth tracking through all engagement geometries, two encoders must be addressed to obtain an angle on one axis. Each encoder produces  $2^{13}$  bits per revolution giving a possible error of  $\pm 1/2 \frac{2}{2^{13}} = 0.38$  mrad each. The error distribution is uniform, so the rms error is 0.19 mrad.

As discussed in Section 3.0, the window is designed to have negligible effect. Even for wide temperature excursions, the tracking errors are estimated to be very small.

The folding mirrors in the tracking channel are mounted together in a thermally-coupled ULE material package, and mirror misalignment is negligible for the expected temperature excursions and gradients.

The lens/sensor package misalignment is conservatively estimated at  $\pm 0.05$  mrad. This misalignment should be essentially systematic when it occurs, resulting primarily from in-flight mechanical shock. The distribution should be approximately uniform, and the rms error is approximately one-half of the peak value.

The target center, with the detection logic described in Subsection 3.4, can be determined to within  $\pm 1/2$  pixel. Using the larger pixel dimension of  $.36 \mu\text{m}$ , this corresponds to an angular error of  $\pm 0.354$  mrad. Again, a uniform distribution gives a  $0.177$  mrad rms error.

The AEOTR-to-aircraft boresight accuracy is sensitively dependent upon details of AEOTR design, mounting technique and mounting location. Since this error reflects an installation factor and not the basic tracking capability of the AEOTR, no value is assigned for this error, and it must be included later.

The errors combine as follows:

Angle encoders	$0.192 \sqrt{2}$	=	0.272 mrad
Lens/CCD			0.025 mrad
Target center			<u>0.177 mrad</u>
rms total LOS error			0.325 mrad

### 6.2.2 LOS Angle Rate

The error sources for determination of LOS angle rate are fewer than for LOS angle since the measurements are differential and systematic errors are canceled. Further, dynamic errors are eliminated by differential measurements if their rates of change are slow compared to the sampling rate. Because of this, the lens/CCD alignment error is canceled, and all low frequency AEOTR/aircraft boresight errors are canceled. The angle encoders must be read twice, however, and this error is increased.

The image position determination is replaced by the error in a single successive-frame cross correlation calculation. This correlation error has an rms value of 0.02 pixel with a corresponding angular error of 0.014 mrad.

The LOS angle rate errors combine as:

Angle encoders	0.192	$\sqrt{4}$	0.384 mrad
Target position			<u>0.014 mrad</u>
rms total			0.384 mrad

The angle rate error is then  $0.384 \text{ mrad}/t_o$  where  $t_o$  is output period. Thus, with a 10-Hz output rate, the LOS angle rate error is 3.84 mrad/s, well within the tolerance goal.

### 6.3 RANGE ERRORS

#### 6.3.1 Range

Using closed-loop ranging with autocalibration as described in Sub-section 3.1, range accuracy is limited primarily by the ability of the system to register two images of the target and the correlation calculation of the autocalibration signal.

Measurements on the demonstration hardware showed an rms error in registration of 0.0127 pixel for a real-world scene and an autocalibration error of 0.0040 pixel using a low spatial frequency target to model the low frequency autocalibration pattern. The rms sum of these errors is 0.0133 pixel or 1/75 pixel. For the AEOTR described in Section 4.0, the pixel pitch is 30  $\mu\text{m}$ , and the  $Bf$  product is  $25 \text{ in}^2$ . The resultant range error at 4000 ft is 121 ft.

The increase of this number over the design goal of a 50-ft range error at 4000 ft is attributed to two factors:

- The registration accuracy of 1/140 pixel projected to apply to this system was based solely on correlation noise, rather than the more difficult problem of high frequency scene information dealt with here.
- Present hardware realizations of correlation processing require a noninterlaced sensor readout so that the resultant minimal pixel pitch is 30  $\mu\text{m}$ , rather than 18  $\mu\text{m}$ .

Note that the measurement of the 1/75 pixel error may itself be pessimistic because of a scale/focal length difference of 0.32 percent between the two lenses.

### 6.3.2 Reduction of Range Error

For the further development of the AEOTR, several factors can be expected to effect the reduction of the range error to 50 ft. Some of these are existing technology, and some are nearly existing technology.

First, improved sensor resolution is now available, and further improvements in the near future are envisioned. Area array CCD's with 25 x 25- $\mu\text{m}$  pixels and no dead spaces are now in production (Hughes Aircraft Company, Industrial Products Division), and interest has been expressed in development of devices with 15 to 17- $\mu\text{m}$  pixels. For the ranger application, the sensor need not be a single large area array, but can be assembled from smaller arrays operated at lower rates and with parallel processing. Possible formats have been discussed. The use of this kind of sensor technology would improve ranging accuracy for three reasons:

- The absence of interline charge transfer registers reduces a correlation processing error because all parts of the image are detected, reducing the spatial frequency-related correlation errors.

- The increased detection area affords a higher responsivity resulting in a higher signal.
- The pixel size is reduced, improving the ranger scale factor ( $Bf/pitch$ ) and increasing the sensor Nyquist frequency, which should further reduce image frequency-related error.

A second improvement factor is that two possibly significant error sources in the LDU will be reduced in the A EOTR. Well-matched lenses will be used resulting in reduced scene dependent error about zero misregistration in closed-loop operation; and autocalibration error will be reduced because the noise for this function comes from only one channel instead of two. Further, because the autocalibration signal is of a known low frequency, filtering for this function can be optimized prior to correlation.

A third improvement area relates to spatial scene filtering and/or temporal data filtering which can further reduce the scene-dependent error. It may be that introducing a deliberate dither to both images simultaneously will translate the scene dependent error to a temporal data error, which can be dealt with by latter filtering which eliminates any need for scene filtering.

Finally, an alternate version of the processing algorithm could exhibit reduced error about zero (or integer) misregistration.

CAI is confident that by using one or more of these methods, the required accuracy of a 50-ft error at a 4000-ft range can be met or even exceeded.

#### 6.3.3 Range Rate

The measurement of range rate is accomplished by calculating the difference of two range measurements divided by the time interval between measurements. Using a 50-ft range error, the range rate error is  $50\sqrt{2/t_0}$ . Clearly, the required accuracy of 50 ft/s at a 4000-ft range can only be achieved by excessively slow output rate or by substantially exceeding the range accuracy.

## APPENDIX A THERMAL ENVIRONMENT OF THE AEOTR

The prediction of the thermal environment for any piece of hardware attached to a supersonic aircraft is a very difficult, if not impossible, task. Even for simple shapes in isolation, aerodynamic and thermal analyses are so sensitive to details of shape and airflow that complete knowledge of a system can never be expected. Rough estimates of bounds based upon a subjective mixture of theory, empirical results and experience can be used to indicate trends to help identify major problem areas. Additional analysis using the results of wind tunnel and flight tests is generally required to adequately characterize flightworthy hardware.

The estimation of the thermal environment of the AEOTR will be made using a simple model to predict the upper limit of temperature excursions and steady-state temperature differentials. In this model, the front of the tracker head is taken to be a hemisphere with its axis parallel to the line of flight. The temperature profile is assumed to fall from stagnation ( $T_s$ ) at the front to 90 percent of stagnation at the sides with a cosine dependence according to:

$$T(\theta) = T_A + (T_s - T_A) \left[ \eta + (1 - \eta) \cos \theta \right] \quad (1)$$

where:

$T_s$  = stagnation temperature

$T_A$  = ambient temperature

$\eta$  = stagnation fraction at the side ( $\theta = 90^\circ$ )

= 0.90

The figure of 90 percent is based on a best estimate for this configuration by experienced aerodynamicists.

The stagnation temperature is estimated from the free stream stagnation temperature:<sup>(\*)</sup>

$$T_s/T_A \approx 1 + 0.2 M^2 \quad (2)$$

where:

M = Mach number

The stagnation temperature for two limiting airspeeds, 600 ft/s and 1500 ft/s as a function of altitude is shown in Figure A.1 for a NACA standard day, a standard polar day and a standard tropical day. Also shown is the ambient temperature for the NACA standard day. It is evident that the differential  $T_s - T_A$  is strong function of airspeed (mach number) and a much weaker function of ambient temperature, in accordance with equation 2. Over the full range of flight parameters, temperature excursions on the order of 300 F° (170 C°) can be expected. As a minimum, the AEOTR design must anticipate these extreme excursions with provision for mechanical stability and heat removal.

Figure A.2 shows the difference between stagnation and ambient temperatures as a function of airspeed between 500 and 1500 ft/s. The curve applies for altitudes up to 50,000 ft and for the NACA standard day. The corresponding curves for the standard polar and tropical days lie within 5 percent of the curve shown. It is evident from equation 2 and from the figures that the tracker head temperature increase over ambient is primarily determined by airspeed, and that the system (skin) temperature parallels ambient temperature with altitude, the offset being determined by airspeed.

In addition to tolerance of the high skin temperatures of the AEOTR, the design must allow for temperature gradients that result from steady-state operation and from transient conditions. With equation 1, estimates of temperature gradients over the head under steady-state conditions were made

(\*) Reconnaissance and Surveillance Window Design Handbook, AFAL-TR-75-200, page 3-47 (WPAFB, Ohio) 1975

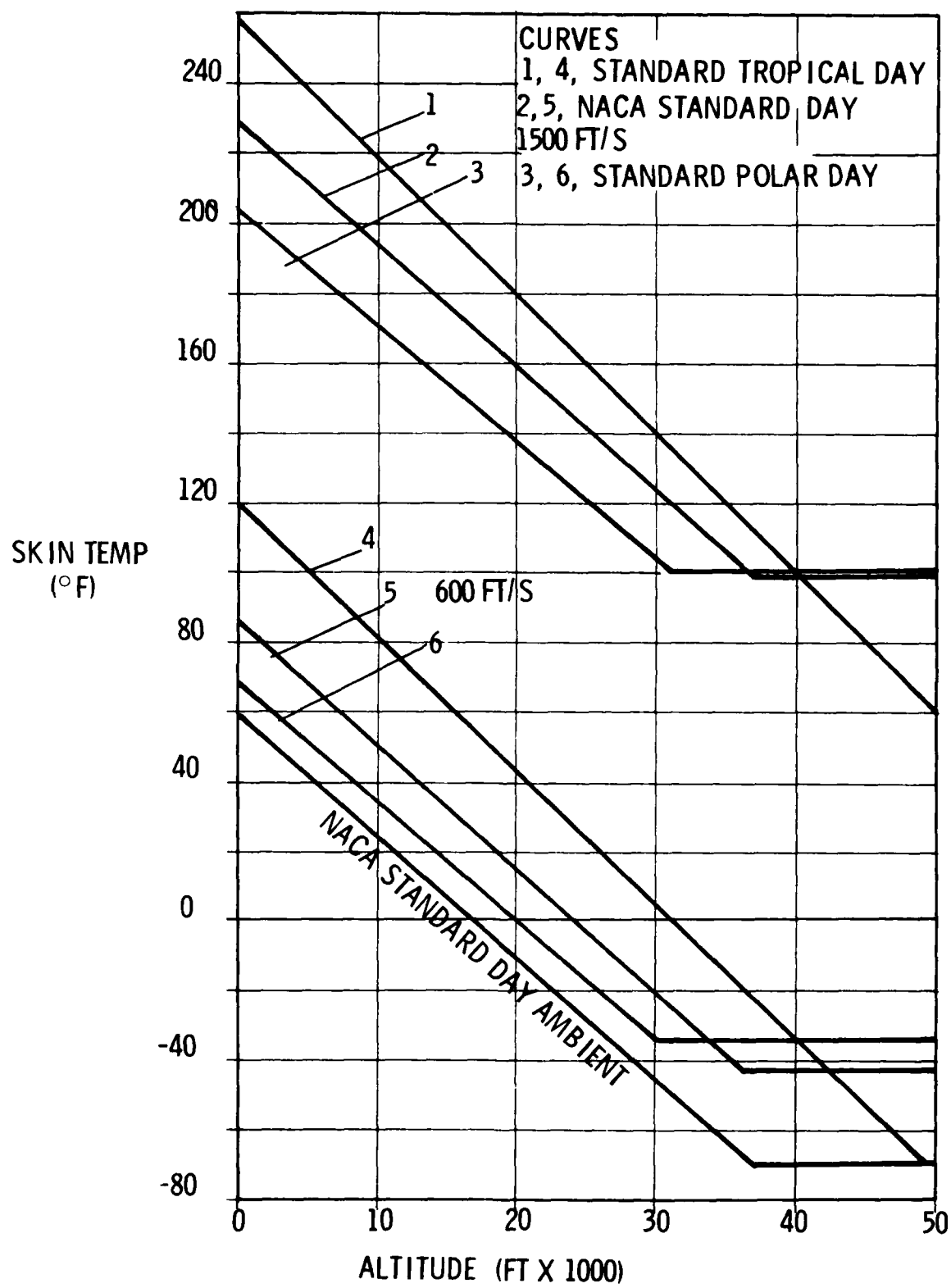


Figure A.1 Stagnation Temperature vs Altitude

$$\begin{aligned}\Delta T &= T_{\text{STAGNATION}} - T_{\text{AMBIENT}} \\ &= T_1 - T_{\text{AMBIENT}} \\ T_A &\text{ FOR NACA STANDARD DAY}\end{aligned}$$

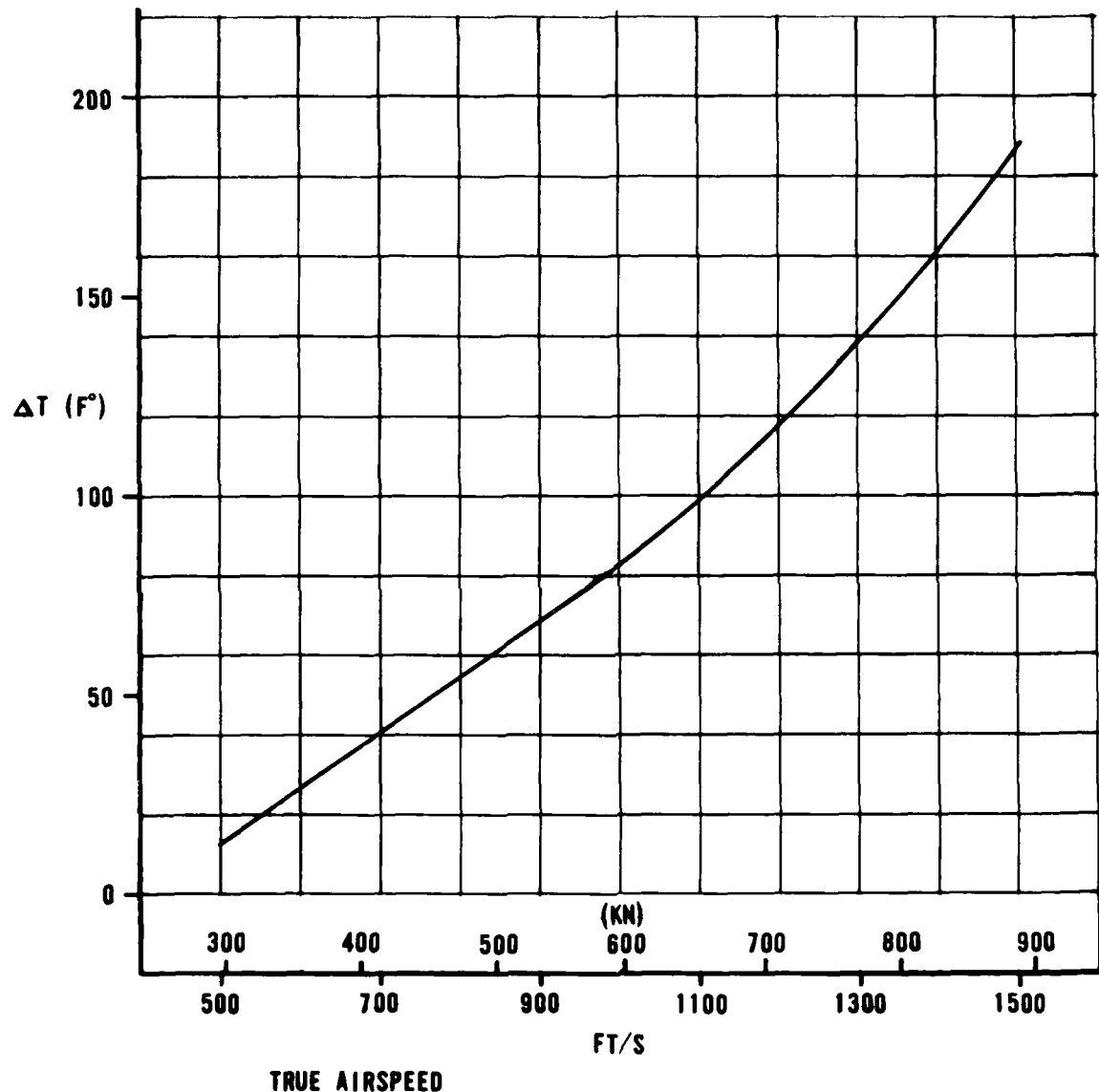
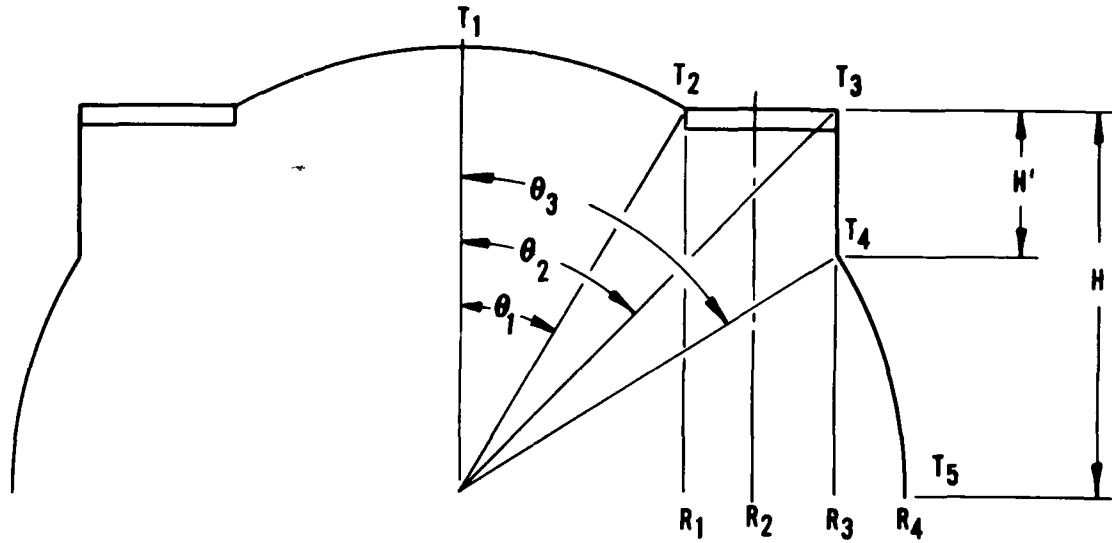


Figure A.2 Temperature Increase Over Ambient

using the angles shown in Figure A.3 for a 4-inch baseline, 6-inch head diameter system. The temperatures at the indicated positions over the head were calculated for the extremes of stagnation temperature and altitude of Figure A.1. These are summarized in Table A-1. For all cases with normal incidence windows, the temperature differential across the window ( $T_2 - T_3$ ) is 4°F or less. In practice, the temperature gradient at the outer edge of the window will likely be significantly greater owing to the abrupt change in surface contour at that point. With slanted windows which are approximately tangent to the sphere and have the same effective aperture ( $R_3 - R_2$ ), temperature differentials ( $T_2 - T_4$ ) are 6°F or less.

In this model of the tracker head, the steady-state temperature gradients over the head are quite small compared to the excursions to be expected under the conditions of rapid changes in flight altitude and speed characteristic of air-to-air gun battle. It is therefore likely that the primary thermal design problems of the tracker head are the temporal transients, rather than spatial gradients. The tracker head design must include provision for some type of temperature stabilization in order to maintain operational capability, as well as stereometric fidelity, over the full operational environment.



6 HEAD INCH DIAMETER		8 HEAD INCH DIAMETER
Bf	20 IN <sup>2</sup>	25 IN <sup>2</sup>
$R_1$ (INCHES)	1.375	1.875
$R_2$ (INCHES)	2.90	2.50
$R_3$ (INCHES)	2.625	3.125
$R_4$ (INCHES)	3.00	4.00
$\theta_1$	27.28	27.95
$\theta_2$	44.55	41.52
$\theta_3$	61.05	51.38

Figure A.3 AEOTR Head Thermal Model Geometry

TABLE A-1  
HEAD TEMPERATURE ESTIMATES

$$T(\theta) = T_A + (T_S - T_A) (0.9 + 0.1 \cos \theta)$$

Speed (ft/s)	Day	Alt (Ft x 1000)	T <sub>1</sub>	T <sub>2</sub>	T <sub>3</sub>	T <sub>4</sub>	T <sub>5</sub>	Δ <sub>1</sub>	Δ <sub>2</sub>
			degrees Fahrenheit						
600	NACA	0	89	89	88	88	86	1	1
		50	-40	-40	-41	-41	-43	1	1
	Polar	0	71	71	70	70	68	1	1
		50	-31	-31	-32	-32	-34	1	1
	Tropical	0	122	122	121	121	119	1	1
		50	-69	-69	-70	-70	-72	1	1
1500	NACA	0	245	243	240	237	226	3	6
		50	117	115	112	109	98	3	6
	Polar	0	222	220	217	214	204	3	6
		50	129	127	124	121	110	3	6
	Tropical	0	288	286	282	280	268	4	6
		50	77	75	72	70	60	3	5

Temperatures for 6-inch diameter head

$$\Delta_1 = T_2 - T_3$$

$$\Delta_2 = T_2 - T_4$$

## APPENDIX B

### AEOTR WINDOW CONSIDERATIONS

As an airborne instrument mounted externally to a high performance fighter aircraft, the AEOTR must not only survive, but function acceptably under extremes of temperature, pressure, turbulence and vibration. The tracker must look at the world through a boundary layer whose effects are not well defined and depend upon aerodynamic design, flight parameters and meteorological conditions. While no one of these areas can be completely described and the effects precisely determined, it is desired to take the approach of minimizing sensitivity to each effect without adversely degrading system performance or integration potential.

With temperature excursions on the order of 250° F, airspeeds of Mach 0.5 to 1.5, and flight altitudes of up to 50,000 ft, the thermal and pressure environments of the AEOTR are severe. Assurance of acceptable performance under these conditions requires careful design attention to the AEOTR windows as the first element in the optical train. Several temperature and pressure effects impact window design, each of which is capable of using the entire rangefinder error budget if ignored. The most important of these effects are the air wedge associated with slanted windows, refractive effects associated with temperature gradients across and along the optical path, and lensing effects resulting from pressure differences across the windows. Following a review of the system error budgets, the magnitudes of these effects are derived, and their implications are discussed.

#### OPTICAL ERROR BUDGET

The criterion for optical stability is derived from the allowable system range error of  $\pm 50$  ft at a 4000-ft range. For a stereometric range-finding system with a baseline  $B$ , focal length  $f$  and image misregistration

accuracy  $\Delta P$ , the required stereometric pointing accuracy is:

$$\delta = \frac{\Delta P}{f}$$
$$= B \frac{\Delta R}{R^2}$$

where:

$R$  = specific range

$\Delta R$  = range error

The error budget for a rangefinder with a 5-inch baseline,  $B$ , is then  $\delta = 1.3 \times 10^{-6}$  rad. The effects which can give rise to an error of this magnitude are considered below. With  $1.3 \mu$  rad as the system error budget, all effects which can contribute significantly to this small number either must be known and controlled or must be amenable to detection and compensation by active means, either mechanical or electronic.

#### WINDOW BOWING

Each of the rangefinder windows is asymmetrical in the sense that it separates two different environments. Errors will be contributed at the windows due to temperature effects in the window and due to temperature and pressure differences between the environments.

A temperature gradient through the window from face to face will bend the window into a watchglass as shown in Figure B.1. A ray incident upon the window at A at an angle  $\phi_4$  is refracted at an angle  $\phi_3$ , traverses the window thickness  $b$ , reaches the second surface at B at an angle  $\phi_2$  and exits at an angle  $\phi_1$ . The ray path within the window has a curvature  $r_r$  because of the index gradient resulting from the temperature differential  $\Delta T$  between faces of the window and non-normal incidence at A. The surfaces of the window are concentric and have radii  $r_g$  and  $r_g + b$ .

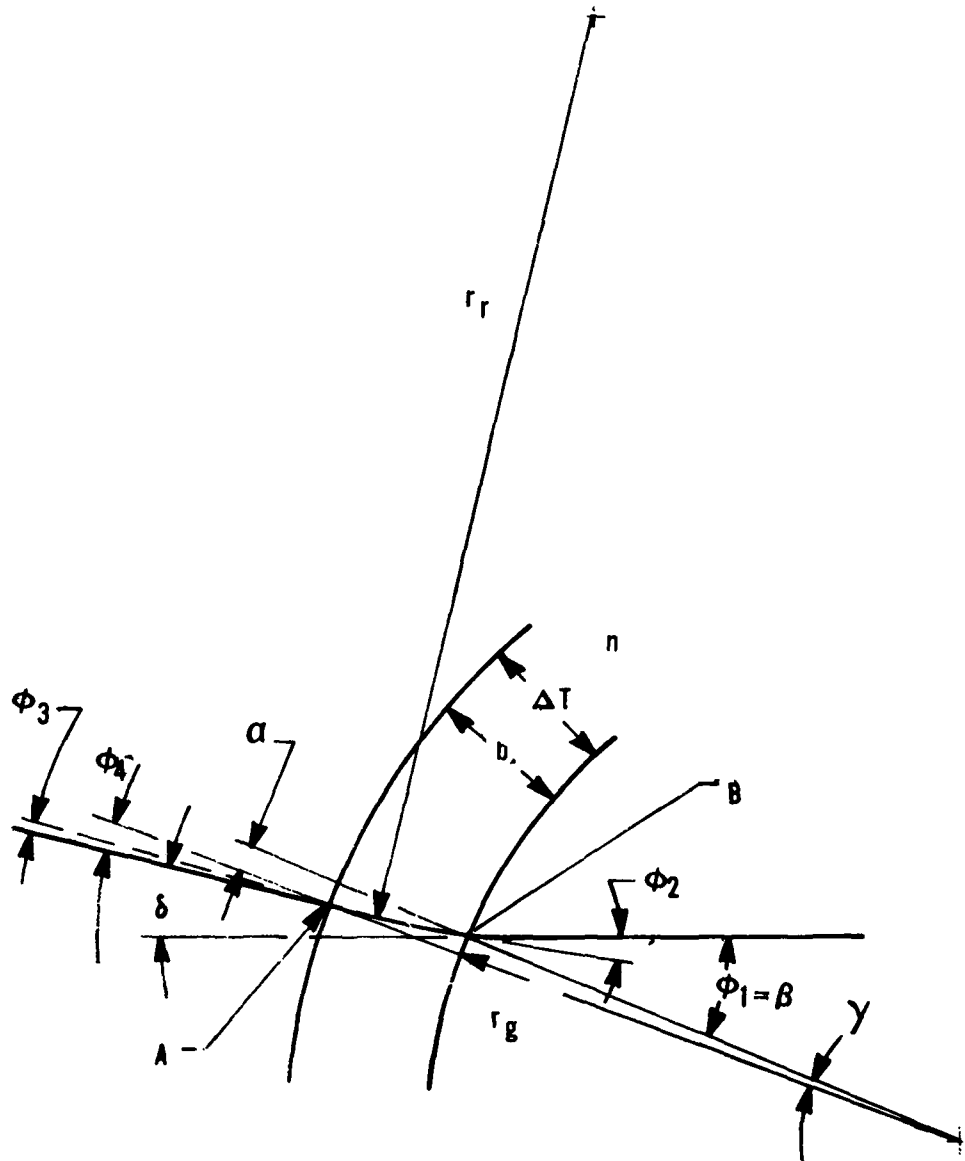


Figure B.1 Window Bowing Geometry

The angles can now be calculated. For convenience, angles are computed from right to left in the figure. From the figure and the laws of refraction:

$$\sin \phi_2 = \frac{1}{n} \sin \phi_1$$

The value of  $a$  is the portion due to the right triangle less the amount of the ray curvature:

$$a = b \tan \phi_2 - \frac{r_r - \sqrt{r_r^2 - a^2 - b^2}}{\cos \phi_2}$$

Using the small addition approximation for the radical and rearranging to solve for  $a$  gives:

$$a^2 + 2 r_r \cos \phi_2 a + b^2 - 2 b r_r \sin \phi_2 = 0$$

Using the quadratic formula and the small addition approximation again yields:

$$a = b \left( \tan \phi_2 - \frac{b}{2 r_r \cos \phi_2} \right)$$

The angle at the second surface will be reduced due to the ray curvature. Using the small angle approximation:

$$\phi_3 = \phi_2 - \frac{\sqrt{a^2 + b^2}}{r_r}$$

The exit angle is:

$$\sin \phi_4 = (n + v \Delta T) \sin \phi_3$$

where:

$$v = \frac{dn}{dT}$$

The radius of curvature of the rays within the glass is found by equating the angle at the center of curvature between the starting wavefront and the wavefront after the time interval:

$$\begin{aligned}\frac{x}{r} &= \frac{\Delta x}{\Delta y} \\ r &= n \frac{\Delta y}{\Delta n} = n \frac{\Delta y}{\Delta T} \cdot 1/(\Delta n/\Delta T) \\ &= n \cdot \frac{\Delta y}{\Delta T}\end{aligned}$$

By the time the ray has traversed the window from A to B, it will have been deflected through an angle:

$$n = \frac{b}{r} = \frac{b}{n} \cdot \frac{\nu}{(\Delta y/\Delta T)}$$

The angle of incidence at B is then the sum of the deflection angle  $\delta_n$  and the wedge angle  $\gamma$ :

$$\phi = \delta_n + \gamma$$

The angle of refraction is then:

$$\phi' = n\phi = n(\delta_n + \gamma)$$

The wedge angle  $\gamma$  is:

$$\gamma = \frac{\Delta X}{d} = \frac{b \alpha \Delta T}{d}$$

The net deflection angle is then:

$$\delta = \phi' - \gamma = n\delta_n + (n-1)\gamma$$

The radius of the glass is determined by the expanded outer surface. The difference in length on the outer and inner surfaces subtended by an arbitrary angle is:

$$\Delta L = (r_g + b) \theta - r_g \theta$$

$$\Delta L = b\theta$$

$$\Delta L = r_g \theta \alpha \Delta T$$

Equating  $\Delta L$  gives:

$$r_g = \frac{b}{\alpha \Delta T}$$

The angle  $\gamma$  is then:

$$\gamma = \frac{a}{r_g}$$

$$\gamma = \alpha \Delta T \left( \tan \phi_2 - \frac{B}{2r_r \cos \phi_2} \right)$$

The radius of curvature of the ray incorporates the normal component of the index gradient:

$$r_r = \frac{n^2 b}{\nu \Delta T \sin \beta}$$

Going back to the angles and using the small angle formulas liberally, the exit angle  $\phi_4$  can be formulated:

$$\phi_4 = \beta + \nu \Delta T \left( \frac{1}{n} - \frac{1}{2} \right) \frac{\sin \beta}{\cos \beta}$$

The deflection angle from the figure is:

$$\delta = \beta - \phi_4 - \gamma$$

$$\delta = \Delta T \sin \beta \left[ \frac{\nu}{\cos \beta} \left( \frac{1}{n^2} - \frac{1}{n} \right) - \frac{\alpha}{\sqrt{n^2 - \sin^2 \beta}} \right]$$

This equation can be used to find the temperature difference  $\Delta T$  which will use the entire error budget  $\delta = 1.3$  rad. This is done in Table B-1 for three glasses and for several window tilt angles. The angle  $\beta = 60^\circ$  corresponds approximately to windows which are tangent to an 8-inch diameter hemispherical head with a 5-inch AEOTR baseline.

The thermal environment of the AEOTR is such that temperature excursions of the order of  $150^\circ C$  can be expected. The implication of the results in Table B-1 is that the entire error budget is used 800 times if the window is tangent to the sphere. A normal incidence window is therefore required if the rangefinder is to tolerate any temperature excursion.

#### AIR WEDGE

The window slant creates an air wedge if there is a difference in pressure or temperature from one side to the other. The refractive index of a gas is proportional to the density of the gas. Then, the gas laws show the density is proportional to the pressure/temperature ratio:

$$n = 1 + \frac{\rho}{\rho_a} (n_a - 1)$$

where:

$\rho$  = density of the air, relative units

$\rho_a$  = density of standard air, same units

a = index at standard conditions

TABLE B-1  
ΔT FOR 1.3  $\mu$ RAD ERROR

Window Tilt Angle $\beta$	Window Material		
	FK51	FK5	LGSK2
60°	.19	.23	.21
33°	.31	.39	.35
10°	1.01	1.31	1.13
1.0°	10.1	13.10	11.3
0.1°	101	131	113

From the laws of refraction:

$$\left[ 1 + \frac{\rho_1}{\rho_a} (n_a - 1) \right] \sin \beta = \left[ 1 + \frac{\rho_o}{\rho_a} (n_a - 1) \right] \sin (\beta + \delta)$$

Using the small angle formula and solving for the deflection:

$$\delta = - \frac{(\rho_1 - \rho_o)}{(\rho_a - \rho_o)} \frac{(n_a - 1)}{(n_a - 1)} \tan \beta$$

Density is proportional to the P/T ratio. Introducing this ratio and rearranging yields:

$$\delta = \frac{P_1 T_o - P_o T_1}{D_a T_1 T_o - P_o T_1} \tan \beta$$

where:

$$D_a = \frac{P}{T_a (n_a - 1)} = \frac{14.7}{(300) (.00028)} = 175 \text{ lb/in}^2/\text{°K}$$

This equation may be solved for  $\Delta P = P_o - P_1$  and  $\Delta T = T_o - T_1$ , separately. The low index of air allows approximations to be made which result in the formulas:

$$\begin{aligned}\Delta P &= -D_a \frac{\delta}{\tan \beta} T \\ \Delta T &= D_a \frac{\delta}{\tan \beta} \frac{T^2}{P}\end{aligned}$$

The tolerable temperature and pressure differentials allowed by the 1.3  $\mu\text{rad}$  error budget are tabulated in table B-2. Nominal values of room temperature and half an atmosphere are inserted.

Thus, for the air wedge to not destroy the tracker accuracy, given the

expected temperature and speed (pressure) excursions, the window must be be within 1.0° of normal incidence. Limits are given in Table B-2.

#### WINDOW BENDING

The formula for the temperature gradient through the window can be used to calculate the tolerable pressure differential that would bend the window. In this case  $r_r$  becomes infinite and, from strain formulas acting on plates:

$$r_g = \frac{E b^3}{.41 \Delta P d^2}$$

where:

$$E = \text{Young's modulus, lb/in}^2$$

Substituting and rearranging yields:

$$\delta = .41 \frac{\Delta P d^2}{E b^2} \frac{\sin \beta}{\sqrt{n^2 - \sin^2 \beta}}$$

$$\Delta P = \frac{\delta E b^2}{.41 d^2} \sqrt{\frac{n^2}{\sin^2 \beta} - 1}$$

The magnitude of this effect is tabulated in Table B-3 for FK51 glass in terms of  $\Delta P$ , the pressure differential required to use the entire error budget and in terms of  $\delta$  for  $\Delta P = 1$  atmosphere. For FK51 glass,  $E = 11.4 \times 10^6 \text{ lb/in}^2$ . A nominal diameter and thickness for the window of 1.25 inch and 0.25 inch, respectively, is assumed.

The errors introduced by pressure-induced window bowing are thus significant for slanted windows and insignificant for normal incidence windows.

TABLE B-2  
AIR WEDGE/TEMPERATURE AND PRESSURE LIMITS

Window Tilt Angle	Tolerable $\Delta P$ with Constant Temperature (lb/in <sup>2</sup> )	Tolerable $\Delta T$ with Constant Pressure (°C)
60°	-.04	1.6
33°	-.10	4.2
10°	-.38	15.6
1.0°	-3.88	158
0.1	-39	1580

TABLE B-3  
WINDOW BENDING

Window Tilt Angle $\beta$	$\Delta P$ Allowed by 1.3 $\mu$ rad Error Budget	Deflection Error With $\Delta P = 1$ Atmosphere
60°	2.0 psi	$9.5 \times 10^{-6}$ radian
33°	3.7	$5.2 \times 10^{-6}$
10°	12.3	$1.6 \times 10^{-6}$
1.0°	123	$1.6 \times 10^{-7}$
0.1°	1230	$1.6 \times 10^{-8}$

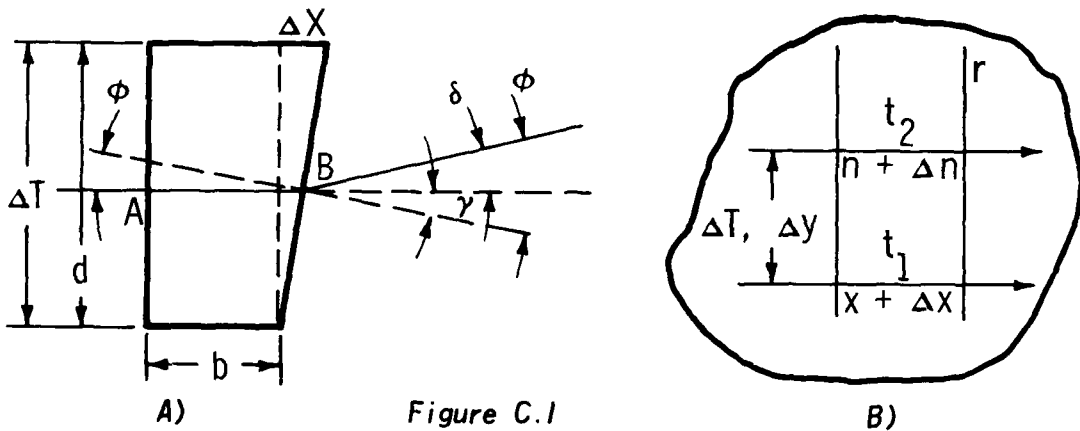
## CONCLUSION

Each of the three effects considered above strongly indicate the need to avoid slanted windows in the rangefinder channels. The errors computed above are compounding rather than cancelling. Since an angular error of  $\delta$  relative to the system symmetry axis for one channel is matched by an error of  $-\delta$  in the other channel. The differential error for the system is then  $2\delta$ . This increased sensitivity is further motivation to use normal incidence windows for the AEOTR.

The error budget for the tracking channel is 1 mrad. Since the effects computed above are linear in  $\delta$ , the allowable temperature and pressure excursions are 770 times larger. From the above results, there is therefore no reason that the tracker window cannot be slanted to improve aerodynamic performance of the tracker head. The combined effects of the temperature and pressure excursions will use only a small part of the error budget, leaving the major portion for electronic sampling and processing error.

APPENDIX C  
DESIGN OF A THERMALLY COMPENSATING WINDOW

The design of a flat window used at normal incidence can be modeled using Figure C.1 below.



The window has a diameter  $d$  and thickness  $b$ . A radial temperature difference  $\Delta T$  across the diameter results in the differential expansion  $\Delta x$  at one edge. A ray entering the window at A is deflected within the window by the transverse index gradient and exits at B at an angle  $\phi$  to the exit face. It is desired to compute the net deflection  $\delta$ .

The general problem of refraction in media with transverse temperature gradients is shown in Figure C.1B. Two initially parallel rays normally incident on the window and separated by a distance  $\Delta y$  experience different refractive indices and path lengths. The transit times through the window are equated:

$$t_1 = \frac{(x + \Delta x) n}{c} = t_2 = \frac{x (n + \Delta n)}{c}$$

which means:

$$\Delta x = n \cdot \frac{x}{n} - \Delta u$$

$$\delta = \varphi' + y = \frac{b\nu}{(\Delta y / \Delta T)} + (n-1) \cdot \frac{b\alpha \Delta T}{d}$$

$$= \frac{b \Delta T}{d} \cdot (\nu + \alpha(n-1))$$

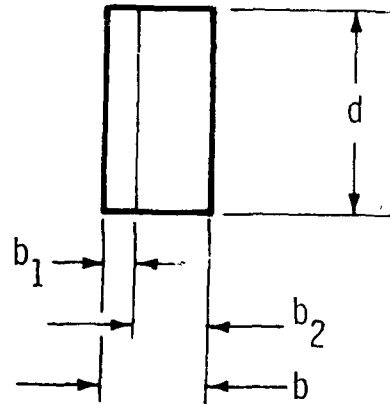
since:

$$\Delta y = d$$

For laminated windows composed of contacted glasses with different values of  $\beta = \nu + (n-1)\alpha$ , the deflections add:

$$\delta = \delta_1 + \delta_2$$

$$\delta_i = \frac{b_i \Delta T}{d} \cdot \beta_i$$



where:

$$i = 1, 2$$

$$\delta = \left[ \frac{b_1 \beta_1}{d} + \frac{b_2 \beta_2}{d} \right] \Delta T$$

To have zero deflection:

$$b_1 \beta_1 + b_2 \beta_2 = 0$$

or:

$$\frac{b_2}{b_1} = -\frac{\beta_1}{\beta_2}$$

The thicknesses of the windows are thus in the inverse ratio of their composite thermal coefficients  $\beta_1$  and  $\beta_2$ . The coefficients must have opposite signs for compensation to be effected. To minimize reflection losses at the boundary, the refractive indices need to be as closely matched as possible. Filling the space between the elements with a liquid having a similar index will reduce reflection losses at the boundary.

Two examples of window designs using the above criterion are given below using FK 51 as the negative beta glass.

Material Properties

Material	$\nu \times 10^6$	$\alpha \times 10^6$	$n - 1$	$\beta \times 10^6$
FK 51	-7.9	13.6	.487	-1.28
FK 5	-2.3	9.2	.487	2.18
LGSK2	-4.5	12.1	.586	2.59

For a window composed of FK 51 and FK 5, typical thicknesses would be:

$$b (\text{FK 51}) = .170 \text{ inch}$$

$$b (\text{FK 5}) = .100 \text{ inch}$$

There is no index step at the interface, although the thermal expansion coefficients are mismatched by a factor of 1.5.

For a window of FK 51 and LGSK2, the thicknesses are:

b (FK 51) = .202 inch

b (LGSK2) = .100 inch

Here the thermal expansion coefficients differ by only 12 percent, while the refractive index step is 0.099 or 6 percent.

## APPENDIX D OPTICAL CONFIGURATIONS

An earlier analysis of the optical configuration for range determination established the conclusion that any product of lens focal length times the stereo base that equals  $25 \text{ in}^2$  or greater would permit a range measurement of 4000 ft with an accuracy of  $\pm 50 \text{ ft}$ . A further constraint imposed on the optical configuration, that of fitting within a relatively small spherical volume, led to the selection of a 5-inch f/l system with a stereo base of 5 inches as meeting both the range detection and volumetric requirements.

Establishment of the focal length and stereo base parameters does not define the specific optical configuration, as there are at least several different configurations that meet the basic nominal requirements. Of the influencing factors that affect the specific optical configuration, the most significant are:

- Light collection efficiency
  - Size and spatial relationships
  - Performance equality between the two "eyes" of the system
  - Most important - the optical mechanical stability of the configuration.
- The following describes various alternatives for the optical configuration, discussing the positive and negative aspects of each.

### SINGLE LENS, SINGLE CCD, COMMON PUPIL.

This approach, described schematically in Figure D.1A, is the most simple of all approaches, at least in terms of the number of components. In this configuration, a single lens and detector are made to see the world simultaneously through both ranger ports by means of a beam divider. The obvious advantage to this system is the inherent stability of the system after the two input beams have been combined. Any motions imparted to either

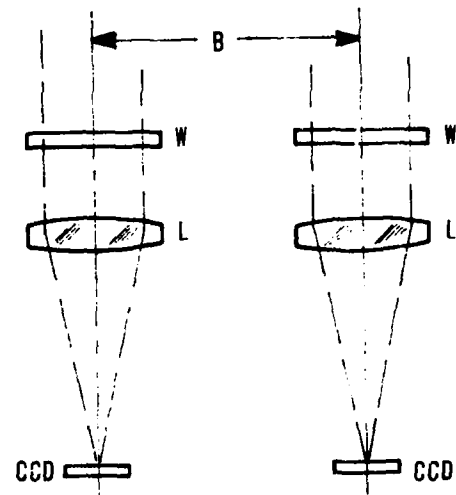
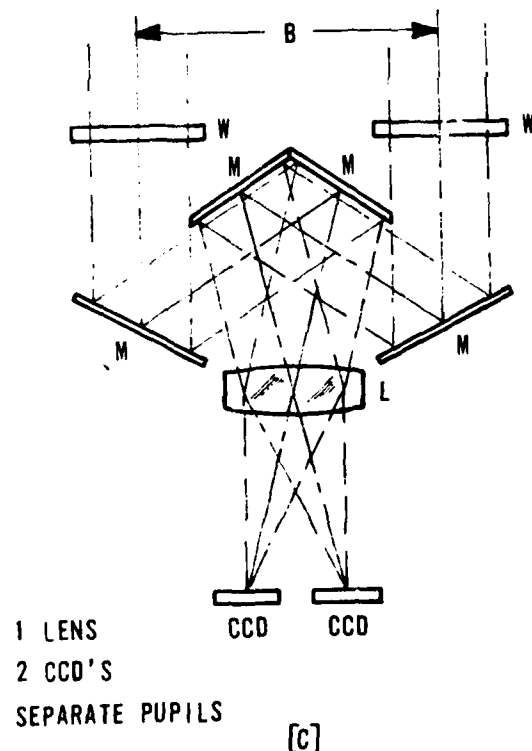
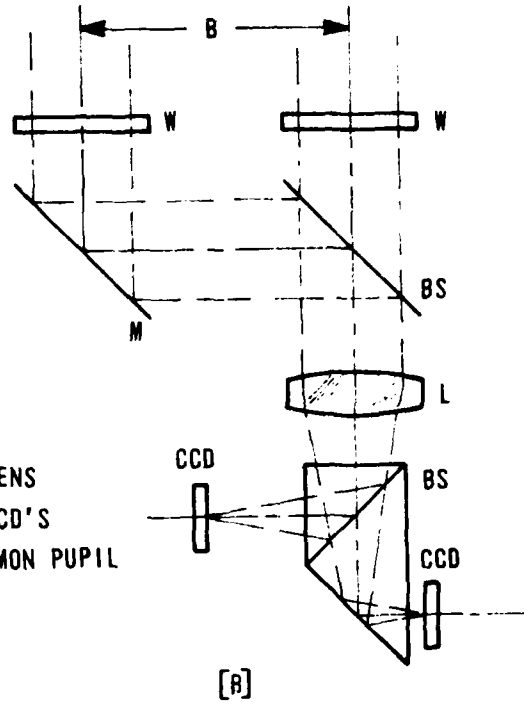
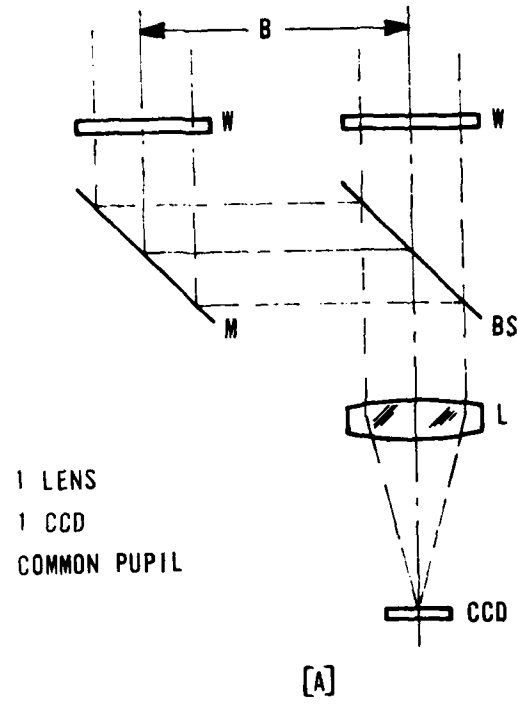
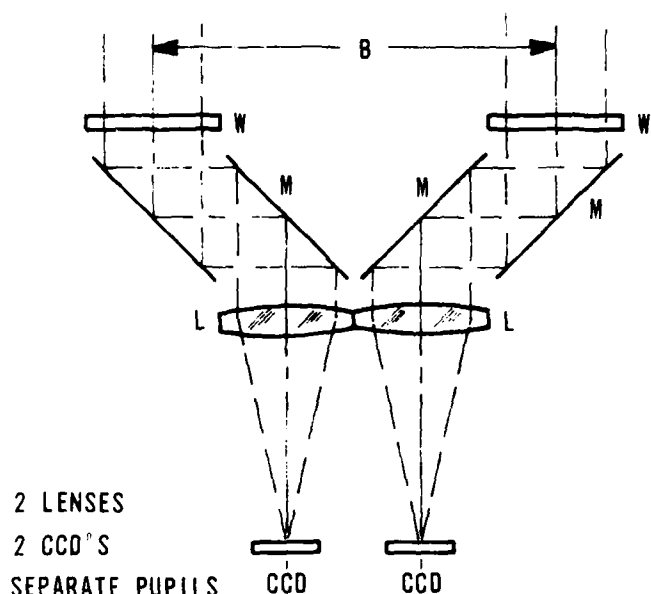
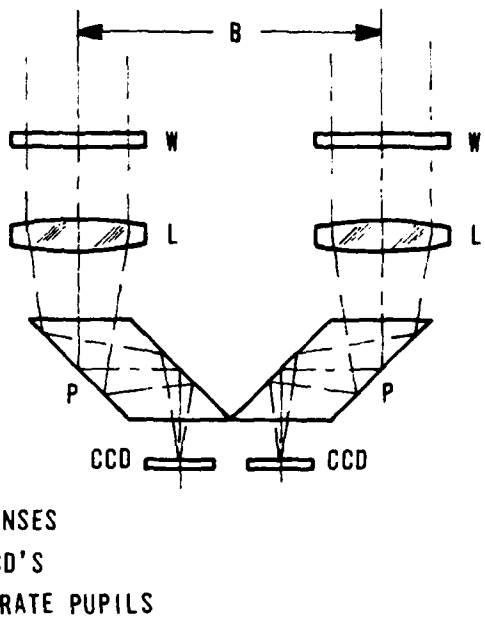


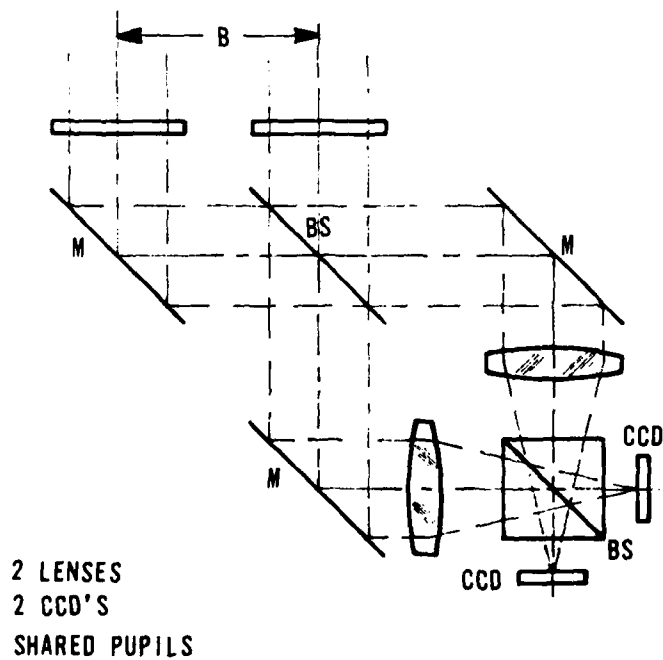
*Figure D.1 Optical Configuration Alternatives  
(Page 1 of 2)*



[E]



[F]



[G]

*Figure D.1 Optical Configuration Alternatives  
(Page 2 of 2)*

the lens or detector as a result of thermal or mechanical stresses have the same effect on either port, thus their effect is zero. Likewise, because the single lens (and its attendant residual aberrations) operates on each port in a like manner, any residual aberrations or manufacturing defects are cancelled by signal subtraction.

This system has two serious faults. At best, only 50 percent of the available light can be used. This is true whether the beam dividing is done neutrally, by spectrum separation or by polarization. While not a fatal fault, it obviously does limit the operating envelope of the ranging function.

The most serious deficiency in this configuration is the inability to affect channel discrimination in an employable manner. Since both ports feed the same detector through the same lens, the only practical method of discrimination between the two signals is by division of time; i. e., alternate sensing between the left and right channels. Switching times that would be required for maintaining a range detection accuracy of  $\pm 50$  ft at a 4000-ft range are completely incompatible with the integration times and data bandwidths at which the CCD detectors can be operated.

#### SINGLE LENS, TWO CCD'S, COMMON PUPIL

In this configuration, shown schematically in Figure D.1B, the addition of one more CCD detector provides a means for channel discrimination that was not present in the previous approach. The additional beamsplitter allows each CCD to "see" through only one or the other port window, thereby permitting simultaneous target detection in both channels. The mechanism for channel discrimination can be either dichroic beam division or beam division by polarization.

The main fault is an inability to prevent some signal from each port impinging on the wrong detector. Because of the broad spectrum that is being dealt with, beam splitting by either spectrum separation or by

polarization is only 80 to 90 percent efficient at each beam dividing surface, resulting in a significant fraction of the energy from the wrong channel reaching each detector. An estimate of the ratio between the desired signal and the undesired signal in each channel is from 4:1 to 6:1. Obviously, in a scene where the contrast is already relatively low, this unwanted signal (which is essentially noise) is intolerable to the scene correlation technique.

#### SINGLE LENS, TWO CCD'S, SEPARATE PUPILS

Another configuration employs one lens and two detectors as shown in Figure D.1C. Each of the detectors is displaced off of the lens optical axis, symmetrically right and left. The main advantage of this approach as compared to the other single lens approaches is the avoidance of any common path between the two channels which totally eliminates the problem of channel discrimination. Also, this scheme has no inherent 50 percent light loss as in the first two schemes.

The four-mirror configuration out in front of the single lens is a potential source of angular alignment errors, but this is no more true in this configuration than in most of the other approaches. As will be argued later, problems relating to internal angular alignment can best be dealt with by a combination of internal volume athermalization and an internal self-calibration technique.

The most serious objection to this configuration is the asymmetrical distribution of lens aberrations imposed on the two images. Because the two CCD detectors are disposed symmetrically with respect to the lens optical axis, and yet the two detectors are both looking at the same scene, there is a "handedness" characteristic in how the lens aberrations influence each image, most notably the lens distortion characteristics. Even a lens with a zero distortion characteristic (the image position is governed by  $f \tan \Theta$ )

will not work in this configuration since the image position in one channel is proportional to  $f \tan(k + \Theta)$  and in the other channel is proportional to  $f \tan(k - \Theta)$ , where  $k$  is the angular offset of the center of each CCD array.

#### TWO LENS, TWO CCD, SEPARATE PUPILS

The most simple concept for stereometric range determination is two simple independent lens and detector systems operating in parallel alignment with a fixed stereo base between them. The basic configuration is shown schematically in Figure D.1D and again with some modification in Figures D.1E and D.1F. Each channel is a completely independent sensor system, the only interdependence between the two being the maintenance of the physical separation and the angular alignment.

This scheme avoids the major objections to any of the one lens configurations. There is no channel discrimination problem since there is no shared pupil or shared path anywhere in the system. For these same reasons, there is also no inherent light loss introduced by beam dividers, etc. Also, there are no problems introduced by a condition of lack of symmetry, since each detector has a nominally identical relationship to its lens and window.

There are two problems associated with the two-lens, two-detector configuration: matching of focal lengths of the two lenses and alignment stability between the two channels.

The matching of focal lengths requirement is a result of needing scalar equality in both channels. A lack of scalar equality will result in an error of range measurement, the magnitude of which is dependent upon where within the detector field of view the target is being sensed. Ordinary manufacturing techniques cannot be relied upon to produce adequate equality in the lens focal lengths, therefore, the design of the rangefinder lenses must incorporate some method for focal length adjustability. An attractive solution

to the problem would be to incorporate into the lens mechanical design a means for adjusting a low sensitivity air space, which would permit fine tuning of the focal length with little effect on the basic image quality. Judgment of scale equality would be performed in the final assembly by an image correlation evaluation of the two channels when both are looking at the same target. Adjustments to one or both lenses would be made until each channel sees the same size target, within a tolerance consistent with the range detection requirements.

Interchannel alignment stability is a problem common to all of the basic configuration schemes, the two-lens configurations being more difficult to solve than the one-lens configurations. Having no components or paths in common, the two-lens configurations of Figures D.1D, D.1E, and D.1F have additional sources of alignment errors arising from mechanical or thermal stresses. It has been argued elsewhere that the only satisfactory solution to addressing the alignment stability problem is to athermalize the optical/mechanical design to the greatest extent possible, and the residual alignment errors will be dealt with via an internal interchannel calibration scheme.

#### TWO LENS, TWO CCD, SHARED PUPILS

Another potential configuration for the rangefinder optics combines some of the desirable characteristics of the single lens schemes with those of the two lens scheme. The basic structure of such a configuration is shown schematically in Figure D.1G. The fundamental idea in this scheme is to average the difference in lens characteristics by allowing both lenses to operate in both sensing channels simultaneously.

Channel discrimination can be achieved in this configuration by either dichroic separation or by beam polarization at the two beamsplitters (BS) in the two paths. There is no inherent 50 percent light loss in the beamsplitter because of recombining at the second splitter, however, the crosstalk between channels caused by inefficiencies at the beamsplitters will result in a ratio

of desired signal to undesired signal of from 4:1 to 6:1. This crosstalk ratio can be improved, but only at the expense of giving up total energy by narrowing the spectral bandwidth of the A EOTR.

This scheme has two serious drawbacks when compared to any of the others. First, for a given focal length, aperture size and stereo base, this configuration consumes more volume than any of the previous configurations. Secondly, being more complex in structure and having more physical components, this configuration is more susceptible to mechanical and/or thermally-induced stress misalignments.

#### PREFERRED CONFIGURATION

Each of the configuration discussed above is afflicted with one or more of the following list of problem areas:

- High illumination loss (50 percent).
- Signal crosstalk between channels.
- Sensitivity to mechanical or thermal stresses upsetting optical alignment.
- Physical space requirements.
- Asymmetric image problems.
- Lens focal length equality in two-lens configurations.

All of the configurations involving common or shared input pupils (Figures D. 1A, D. 1B and D. 1G) were eliminated for reasons of insufficient channel discrimination, brought about by inefficiencies in beam division by polarization or by spectrum. The unwanted crosstalk noise cannot be brought to a level low enough to not seriously impair range finding performance in a low contrast scenario.

The single-lens, two-CCD configuration of Figure D.1C, and any other configuration in which the two channels would employ detectors in a nonsymmetrical arrangement, was eliminated from further consideration because of geometric positional errors inherent in the configuration.

The configuration chosen is the two completely independent channels, two lenses, two CCD's, with no common light path between them. With no inherent light loss and no channel discrimination problems to deal with, the only significant problem areas to be dealt with are focal length equality and system stability. In addressing the focal length equality requirement, the design of the objective must incorporate a mechanism for adjusting the focal length of each objective by means of some insensitive air space change. The system stability requirement will be dealt with by means of careful mechanical mount and athermalization design, which is acknowledged to be not quite sufficient for the range accuracy required. The residual alignment errors arising from mechanical or thermal stress will be measured by means of an internal calibration scheme which will be operating simultaneously with the range measurement system.

## APPENDIX E DETECTOR RADIOMETRIC CONSIDERATIONS

The operating limits of a video system may be estimated by comparing the detector signal irradiance under given conditions of scene irradiance, target contrast and atmospheric transmission with the noise equivalent exposure for the image detector. For the following analysis, the Fairchild CCD 211 is assumed to be the image sensor.

For the general case of an unstructured sky background, the detector signal irradiance is given by:

$$I_{d, ac} = \frac{\pi}{4} \cdot \frac{BR_{TC} T}{F^2}$$

where:

B = sky brightness (fL)

R<sub>TC</sub> = target differential contrast = 0.05

T = atmospheric transmission

F = optical system aperture

The CCD noise equivalent signal is:

$$I_{dN} = \frac{I_s R_w}{R_D t_{int}}$$

where:

I<sub>s</sub> = device saturation exposure

R<sub>w</sub> = tungsten to solar luminous efficiency factor

= 2.5

R<sub>D</sub> = device dynamic range

= 1000

t<sub>int</sub> = exposure time

In order to have a signal-to-noise ratio of 10, the following condition must hold:

$$I_{d, ac} \quad 10 I_{d, N} = \frac{\pi}{4} \cdot \frac{BT R_{TC}}{F^2}$$

or:

$$BT \quad 10 \frac{I_s R_w}{R_D t_{int}} = \frac{4 F^2}{\pi R_{TC}}$$

For the video channels under consideration here, the brightness-transmission products result in the requirements of Table E-1.

Figure E.1 displays the maximum available signal-to-noise ratios for the above systems as a function of lighting conditions and atmospheric transmission during twilight. The figure shows that acceptable performance can be expected during daylight operation and for several minutes into twilight.

In the case of earth background, the detector irradiance signal is:

$$I_{d, ac} = \frac{I_g \Delta p T}{4 F^2}$$

where:

$I_g$  ground irradiance

$\Delta p$  reflectivity difference between target and background

For a unity signal-to-noise ratio, the required apparent reflected irradiance is:

$$I_g \Delta p T = \frac{I_s R_w}{R_D t_{int}} = 4 F^2$$

For the above systems, this constraint assumes the values in Table E-2.

Apparent reflected irradiance requirements are graphically illustrated in Figure E.2 where the minimum value of  $(I_g \Delta p T)$  is plotted as a function of ground reflectance. A target reflectance of 10 percent is assumed.

AD-A089 143

CAI BARRINGTON ILL  
ADVANCED ELECTRO-OPTICAL TRACKER/RANGER.(U)  
JUN 80 R A BENNETT, D N DEFOE

F/6 17/8

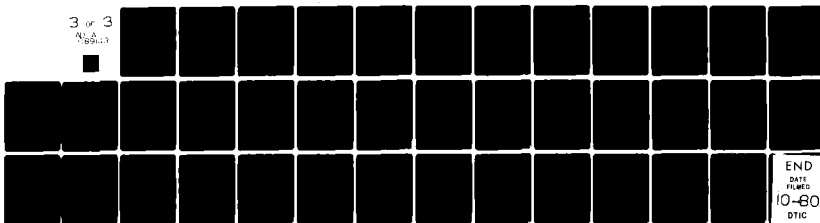
UNCLASSIFIED CAI-7323-0180-5

AFWAL-TR-80-1034

F33615-78-C-1562

ML

3 or 3  
AIA  
NBB17



END  
DATE  
FILED  
10-80  
DTIC

TABLE E-1  
APPARENT BRIGHTNESS REQUIREMENTS  
WITH SKY BACKGROUND

Channel	Focal Length	F	$t_{int}$ (ms)	$I_{dN}$ (fc)	BT	
					SNR = 1 (fL)	SNR = 10 (fL)
Tracker	2 inch	2	0.5	0.02	2	20
Ranger	5 inch	4	2.0	$5 \times 10^{-3}$	2	20
Video	9 inch	7.2	16	$6.3 \times 10^{-4}$	0.8	8.2
Video	600 mm	8	16	$6.3 \times 10^{-4}$	1.0	10.2

TABLE E-2  
APPARENT REFLECTED IRRADIANCE FOR SNR = 1

System	$I_{dN}$ (fc)	$I_g \Delta p T$ (fc)
Tracker	.02	.32
Ranger	$5 \times 10^{-3}$	.32
Video	$.63 \times 10^{-3}$	.13
Video	$.63 \times 10^{-3}$	.16

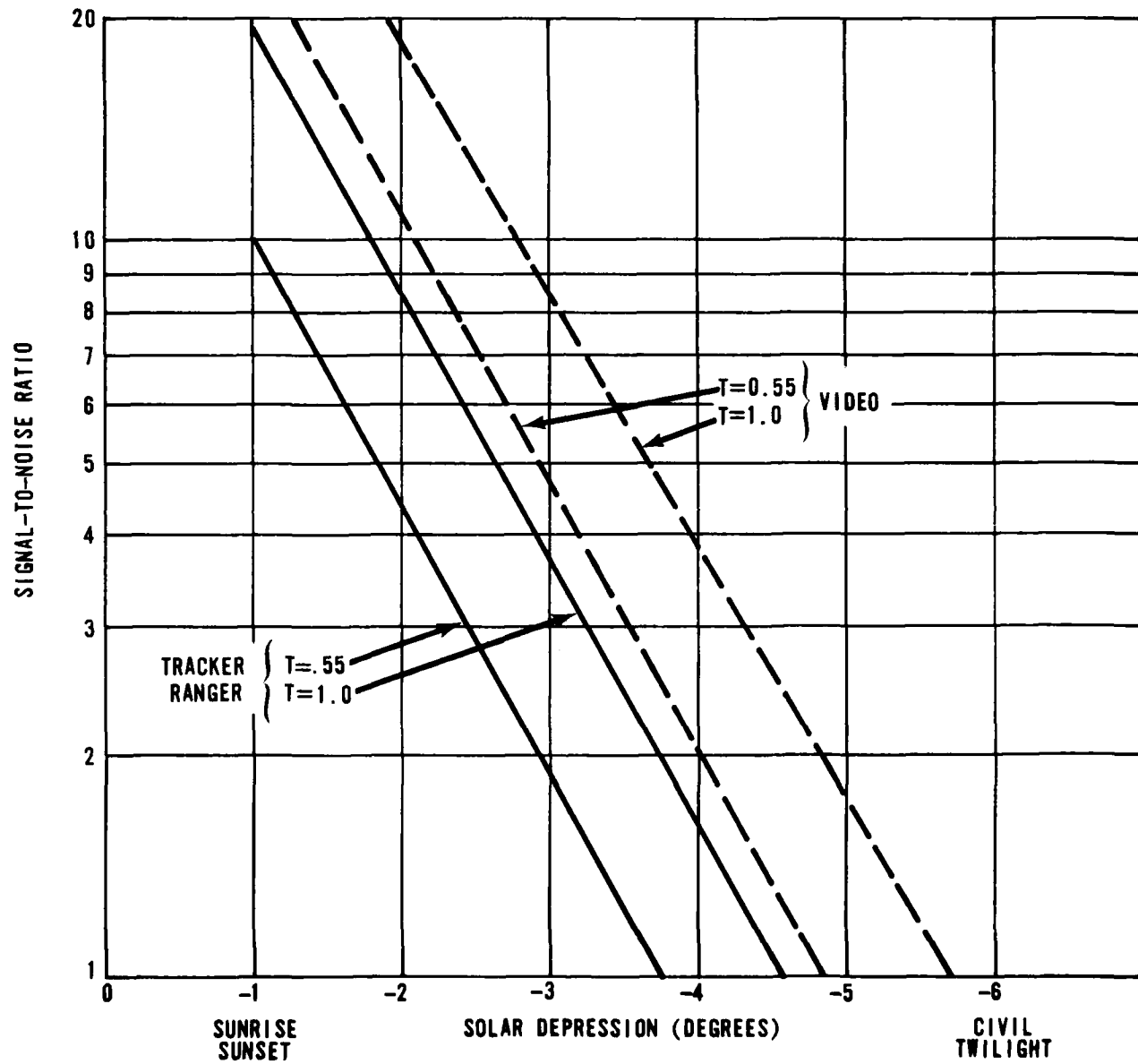
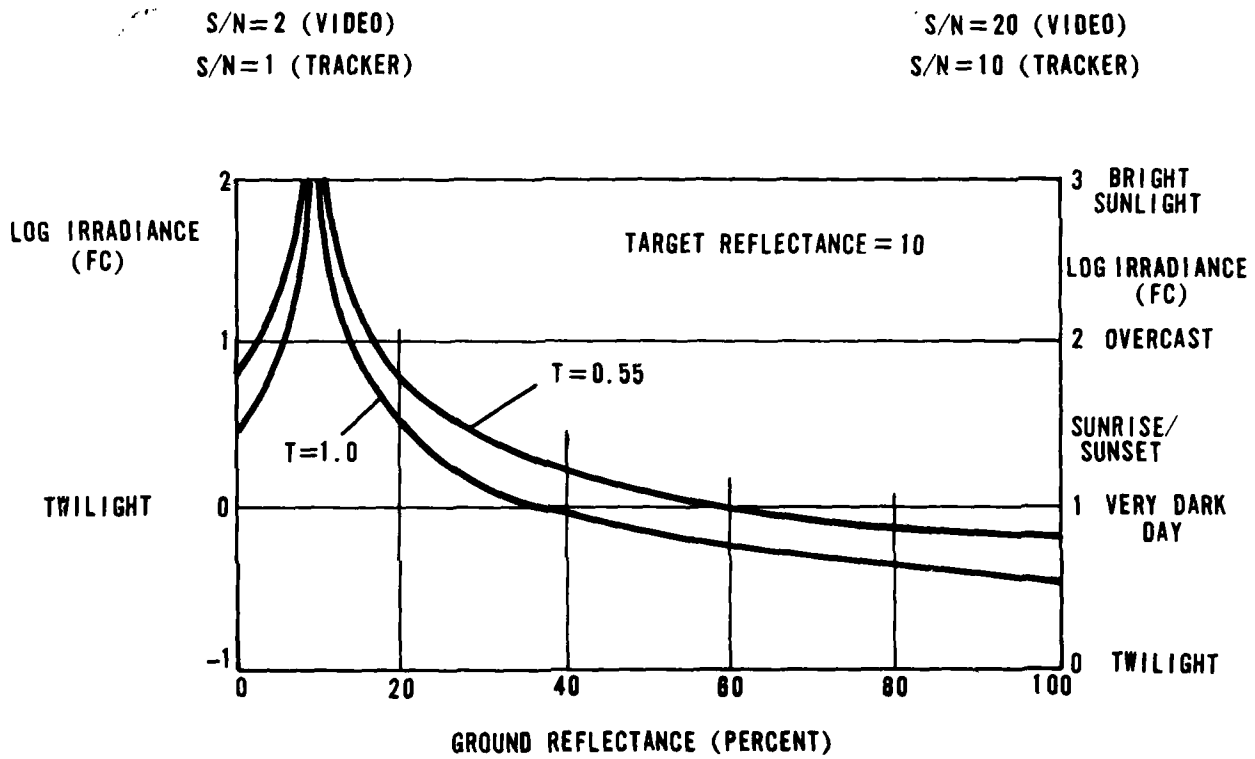


Figure E.1 Lighting Dependence Of SNR



**Figure E.2**  
*Apparent Reflected Irradiance Requirements For System Operation*

## APPENDIX F DISPLAY OF TARGET VIDEO

Several options exist in regard to the display of detected target video. It is desirable to present an image which allows maximum use of information in the signal without unnecessary complication of the sensor/display interface.

The video display units (VDU) of current generation fighter aircraft operate at 525/60 and 875/60 standard resolutions and frame rates, and with aspect ratios of 1:1. Three potential difficulties are immediately apparent when supplying these VDU's with video derived from the sensors of the AEOTR. First, the AEOTR video sensor frame rates are incompatible with the 60 field/s rates of the VDU's. Second, the sensor aspect ratios are 3:4 rather than 1:1, and display at 1:1 aspect requires the loss of at least 25 percent of the video information or a distorted image. Finally, the AEOTR head is roll stabilized, which implies that the displayed target video will in general be rotated relative to the attacker platform.

The sensor/VDU rate mismatch may be addressed by some form of scan conversion or by the use of a dedicated video sensor operated at the standard rate. Space limitations in the AEOTR head obviate against a dedicated sensor unless additional performance such as greater resolution requirements are discussed in a separate subsection under that title in this report. The approach followed in this appendix is the design of an appropriate scan conversion technique to assure rate compatibilities.

The use of scan conversion is also appropriate for the second technical difficulty, aspect ratio mismatch. The loss of one-fourth of the video information required for conversion from 3:4 to 1:1 aspect is insignificant for

the target image sizes expected here, as long as the target tracker subsystem is able to keep the target within the 1:1 frame. In fact, if the target can be held near the center of the field of view, the elimination of scenery at the frame edges amounts to clutter reduction and does allow greater flexibility in such image processing procedures as contrast stretching.

The above two difficulties can be readily addressed by rate and aspect-adjusting scan conversion. The problem of image rotation, however, requires consideration at significant depth to achieve a satisfactory solution. For this problem, several options are available.

The first option that presents itself is to simply display the video from the sensor as it is imaged. This approach is considered unsatisfactory because the target on the display will not in general have the same orientation as the one seen through the cockpit canopy. Adding to the confusion would be the rotation of any background imagery, particularly the horizon. Since the position and approximate size of the target in the format is determined by other subsystems of the AEOTR, it is possible to display only the target and the immediately surrounding background. This would reduce confusion arising from rotating backgrounds, but the target image would still rotate.

A second option will be described which will allow readout of the stored image with a slanted raster pattern. Prior to that, a brief discussion concerning imaging format is appropriate.

The assumed sensor for the present application is the Fairchild CCD 211, with a 244 row x 190 column photosite matrix and a 3:4 aspect ratio. For a square image presentation, only 3/4 of the horizontal pixels, namely 142, need be displayed. A square frame would then have

dimensions of 244 pixels vertically by 142 pixels horizontally. The previously-discussed disparity between horizontal and vertical resolution of the available area array CCD's implies that the displayed image will have a vertical and horizontal resolution which depends upon rotation angle. While it is possible to design a scan converter which can handle a square image with  $244 \times 142$  picture elements, a very large memory is required and the processing becomes rather cumbersome. A more straightforward approach is to reduce the vertical resolution to approximately the horizontal resolution by combining vertical pixels in pairs using a simple CCD clocking technique. The approach is reinforced by the fact that it will most likely be necessary to perform this reduction of resolution on the tracking sensor alone to simplify target tracking. The resulting image format will then be 142 pixels horizontal by 122 vertical. If the target image is displayed having  $122 \times 142$  pixels, then a memory size of 17,324 words would be required. The analog-to-digital conversions produce words of 8 bits which could be stored, although only 4 or 5 bits should be required to provide an acceptable level of contrast for the pilot. This consideration also impacts the memory size.

The second video display option results from these considerations. The major change involves an alteration of the number of pixels stored by the scan converter. Since, with rotation, the roles of vertical and horizontal become mixed, it is desirable to have the same number of pixels in each direction so that no distinction need be made between the axes. This also makes the memory addressing much less complex. With the CCD vertical axis having 122 pixels, the horizontal would be limited to 122 also. This is close to 128, the nearest binary coding level. The memory could then have a size of  $128 \times 128$  words or 16 K (16,384), and little of this space would be wasted. However, by limiting the pixel number in the horizontal direction to 122, the problems with aspect ratio again appear.

If a 1:1 correspondence is made between the CCD pixels and the memory words, with each pixel stored in a unique memory location, the aspect ratio stored is no longer 1:1, but  $122/190 \times 4/3$  or .86. If this is displayed in a 1:1 format, a 17 percent stretching will occur in the CCD horizontal axis. If there is no rotation of the image, this distortion can be compensated by compressing the image as it is read out of the memories by increasing the data readout rate. With rotation of the image sensor, this technique is less straightforward. For a rotation of  $90^\circ$ , the displayed axis that is stretched is the vertical axis. The compression used for the horizontal axis cannot be employed since the number of lines per displayed television field is a constant, and compression in the vertical direction is not possible. However, it is possible to expand the horizontal axis to produce an image with the correct aspect ratio. Thus, at  $0^\circ$  and  $180^\circ$  maximum compression occurs (17 percent), and at  $90^\circ$  and  $270^\circ$  maximum expansion is used. This compensation for aspect ratio also affects the displayed image size by the same  $\pm 17$  percent.

Another solution for compensating image roll while correcting aspect ratio differences is to resample the data so that the 122 points to be stored are distributed over the 142 pixels that form the image square. With this technique, the image stored in the memory has the correct aspect ratio and requires no further compensation or image scale change. This method requires additional hardware to perform the resampling and would include some type of aliasing filter, as well as another high speed analog-to-digital converter. The image resolution will certainly be degraded by the inclusion of this filtering and resampling. This processing method does, however, reduce the circuit complexities associated with scan conversion.

The actual scan conversion will be effected by appropriate memory

readout addressing. A separate counter for both horizontal and vertical axes will be programmed as to where to start counting (in the counting memory matrix) and at what rate. The rotation angle obtained from the servo computer will determine these parameters. The starting position and counting rate must be specified for each line to be displayed and for all possible angles.

The starting point for the first line in the field will be stored in a ROM, along with the vertical and horizontal counters advance rates and the incremental displacement of the starting point for each of the subsequent video lines. If a standard 1024-word ROM is used, the angular resolution for derotation of the image is  $0.35^\circ$ , which should be imperceptible.

To compute the starting point for each line in the frame, the incremental displacement obtained from the ROM is summed with the starting point of the preceding line, the displacement factors following a sinusoid. The hardware to address the video matrix is thus a dual set of presetable counters, the origin point ROMs and an accumulation register to compute the next origin.

The actual display formatting can take several forms. With 122 lines of active video, the active portion of the image can occupy the center 1/4, the center 1/2 or the entire screen of the display. This is possible because the 122 lines of video divide nicely into the 481 active television lines of the 525-line system. The final choice should be based on screen size, pilot viewing distance and overall sensor/display system resolution. Good display engineering practice requires that the target image cover at least 12 to 20 arc minutes.<sup>(\*)</sup> With 10 TVL covering this dimension (Johnson criterion) the entire image of 122 TVL will have a size

(\*) Human Engineering Guide to Equipment Design, H. D. van Cott and R. G. Kinkade, Ed. USGPO, 1972, Chapter 3.

of 1.4 inches at a nominal viewing distance of 28 inches.

It may be possible to scan convert the entire 244 vertical lines of a dedicated display sensor. This additional resolution would provide substantial improvement in target identification, although the smallest scale readout format option is eliminated. Doubling the number of video lines doubles the size of the scan conversion memory buffer, which impacts hardware and packaging constraints.

In general the displayed image will be a circle with a diameter of 122 pixels, the corners of the stored image being truncated. Display updating will occur at rates consistent with both the sensor and monitor frame rates. Updates of up to 10 to 20/s should be possible using a single memory buffer. The proposed scan conversion system will be compatible for use with all current cockpit video displays.

## APPENDIX G

### CORRELATION MODELING PROGRAM COMPUTER RESULTS

#### OVERVIEW

A computer program was developed in order to model the AEOTR ranges more realistically than previous efforts, and to provide a versatile tool which would allow the study of the interaction of various factors of design and external conditions.

Previous computer work had been based on whole pixel image shifts. An early and significant finding of the work done with the new program was the severely detrimental effect of high frequency image content at fractional pixel shifts. Hence, most of the subsequent work was devoted to minimizing the effect and attempting to achieve the accuracy which had been stated for the simpler case, and is necessary to meet the design criteria.

In this vein, several filters were studied, including hyperbolic secant, hanning, polynomial, rectangular and a more realistic 32-tap TAD (tapped analog delay line) filter approximation of a rectangular function. The optimum filter appears to be a rectangular filter with a .75 x Nyquist cutoff. The TAD filter version of this, however, seems to offer little, if any, improvement over no filter at all.

The most significant improvement in results came with a slight modification of CAI's algorithm to use a closer set of points on the correlation function in computing the fractional pixel shift. Nevertheless, some realizable filter is still required if the results are to show the desired degree of accuracy. At this point, it is not known how to more closely approach the accuracies permitted by an ideal filter.

It should be pointed out that other filter designs with differing characteristics need to be examined before these results can be said to necessitate a revision of design goals. For example, while we know that a perfectly sharp cutoff without ripple is optimum, the only real filter attempted so far was an attempt to maintain sharpness at the expense of ripple. Perhaps a gaussian filter with more rounded rolloff but no ripple would show better results.

Note that the error is not a function of noise, but of aliasing. In fact, the results show little effect from the addition of noise.

Several other tests were made on the effects of clutter, motion and target control structure. Clutter and motion had little effect. The exception was an exceptionally strong transition in the background as the crossing of a horizon. In this case, it was shown that light windowing mitigated the problem to a large degree. Target contrast structure, as might be expected from the discussion above, had detrimental effect at long ranges. This deterioration can be related to the high frequency problem.

In conclusion, the computer results indicate a difficult problem with high image frequency content, but nevertheless good results and little problem with clutter and motion. Failing the discovery of an effective realizable spatial filter, two paths are open in order to achieve higher accuracy correlation. First would be to transform the image into the frequency domain where the ideal filter can easily be applied, followed by an inverse transform. This path would yield higher accuracy than previously stated. The second option would be to implement closed cycle ranging in which the world image is artificially shifted to give a whole pixel shift and the range measured on the more accurate and static image of the autocalibration scheme. It is this second approach which is considered to be simpler and more quickly realizable in hardware.

### Program Description

CAI's tracker simulation program is a comprehensive and versatile tool for studying the effects on tracker performance of a wide assortment of variables and conditions.

In the most general case, the program creates a scene which comprises a target, cluttered ground and cluttered sky, each with their own relative motion in the scene, images the scene with noise, cross correlates successive images, calculates target motion from the cross correlation matrix and outputs error statistics at the end of a set of several integrations. The variables which can be studied include target brightness, target range, the view of the target and the rate of target motion, background mean brightness, variance of the clutter brightness, mean area of the clutter, variance of the area, density of clutter, rate of background motion, the presence of a horizon and, if so, rate of horizon motion, separate statistical values for sky clutter and rate of sky motion, relative noise level, the size and location of the window used for correlation, size of the correlation matrix, the method of choosing the peak corresponding to target motion in the correlation matrixes and the method of calculating fractional pixel shift.

Additionally, the CCD geometry and dynamic range, optical focal length and MTF, and the type of target can be easily changed within the program. New variables can be added with minimal effort and new approaches quickly incorporated.

The flow chart for the tracker simulation program is shown in Figure G. 1. Briefly, the mathematical approach is to create perfect transforms of each scene portion, apply the appropriate filters for pixel sampling, motion blur, MTF, and so on, then loop for scene integrations apply the shift theorem to each scene portion, transforming to the spatial domain and adding the scene portions opaquely (with partial opacity at the boundaries). By filling out

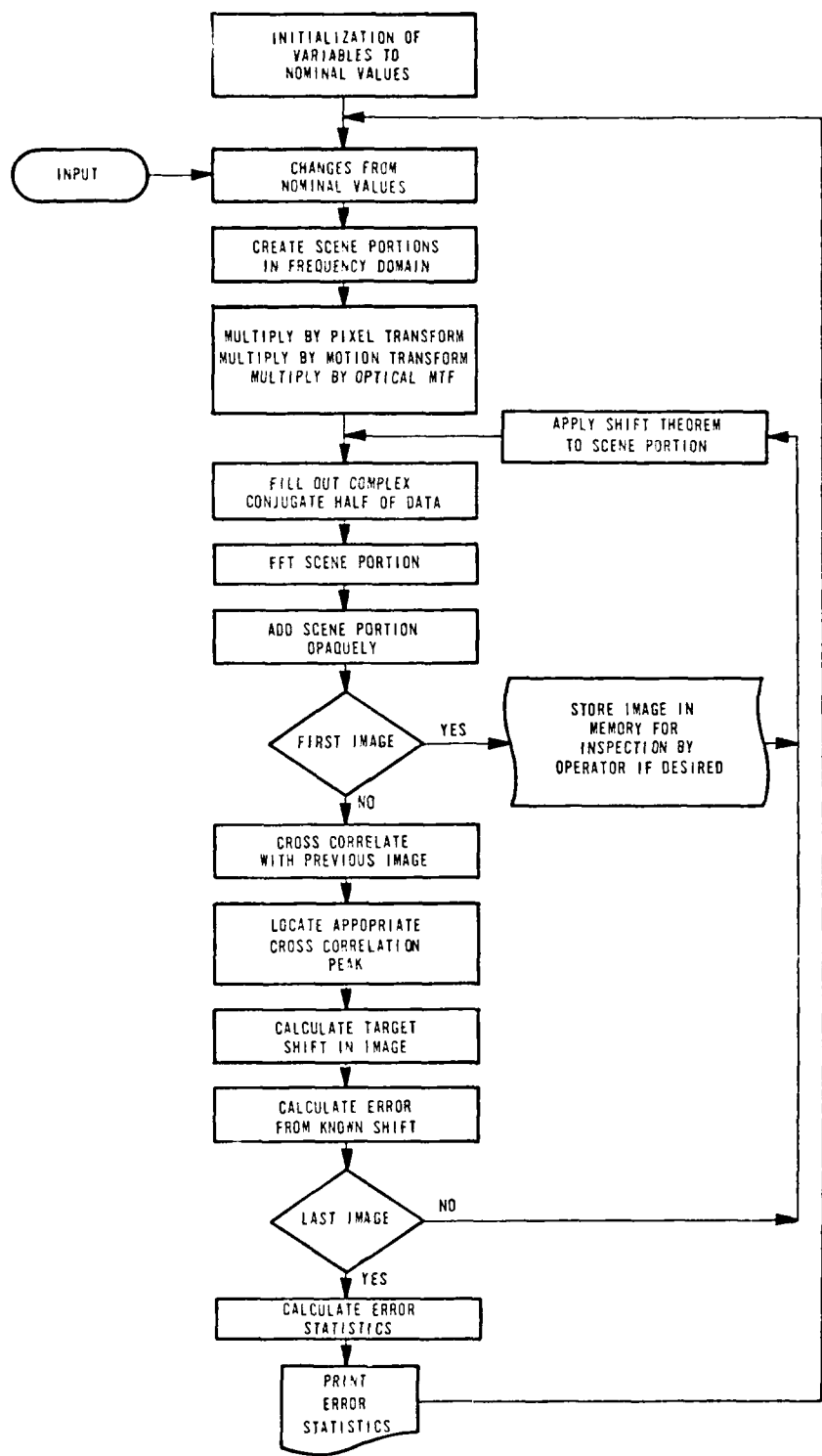


Figure G.1 AEOTR Simulation Program Flow Chart

the conjugate half of the frequency data just before the transform to the spatial domain, the spatially small components of the scene are properly preserved.

Some of the questions intended to answer are:

- The effects of quantization of the image.
- The effects of window size for correlation.
- The effects of background.
- Appropriate methods of adapting window size.
- The performance with small and/or low contrast targets.
- The effects of image processing such as image subtraction.
- Techniques for target detection.

A summary of the program results in graphical and tabular form follows to display the sensitivity of correlation processing on a range of parameters.

#### GRAPHS OF COMPUTER RESULTS

Figure G.2 shows the effect of filter width for a single ranging case. The filter used was a hyperbolic secant defined as Sech ( $W-I$ ) when  $W$  is the ordinate value and  $I$  is the sample number, measured from the origin, of the frequency domain representation of the scene. These results have little quantitative meaning because the frequency samples are not defined in terms of Nyquist frequency. The only conclusion to be drawn from this graph is that filter width can have an effect on accuracy.

Figure G.3 shows the problem of high spatial frequencies in the scene by plotting the computed accuracy as a function of image shift independent of true image relative displacement. Depending on the position of the image,

FILTER : HYPERBOLIC SECANT  
WINDOW : 16 x 8  
NOISE : 0  
BACKGROUND : UNIFORM BRIGHTNESS = 1.0  
TARGET: MIG 23, HEAD ON, UNIFORM BRIGHTNESS = .95, RANGE 4,000 FT

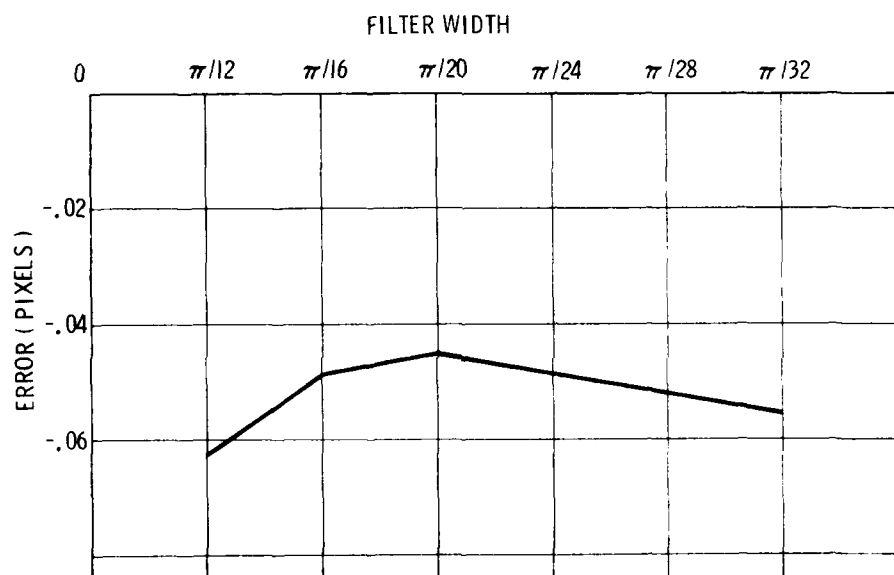


Figure G.2 Ranging Error Vs Filter Width

FILTER : HYPERBOLIC SECANT  
WINDOW : 16 x 8  
NOISE : 0

BACKGROUND : UNIFORM BRIGHTNESS = 1.0  
TARGET : MIG 23, HEAD ON, UNIFORM BRIGHTNESS = .95,  
RANGE = 4,000 FT

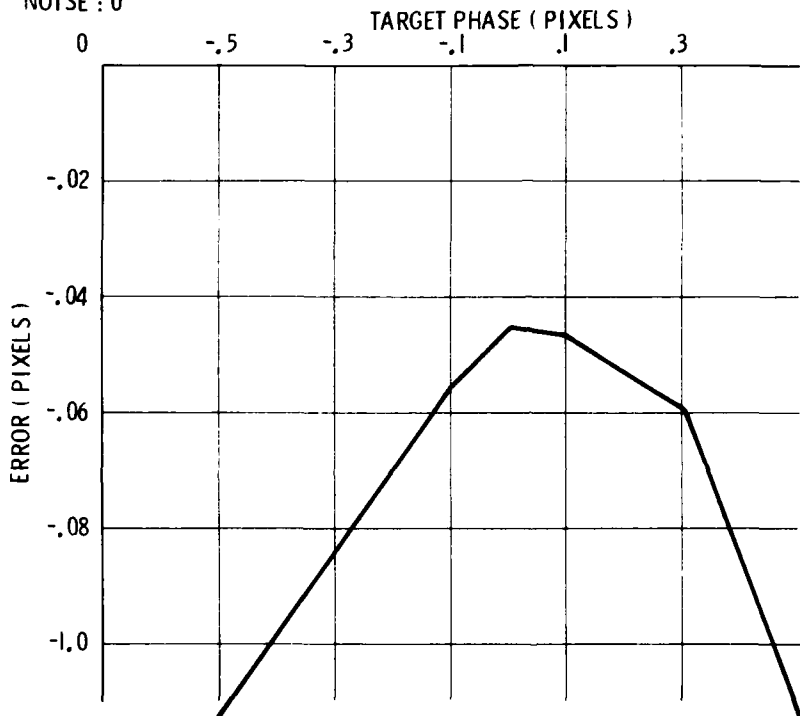


Figure G.3 Ranging Error Vs Target Phase

measured in fractions of a pixel, wide variations in calculated results occur.

Figure G.4 shows the same problem of high frequency information as the actual relative image displacement varies. It was at this point that a modification of CAI's algorithm was implemented to use a closer set of points on the correlation function in computing the fractional pixel shift. The improvement this modification offered is illustrated in Figure G.4 with the data points represented by circles (solid for phase = 0, dashed for phase = -.5). Note that image size is also a parameter in this graph because the relative displacement was controlled by setting the range. Also, the filter has been changed to a Hanning function which is defined in terms of Nyquist frequency.

Figure G.5 is a graph of conditions similar to those in Figure G.3, but using a Hanning filter in place of the hyperbolic secant.

Because of the less than desirable results generated this far, a modification of CAI's algorithm was implemented in hopes of improving the error. In fact, improved results were recorded as shown by the data points in Figure G.4 marked by circles.

Figure G.6 returns to the problem of filter implementation by testing filter shape. Using a polynomial approximation to the Hanning function and raising the value to a power creates a progressively more square cutoff as the power is raised. The results show that a rectangular filter allows the greatest accuracy in measurement. Several other data points were taken to check on the effect of filter width.

Figure G.7 shows some data for a truly rectangular filter with various cutoff frequencies. In general, the optimum cutoff appears to be a lower than Nyquist frequency in the region of .85 Nyquist. Further work used a .75 Nyquist cutoff filter.

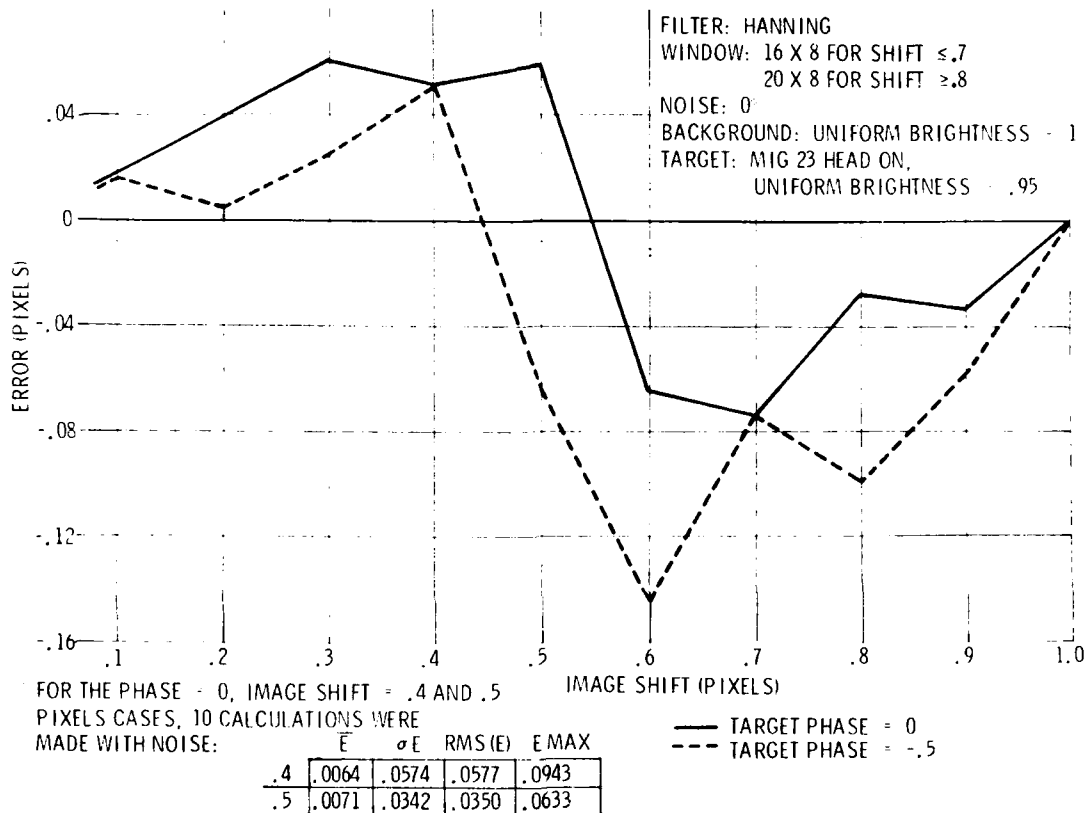


Figure G.4 Ranging Error Vs Image Shift

FILTER : HANNING  
WINDOW : 16 x 8  
NOISE : 0

BACKGROUND : UNIFORM BRIGHTNESS = 1  
TARGET : MIG 23, HEAD ON, UNIFORM BRIGHTNESS = .95  
RANGE = 3,919 FT (.6 - PIXEL IMAGE SHIFT )

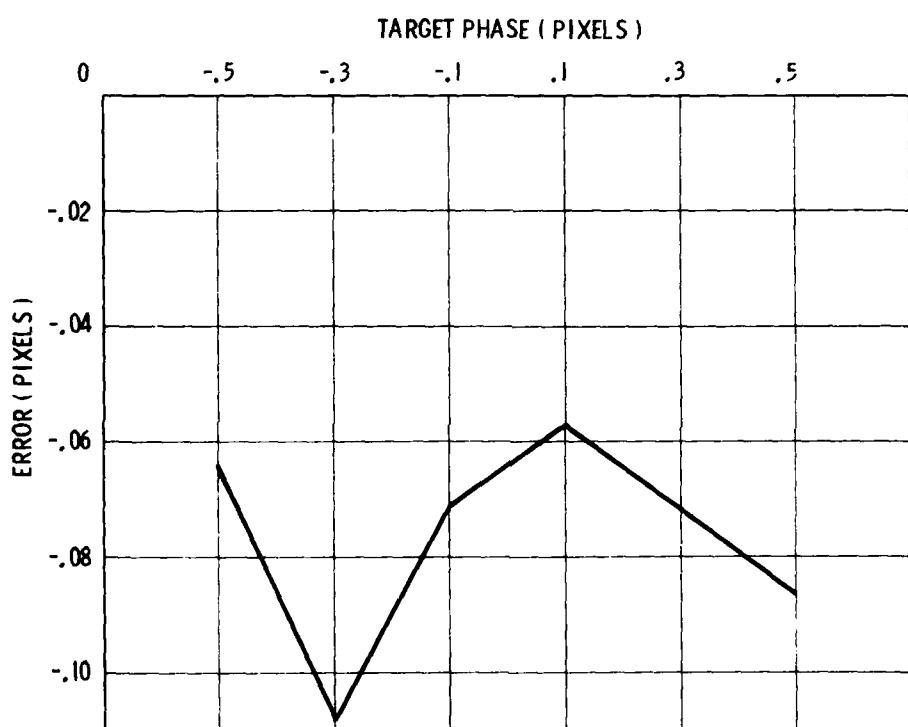


Figure G.5 Ranging Error Vs Target Phase

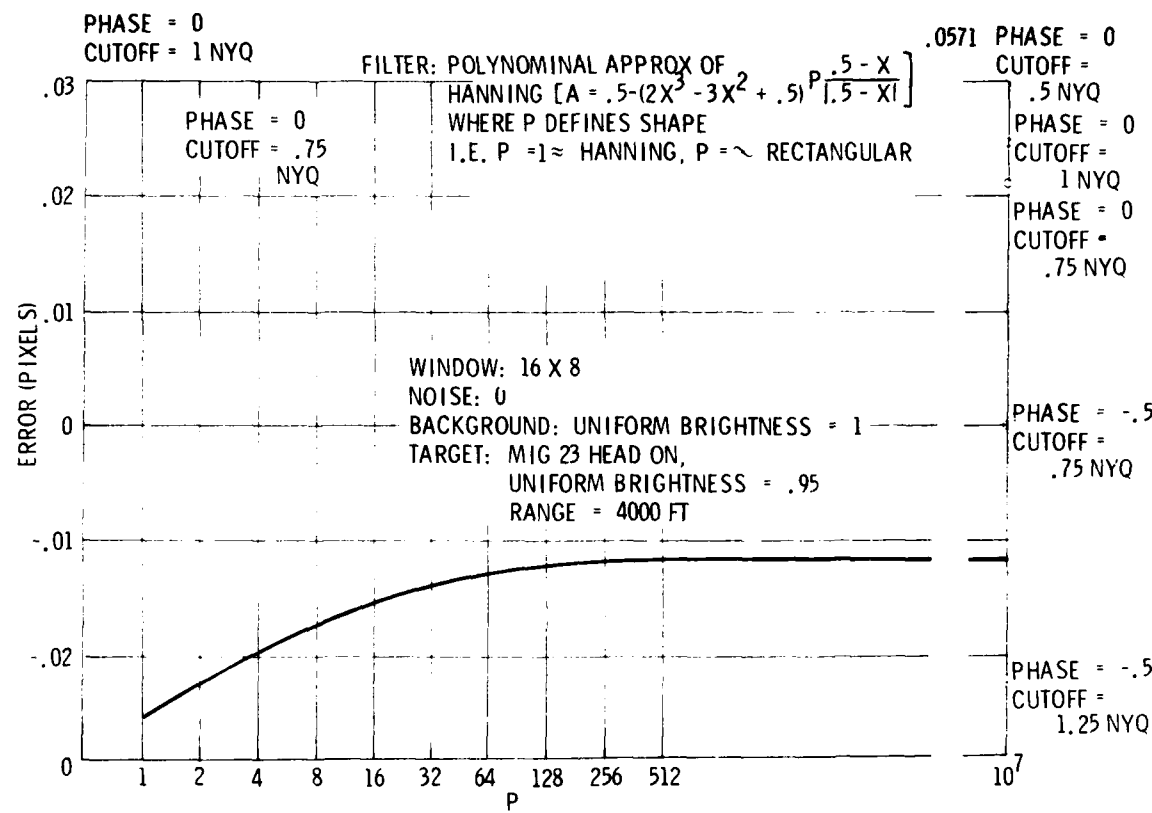


Figure G.6 Ranging Error Vs Filter Shape

BACKGROUND : UNIFORM BRIGHTNESS = 1.0  
TARGET : MIG 23, HEAD ON, UNIFORM BRIGHTNESS = .95

FILTER : RECTANGULAR  
WINDOW : 16 x 8  
NOISE : 0

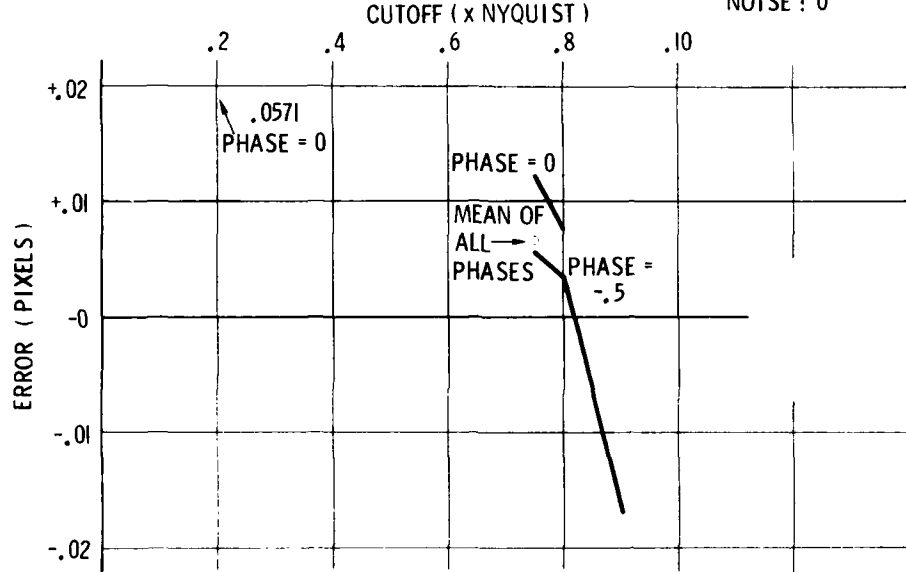
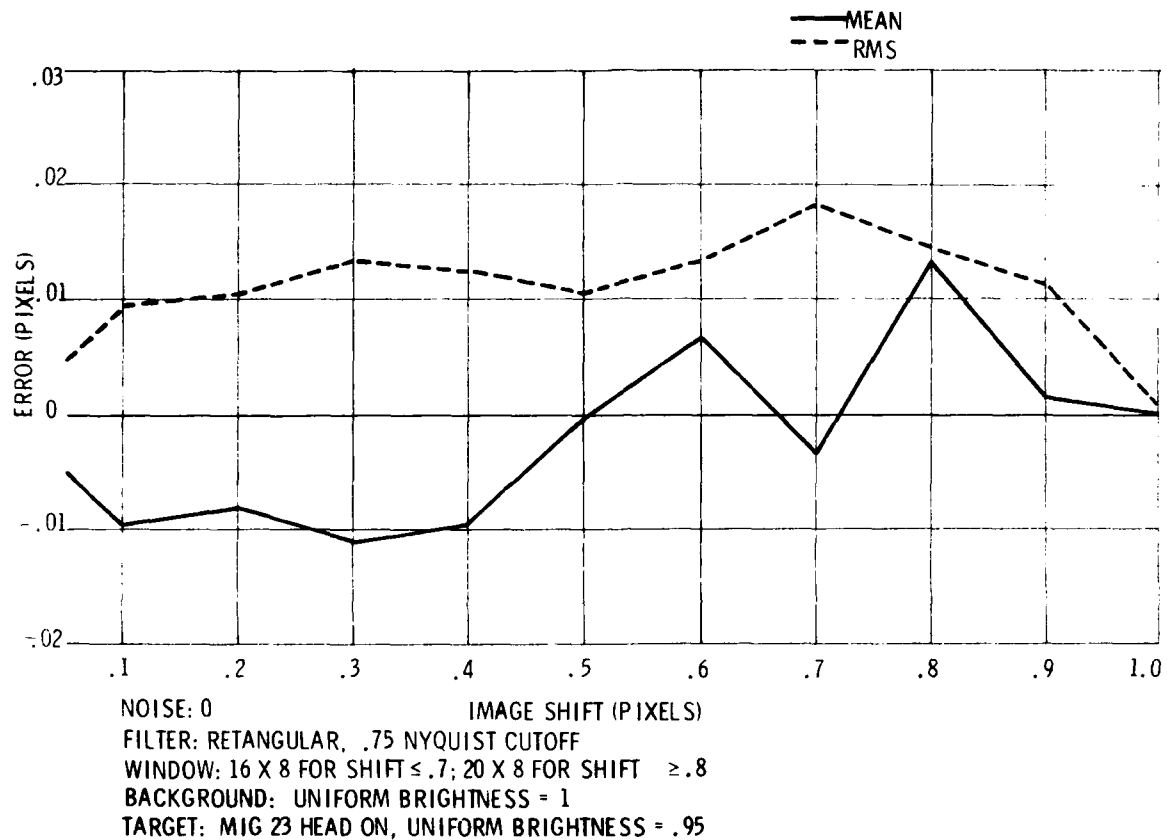


Figure G.7 Ranging Error Vs Cutoff Frequency

Figure G.8 returns to the investigation of actual image displacement at two phases for this new filter. Results are quite promising with errors consistently less than .02 pixels and generally around .01 pixel.

Figure G.9 introduces noise to the calculations showing some general degradation, but still satisfactory accuracies.

At this point several, checks were made on the effects of structured targets and cluttered background. A single test for structured target revealed a 50 percent degradation. This is attributed to an increase in high spatial frequency information. Ranging tests at three different ranges were made with background clutter and the target contrast statistically buried with the same mean brightness and a standard deviation in brightness one-half that of the background. These tests showed a degradation in the mean error, but no appreciable degradation in the rms error. Tracking against a moving background with equal brightness statistics for both target and background showed some effect pulling the misregistration calculation in the direction of background motion, but insufficient to confuse the tracker. As a cross check, the background was held stationary while the target moved. For this case, no appreciable error in tracking was noted. From these results we can conjecture that motion acted as a low pass filter on the scene information and that the correlation algorithm shows a preference for low frequency information. Finally, tracking across a moving horizon was tested, showing wide swings in the tracking error, both in the direction of the horizon motion and in the opposite direction. Thus, with any strongly contrasted, low frequency background, trouble is expected in correlation. Tight windowing alleviates, but does not eliminate, this problem. This area deserves further study to determine the logic required to overcome potential breaklock in these cases.



**Figure G.8 Ranging Error Vs Image Shift (All Phases)**

FILTER: RECTANGULAR

WINDOW: 16 X 8

NOISE: .1 (10:1 S/N)

BACKGROUND: UNIFORM BRIGHTNESS = 1.0

TARGET: MIG 23 HEAD ON,

UNIFORM  
BRIGHTNESS = .95

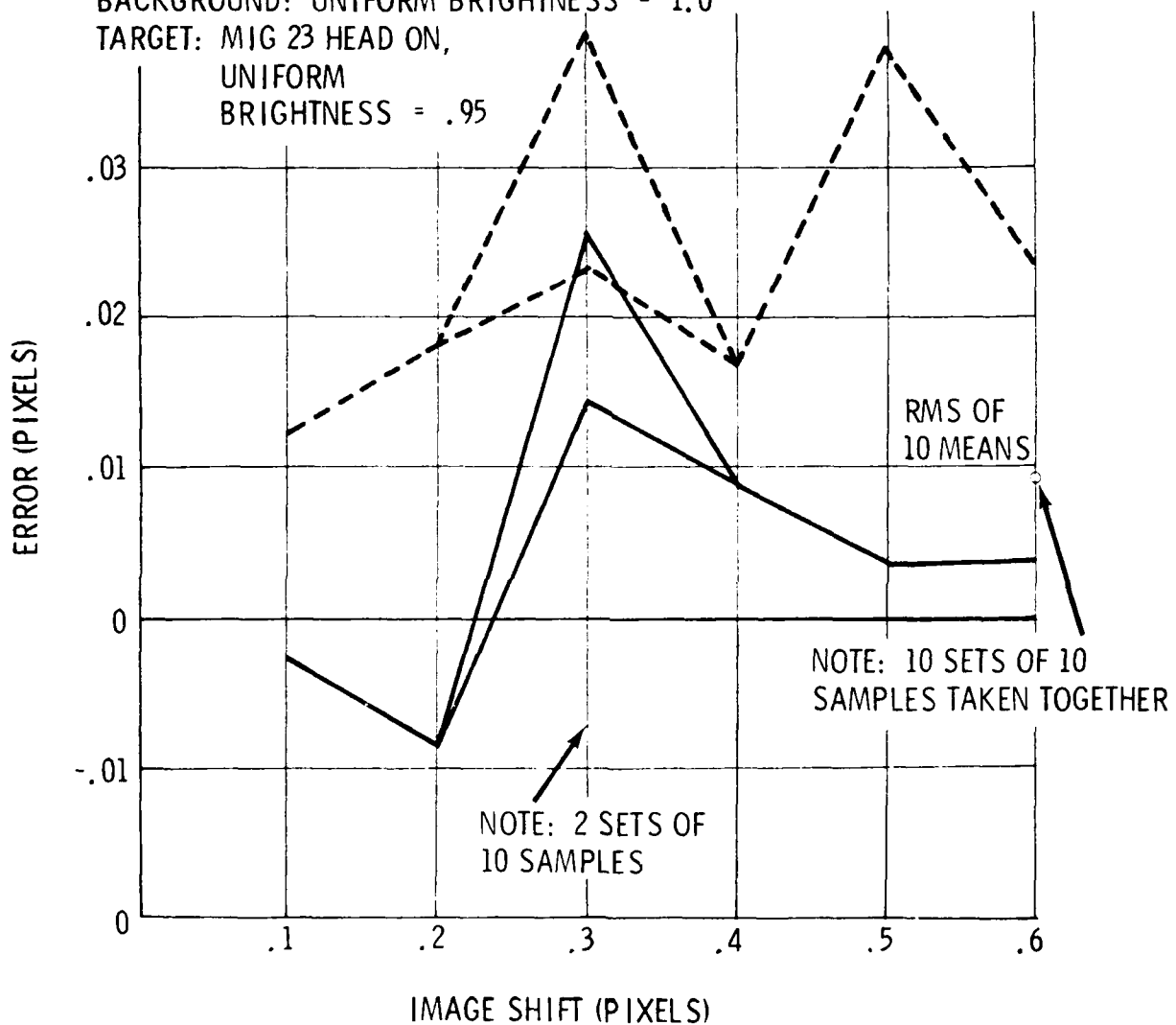


Figure G.9 Ranging Error Vs Image Shift

Giving the target a mean brightness of 1 (same as background), but with internal contrasts of .05, the test for a noiseless case and target range of 4000 ft produced an error of .0195 pixel, compared to the unstructured target error of .0120 pixel. Then, to check the ranging against clutter, the background was composed of overlaid "cluts" 36 pixels in area (random eccentricity and orientation), a density of coverage = .5, mean brightness = 1, standard deviation of brightness = .1. Note that the target is well buried. The target image was rotated 90° to give a less eccentric image and the window size was set at 6 x 6. Five different backgrounds were calculated to give the following results:

Error Statistics (pixels)

Range (ft)	$\bar{\epsilon}$	$\delta_\epsilon$	$R_{ms(\epsilon)}$	$\epsilon_{max}$
5039	.0430	.0407	.0592	.0725
18000	-.0170	.0043	.0175	-.0226
24000	-.0120	.0034	.0125	-.0183

Tracking against clutter was also tested for cluts 25 pixels in area, density of 1, mean brightness = 1, brightness s. dev. = .05, target range = 4000 ft, and with the background moving diagonally, in 1 integration,

Error (pixels)

-.5 pixels	-.0634
-.25 pixels	-.0182

As a cross check with the background stationary and the target moving .1 pixel per integration, 6 x 6 window, target image rotated 90°, cluts covering 36 pixels with a density of 1, mean brightness = 1 and brightness S. Dev. = .05, target range = 7200 ft, the statistics for 5 backgrounds are:

$\bar{\epsilon}$	$\delta_\epsilon$	RMS ( $\epsilon$ )	$\epsilon_{MAX}$
.0071	.0053	.0088	-.0120

Finally, a test was made for tracking across a horizon. For a sky brightness of 2., ground brightness of 1.. and target brightness of 1.5. the horizon starting above the window and moving down through it at a rate of 1 pixel per integration, the results show the tracker giving large errors in one direction and then the other direction. but only on a few frames. The tracker would not be expected to break lock.

In Figure G.10, the results for a real spatial filter to approximate the ideal rectangular frequency filter are graphed. Clearly. the computer results show wholly inadequate results for purposes of ranging.

Comparing the real spatial filter to no filter at all in some sample cases showed questionable utility. Although for a given range, it appeared that there may exist a cutoff which reduces the error to an acceptable level, there is no guarantee that this would hold for all ranges. Again, with no filter, an unstructured target showed considerably improved results compared to a structured target.

Figures G.11 and G.12 compare the error for an unstructured target with no filter and a real spatial filter respectively to Figure G.10 (structured target with real filter). Results are better and roughly equivalent in each case. Nevertheless, at certain ranges the errors are considerably larger than desired, especially considering the mean error.

The effectiveness of ideal low-pass filters was compared with no filter for structured targets at 4000-ft range with no video noise. The errors were:

Cutoff	Error (pixel)
0.75 Nyquist	0.0279
1.00 Nyquist	0.0312
No filter	0.0360
Unstructured target and no filter	0.0021

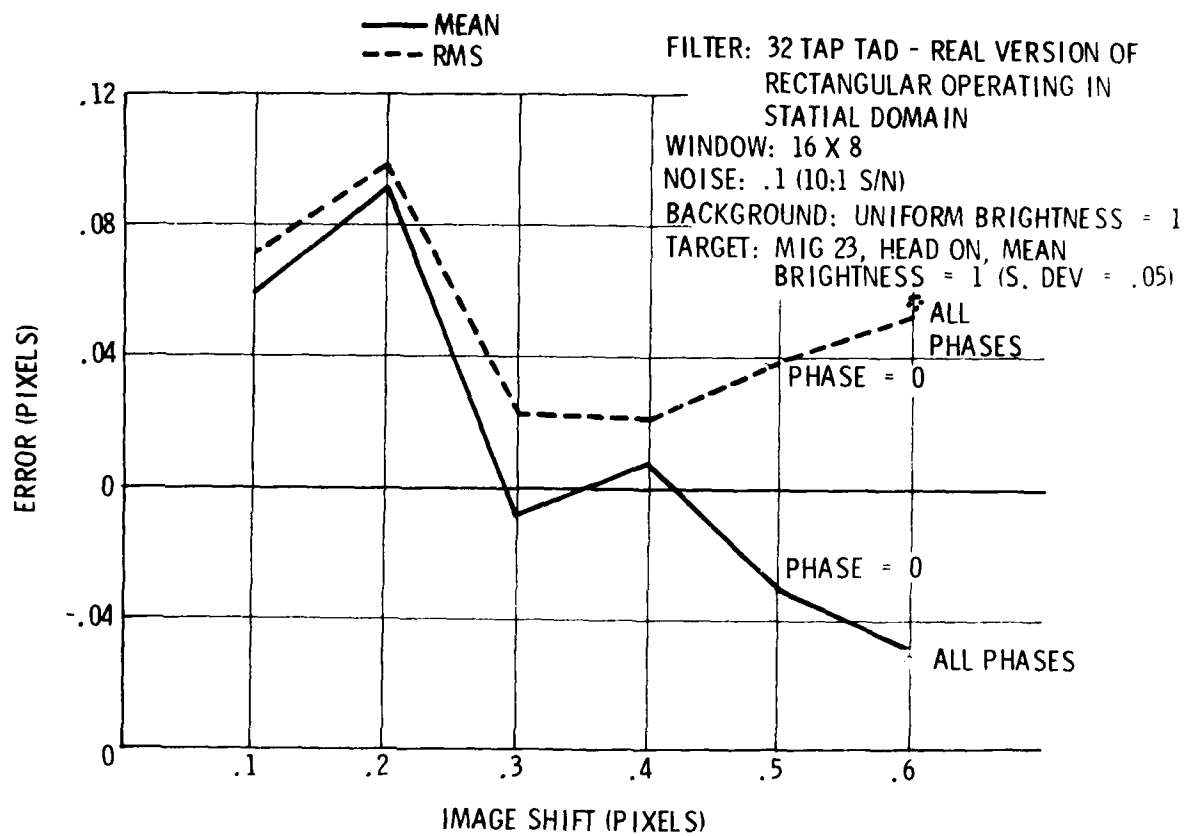
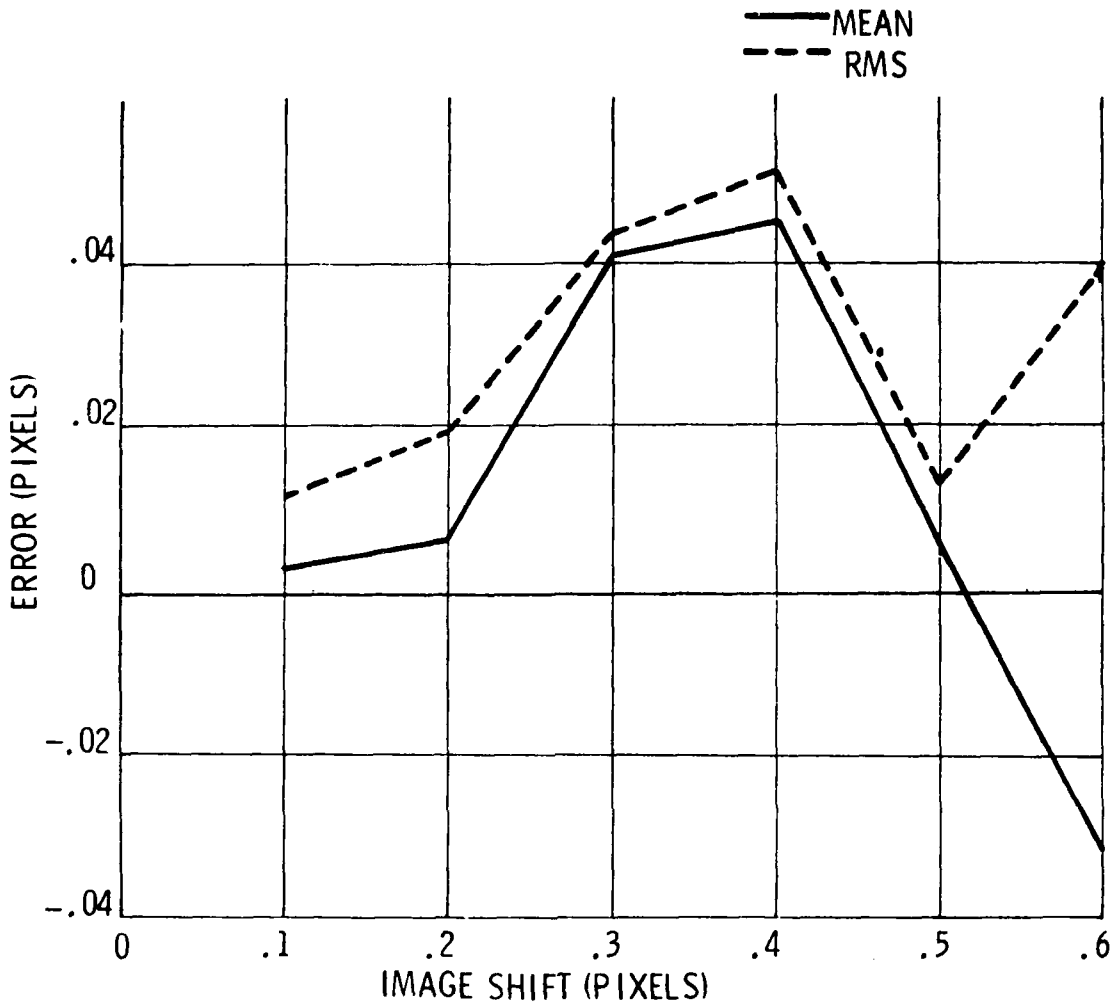
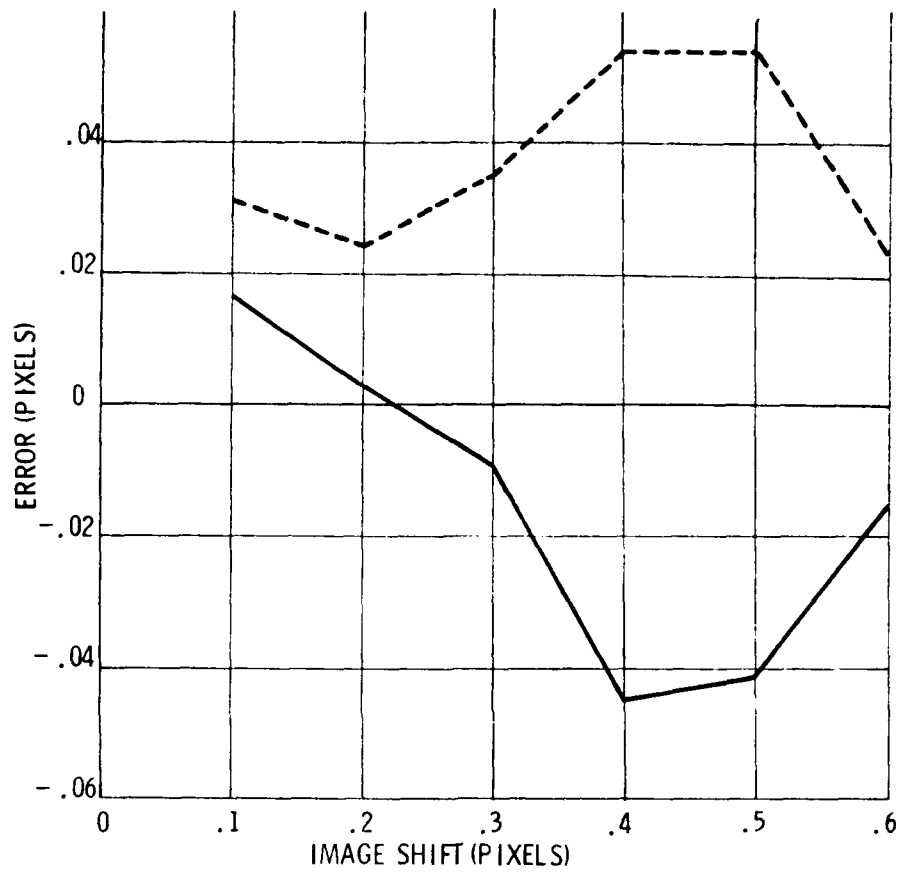


Figure G.10 Ranging Error Vs Image Shift



FILTER: NONE  
 WINDOW: 16 X 8  
 NOISE: 1 (10: 1 S/N)  
 BACKGROUND: UNIFORM BRIGHTNESS = 1  
 TARGET: MIG 23 HEAD ON, UNIFORM BRIGHTNESS = .95

Figure G.11 Range Error Vs Image Shift



FILTER: 32 TAP TAD FILTER  
 REAL SPATIAL  
 VERSION OF .75 NYQUIST CUTOFF  
 RECTANGULAR FILTER  
 WINDOW: 16X 8  
 BACKGROUND: UNIFORM BRIGHTNESS: = 1  
 TARGET: MIG 23 HEAD ON, UNIFORM BRIGHTNESS = .95  
 NOISE: 1 (10: 1 S/N)

Figure G.12 Ranging Error Vs Image Shift

In summary, high spatial frequency scene information appears to increase the expected error in correlation. While an ideal frequency filter gives acceptable results, in nearly all cases, the transformed version of this filter approximated by a 32-tap TAD filter does not work. The conclusion is to either transform the image to apply an ideal filter, find an improved filter for the spatial domain, or close the loop by artificially registering the two images and measuring the displacement by means of the known static image used for autocalibration.

NOTE:

Where "Image Shift" appears as a parameter in the following graphs, specific ranges known to result in such shifts were used. An effect buried in this method is changing image size with range.

Image Shift (pixels)	Range (ft)
.1	23,518
.2	11,759
.3	7,839
.4	5,879
.5	4,703
.6	3,919
.7	3,359
.8	2,939
.9	2,613
1.0	2,354

## APPENDIX H

### Composite Mapping for Target Discrimination

Douglas N. DeFoe

CAI, a Division of Recon/Optical, Inc.  
550 West Northwest Highway, Barrington, Illinois 60010

#### Abstract

Autonomous operation of tracking systems implies the need for abilities which are predicated on discriminating a target from nontarget objects and noise. Intelligent discrimination is most often hampered by lack of explicit information, hence requiring elaborate processing to extract implicit information for an electronic "brain." The fact that it is now possible to construct sensors which provide not only brightness information on a two-dimensional map, but also motion and range on equivalent maps, bypasses the aforementioned processing to directly provide sufficient explicit information for the discrimination of targets. The only processing then required is to combine the information in a composite map such that targets stand out clearly from nontargets. This is particularly true of airborne targets where range and motion are generally quite distinct relative to their background. This general philosophy pertains as well to ground targets, in that sensing directly those characteristics which distinguish them from other objects greatly facilitates the tasks of locating and identifying such targets. For ground targets, sensors designed to sense characteristics such as straight lines, smooth surfaces, color, symmetry and motion would, by use of appropriate composite mapping, detect and acquire predefined classes of targets with high levels of discrimination.

#### Introduction

Under Air Force Contract F33615-78-C-1562, CAI was tasked with conducting the preliminary engineering design of an Advanced E-O Tracker/Ranger system for use on a modern fighter aircraft in a gun director mode. One of the subtasks defined was to develop an approach to long range autonomous detection and acquisition. The system and signal processing as discussed here, while not immediately intended for an autonomous vehicle, is an autonomous system on board a manned platform.

The system is autonomous in the functions of search, detection, acquisition, windowing, tracking and ranging for gun fire control. Notably lacking in the chain for fully autonomous operation are recognition and engagement decisions. Nevertheless, detection is at this point philosophically related to present efforts in recognition, in that these efforts are devoted primarily towards the extraction of attributes known to belong to classes of objects, namely, specific predefined targets, rather than the more general effort of duplicating whatever it is that a brain does when it recognizes objects. Not only is the current approach to recognition a form of detection, but thoughts on engagement decisions also point to a detection form of logic, albeit in this case the detection of target attributes which relate to the importance and threat of a target. Hence, the signal processing which accomplishes detection in this ranger/tracker is extendable in concept to the tasks of recognition and threat assessment required for a fully autonomous vehicle.

#### The System

In order to clarify the problem addressed here, the system up to the point of detection processing needs to be defined. The platform is to be an advanced fighter aircraft operating at its full potential, so that we expect high g forces, wide variation in temperature and pressure associated with subsonic, transonic and supersonic flight and, in general, an extremely hostile environment for an imaging sensor. Furthermore, the engagement scenarios are complex and short lived, and available munitions are in short supply. Shooting first and making it count is of life-and-death importance. The tracker/ranger system is shown in figure 1.

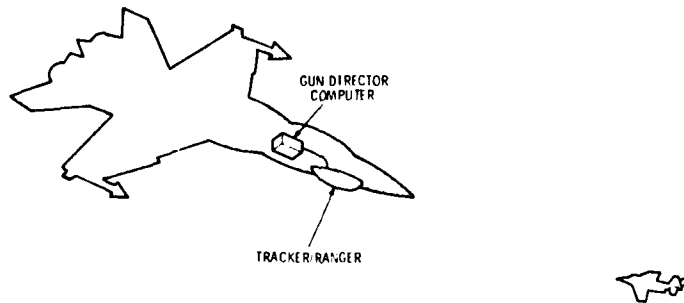


FIGURE 1. TRACKER/RANGER SYSTEM

The target is of course another aircraft. The only signature we can be assured of is 't' at its range is different, generally closer, than the rest of the world and that it must be moving. Secondarily, its size is bounded, it may exhibit a variation in contrast from the background and its shape should be a view of a limited set of volumes. Clearly range, motion and brightness cover most of the distinctive attributes the target possesses.

#### Collection of Information

Fortunately, range and motion are precisely the data which are required to solve the fire control equation and therefore, which the system was designed to provide. Naturally, brightness is the first output. In terms of qualitative information, we have most of what is desired for airborne target detection. This information is gathered by a three-lens imaging subsystem. One of the lenses and charged coupled device (CCD) sensors is used for tracking in the familiar manner as shown in figure 2. Two images of the world are taken, displaced in time. If an object has moved in that time, its motion is detectable by comparing the two images. Correlation of these images allows the measurement of velocity in image space. Two lenses and CCD's, imaging the world with parallel optical axes, are used for ranging. Because the light from an object at a finite distance must enter the two lenses relatively non-parallel, the two corresponding images must be relatively displaced in their respective image planes. Again, by correlation, the image shift can be calculated and the range determined. Knowing the range allows the calculation of the object size and object velocity.

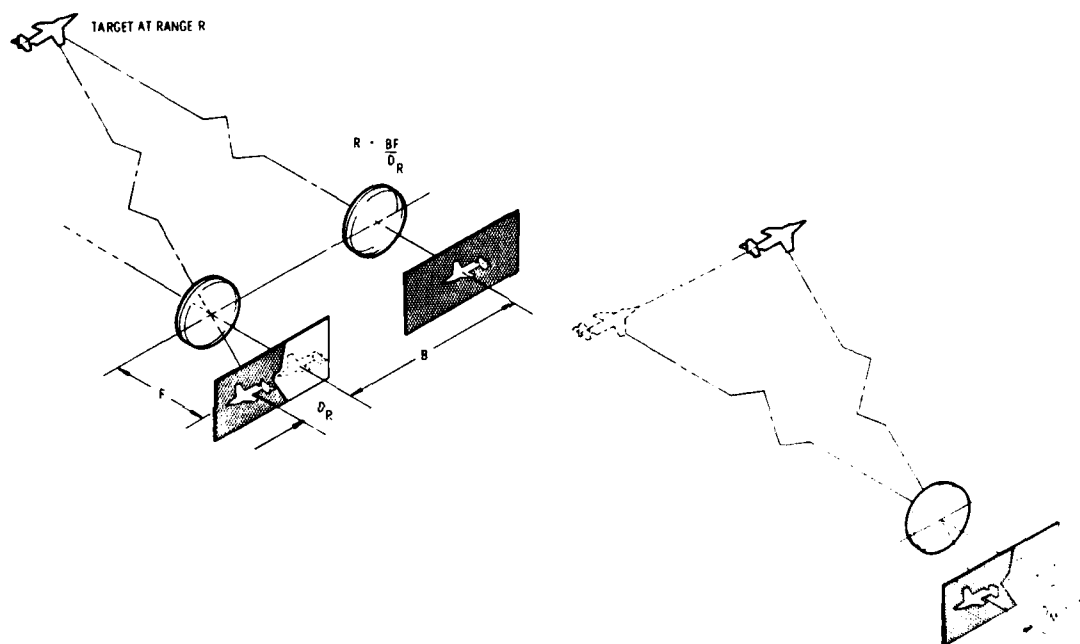


FIGURE 2. RANGING AND TRACKING GEOMETRY

The ability to discriminate objects by means of range and motion depends on the accuracy of measurement which, in turn, depends on the focal length of the lens, the dimension of a pixel, the separation between the two images, be it spatial or temporal, and the inherent limitation of the image displacement measuring algorithm. Without detailing the tradeoffs involved in defining the physical parameters of the system, for the latter factor CAI has achieved correlation accuracies of 1/50th of a pixel for a signal-to-noise ratio of 10:1. With low pass filtering to reduce the effect of noise, the error drops to a fraction of this value. These numbers, shown in figure 3, have been achieved on brassboard demonstration hardware.

The following are the physical parameter values of this sensor: 5-inch focal length; 4.5-inch separation between the range lenses; 4-ms integration time; and  $30 \times 36\text{-}\mu\text{m}$  pixel size. These numbers define the physical accuracies as shown in figure 4.

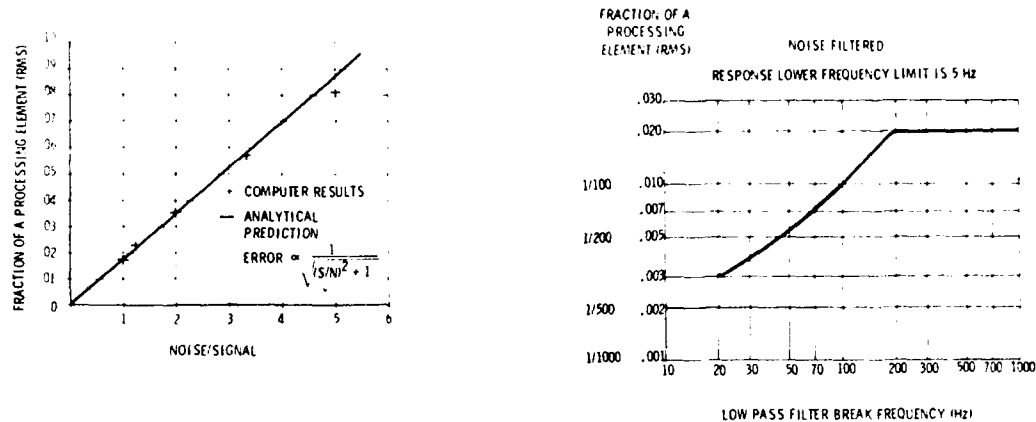


FIGURE 3. CORRELATOR DEMONSTRATOR ACCURACY

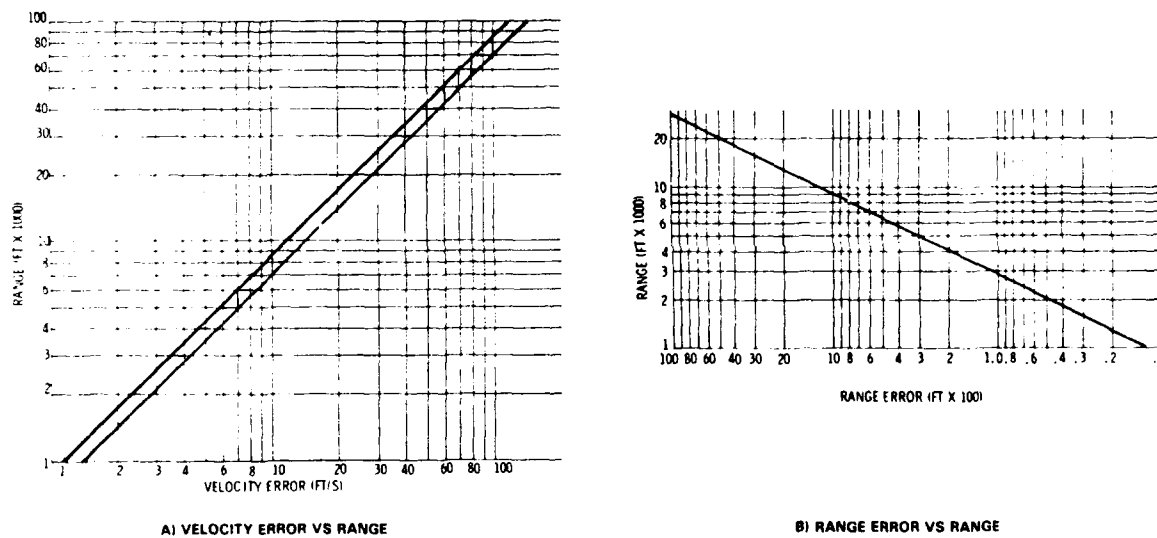


FIGURE 4. ACCURACY IN PHYSICAL UNITS

The package as a whole, shown in figure 5, consists of an approximately spherical, 8-inch diameter head to house the three lenses and CCD's, a third axis torque motor and encoder. A cylinder behind this head houses the primary torque motors, encoders, electronics and other subsystems. The field-of-regard for this tracker is a right angle cone.

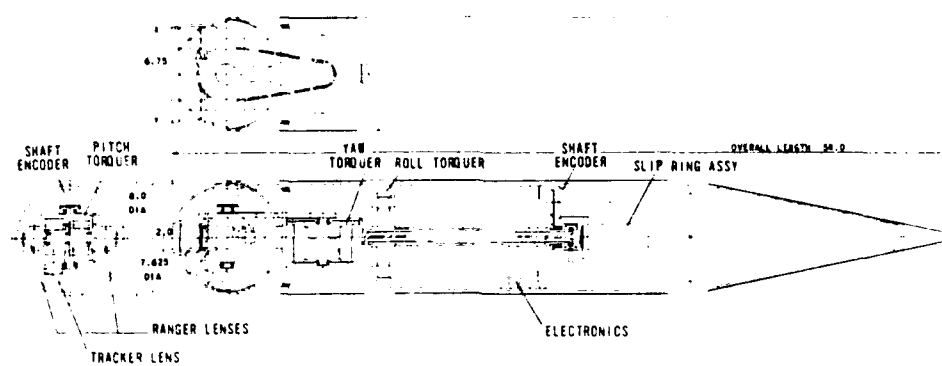


FIGURE 5. AIRBORNE E-O TRACKER

Generation of Attribute Maps

As an overview, the general processing CAI uses is parallel processing to detect the attributes of interest on maps of the field-of-view and combining these raw maps in a composite map by an appropriate equation. This is shown in figure 6. The composite map, then, shows all the positions in the focal plane at which an object with the attributes of a target is imaged. In the equation which combines the various types of information generated, it should be remembered that no single attribute is either necessary or sufficient to define the presence of a target. In other words, we hold to the statement that the probability that an object belongs to a particular class is at least as much a function of degree of concurrence as it is a function of magnitude of occurrence.

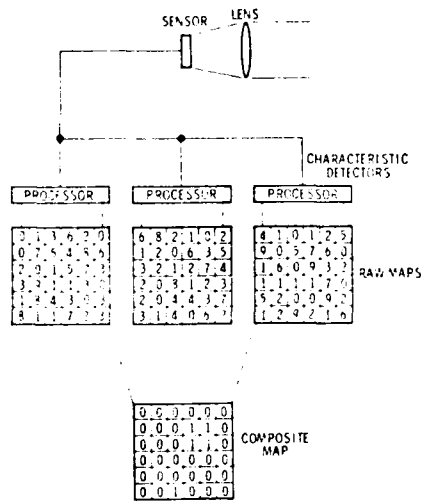


FIGURE 6. COMPOSITE MAPPING

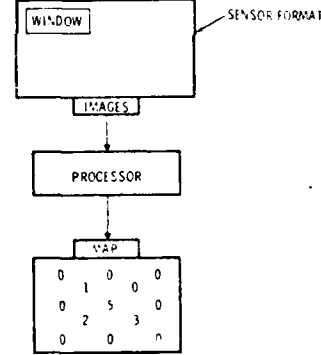


FIGURE 7. INFORMATION FLOW

Obtaining a map format for brightness is quite obvious. However, it is less clear how to generate such maps of correlation data, especially at rates of 250 frames of 23,180 pixels each per second. This process, shown in figure 7, will be described in some detail. To begin with, correlation is done on small subframes or windows in the field-of-view. Adequate correlation accuracy is achieved with windows as small as 36 pixels (6 x 6). By shifting the windows about in the field, correlation results for an array of windows can be determined. If the shift is on a pixel-by-pixel basis, the correlation results are generated essentially on a pixel-by-pixel basis. While this may appear to be a case of oversampling because the window is six times larger in each direction than the sample spacing, in fact CAI's processing algorithm tends to distinguish between two correlation curves even when those curves are superimposed and displaced from one another by less than a pixel. Thus, the resolution of correlation processing is considerably better than the window size alone would lead one to believe.

Having described how the generation of raw attribute maps can be accomplished conceptually, the means of achieving speed of operation remains to be shown. As mentioned above, the integration time for the sensors is 4 ms. In fact, this time was determined by the ability to correlate the set of 21,344 windows [(190-6) x (122-6)] in a frame. The processing which allows this high speed is a pipeline implementation of CAI's correlation algorithm which is shown in figure 8. Essentially, the correlation result (image shift) is built up as the CCD's are read out. After the last pixels of a window have been read, only a few arithmetic operations remain to compute the fractional pixel image shift. Being able to match the correlation speed to the imagery rate allows an expansion of the pipeline operation to processing the set of windows in pipeline. Since the correlation result is built on summing partial results, these partial results can be manipulated to give a running output of image displacement similar to a video signal and at the same rate as the actual video signal. With a slight delay in the video, the three signals of range, motion and brightness are output in parallel.

These signals are now used in a target detection processor. First, the considerations which define the equation need to be addressed.

1) Brightness is not in itself reliable information. In the absence of range or motion information indicating the probable presence of a target, brightness variation should be ignored. However, where range or motion information indicates the presence of a target, unusual brightness should be considered corroborating information.

2) Against a fairly close background, it is uncertain whether range or motion of a target will be a distinctive characteristic. However, against a nearly infinitely distant background, target range is assured to be a distinctive characteristic. Hence, for a mean range greater than some threshold, it is appropriate to weight the equation in favor of range information.

3) Because the system is mounted in an airborne platform, motion information is relative rather than absolute. Furthermore, if there is a target in the field-of-view, it is not known a priori whether an exceptional or unusual value for motion would pertain to a target or to background. For a target covering a small portion of the field, target motion would be unusual, while for a target covering a large portion of the field, the background motion would be the unusual value. This ambiguity can be resolved if one assumes that targets are always nearer in range than background. For any composite map location, then, the sign of the amplitude should be solely determined by the range map value for that location.

4) Motion can be reduced from a vector to a scalar because, for this application, we are interested only in detecting a distinctive vector. The reduction of order is accomplished by subtracting the mean vector and taking the magnitude of the resultant for each map location.

5) Again, because only distinctive values are of interest for detection and acquisition, each map should be normalized by subtracting the mean and dividing by the standard deviation prior to the generation of a composite map.

Taking these considerations into account, the equation for amplitude of the scalar map at location (i, j) is given by:

$$C_{ij} = \left[ D_{M, ij} \frac{D' R_{ij}}{|D' R_{ij}|} + D' R_{ij} \right] \times \left[ |B_{ij}| + 1 \right]$$

where:

$C_{ij}$  = composite map value

$D_{M, ij}$  = normalized scalar motion map value

$D' R_{ij}$  = normalized range map value allowing for the weighting discussed above

$B_{ij}$  = is the normalized grey level

The range map is weighted by offsetting the mean value to a value midway between the actual mean and the value for the maximum desired detection range. The effect is to make it much less probable that composite map values for background will be positive, and only slightly less probable that values for targets will be positive. Because the motion and brightness components are absolute valued, a stronger distinction between target and background is forced.

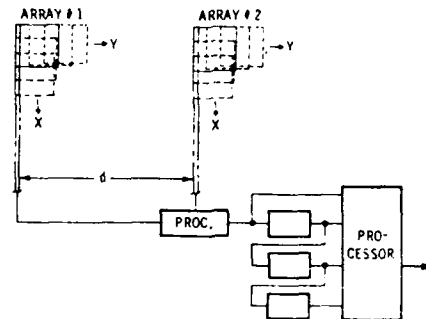


FIGURE 8. PIPELINE SUBFIELD PROCESSING

By this equation, a composite map is generated. A threshold is set as a tradeoff between false alarm rate and probability of detection. A further constraint on the detection logic is imposed such that three adjacent map locations must have amplitudes greater than threshold for the system to indicate the presence of a target.

At this point, several features of this method of processing are worth enumerating. First, detection, acquisition and windowing are all accomplished by this single mapping, in that acquisition is merely a decision to track a detected target and the window is automatically defined as that set of pixels on which a target is detected. Secondly, multiple targets are processed in parallel. Further, the composite map value is more a measure of confidence in the presence of a target than a measure of some specific attribute. Reacquisition is efficiently accomplished with level gating prior to normalization of the raw maps, such that the processing ignores values of brightness, range and motion outside of calculated bounds on the last known values of the target. As the time since breaklock lengthens, the bounds expand until the system has reverted to the acquisition mode. In addition, the composite map can be filtered for position so that the expected position of the target is weighted more heavily than the surround. In fact, this entire detection logic can be used as a sort of combined moving target, centroid and floating range tracker. Finally, the constraint of spatial coherence has been imposed by the three adjacent pixel rule as a heavy noise filter. A similar constraint of temporal continuity could be imposed after lockon as a further noise filter, but for the sake of covering the field-of-regard in a reasonable time, was not included for the detection mode. Nevertheless, a false alarm due to noise would be expected to disappear on the subsequent frame and thus have minimal effect on the system.

#### Summary

A block diagram of the signal processing for the entire system is given as figure 9. Starting with the sensors at the left, image data flows into the ranging processor and the tracking processor and from these to the control computer and on to the gun director computer. External cuing and tracking commands are allowed. The bottom of the diagram shows the detection processor using only imagery from the ranging sensors. The tracker sensor is not used because that lens has a shorter focal length and thus a scaled format. The detection logic has its own correlation processing implemented in pipeline for both motion and range. The three raw maps are input to the composite mapper and from there to the detection computer, which essentially consists of the thresholding, three adjacent pixels and object size logic. Output from this computer are the windows and confidence measure of detected targets to the system control computer for lockon and tracking decision.

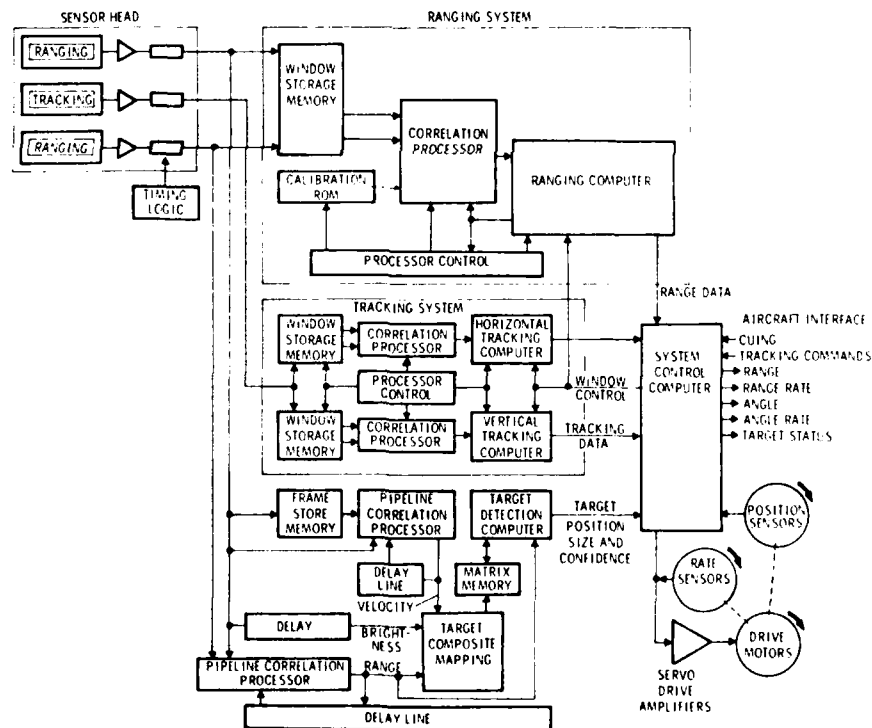


FIGURE 9. TRACKER/RANGER BLOCK DIAGRAM

### Results

Excellent results have been predicted on computer statistical runs for probability of detection. In the following results, the threshold level has been set to keep the false alarm rate at one per hour and at one per 10 min. In general, the effect is not great and the operator can set the threshold, depending on personal tolerance to nuisance and threat environment without agonizing over the decision. Also, in each of the following figures are three curves showing the effect of target image coverage in pixels. The variation between 4, 9 and 16 pixels of coverage shows significant effect. To give these numbers some meaning at the ranges in question, we would expect a target about the size of a MIG 23 to cover from 4 pixels for a head-on view to 36 pixels for a full top or bottom view.

Figures 10 and 11 show results for a target at a range of 18,000 ft against an infinitely distant background. The former shows the effect of motion (perpendicular to the line-of-sight) assuming brightness of the target to be statistically indistinguishable from the background. The latter shows the effect of some mean brightness difference in terms of standard deviations of the entire frame, exclusive of any detectable motion.

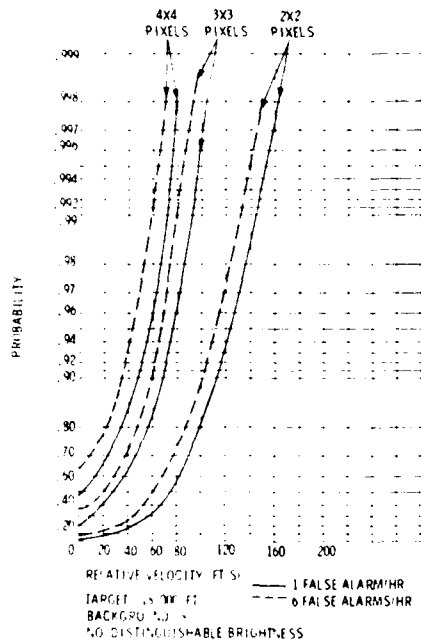


FIGURE 10.  
PROBABILITY OF DETECTION VS VELOCITY

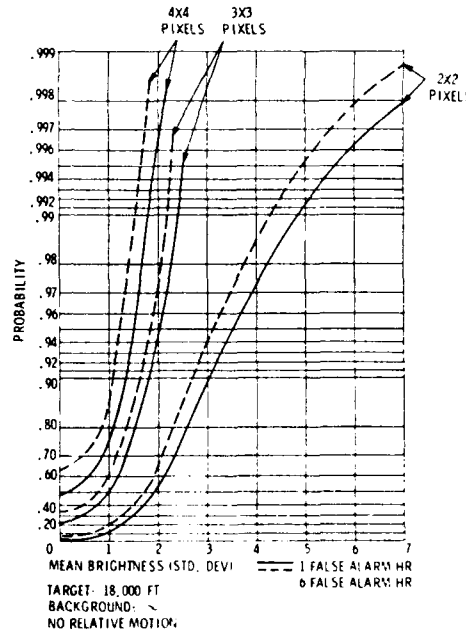


FIGURE 11.  
PROBABILITY OF DETECTION VS BRIGHTNESS

Figures 12 and 13 show similar results for a target at 24,000-ft range and figure 14 shows results for the case of virtually indistinguishable range as in looking down at a low flying target. In this graph, motion is the only information on which the mapping equation is working, as brightness is again considered statistically buried in the background.

Clearly, both the discriminating abilities of the system and the composite mapping method show that the system should detect targets in even the worst cases. In general, a target is expected to have combinations of range, motion, brightness and coverage which will show significantly improved detection probabilities than these limited cases show. Equally important is the low false alarm rates achievable for these results which should be more than satisfactory for either man in the loop or autonomous systems.

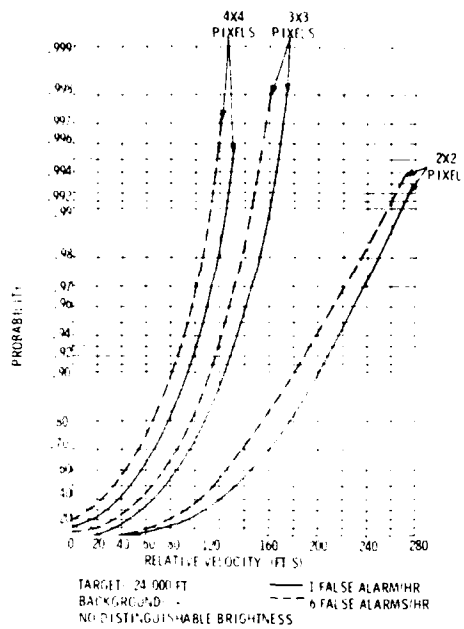


FIGURE 12.

#### PROBABILITY OF DETECTION VS VELOCITY

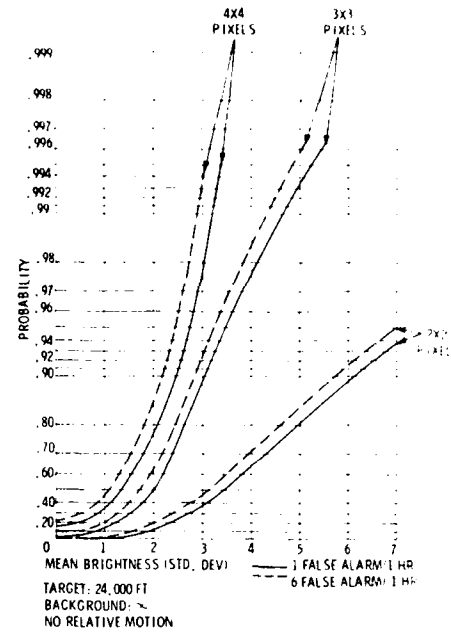


FIGURE 13.

#### PROBABILITY OF DETECTION VS BRIGHTNESS

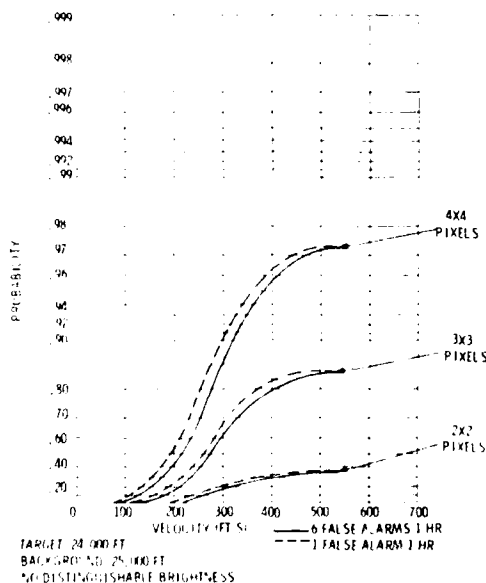


FIGURE 14.

#### PROBABILITY OF DETECTION VS VELOCITY

#### Conclusions

As demonstrated by the Advanced E-O Tracker/Ranger system designed by CAI, composite mapping is a technique which offers the ability to detect and acquire targets of a particular class with great precision, as well as provide an automatic windowing function. Since this technique is essentially a form of image processing which, loosely speaking, makes objects of a particular class "bright," multiple targeting is a built-in feature. Further, it has potential as a method of target recognition. Carrying the analogy of brightening targets along, some characteristics which indicate target type within a class can be included to give the map "color." Threat assessment might require a different set of characteristics, but is just as easily implemented. It is not difficult to perform a variety of analyses once the hardware for mapping various characteristics exists in a sensor. Both motion detection and range detection are realizable procedures with today's technology. Together, they provide the basis for the autonomous targeting of aircraft by passive imaging sensors.